Acta Pharmacologica Sinica (2010) 31: 137–144
© 2010 CPS and SIMM All rights reserved 1671-4083/10 $32.00
www.nature.com/aps

Original Article

Baicalin attenuates oxygen-glucose deprivation-induced injury by inhibiting oxidative stress-mediated 5-lipoxygenase activation in PC12 cells

Cheng-tan LI[1, 2], Wei-ping ZHANG[1], San-hua FANG[1], Yun-bi LU[1], Li-hui ZHANG[2], Ling-ling QI[1], Xue-qin HUANG[1], Xiao-jia HUANG[1], Er-qing WEI[1, *]

[1]Department of Pharmacology, School of Medicine, Zhejiang University, Hangzhou 310058, China; [2]Hangzhou Key Laboratory of Neurobiology and Department of Pharmacology, School of Basic Medicine, Hangzhou Normal University, Hangzhou 310036, China

---

Aim: To determine whether the flavonoid baicalin attenuates oxygen-glucose deprivation (OGD)-induced injury by inhibiting oxidative stress-mediated 5-lipoxygenase (5-LOX) activation in PC12 cells.
Methods: The effects of baicalin and the 5-LOX inhibitor zileuton on the changes induced by OGD/recovery or H_2O_2 (an exogenous reactive oxygen species [ROS]) in green fluorescent protein-5-LOX-transfected PC12 cells were compared.
Results: Both baicalin and zileuton attenuated OGD/recovery- and H_2O_2-induced injury and inhibited OGD/recovery-induced production of 5-LOX metabolites (cysteinyl leukotrienes) in a concentration-dependent manner. However, baicalin did not reduce baseline cysteinyl leukotriene levels. Baicalin also reduced OGD/recovery-induced ROS production and inhibited 5-LOX translocation to the nuclear envelope and p38 phosphorylation induced by OGD/recovery and H_2O_2. In contrast, zileuton did not show these effects.
Conclusion: Baicalin can inhibit 5-LOX activation after ischemic injury, which may partly result from inhibition of the ROS/p38 mitogen-activated protein kinase pathway.

Keywords: baicalin; 5-lipoxygenase; rat pheochromocytoma (PC12) cell; oxygen-glucose deprivation; reactive oxygen species; p38 mitogen-activated protein kinase

---

Acta Pharmacologica Sinica (2010) 31: 137–144; doi: 10.1038/aps.2009.196

Introduction

5-Lipoxygenase (5-LOX, EC 1.13.11.34) is a key enzyme in catalyzing the conversion of arachidonic acid to its metabolites, including leukotriene B_4 (LTB_4), cysteinyl leukotrienes (CysLTs, namely LTC_4, LTD_4, and LTE_4) and 5S-hydroxy-6,8,11,14-eicosatetraenoic acid (5-HETE)[1, 2]. 5-LOX is distributed in the cytosol, nucleus, or both in resting cells depending on the cell type[2, 3]. When cells are stimulated, 5-LOX is translocated from the intracellular pool to the nuclear envelope where it interacts with its co-factors, 5-LOX activating protein (FLAP) and phospholipase A_2, to form an active complex for metabolite production[3]. Therefore, as one of the characteristics of 5-LOX activation, its translocation to the nuclear envelope is critical for its enzymatic activation and is a target for anti-inflammatory 5-LOX inhibitors[3].

5-LOX metabolites play an important role in inflammatory diseases of the peripheral tissues and the central nervous system, such as bronchial asthma[4, 5] and ischemic brain injury[6–9]. In these diseases, various stimuli activate 5-LOX through two main ways. Specifically, elevation of intracellular calcium that generally occurs after excitotoxicity and mitogen-activated protein kinase (MAPK)-regulated phosphorylation that can be induced by oxidative stress[3] both activate 5-LOX. Previously, we reported that 5-LOX can be activated after ischemic brain injury in rats[8, 10], after oxygen-glucose deprivation (OGD)-induced ischemic injury in cultured neurons and in pheochromocytoma (PC12) cells[11–14]. In primary neuron cultures, OGD induces release of excitatory amino acids that activate NMDA receptors to elevate intracellular calcium, resulting in 5-LOX translocation to the nuclear envelope and activation of 5-LOX to produce CysLTs[12]. Calcium-dependent 5-LOX activation is also found in PC12 cells after exposure to NMDA[15]. In addition, we recently found oxidative stress-induced 5-LOX activation in ischemic PC12 cells. OGD increases the release of reactive oxygen species (ROS), which activate 5-LOX through the p38 MAPK pathway[14]. Therefore, ischemic 5-LOX activation

---

[*] To whom correspondence should be addressed.
E-mail weieq2006@zju.edu.cn
Received 2009-10-22 Accepted 2009-12-03

can be regulated by both elevated intracellular calcium after excitotoxicity and the activated MAPK pathway after oxidative stress.

Baicalin is one of the predominant flavonoids isolated from the dry roots of *Scutellaria baicalensis* Georgi (Huang Qin) with multiple pharmacological effects in peripheral organs and tissues[16–19]. Baicalin also exerts a protective effect on ischemic brain injury[20–23]. Previously, we reported that baicalin attenuates *in vitro* ischemic-like injury in rat primary cortical neurons[13] and hippocampal slices[24], and this effect partly relates to the inhibition of NMDA receptor-mediated 5-LOX activation in the neurons[13].

Thus, baicalin can inhibit ischemic 5-LOX activation induced by excitotoxicity; however, whether it also inhibits oxidative stress-induced 5-LOX activation is unknown. Therefore, to determine whether baicalin can inhibit oxidative stress-induced 5-LOX activation, we investigated the effect of baicalin on the changes induced by OGD and hydrogen peroxide (H_2O_2, an exogenous ROS) in green fluorescent protein (GFP)-5-LOX-transfected PC12 cells. To clarify the properties of 5-LOX inhibition, we compared the effects of baicalin and the 5-LOX inhibitor zileuton, an iron-ligand inhibitor, on these cells following OGD[25, 26].

Materials and methods

Materials

Dulbecco's modified Eagle's medium (DMEM) and horse serum were purchased from Gibco (Carlsbad USA). Fetal bovine serum (FBS) was obtained from Sijiqing Biol Inc. (Hangzhou, China). The polyclonal antibody against 5-LOX and CysLT enzyme immunoassay (EIA) kit were purchased from Cayman Chemicals (Ann Arbor, MI, USA). The monoclonal antibody against phosphorylated p38 and the polyclonal antibody against p38 were obtained from Santa Cruz Biotechnology Inc (Santa Cruz, USA). 3-(4,5-dimethyml-2-thiazolyl)-2,5-diphenyl-2H-tetraxolium bromide (MTT), 2,7-dichlorofluorescin diacetate (DCF-DA), baicalin, and H_2O_2 were purchased from Sigma-Aldrich (St Louis, USA) and zileuton from Gaomeng Pharmaceutical Co (Beijing, China).

Cell culture and 5-LOX transfection

PC12 cells were purchased from the Institute of Cell Biology at the Chinese Academy of Sciences (Shanghai, China) and maintained at 37 °C in a humidified incubator containing 5% CO_2 in high-glucose DMEM supplemented with 10% heat-inactivated horse serum, 5% FBS, 100 U/mL penicillin and 100 μg/mL streptomycin.

The pEGFP-C2/5-LOX (GFP-5-LOX) and pEGFP-C2 null vectors (gifts from Professor Funk CD, University of Pennsylvania, USA [now in Queen's University, Canada]) were transfected into PC12 cells as we recently reported[14]. PC12 cell lines stably expressing GFP or GFP-5-LOX have been characterized by fluorescence microscopy and Western blot analysis[14]. To detect GFP-5-LOX translocation, the transfected cells cultured on glass slips were washed with phosphate buffered saline (PBS) and immediately fixed with 4% paraformaldehyde. Then the cells were observed under a fluorescence microscope (Olympus BX51, Tokyo, Japan).

OGD, H_2O_2 and agent treatments

PC12 cells were exposed to OGD as described previously[11, 12, 14]. Briefly, cells were rinsed twice and incubated in glucose-free Earle's solution. The cells were then introduced into an anaerobic chamber containing a mixture of 95% N_2 and 5% CO_2 at 37 °C for 2 h. This procedure decreased pO_2 in the solutions from 154.0±7.3 to 23.9±5.1 mmHg (mean±SD, n=5). At the end of 2-h OGD, the media were replaced and cells were cultured in normal condition for 0.5 h (for ROS measurement), 1.5 h (for p38 determination), 2 h (for 5-LOX translocation), 3 h (for measurement of CysLTs) or 24 h (for cell viability) of recovery, as previously reported[14]. H_2O_2 was freshly prepared from an 8.8 mol/L stock solution before use, and PC12 cells were treated with H_2O_2 160 μmol/L for 20 min (for p38 determination), 40 min (for 5-LOX translocation) or 24 h (for cell viability) at 37 °C, as previously reported[14]. Baicalin and zileuton at designated concentrations were continuously applied from 30 min before exposure to OGD or H_2O_2 until the end of recovery or H_2O_2 treatment.

Cell viability and death assay

Cell viability was determined by MTT assay. Briefly, at the end of the experiments, the cells cultured on 96-well plates were incubated with 0.5 mg/mL MTT for 2 h at 37 °C. Then the supernatant was carefully removed, 100 μL of dimethyl sulfoxide was added into each well, and the absorbance of 490 nm of the MTT product formazan was determined on a Microplate Recorder (ELX 800, Bio-TEK instruments Inc, USA). The results are expressed as the percentage of control. Because the main type of OGD/recovery-induced cell death is necrosis[14], we detected necrotic cells by propidium iodide (PI) staining. Cells were planted on glass coverslips. After treatment, cells were stained with 10 mg/mL of PI (Sigma-Aldrich) for 10 min at 37 °C. Then the cells were photographed under a fluorescence microscope (Olympus BX51) at excitation and emission wavelengths of 536 nm and 620 nm, respectively. The necrotic cells with red nuclei stained by PI were counted by a researcher who was blind to the treatments, and reported as percentages of total cells.

Western blotting analysis

Cells were collected and washed twice with ice-cold PBS, pH 7.4, then lysed for 30 min on ice in lysis buffer (100 mmol/L NaCl, 1% Nonidet P-40, 0.1% SDS, 1% deoxycholic acid, 10% glycerol, 1 mmol/L EDTA, 1 mmol/L sodium orthovanadate, 50 mmol/L sodium fluoride, 1 mmol/L phenylmethylsulfonyl fluoride, 10 μg/mL leupeptin, and 1 μg/mL aprotinin). Cell lysates were obtained by centrifugation at 12000×g for 15 min at 4 °C. Protein samples (60 μg) were separated by 10% sodium dodecyl sulfate (SDS)-polyacrylamide gel electrophoresis and transferred to nitrocellulose membranes. The membranes then were blocked by 10% fat-free milk and incubated with a mouse monoclonal antibody against phosphorylated p38 (1:300) or a rabbit polyclonal antibody against p38 (1:300). Then they were incubated with horseradish peroxidase (HRP)-conjugated goat anti-rabbit IgG (0.16 mg/L, Sigma-Aldrich) or HRP-conjugated goat anti-mouse IgM (1:3000, Zhongshan Biotechnology, Beijing, China) after repeated washing. Finally, the membranes were incubated with enzymatic chemiluminescence reagents and exposed on an X-ray film. The protein bands on the X-ray film were quantitatively analyzed with a laser densitometer (Ultro Scan XL, Pharmacia LKB Co, Stockholm, Sweden).

Measurement of CysLTs

Samples (100 μL) were removed from culture media after 2-h OGD and 0.5-h recovery and prepared according to previously reported method[12, 14]. Produced CysLTs (including LTC_4, LTD_4, and LTE_4) were measured by EIA kits according to the manufacturer's instructions and calculated as pg/mg protein.

Measurement of intracellular ROS

Following 2-h OGD and 0.5-h recovery, cells cultured on 96-well plate were rinsed with Earle's solution and incubated with 25 μmol/L DCF-DA in Earle's solution with glucose for 30 min at 37 °C. Then the cells were rinsed twice to remove excess probe, and fluorescence was measured with a multiwell plate fluorescence reader (FluoStar, Offenburg, Germany). The results are expressed as the percentage of control.

Statistical analysis

Data are reported as mean±SD. Statistical comparisons were made by one-way ANOVA followed by Tukey's multiple comparisons tests or unpaired Student's *t*-tests to detect significant difference using SPSS 10.0 for Windows. $P<0.05$ was considered to be statistically significant.

Results

OGD/recovery-induced injury

Cell injury was aggravated in GFP-5-LOX-transfected PC12 cells after 2-h OGD and 24-h recovery. Baicalin (1–10 μmol/L) and zileuton (1–100 μmol/L) attenuated the reduction in cell viability after OGD/recovery in both GFP- and GFP-5-LOX-transfected PC12 cells (Figure 1A and 1B). In addition, baicalin (0.1 μmol/L) increased the cell viability in GFP-5-LOX-transfected PC12 cells (Figure 1A). As analyzed by PI staining (Figure 1C), baicalin (0.1–10 μmol/L) and zileuton (0.1–10 μmol/L) reduced OGD/recovery-induced necrosis in a concentration-dependent manner (Figure 1D and 1E). Baicalin (0.01 μmol/L) also reduced the necrosis in GFP-5-LOX-transfected PC12 cells (Figure 1D). These results confirm that OGD/recovery injury was more severe in GFP-5-LOX-transfected PC12 cells than in GFP-transfected cells and indicate that both agents exerted protective effects on OGD/recovery-induced cell injury.

OGD/recovery-induced 5-LOX translocation

The transfected GFP-5-LOX was localized in cell nuclei, as determined by fluorescence microscopy. Specifically, GFP-5-LOX was translocated into the nuclear envelope after 2-h OGD and 2-h recovery (Figure 2A). Baicalin (0.1–10 μmol/L) significantly inhibited GFP-5-LOX translocation in a concentration-dependent manner, but zileuton did not have this effect (Figure 2B and 2C).

OGD/recovery-induced production of CysLTs

After 2-h OGD and 3-h recovery (a peak time point for CysLT production), CysLT levels increased from 139.8±13.9 to 261.1±33.7 pg/mg proteins in the culture media. Baicalin and zileuton (10 μmol/L) significantly reduced OGD/recovery-induced production of CysLTs. However, baicalin, but not zileuton, did not reduce the baseline level of CysLTs (Figure 3). We did not measure CysLT levels after exposure to H_2O_2 because the measurement failed in our recent study[14].

OGD/recovery-induced ROS production and H_2O_2-induced injury

We measured intracellular levels of ROS by 2,7-dichlorofluorescin diacetate (DCF-DA) assay in the wild-type PC12 cells but not in the GFP- or GFP-5-LOX-transfected cells because the GFP fluorescence interferes with the fluorescence generated in the assay. After 2-h OGD and 0.5-h recovery (a time point when ROS production reached the maximum), ROS increased from 100%±11% to 412%±93%. Baicalin (0.1–10 μmol/L) reduced ROS production in a concentration-dependent manner, but zileuton did not affect ROS production (Figure 4A and 4B).

To further determine the effects of baicalin and zileuton on oxidative stress-induced injury, we used the exogenous ROS H_2O_2 to induce oxidative injury in PC12 cells. H_2O_2 (160 μmol/L) reduced cell viability more profoundly in GFP-5-LOX-transfected cells than in GFP-transfected cells. However, baicalin and zileuton (1–10 μmol/L) significantly decreased the reduction in viability (Figure 4C and 4D). Baicalin (0.1 μmol/L) also reduced H_2O_2-induced cell injury in GFP-5-LOX-transfected PC12 cells (Figure 4C).

H_2O_2-induced 5-LOX translocation

Similar to OGD injury, H_2O_2 (160 μmol/L for 40 min) induced GFP-5-LOX translocation to the nuclear envelope by 54.7%±7.3%. Furthermore, baicalin (1−10 μmol/L) inhibited GFP-5-LOX translocation in a concentration-dependent manner, but zileuton did not (Figure 5).

Phosphorylation of p38

Phosphorylation of p38 is induced by OGD/recovery (the maximum phosphorylation was induced by 2-h OGD and 1.5-h recovery) or H_2O_2 (the maximum by 160 μmol/L for 20 min)[14]. Thus, we observed the effects of the agents on p38 phosphorylation after OGD/recovery and exposure to H_2O_2 in such conditions. We found that baicalin (1−10 μmol/L), but not zileuton (1−10 μmol/L), significantly inhibited p38 phosphorylation induced by OGD/recovery and H_2O_2 (Figure 6).

Discussion

In the present study, we found that baicalin attenuated isch-

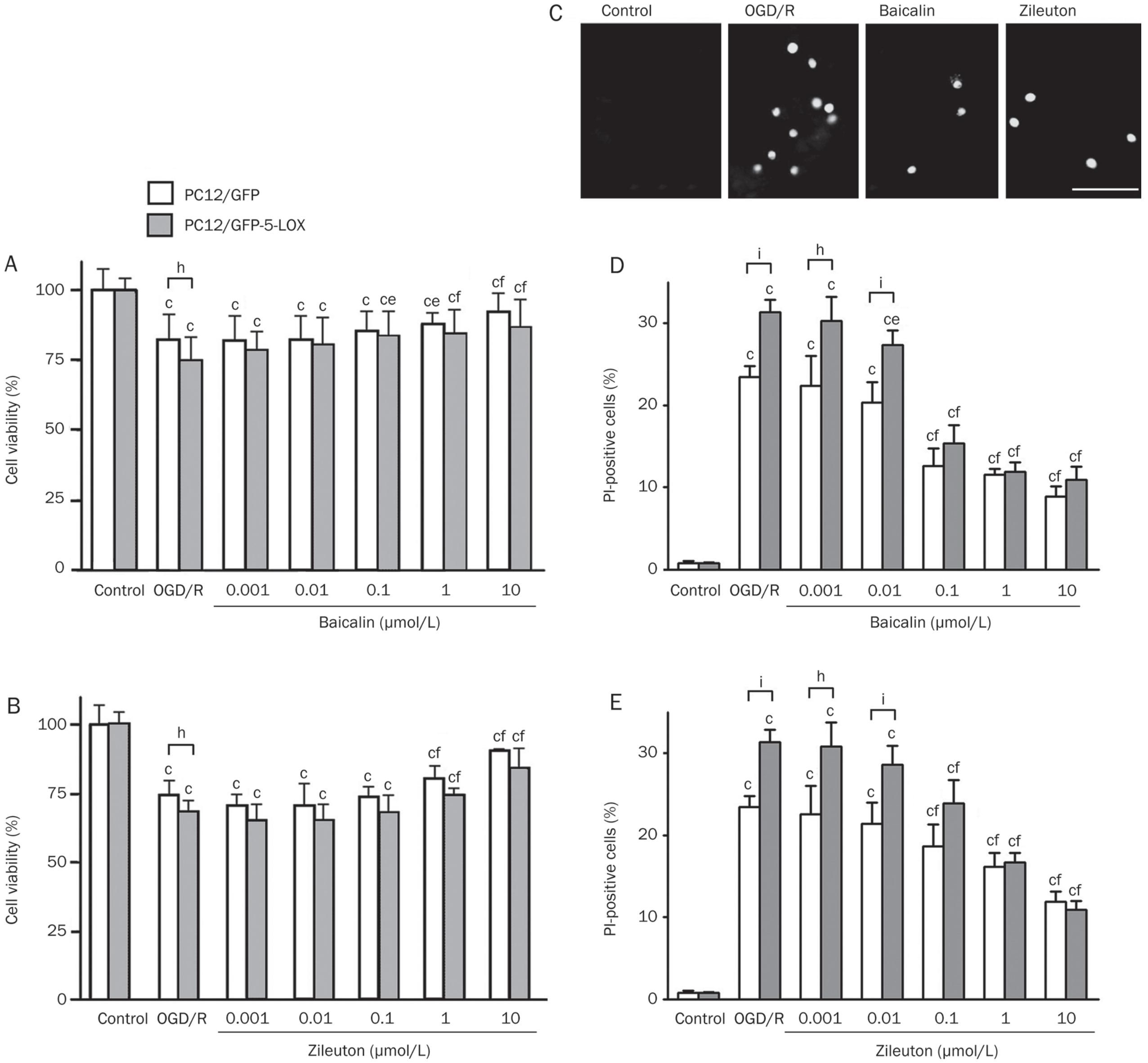

Figure 1. Effects of baicalin and zileuton on cell injury induced by OGD/recovery in PC12 cells. Cell viability was reduced after 2-h OGD and 24-h recovery in both GFP- and GFP-5-LOX-transfected cells. (A and B) Viability was significantly lower in GFP-5-LOX-transfected cells than in GFP-transfected cells. Baicalin and zileuton attenuated OGD/recovery-induced injury in both type cells in a concentration-dependent manner. (C) Cell death (necrosis) was evaluated by PI fluorescence staining in GFP-5-LOX-transfected PC12 cells (Scale bar=40 μm). (D and E) Baicalin and zileuton inhibited OGD/recovery-induced cell death in a concentration-dependent manner. Data are reported as mean±SD. *n*=15−17 (A and B) or 4 (D and E). $^{b}P<0.05$, $^{c}P<0.01$ *vs* corresponding control; $^{e}P<0.05$, $^{f}P<0.01$ *vs* OGD/recovery alone; $^{h}P<0.05$, $^{i}P<0.01$ *vs* GFP-transfected cells.

emic injury in PC12 cells, and this effect was partly mediated by oxidative stress-induced 5-LOX activation through the p38 MAPK pathway. These results support our recent findings that baicalin protects against OGD injury[13]. This protective action is mediated via inhibition of 5-LOX activity. As evidence supporting the involvement of 5-LOX in injury, both baicalin and the 5-LOX inhibitor zileuton inhibited the production of CysLTs and attenuated cell injury after exposure to OGD and H_2O_2. However, baicalin showed a different action from zileuton on 5-LOX activation. Specifically, baicalin inhibited 5-LOX translocation and activation by reducing ROS production after exposure to OGD and p38 phosphorylation after exposure to OGD and H_2O_2 whereas zileuton directly inhibited 5-LOX enzymatic activity.

In the present study, we used PC12 cells transfected with GFP-5-LOX to visualize 5-LOX translocation and to enhance 5-LOX expression. The transfected GFP-5-LOX was primarily localized in nuclei[14, 27]. We previously demonstrated involvement of the ROS/p38 MAPK pathway of 5-LOX activation after ischemic-like injury as well as the two modes of action of 5-LOX inhibitors (anti-oxidative or direct inhibitors) in GFP-5-LOX-transfected PC12 cells[14]. Here we found that

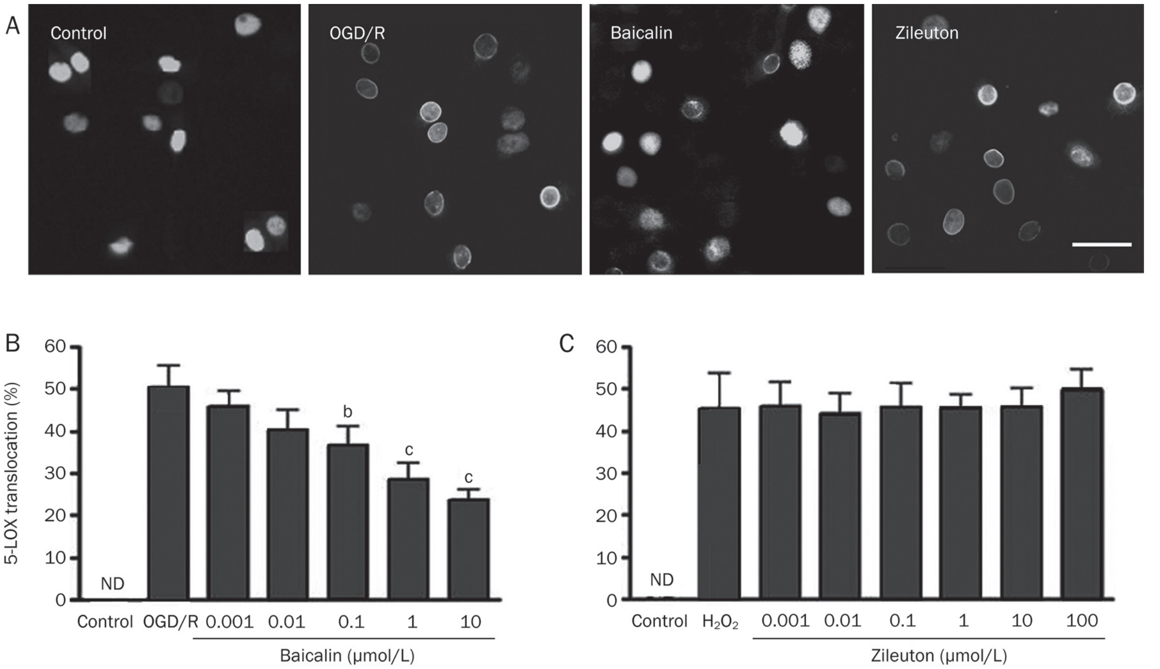

Figure 2. Effects of baicalin and zileuton on 5-LOX translocation after OGD/recovery in GFP-5-LOX-transfected PC12 cells. (A) GFP-5-LOX was translocated into the nuclear envelope after 2-h OGD and 2-h recovery, which was inhibited by baicalin (1 μmol/L) but not by zileuton (1 μmol/L). Scale bar=40 μm. (B and C) Concentration-dependent results are summarized as mean±SD. *n*=6. $^bP<0.05$, $^cP<0.01$ *vs* OGD/recovery alone. ND, not detectable.

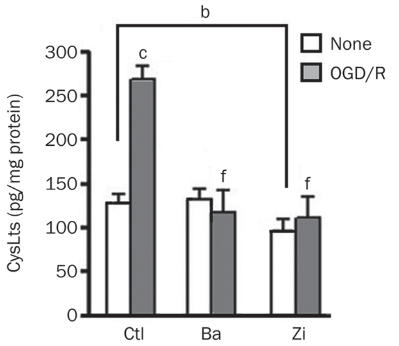

Figure 3. Effects of baicalin and zileuton on production of CysLTs after OGD/recovery in GFP-5-LOX-transfected PC12 cells. Baicalin (Ba, 10 μmol/L) reduced only the increased production whereas zileuton (Zi, 10 μmol/L) reduced both baseline and the increased production of CysLTs after OGD/recovery. Data are reported as mean±SD. *n*=4. $^bP<0.05$, $^cP<0.01$ *vs* control (no treatment). $^fP<0.01$ *vs* OGD/recovery alone.

baicalin acts as an anti-oxidative inhibitor for 5-LOX. Unlike the typical 5-LOX inhibitor zileuton, baicalin did not inhibit baseline 5-LOX enzymatic activity but did inhibit the activity after OGD/recovery. Consistently, it has been reported that baicalin shows no inhibition of isolated potato 5-LOX[28] and non-stimulated rat cortical neurons[13]. Moreover, baicalin showed anti-oxidative activity because it reduced ROS production. These results indicate that baicalin might inhibit oxidative stress-induced 5-LOX activation rather than directly inhibit 5-LOX. Therefore, in addition to inhibiting 5-LOX activation induced by the elevated intracellular Ca^{2+} via NMDA receptor activation[13], baicalin also inhibits 5-LOX activation via the ROS/p38 MAPK pathway. In addition, there is cross-talk between NMDA-induced excitotoxicity and oxidative stress[29, 30], and baicalin inhibits 5-LOX activation after NMDA receptor-mediated excitotoxicity[13]. Whether baicalin affects a common pathway of 5-LOX activation in both pathological processes requires further investigation.

The signaling family of MAPKs includes extracellular signal-regulated kinases (ERKs), c-Jun N-terminal kinases/stress-activated protein kinases (JNK/SAPKs), and p38 enzymes[31–33]. As one type of cell stress, ROS activates the p38 MAPK signal pathway, but not the ERK and JNK pathways, after OGD-induced ischemic injury in PC12 cells[14]. In a human B-lymphocyte cell line and in human polymorphonuclear leukocytes, p38 MAPK is activated independently of Ca^{2+} by chemical stress (sodium arsenite), osmotic stress (sorbitol, NaCl), heat shock or oxidative stress (H_2O_2, diamide), which leads to 5-LOX phosphorylation and activation[34, 35]. Recently, we found that the p38 inhibitor SB203580 inhibited 5-LOX activation induced by OGD/recovery and H_2O_2[14]. In the present study, baicalin inhibited p38 phosphorylation induced by both OGD/recovery and H_2O_2, supporting the conclusion that it inhibits 5-LOX activation through the ROS/p38 MAPK pathway. Our findings also confirm the role of p38 MAPK in cell stress-induced 5-LOX activation[3].

In the present study, we compared the effects of baicalin and zileuton. Zileuton is a specific 5-LOX inhibitor that chelates

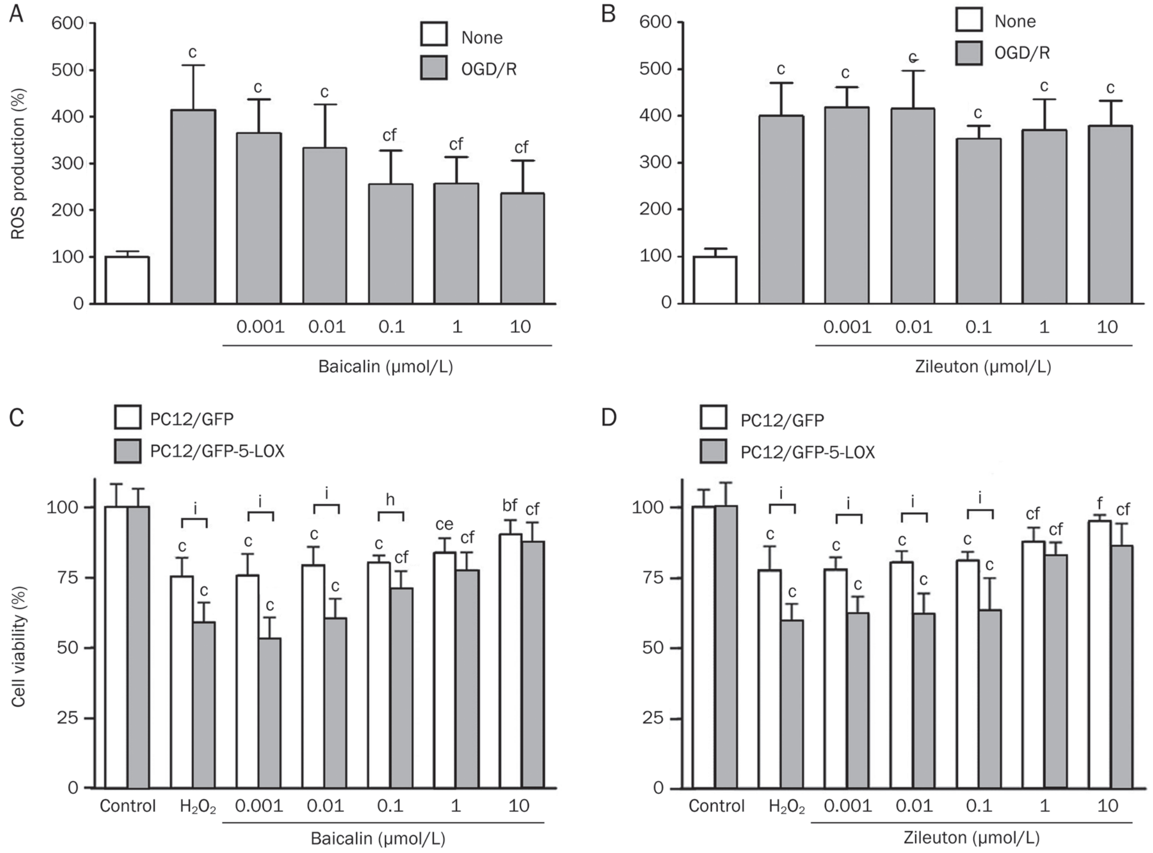

Figure 4. Effects of baicalin and zileuton on OGD/recovery-induced ROS production and H_2O_2-reduced viability in PC12 cells. (A and B) ROS production was determined after 2-h OGD and 0.5-h recovery in the absence or presence of baicalin and zileuton in wild-type PC12 cells. Baicalin, but not zileuton, inhibited ROS production. (C and D) Exposure to H_2O_2 (160 mol/L) for 24 h reduced cell viability in GFP-5-LOX-transfected PC12 cells. Over-expression of 5-LOX augmented H_2O_2-induced injury in PC12 cells. Baicalin (C) and zileuton (D) attenuated the reduced viability. Data are reported as mean±SD. *n*=8. $^{b}P<0.01$, $^{c}P<0.01$ *vs* control; $^{e}P<0.05$, $^{f}P<0.01$ *vs* OGD alone; $^{h}P<0.05$, $^{i}P<0.01$ *vs* GFP-transfected cells.

iron at the active site with weak redox-active properties[36, 37]. Unlike baicalin, it did not possess substantial anti-oxidative activity, as shown in the present and previous studies[14]. In addition, zileuton did not inhibit p38 phosphorylation and 5-LOX translocation but did inhibit 5-LOX enzymatic activity and cell injury after exposure to OGD/recovery or H_2O_2. These findings indicate that baicalin inhibits 5-LOX activation partly through anti-oxidative activity and inhibition of the ROS/p38 MAPK pathway whereas zileuton directly inhibits 5-LOX activity.

Taking these results together, we conclude that baicalin is not a direct 5-LOX inhibitor but can inhibit oxidative stress-induced 5-LOX activation and the resultant cell injury in PC12 cells via inhibition of the ROS/p38 MAPK pathway in addition to inhibition of NMDA receptor activation, as shown in neurons[13]. Furthermore, baicalin exerts various effects[16–19] and can protect against ischemic injury[20–23] and inflammation[18, 22, 38]. One of the mechanisms of baicalin may include inhibition of 5-LOX activation in these disorders.

Acknowledgements

This study was supported by the National Natural Science Foundation of China, No 30672449 and No 30772561. We thank Professor CD FUNK, the Center for Experimental Therapeutics and the Department of Pharmacology at the University of Pennsylvania, USA (now at the Department of Physiology, Queen's University, Canada), for kindly providing the pEGFP/C2-5-LOX and pEGFP/C2 vectors.

Author contribution

Cheng-tan LI, Wei-ping ZHANG, San-hua FANG, Yun-bi LU, and Er-qing WEI designed the study. Cheng-tan LI, Li-hui ZHANG, Ling-ling QI, Xue-qin HUANG, and Xiao-jia HUANG performed the experiments. Cheng-tan LI, Li-hui ZHANG, San-hua FANG, Er-qing WEI wrote the manuscript.

References

1 Murphy RC, Gijon MA. Biosynthesis and metabolism of leukotrienes. Biochem J 2007; 405: 379–95.
2 Rubin P, Mollison KW. Pharmacotherapy of diseases mediated by 5-lipoxygenase pathway eicosanoids. Prostaglandins Other Lipid Mediat 2007; 83: 188–97.
3 Radmark O, Samuelsson B. 5-lipoxygenase: regulation and possible involvement in atherosclerosis. Prostaglandins Other Lipid Mediat 2007; 83: 162–74.

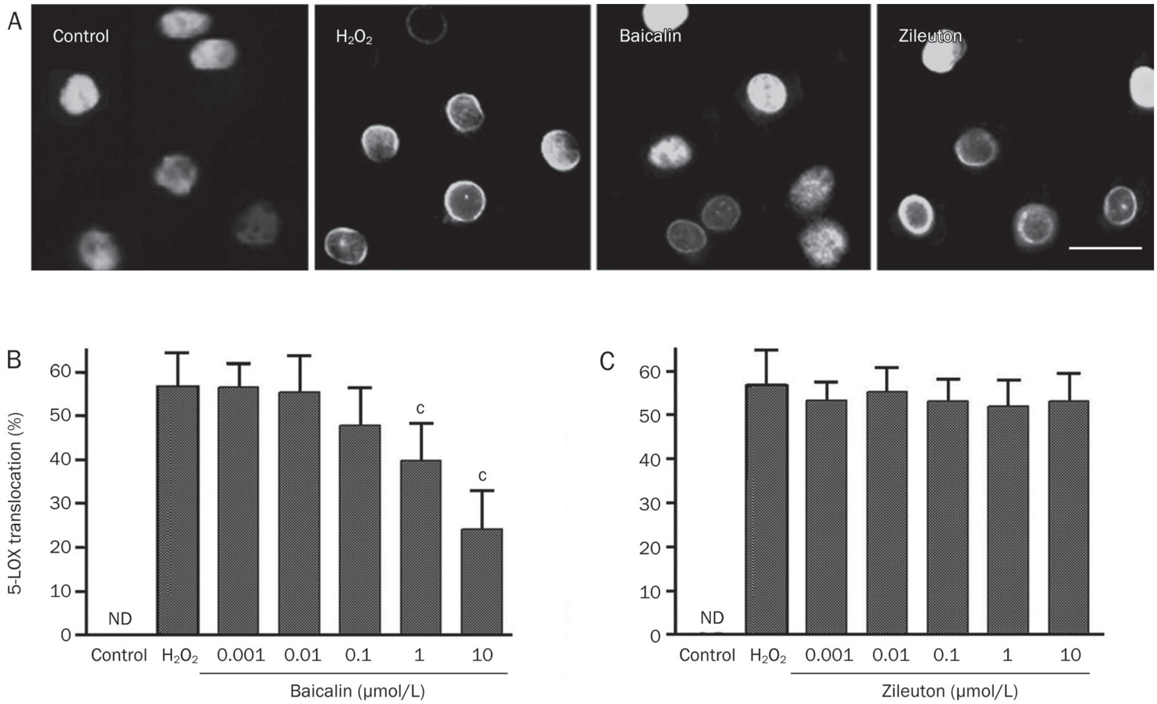

Figure 5. Effects of baicalin and zileuton on H_2O_2-induced 5-LOX translocation in GFP-5-LOX-transfected PC12 cells. (A) H_2O_2 (160 μmol/L)–induced 5-LOX translocation was significantly inhibited by baicalin (1 μmol/L) but not by zileuton (1 μmol/L). Scale bar=20 μm. (B and C) Concentration-dependent results are reported as mean±SD. *n*=6–8. [c]*P*<0.01 *vs* H_2O_2 alone. ND, not detectable.

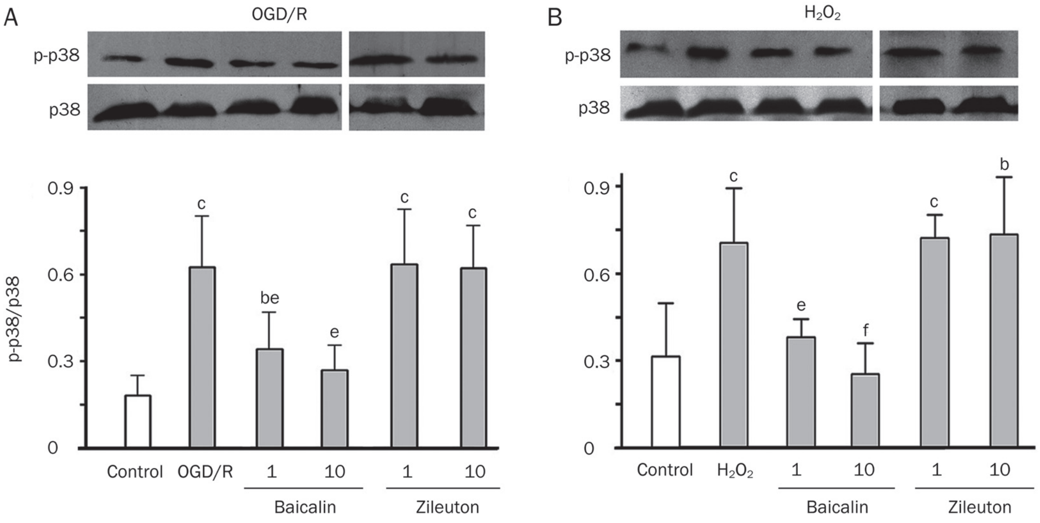

Figure 6. Effects of baicalin and zileuton on OGD/recovery- or H_2O_2-induced p38 phosphorylation in GFP-5-LOX transfected PC12 cells. Phosphorylation of p38 was inhibited by baicalin (1 and 10 μmol/L) but not by zileuton after 2-h OGD/1.5-h recovery (A) and exposure to H_2O_2 (160 μmol/L) for 20 min (B). Data are reported as mean±SD. *n*=4–6. [b]*P*<0.05, [c]*P*<0.01 *vs* corresponding control; [e]*P*<0.05, [f]*P*<0.01 *vs* OGD/recovery or H_2O_2 alone. ND, not detectable.

4 Adamjee J, Suh YJ, Park HS, Choi JH, Penrose JF, Lam BK, *et al.* Expression of 5-lipoxygenase and cyclooxygenase pathway enzymes in nasal polyps of patients with aspirin-intolerant asthma. J Pathol 2006; 209: 392–9.

5 Friedman BS, Bel EH, Buntinx A, Tanaka W, Han YH, Shingo S, *et al.* Oral leukotriene inhibitor (MK-886) blocks allergen-induced airway responses. Am Rev Respir Dis 1993; 147: 839–44.

6 Ohtsuki T, Matsumoto M, Hayashi Y, Yamamoto K, Kitagawa K, Ogawa S, *et al.* Reperfusion induces 5-lipoxygenase translocation and leukotriene C4 production in ischemic brain. Am J Physiol 1995; 268: H1249–57.

7 Ciceri P, Rabuffetti M, Monopoli A, Nicosia S. Production of leukotrienes in a model of focal cerebral ischaemia in the rat. Br J Pharmacol 2001; 133: 1323–9.

8 Zhou Y, Fang SH, Ye YL, Chu LS, Zhang WP, Wang ML, *et al.* Caffeic acid ameliorates early and delayed brain injuries after focal cerebral ischemia in rats. Acta Pharmacol Sin 2006; 27: 1103–10.

9 Chu LS, Fang SH, Zhou Y, Yu GL, Wang ML, Zhang WP, *et al.* Minocycline inhibits 5-lipoxygenase activation and brain inflammation after focal cerebral ischemia in rats. Acta Pharmacol Sin 2007; 28: 763–72.

10 Zhou Y, Wei EQ, Fang SH, Chu LS, Wang ML, Zhang WP, *et al.* Spatiotemporal properties of 5-lipoxygenase expression and activation in the brain after focal cerebral ischemia in rats. Life Sci 2006; 79: 1645–56.

11 Song Y, Wei EQ, Zhang WP, Zhang L, Liu JR, Chen Z. Minocycline protects PC12 cells from ischemic-like injury and inhibits 5-lipoxygenase activation. Neuroreport 2004; 15: 2181–4.

12 Ge QF, Wei EQ, Zhang WP, Hu X, Huang XJ, Zhang L, *et al.* Activation of 5-lipoxygenase after oxygen-glucose deprivation is partly mediated via NMDA receptor in rat cortical neurons. J Neurochem 2006; 97: 992–1004.

13 Ge QF, Hu X, Ma ZQ, Liu JR, Zhang WP, Chen Z, *et al.* Baicalin attenuates oxygen-glucose deprivation-induced injury via inhibiting NMDA receptor-mediated 5-lipoxygenase activation in rat cortical neurons. Pharmacol Res 2007; 55: 148–57.

14 Li CT, Zhang WP, Lu YB, Fang SH, Yuan YM, Qi LL, *et al.* Oxygen-glucose deprivation activates 5-lipoxygenase mediated by oxidative stress through the p38 mitogen-activated protein kinase pathway in PC12 cells. J Neurosci Res 2009; 87: 991–1001.

15 Song Y, Wei EQ, Zhang WP, Ge QF, Liu JR, Wang ML, *et al.* Minocycline protects PC12 cells against NMDA-induced injury via inhibiting 5-lipoxygenase activation. Brain Res 2006; 1085: 57–67.

16 Li-Weber M. New therapeutic aspects of flavones: the anticancer properties of Scutellaria and its main active constituents Wogonin, Baicalein and Baicalin. Cancer Treat Rev 2009; 35: 57–68.

17 Wan JY, Gong X, Zhang L, Li HZ, Zhou YF, Zhou QX. Protective effect of baicalin against lipopolysaccharide/D-galactosamine-induced liver injury in mice by up-regulation of heme oxygenase-1. Eur J Pharmacol 2008; 587: 302–8.

18 Liu LL, Gong LK, Wang H, Xiao Y, Wu XF, Zhang YH, *et al.* Baicalin inhibits macrophage activation by lipopolysaccharide and protects mice from endotoxin shock. Biochem Pharmacol 2008; 75: 914–22.

19 Chang WT, Shao ZH, Yin JJ, Mehendale S, Wang CZ, Qin Y, *et al.* Comparative effects of flavonoids on oxidant scavenging and ischemia-reperfusion injury in cardiomyocytes. Eur J Pharmacol 2007; 566: 58–66.

20 Zhang Z, Wu R, Li P, Liu F, Zhang W, Zhang P, *et al.* Baicalin administration is effective in positive regulation of twenty-four ischemia/reperfusion-related proteins identified by a proteomic study. Neurochem Int 2009; 54: 488–96.

21 Jung SH, Kang KD, Ji D, Fawcett RJ, Safa R, Kamalden TA, *et al.* The flavonoid baicalin counteracts ischemic and oxidative insults to retinal cells and lipid peroxidation to brain membranes. Neurochem Int 2008; 53: 325–37.

22 Chang CP, Huang WT, Cheng BC, Hsu CC, Lin MT. The flavonoid baicalin protects against cerebrovascular dysfunction and brain inflammation in experimental heatstroke. Neuropharmacology 2007; 52: 1024–33.

23 Zhang ZJ, Li P, Wang Z, Li PT, Zhang WS, Sun ZH, *et al.* A comparative study on the individual and combined effects of baicalin and jasminoidin on focal cerebral ischemia-reperfusion injury. Brain Res 2006; 1123: 188–95.

24 Liu LY, Wei EQ, Zhao YM, Chen FX, Wang ML, Zhang WP, *et al.* Protective effects of baicalin on oxygen/glucose deprivation- and NMDA-induced injuries in rat hippocampal slices. J Pharm Pharmacol 2005; 57: 1019–26.

25 Carter GW, Young PR, Albert DH, Bouska J, Dyer R, Bell RL, *et al.* 5-lipoxygenase inhibitory activity of zileuton. J Pharmacol Exp Ther 1991; 256: 929–37.

26 Sirois P, Borgeat P, Lauziere M, Dube L, Rubin P, Kesterson J. Effect of Zileuton (A-64077) on the 5-lipoxygenase activity of human whole blood *ex vivo.* Agents Actions 1991; 34: 117–20.

27 Chen XS, Zhang YY, Funk CD. Determinants of 5-lipoxygenase nuclear localization using green fluorescent protein/5-lipoxygenase fusion proteins. J Biol Chem 1998; 273: 31237–44.

28 Burnett BP, Jia Q, Zhao Y, Levy RM. A medicinal extract of Scutellaria baicalensis and Acacia catechu acts as a dual inhibitor of cyclooxygenase and 5-lipoxygenase to reduce inflammation. J Med Food 2007; 10: 442–51.

29 Guan ZZ. Cross-talk between oxidative stress and modifications of cholinergic and glutaminergic receptors in the pathogenesis of Alzheimer's disease. Acta Pharmacol Sin 2008; 29: 773–80.

30 Hernandez-Fonseca K, Cardenas-Rodriguez N, Pedraza-Chaverri J, Massieu L. Calcium-dependent production of reactive oxygen species is involved in neuronal damage induced during glycolysis inhibition in cultured hippocampal neurons. J Neurosci Res 2008; 86: 1768–80.

31 Pearson G, Robinson F, Beers Gibson T, Xu BE, Karandikar M, Berman K, *et al.* Mitogen-activated protein (MAP) kinase pathways: regulation and physiological functions. Endocr Rev 2001; 22: 153–83.

32 Kumar S, Boehm J, Lee JC. p38 MAP kinases: key signalling molecules as therapeutic targets for inflammatory diseases. Nat Rev Drug Discov 2003; 2: 717–26.

33 Cuenda A, Rousseau S. p38 MAP-kinases pathway regulation, function and role in human diseases. Biochim Biophys Acta 2007; 1773: 1358–75.

34 Werz O, Klemm J, Radmark O, Samuelsson B. p38 MAP kinase mediates stress-induced leukotriene synthesis in a human B-lymphocyte cell line. J Leukoc Biol 2001; 70: 830–8.

35 Werz O, Burkert E, Samuelsson B, Radmark O, Steinhilber D. Activation of 5-lipoxygenase by cell stress is calcium independent in human polymorphonuclear leukocytes. Blood 2002; 99: 1044–52.

36 Werz O, Steinhilber D. Development of 5-lipoxygenase inhibitors--lessons from cellular enzyme regulation. Biochem Pharmacol 2005; 70: 327–33.

37 Werz O, Steinhilber D. Therapeutic options for 5-lipoxygenase inhibitors. Pharmacol Ther 2006; 112: 701–18.

38 Tian H, Zhang X, Wu C, Chen L, Ying R, Ye J, *et al.* Effects of baicalin and octreotide on the serum TNF-alpha level and apoptosis in multiple organs of rats with severe acute pancreatitis. Inflammation 2009; 32: 191–201.

Acta Pharmacologica Sinica (2010) 31: 145–149
© 2010 CPS and SIMM All rights reserved 1671-4083/10 $32.00
www.nature.com/aps

Original Article

Central administration of kisspeptin-10 inhibits natriuresis and diuresis induced by blood volume expansion in anesthetized male rats

Xu HAN[1], Ming YAN[2], Xiao-fei AN[1,*], Ming HE[3], Jiang-yi YU[1]

[1]Department of Endocrinology, Jiangsu Province Hospital of Traditional Chinese Medicine, Nanjing 210029, China; [2]National Drug Screen Laboratory, China Pharmaceutical University, Nanjing 210009, China; [3]Department of Physiology, School of Medicine, Shanghai Jiaotong University, Shanghai 200025, China

Aim: To investigate the possible role of hypothalamic kisspeptin in the regulation of body fluid metabolism and maintenance of internal homeostasis.
Methods: Natriuresis and diuresis were induced by blood volume expansion (VE) in anesthetized male rats and kisspeptin-10 was intracerebroventricularly (icv) administered. Radioimmunoassay (RIA) was used to measure the plasma arginine vasopressin (AVP) and atrial natriuretic peptide (ANP) concentrations during the VE. The mediation of the renal sympathetic nerve was also investigated in rats with bilateral renal sympathetic denervation.
Results: The increased urine flow and sodium excretion induced by VE were significantly inhibited by icv injection of 5 nmol kisspeptin-10 ($P<0.05$), which peaked 20 min after the decrease in VE. The mean arterial blood pressure and heart rate did not change during the experiment. Plasma AVP concentrations were significantly increased 20 min after icv injection of 5 nmol kisspeptin-10 during VE ($P<0.05$), while pretreatment with 5 nmol kisspeptin-10 did not significantly change plasma ANP concentrations. Furthermore, pretreatment with 5 nmol kisspeptin-10 could significantly inhibit VE-induced natriuresis and diuresis in renal sympathetic denervated rats ($P<0.05$).
Conclusion: Central administration of kisspeptin-10 inhibited VE-induced natriuresis and diuresis. This effect was likely mediated by increasing AVP release independent of plasma ANP concentration and renal sympathetic nerve activity.

Keywords: kisspeptin; natriuresis; diuresis; volume expansion; hypothalamus

Acta Pharmacologica Sinica (2010) 31: 145–149; doi: 10.1038/aps.2009.179; published online 21 December 2009

Introduction

The hypothalamo-neurohypophysial system plays a fundamental role in the maintenance of body fluid homeostasis by secreting vasopressin and oxytocin (OT) within the paraventricular nucleus (PVN) and supraoptic nucleus (SON) in response to volume expansion (VE)[1]. Blood VE increases the release of atrial natriuretic peptide (ANP) from the right atrium by stretching the atrial myocytes and activating the afferent inputs of baroreceptors to induce OT secretion in the hypothalamus. Isotonic VE also induces a decrease in renal sympathetic nerve activity and arginine vasopressin (AVP) secretion from the SON and PVN, resulting in a decrease in reabsorption of sodium and water in the kidney[2, 3]. The natriuresis and diuresis induced by VE prevents body fluid augmentations to maintain blood pressure (BP) and internal homeostasis.

Renal functions are controlled mainly by hormone factors and by the sympathetic nervous system. The renal sympathetic nerve is also involved in the volume reflex, especially during acute VE, while the detailed central nervous pathway and neurotransmitter substances underlying the reflex still remain to be elucidated[4–6]. The PVN and SON of the hypothalamus and anteroventral portion of the third ventricle (AV3V) have been shown to be important sites in the forebrain for receiving and integrating various peripheral and central signals in blood volume change[7, 8].

Kisspeptins, novel peptides encoded by Kiss-1 gene, are endogenous ligands of the G protein-coupled receptor 54 (GPR54)[9]. The distribution of kisspeptins and its receptor in many discrete hypothalamic nuclei implies that it may be related to the regulation and integration of neuroendocrine signals[10, 11]. Accumulating data suggest that kisspeptins play a major role in gonadotropin-releasing hormone (GnRH) secretion, reproductive function and puberty activation[12, 13].

---

* To whom correspondence should be addressed.
E-mail anxiaofei2000@163.com
Received 2009-09-25 Accepted 2009-11-17

Apart from regulation of the hypothalamic-pituitary-ovary axis (HPOA), the functional role of kisspeptin in the hypothalamus remains obscure. Recent immunocytochemical staining studies have shown that kisspeptin–positive neurons and fibers are abundantly located in the anteroventral periventricular nucleus (AVPV), the PVN and the SON in the hypothalamus[10], which are related to the central regulation of volume reflex[1, 2]. Unexpectedly, we observed in our previous studies that sodium excretion and urine flow were attenuated for 20 to 60 min after intracerebroventricular (icv) administration of 0.5 or 5 nmol kisspeptin-10, an agonist of GPR54, in anesthetized male rats (unpublished data). We postulate that hypothalamic kisspeptin could be involved in the central nervous pathway for the mediation of VE-induced natriuresis and diuresis. To test the hypothesis, we investigated the effects of the central administration of kisspeptin-10 on VE-induced natriuresis and diuresis and plasma AVP and ANP concentrations in anesthetized male rats with or without renal sympathetic nerve denervation.

Materials and methods

Animals and drugs

Male Sprague-Dawley rats weighing 180−200 g were obtained from the Animal Center of Nanjing University. They were kept in an air-conditioned room with controlled lighting (light 12 h/dark 12 h) and given free access to laboratory chow and tap water. Kisspeptin-10 (the biologically active C-terminal decapeptide) was purchased from Phoenix Pharmaceutical Company (Belmont, CA) and dissolved in artificial cerebrospinal fluid (ACSF; 128 mmol/L NaCl, 2.5 mmol/L KCl, 1.4 mmol/L $CaCl_2$, 1.0 mmol/L $MgCl_2$ and 1.2 mmol/L Na_2HPO_4; pH 7.4). All other reagents and solvents were of analytical grade. All experimental protocols were approved by the local Animal Welfare and Ethics Committee.

Intracerebroventricular injection

Implantation of the cannula was performed stereotaxically under anesthesia with sodium pentobarbital (40 mg/kg, *ip*). Stereotaxic surgical procedures were used to implant one 22-gauge stainless steel guide cannula with a removable 28 gauge inner stylette to the left lateral ventricle (Bregma -1.0 mm; L: 1.5 mm; H: 3.0 mm)[14]. The device was fixed onto the skull with anchor screws. The experiments with icv injection were performed at least 7 d after surgery. The anesthetized intact or renal sympathetic nerve denervated rats were given ACSF (5 μL, as control) or kisspeptin-10 (0.05, 0.5, or 5 nmol) by icv 20 min before VE. Kisspeptin-10 dissolved in 5 μL ACSF was infused through the 28-gauge cannula using an infusion pump at a flow rate of 2 μL/min. The injection needle was kept in place for 10 min after the injection. After a 120 min observation period, all animals were injected with 4% brilliant blue by icv to verify the cannula placement (Figure 2).

Experimental procedure

All rats were water deprived for 12 h one day before the experiments. On the day of the experiment, the rats were anesthetized with inactin (100 mg/kg body wt) for renal function experiments. The trachea was intubated to facilitate ventilation. The left femoral vein was catheterized with polyethylene (PE) tubing (PE-50, filled with saline) for VE. The right femoral artery was cannulated with PE tubing (PE-50, filled with 100 U/mL heparinized saline) for monitoring arterial blood pressure and heart rate. The pressure signal was sent to a computer recording and analyzing system (PowerLab, AD Instruments) by pressure transducers. A continuous perfusion of 0.9% NaCl solution through the catheter in the right femoral vein was used for VE stimulation. The total perfusion volume was 4% of the body weight and was infused at a constant flow rate over a period of 40 min. In the test of renal sympathetic nerve denervation, bilateral renal sympathetic nerve trunks were isolated and destroyed using 95% ethanol[15].

AVP and ANP radioimmunoassay

Sequential blood samples (200 μL each) were taken through the PE tubing from the right femoral artery at 20 min intervals during the 120 min period. The same volume of physiological saline was replaced at each bleeding. Blood plasma (100 μL) was separated from each blood sample by centrifugation and stored at -20 °C until the determination of AVP. Plasma AVP and ANP concentrations were measured using Sep-Pak C18 cartridge extraction. Samples for AVP extraction were acidified with 1 mol/L HCl and extracted. Acidified plasma samples were added slowly to the columns and then washed with 0.1% trifluoroacetic acid (TFA). The absorbed AVP was eluted with 50% methanol and 0.1% TFA, and the eluates were dried in a Speed-Vac concentrator. The assay sensitivity was 1.2 pg for AVP/tube. The intra- and inter-assay coefficients of variations were 5% and 7%. The plasma ANP concentration was also determined using an RIA kit (Peninsula Laboratories, Belmont, CA, USA) after extraction of ANP from plasma with C_{18} Sep-Pak cartridges eluted with a buffer containing 60% acetonitrile in 1% TFA. Immunoreactive ANP concentration is expressed as pmol/L.

Measurement of urine and sodium excretion

The ureters were catheterized with PE-10 tubing for sequential urine collection every 20 min during the VE, and the urine volume of each period was measured. Sodium concentration and volume of each urine fraction were measured using the automatic biochemical analyzer (Beckman Coulter Corporation, Miami, USA). The data are expressed as micromoles per minute per 100-gram body weight ($\mu mol \cdot min^{-1}$ per 100 g BW) and microliters per minute per 100-gram body weight ($\mu L \cdot min^{-1}$ per 100 g BW), respectively.

Statistical analysis

All results are expressed as mean±standard deviation (SD) and were analyzed using SPSS 13.0 (SPSS, Chicago, IL). The data in Figure 1 were analyzed using a two-way repeated measures analysis of variance (ANOVA) with time as the repeated measure. The significance of difference was determined using the Newman-Keuls test. When only two treatment groups were being compared, a Student's *t*-test was used. A probability of $P<0.05$ was considered statistically significant.

Results

Effect of kisspeptin-10 icv injection on natriuresis and diuresis induced by VE in anesthetized male rats

In the normal group, sodium excretion and urine flow began to gradually increase simultaneously with VE and reach the peak at 80 min (1.25±0.26 μmol·min^{-1} per 100 g and 22.25±3.34 μL·min^{-1} per 100 g, respectively). In animals receiving an icv injection of kisspeptin-10, however, VE-induced natriuresis and diuresis also occurred at time points from 40 to 120 min, but occurred with lower amplitudes. This increase in sodium excretion and urine flow in response to VE were attenuated by icv administration of 0.05 and 0.5 nmol kisspeptin-10 during time points from 40 to 120 min but with no statistical significance (Figure 1A and 1B). Kisspeptin-10 (5 nmol) had a significant inhibitory effect on VE-induced natriuresis and diuresis from 60 to 100 min, especially in the strongest response at 80 min (0.78±0.21 μmol·min^{-1} per 100 g and 16.94±5.53 μL·min^{-1} per 100 g) compared with controls (F=5.18 and 5.75, $P<0.05$).

Effect of kisspeptin-10 icv injection on heart rate and mean arterial pressure during VE-induced natriuresis and diuresis

Central injection of 5 nmol kisspeptin-10 was ineffective at producing any significant changes in mean arterial blood pressure or heart rate during VE. The mean arterial blood pressure of the intact rats with VE fluctuated in the range of 92±16 and 112±18 mmHg during the experiment. There was no significant change between the 5 nmol kisspeptin-10 group and the control group at all the time points. Moreover, no significant change in heart rate was observed between the two groups (range of 295±36 and 325±38, respectively).

Effect of kisspeptin-10 icv injection on plasma AVP and ANP concentrations during VE in anesthetized male rats

Central injection of 5 nmol kisspeptin-10 caused a stimulatory effect on plasma AVP concentration during VE (Figure 1C). The concentration of plasma AVP in anesthetized male rats with VE was 3.6±1.4 compared with 2.4±0.8 pg/mL in the control group during observation. There was a decreasing tendency, but this did not reach statistical significance. In comparison to the control group, plasma AVP concentrations increased significantly (from 3.2±1.2 to 9.5±2.6 pg/mL) 20 min after the icv injection of 5 nmol kisspeptin-10 (F=5.82, $P<0.05$). This effect lasted approximately 20 min. Volume expansion induced an obvious plasma ANP increase from the 40 min time point in both groups (Figure 1D). In contrast to plasma AVP, there was no statistically significant difference in ANP concentrations between the two groups throughout the experiment, showing that 5 nmol kisspeptin-10 had no significant effect on plasma ANP concentrations.

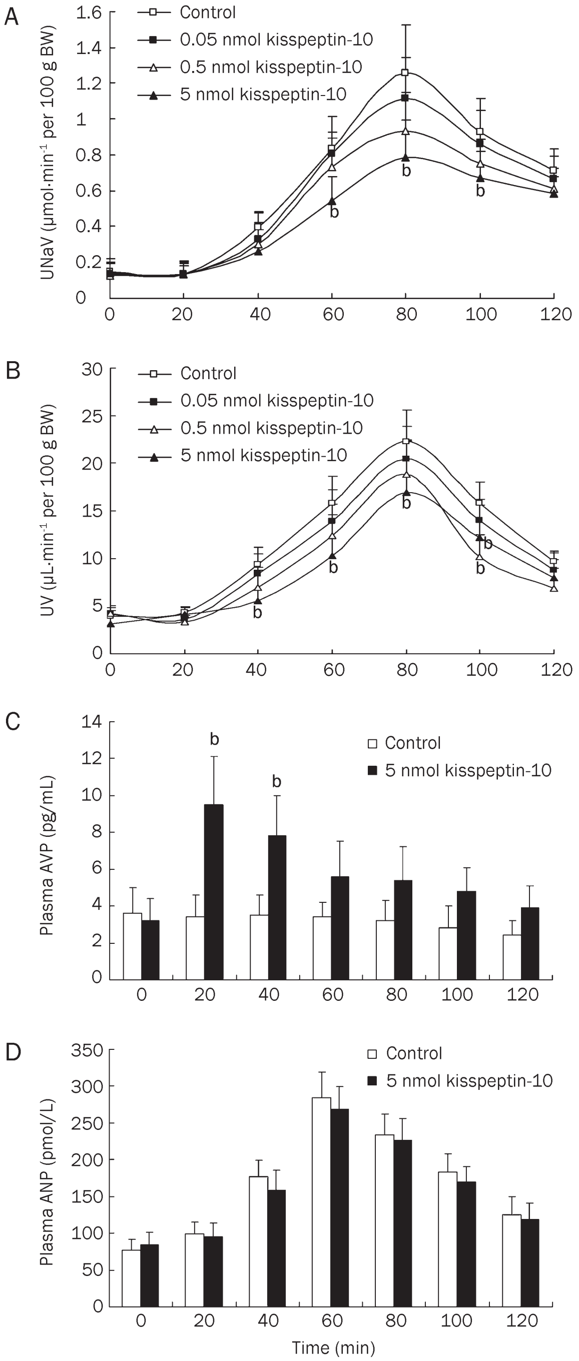

Figure 1. (A and B) Dose-dependent inhibition of kisspeptin-10 on VE-induced natriuresis and diuresis induced in anesthetized male rats. The icv administration of kisspeptin-10 or ACSF (as a control) was given at t=0. (C and D) Time-dependent increase of plasma AVP and ANP concentrations by icv injection of kisspeptin-10 during VE in anesthetized male rats. A total of 5 nmol kisspeptin-10 or ACSF (as control) was given at t=0. The sodium concentration and volume of each urine fraction were measured every 20 min for 2 h. The VE of 4% body weight lasted 40 min (from t=20 to t=60). n=10. Data are mean±SD. $^{b}P<0.05$ *vs* control.

Effect of kisspeptin-10 icv injection on VE-induced natriuresis and diuresis in anesthetized male rats with bilateral renal sympathetic denervation

In renal sympathetic nerve denervated rats, similar increases in VE-induced urine flow and sodium excretion were observed, with a slight increase that reached a peak at 80 min (1.41 ± 0.31 μmol·min^{-1} per 100 g and 24.28 ± 3.85 μL·min^{-1} per 100 g BW, respectively). A significant inhibitory effect on VE-induced natriuresis and diuresis also occurred in the 5 nmol kisspeptin-10 group (Figure 2C and 2D). The sodium excretion and urine flow were decreased significantly by pretreatment with icv administration of 5 nmol kisspeptin-10 at 60 to 80 min compared with the control group. The highest response level also occurred at 80 min (0.95 ± 0.23 μmol·min^{-1} per 100 g and 18.84 ± 3.13 μL·min^{-1} per 100 g BW, respectively) (F=4.65 and 4.92, $P<0.05$).

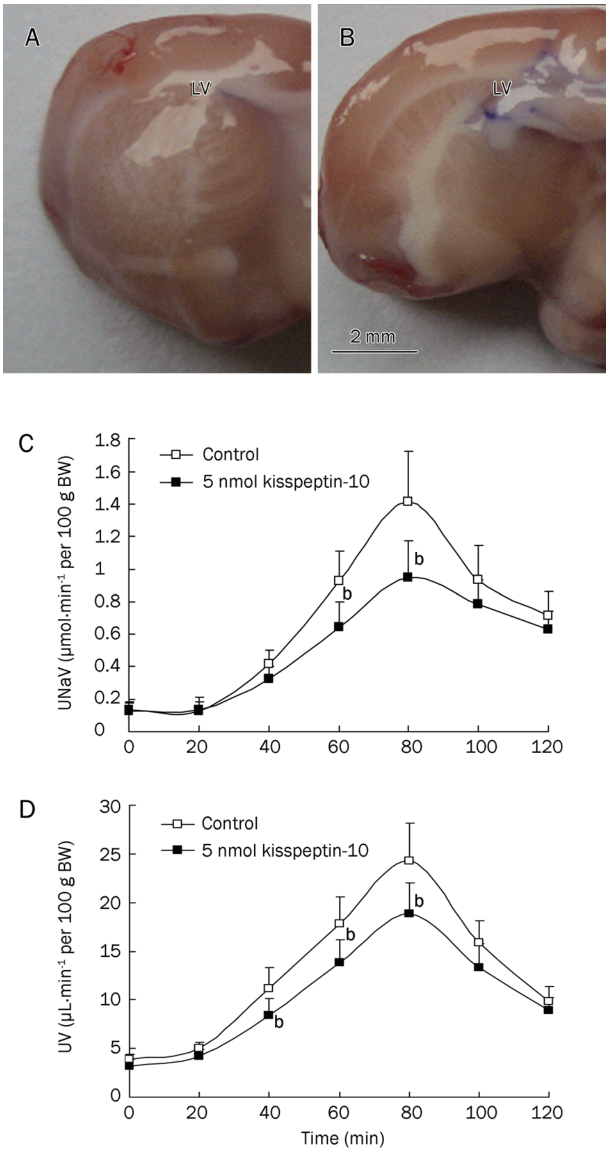

Figure 2. (A and B) The lateral ventricles were stained by 4% brilliant blue injected through the internal cannula after 120 min of observation to verify the proper cannula placement. (C and D) Time-dependent effect of icv injection of kisspeptin-10 on VE-induced natriuresis and diuresis in anesthetized male rats with bilateral renal sympathetic denervation. A total of 5 nmol kisspeptin-10 or ACSF (as a control) was given at t=0. The sodium concentration and volume of each urine fraction were measured every 20 min for 2 h. The VE of 4% body weight lasted 40 min (from t=20 to t=60). n=10. Data are mean±SD. $^{b}P<0.05$ *vs* control.

Discussion

Kisspeptin and its receptor are densely distributed in several nuclei of the hypothalamus, suggesting that kisspeptin might mediate and modulate hypothalamic functions[11]. Previous studies have demonstrated that kisspeptin and GPR54 signaling in the brain serve as an important conduit for controlling GnRH secretion in developing and adult animals[12, 16]. In the present study, we observed that central administration of kisspeptin-10 could inhibit VE-induced natriuresis and diuresis in anesthetized male rats. To our knowledge, this is the first study suggesting that hypothalamic kisspeptin might participate in the central regulation of body fluid homeostasis.

We observed that icv injection of 5 nmol kisspeptin-10 significantly inhibited VE-induced natriuresis and diuresis and that this inhibitory effect lasted at least 80 min. Due to the limitation of our observation intervals, we cannot exclude the possibility that kisspeptin-10 may only postpone the sodium and water excretion surge or prolong the duration after VE. Expansion of the blood volume induces natriuresis and diuresis, and this volume reflex plays an important role in the regulation of water and electrolytes balance[1]. The release of ANP from the atrial myocytes[17], changes in renal sympathetic nerve activity[4, 5] and hypothalamic AVP release from the PVN[1] are regarded as the chief efferent regulators in the volume reflex, including the experimentally induced VE performed in our experiments. Sympathetic innervation in the kidney elicits important effects on the regulation of renal blood flow, rennin release and reabsorption of sodium and water[1, 5]. Inconsistent with our anticipation, the inhibitory effect of kisspeptin is not likely to be mediated by the renal sympathetic nerves because bilateral renal denervation could not abolish the attenuation caused by central injection of 5 nmol kisspeptin-10. The lack of significant change in mean blood pressure and heart rate suggests that the effect of central administration of kisspeptin did not lead to the activation of the efferent visceral sympathetic nervous system.

The current study concentrated on the possible role of the renal sympathetic nerves in the mediation of the effect of kisspeptin-10. We observed differences in values between intact and renal sympathetic nerve denervated rats during VE, especially peak differences. In denervated rats, VE-induced increases in urine flow and sodium excretion at the peak were slightly elevated compared with the intact control group; however, the difference did not reach statistical significance. We performed bilateral renal sympathetic denervation according to the method described by Patel *et al*[15]. This method has been shown to decrease the norepinephrine level in kidneys to an undetectable range. It should be noted that we did not confirm the effectiveness of this method by measuring the NE content in the surgically denervated kidneys, as done in Patel *et al*[15]. Moreover, due to the complexity of our surgical procedures, we did not simultaneously record the activity from the renal sympathetic nerve. We therefore cannot determine if the function of the renal sympathetic nerves were blocked completely.

The neuroendocrine system plays a vital role in the maintenance of body fluid homeostasis by secreting AVP and OT in response to a variety of signals, including osmotic stimulus or volume expansion[1]. The PVN, SON, and AVPV in hypothalamus have been deemed important integrating sites governing AVP and ANP release[1, 2, 17]. Using immunocytochemistry, the recent detailed account of kisspeptin neuroanatomy has shown that kisspeptin neurons are more abundantly distributed in the AVPV than elsewhere in hypothalamus. Meanwhile, kisspeptin fibers are densely located in the PVN and SON, running along the wall of the third ventricle[10]. The negative effect of kisspeptin on volume reflex is probably related to processes of the neuroendocrine system, such as increasing AVP release or decreasing ANP into circulation. As shown in our studies, the inhibitory effect of kisspeptin-10 on VE-induced natriuresis and diuresis is not likely to be mediated by altering plasma ANP release because the 5 nmol kisspeptin-10 icv injection had no significant effect on plasma ANP concentrations. Our studies demonstrated that plasma AVP concentration increased 20 min after central injection of 5 nmol kisspeptin-10 during VE, suggesting that the negative effect of kisspeptin-10 on VE-induced natriuresis and diuresis is partly mediated by its stimulatory influence on AVP release. We postulate that the swift effect of the icv injection of kisspeptin-10 on AVP release are probably mediated by nuclei around the third ventricle, where it could diffuse and reach in a short period of time. The administered kisspeptin is likely to diffuse along with ventricular cerebrospinal fluid and modulate neuronal activity in nuclei located in the periventricular area of the third ventricle, such as neurons within PVN and SON. Certainly, the mechanism underlying hypothalamic kisspeptin-10 in neuroendocrine control of AVP release remains to be elucidated.

To our knowledge, this is the first study to show that central administration of kisspeptin-10 inhibits natriuresis and diuresis induced by blood volume expansion in anesthetized male rats. This effect is probably mediated by increasing AVP secretion and is independent of plasma ANP concentration and renal sympathetic nerve activity. The role of kisspeptin in the regulation of body fluid homeostasis remains to be elucidated.

Acknowledgements

Project was supported by Nature Scientific Foundation of Jiangsu Province (BK2008490).

Author contribution

Xiao-fei AN designed the research; Xu HAN, Xiao-fei AN, and Ming YAN performed the research; Ming HE and Jiang-yi YU contributed new analytical tools and reagents; Ming YAN and Xiao-fei AN analyzed the data; and Xiao-fei AN wrote the paper.

References

1 Antunes-Rodrigues J, Castro MD, Klias LK, Valenc MM, McCann SM. Neuroendocrine control of body fluid metabolism. Physiol Rev 2004; 84: 169–208.

2 Coote JH. A role for the paraventricular nucleus of the hypothalamus in the autonomic control of heart and kidney. Exp Physiol 2005; 90: 169–73.

3 Leng G, Brown CH, Russell JA. Physiological pathways regulating the activity of magnocellular neurosecretory cells. Prog Neurobiol 1999; 57: 625–55.

4 Wongmekiat O, Johns E. Role of nitric oxide and renal nerves in the renal responses to acute volume expansion in anaesthetized rats. Exp Physiol 2001; 86: 47–54.

5 Young PJ, Miller JH. Renal nerve and alpha 2-adrenergic action during acute volume expansion in the anaesthetized rat. Clin Exp Pharmacol Physiol 1999; 26: 608–13.

6 Li YF, Mayhan WG, Patel KP. Role of the paraventricular nucleus in renal excretory responses to acute volume expansion: role of nitric oxide. Am J Physiol Heart Circ Physiol 2003; 285: H1738–46.

7 Bealer SL. Anteroventral third ventricle periventricular tissue contributes to cardiac baroreflex responses. Clin Exp Pharmacol Physiol 2000; 27: 460–4.

8 Rinaman L. Visceral sensory inputs to the endocrine hypothalamus. Front Neuroendocrinol 2007; 28: 50–60.

9 Messager S, Chatzidaki E, Ma D, Hendrick AG, Zahn D, Dixon J, *et al*. Kisspeptin directly stimulates gonadotropin-releasing hormone release via G protein-coupled receptor 54. Proc Natl Acad Sci USA 2005; 102: 1761–6.

10 Clarkson J, Tassigny X, Colledge WH, Caraty A, Herbison AE. Distribution of kisspeptin neurons in the adult female mouse brain. J Neuroendocrinol 2009; 21: 673–82.

11 Mikkelsen JD, Simonneaux V. The neuroanatomy of the kisspeptin system in the mammalian brain. Peptides 2009; 30: 26–33.

12 Gottsch ML, Clifton DK, Steiner RA. Kisspepeptin-GPR54 signaling in the neuroendocrine reproductive axis. Mol Cell Endocrinol 2006; 25: 91–6.

13 Smith JT, Clifton DK, Steiner RA. Regulation of the neuroendocrine reproductive axis by kisspeptin-GPR54 signaling. Reproduction 2006; 131: 623–30.

14 Paxinos G, Watson C. The rat brain in stereotaxic coordinates. 5th ed. San Diego: Academic Press; 2005.

15 Patel KP, Kline RL. Influence of renal nerves on noradrenergic responses to changes in arterial pressure. Am J Physiol Regul Integr Comp Physiol 1984; 247: R615–R620.

16 Dungan HM, Clifton DK, Steiner RA. Minireview: kisspeptin neurons as central processors in the regulation of gonadotropin-releasing hormone secretion. Endocrinology 2006; 147: 1154–8.

17 Antunes-Rodrigues J, Favaretto AL, Ballejo G, Gutkowska J, McCann SM. ANP as a neuroendocrine modulator of body fluid homeostasis. Rev Bras Biol 1996; 56: 221–31.

npg
Acta Pharmacologica Sinica (2010) 31: 150–159
© 2010 CPS and SIMM All rights reserved 1671-4083/10 $32.00
www.nature.com/aps

Original Article

Repurposing an old drug for a new use: glybenclamide exerts antiplatelet activity by interacting with the thromboxane A_2 receptor

Harold J TING, Wallace J MURRAY, Fadi T KHASAWNEH*

Department of Pharmaceutical Sciences, College of Pharmacy, Western University of Health Sciences, Pomona, CA 91766, USA

Aim: To investigate the potential antagonistic activity of the antidiabetic agent glybenclamide for the human platelet thromboxane A_2 receptor (abbreviated as TPR).
Methods: Platelets were obtained from healthy donors. Aggregation studies were performed in a model 700 aggregometry system. Radioactivity was counted in a Beckman LS 6000 liquid scintillation counter and calcium imaging was performed using an LS50B PerkinElmer Fluorescence Spectrometer.
Results: It was found that glybenclamide: 1) inhibited aggregation induced by the TPR agonist U46619 (IC_{50}=2.3±0.31 μmol/L) and by the thromboxane A_2 precursor arachidonic acid (IC_{50}=2.6±0.24 μmol/L); 2) displaced SQ29,548 from its binding sites on platelets; 3) lacked any detectable effects on aggregation stimulated by ADP, or the thrombin receptor activating-peptide 4; 4) blocked calcium mobilization induced by U46619, but not by ADP; and 5) failed to raise cAMP levels.
Conclusion: The findings indicate that glybenclamide exerts inhibitory effects on platelets by interacting with TPR. Thus, glybenclamide or a rationally designed derivative has the potential to serve as an antithrombotic agent.

Keywords: platelet; thromboxane receptor; thrombosis; drug-repurposing; antagonist

Acta Pharmacologica Sinica (2010) 31: 150–159; doi: 10.1038/aps.2009.195

Introduction

Platelet activation is a complex process with independent, yet overlapping pathways for activation[1–6]. One such pathway is triggered by an arachidonic acid derivative, known as thromboxane A_2 (TXA_2), which acts by interacting[7–9] with a seven-transmembrane receptor (abbreviated as TPR). The TXA_2 pathway has been shown[10–12] to play an essential role in hemostasis, and in the development of thrombotic disorders; making it a target for therapeutic interventions. Based on these considerations, therapeutic strategies have focused on either modulating the synthesis of TXA_2[13, 14], or interfering with its receptor binding. While, the former has been successfully targeted by the platelet COX-1 inhibitor aspirin, this therapeutic agent is associated with undesirable adverse effects (such as gastric ulcers)[15, 16], and resistance[17]. Regarding TPR antagonists; while many were developed[18–21], none of them is currently available for clinical use. Thus, there is still considerable interest in developing TPR antagonists.

To this end, estimates indicate that it may require 15 years to bring a new drug into the market, with a cost of hundreds of millions of dollars[22]. Furthermore, despite all efforts, only 20-30 drugs receive approval by the Food and Drug Administration (FDA) in the USA in any given year[23]. One solution to these limitations is to discover new uses for currently prescribed drugs; the "repurposing old drugs for new uses" approach[24–26]. Based on these considerations, we elected to undertake a similar approach in our pursuit of a TPR antagonist. Thus, we searched for drugs that share structural similarity with a TPR antagonist, namely SQ29,548[20]. We noticed significant similarity between the antidiabetic sulfonylurea glybenclamide[27], and SQ29,548, particularly with regard to the latter's pharmacophores[28]. Consequently, we hypothesized that glybenclamide exhibits TPR antagonistic activity. In this connection, given that sulfonylureas were pursued as antiplatelet agents, and although none of these studies was comprehensive, others have also investigated the antiplatelet effects of antidiabetics of the sulfonylurea class; including glybenclamide. For example, it was found that glybenclamide did not inhibit platelet aggregation induced by thrombin, but suppressed (calcium) Ca^{2+} release from internal Ca^{2+} stores induced by the same agent[29]. These data are contradictory since Ca^{2+} mobilization is known to play an essential role in

---

* To whom correspondence should be addressed.
E-mail fkhasawneh@westernu.edu
Received 2009-10-29 Accepted 2009-12-22

thrombin-dependent platelet activation[30]. Other studies have shown that glybenclamide inhibited both the cyclooxygenase and 12-lipoxygenase pathways in platelets[29], but in a later study the authors contradicted their own findings with regard to the inhibition of the lipoxygenase pathway[31]. Another study on the vasculature, showed that glybenclamide acts by interacting with TPRs[32], thereby contradicting the finding that glybenclamide inhibits the cyclooxygenase pathway. In summary, there are clear inconsistencies concerning the biological effects of glybenclamide on platelet function. While the reasons for these apparent discrepancies are not known, they may derive from variations in the experimental conditions/platelet preparations, inconsistency in the dose used in the various experimental approaches, or inherent differences in the potency of the ligands employed. Finally, in line with the principles of drug rediscovery, it is noteworthy that aspirin itself was initially used as an analgesic[33, 34], before its anti-platelet activity was discovered[13, 14].

Based on these considerations, we investigated two aspects of glybenclmaide's biology: (1) its functional effects on three different pathways of activation in human platelets; and (2) the potential mechanism by which it produces these effects (*eg*, TPR-dependent mechanism of action).

Materials and methods

Reagents

U46619, arachidonic acid, SQ29,548 and PGI_2 were from Cayman Chemical (Ann Arbor, MI). ADP, stir bars and other disposables were from (Chrono-Log; Havertown, PA). [^{3}H]SQ29,548 was purchased from PerkinElmer Life Sciences (Shelton, CT). Glybenclamide, Protease activated receptor 4 (PAR4) activating peptide (TRAP4; AYPGKF-NH_2), phosphodiesterase inhibitor Ro20-1724, protein kinase A, protein kinase A inhibitor, Cellosolve, isoflurane and indomethacin were from Sigma Aldrich (St Louis, MO). [^{3}H]cAMP was from Amersham Biosciences (Piscataway, NJ), and cold cAMP from Assay Designs (Ann Arbor, MI). The Adenylate cyclase inhibitor SQ22536 was from Enzo Life Sciences International, Inc (formerly BIOMOL international; Plymouth Meeting, PA). Sodium citrate (3.8% *w/v*) solution, 60 mL syringes, 50 mL conical tubes were obtained from Fisher Scientific (Hanover Park, IL). The Fura2/AM dye and Pluronic F-127 were from Molecular Probes (Eugene, OR). Human platelets were from healthy volunteers who denied taking any medication in the last 10 days prior to collection. Note: volunteers gave their informed consent before they were allowed to donate blood.

Human platelet functional studies

Blood was withdrawn by venipuncture of the cephalic vein into a 60 mL syringe (Kendall) from human volunteers. Coagulation was inhibited by addition of 3.8% *w/v* sodium citrate solution in a ratio of 9 parts blood to 1 part citrate. Blood was then spun at 160×*g* for 10 min in a 50 mL centrifuge tube. Resultant supernatant was carefully pipetted out and then recentrifuged at least once to sediment out nucleated cells, forming platelet rich plasma (PRP). Platelet poor plasma (PPP) was prepared by spinning blood at 2000×*g* for 15 min. PRP was diluted with PPP to adjust platelet count to 2×10^8–3×10^8 platelets/mL. All aggregation experiments were performed after incubation with 10 μmol/L indomethacin for 2 min to prevent thromboxane A_2 generation, except when arachidonic acid was used as the aggregating agonist. The control traces were obtained by the addition of vehicle, U46619, arachidonic acid, ADP, or TRAP4 to PRP after establishing baseline light transmission for at least 1 min. The effect of these agents was measured using the turbidimetric method[35] with a model 700 whole blood lumi-aggregometer (Chronolog Corporation; Havertown, PA). The aggregation traces were captured using the Aggrolink8 software (Chronolog Corporation; Havertown, PA).

Human platelet function inhibition studies

For the inhibition of platelet function studies, PRP was incubated with 1–10 μmol/L glybenclamide, 150 nmol/L or 1 μmol/L SQ29,548 or vehicle controls for 5 min prior to stimulation with 1 μmol/L U46619, 0.5 mmol/L arachidonic acid, 15 μmol/L ADP, or 40 μmol/L TRAP4. Furthermore, the reversal of inhibition was performed after first incubating with the adenylate cyclase inhibitor (300 μmol/L) SQ22536 for 45 min, then adding 1 nmol/L PGI_2, or 10 μmol/L glybenclamide before stimulation with 1 μmol/L U46619 or 0.5 mmol/L arachidonic acid.

Displacement binding in intact platelets.

Resuspended platelets were prepared as previously described[36, 37]. The platelet suspension (1×10^9 platelets/mL) was incubated with 1 nmol/L [^{3}H]SQ29,548 at RT for 10 min, and then increasing concentrations of the displacing ligand glybenclamide (0.035–30 μmol/L) were added for an additional 45 min. Next, the [^{3}H]SQ29,548 bound platelets were captured by running through 0.45 micron Millipore filters over a vacuum suction unit. The filters were then washed once and counted for radioactivity in a Beckman LS 6000 liquid scintillation counter. To calculate the non-specific binding, the same concentration of radioligand was competed against 1000-fold excess of unlabeled SQ29,548.

Assay of platelet adenosine 3', 5'-cyclic monophosphate (cAMP)

Human PRP (500 μL) samples were collected in an eppendorf tube and treated with vehicle, (1 nmol/L) PGI_2, or (10 μmol/L) glybenclamide. Next, the phosphodiesterase inhibitor RO20-1724 (100 μmol/L) was added, and platelets were spun down and immediately frozen in liquid nitrogen. The platelet pellet was then resuspended, sonicated, boiled for 4 min, spun down, and the supernatant was transferred to a new tube. The concentration of cAMP in the supernatant was measured as previously described[38]. The standard curve samples were prepared by adding known concentrations of unlabeled cAMP to the supernatant obtained from vehicle treated platelets.

Platelet calcium mobilization

Platelets were isolated from blood, washed, and then suspended in Tyrode's buffer without calcium. Platelets were then loaded with Fura-2/AM (5 μmol/L) in the presence of

Pluronic F-127 (0.2 μg/mL; Molecular Probes) for 30 min at 37 °C. Next, platelets were washed once and resuspended in Tyrode's buffer containing 0 or 1 mmol/L Ca^{2+}. Platelets were then activated with U46619 (1 μmol/L), arachidonic acid (0.5 mmol/L), ADP (15 μmol/L) or TRAP4 (40 μmol/L), in the presence or absence of glybenclamide (10 μmol/L). Calcium measurements were done by alternating excitation between 340 and 380 nm, and measuring fluorescence/emission at 509 nm using an LS 50B Fluorescence Spectrometer (PerkinElmer).

Data analysis

All experiments were performed at least three times, with blood obtained from at least three different donors. Data were analyzed using GraphPad PRISM statistical software (San Diego, CA). The displacement binding curve was generated using non-linear regression analysis, with a one site competition model, whereas the standard cAMP curve was generated by applying linear regression. Results were compared using unpaired 2-tailed Student's *t* test, with $P<0.05$ considered to be statistically significant. IC_{50} values are represented as mean±SEM.

Results

Glybenclamide inhibits TPR-/U46619-induced platelet aggregation

Given the structural similarity between glybenclamide and SQ29,548 (Figure 1), and in order to investigate whether the oral sulfonylurea glybenclamide (an antidiabetic agent) has the capacity to inhibit platelet TPR signaling, platelet aggregometry experiments were performed. Our initial studies demonstrated that addition of TXA_2 mimetic U46619 (1 μmol/L) to human PRP produced a typical shape change and aggregation response (Figure 2A). Furthermore, it was also found that 1 μmol/L of glybenclamide produced a significant inhibition of the U46619-induced platelet activation (Figure 2A; 1 μmol/L trace). This inhibitory effect of glybenclamide was found to be concentration-dependent (Figure 2A; 1−10 μmol/L traces and inset), with an IC_{50} = 2.3±0.31 μmol/L. This finding demonstrates that glybenclamide has the capacity to block platelet aggregation, and that the underlying mechanism perhaps involves TPRs. To test this notion, the next set of experiments investigated the effects of glybenclamide on a separate agonist, namely the TXA_2 precursor arachidonic acid, which also triggers platelet aggregation by activating TPRs.

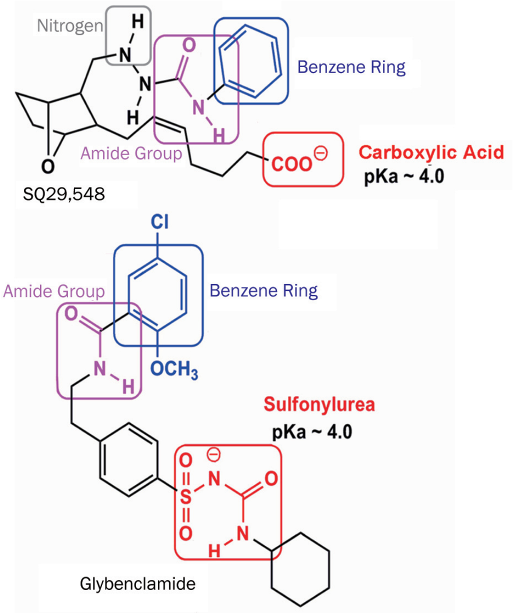

Figure 1. The chemical structure of the TPR antagonist SQ29,548 (top panel), and the sulfonylurea glybenclamide (bottom panel). The analogous moieties are highlighted using a matching color font, whereas the unshared pharmacophore is indicated by the grey font in SQ29,548.

Glybenclamide inhibits TPR-/arachidonic acid-induced platelet aggregation

Similar to U46619, it was found that glybenclamide exerted concentration-dependent (1−10 μmol/L) inhibition on platelet activation stimulated by 0.5 mmol/L arachidonic acid (Figure 2B), with an IC_{50}=2.6±0.24 μmol/L. These data further suggest that the underlying mechanism by which glybenclamide inhibits platelets is through TPR blockade. To confirm the interaction with platelet TPRs, displacement binding studies between glybenclamide and a well-characterized radiolabeled TPR antagonist (*ie*, $[^3H]$SQ29,548) were performed.

Glybenclamide displaces $[^3H]$SQ29,548 from its TPR binding sites

If glybenclamide exerts its inhibitory effects via TPR antagonism, then it would be expected to displace TPR ligands from their binding sites. Using radioligand displacement studies, it was found that glybenclamide, indeed, had the capacity to completely displace $[^3H]$SQ29,548 from its binding sites on platelets (Figure 3), demonstrating an interaction with TPRs. While this finding clearly indicates that the mechanism by which glybenclamide inhibits platelets involves TPR antagonism, it does not rule out the potential for generalized inhibitory effects on platelet, through a cAMP-dependent mechanism. To test this possibility, we examined the effects of glybenclamide on platelet aggregation mediated by TPR-independent mechanisms (*ie*, ADP and the thrombin receptor activating peptide 4 [TRAP4]).

Glybenclamide is devoid of inhibitory effects on ADP-induced platelet aggregation

If cAMP indeed contributes to the inhibitory effects of glybenclamide on platelet function, one would expect glybenclamide blockade of platelet aggregation in response to all agonists, *eg*, ADP and TRAP4. Our results demonstrated that pretreating platelets with glybenclamide (1 μmol/L) did not produce any detectable effects on platelet aggregation in response to 15 μmol/L ADP (data not shown). Moreover, even at a concentration as high as 10 μmol/L, which completely blocked aggregation by U46619 or arachidonic acid (Figure 2A and 2B, respectively), glybenclamide appeared to be devoid of any inhibitory effects on platelet aggregation by ADP (Figure 4A). This finding suggests that the mechanism by which glybenclamide inhibits platelet aggregation is cAMP independent.

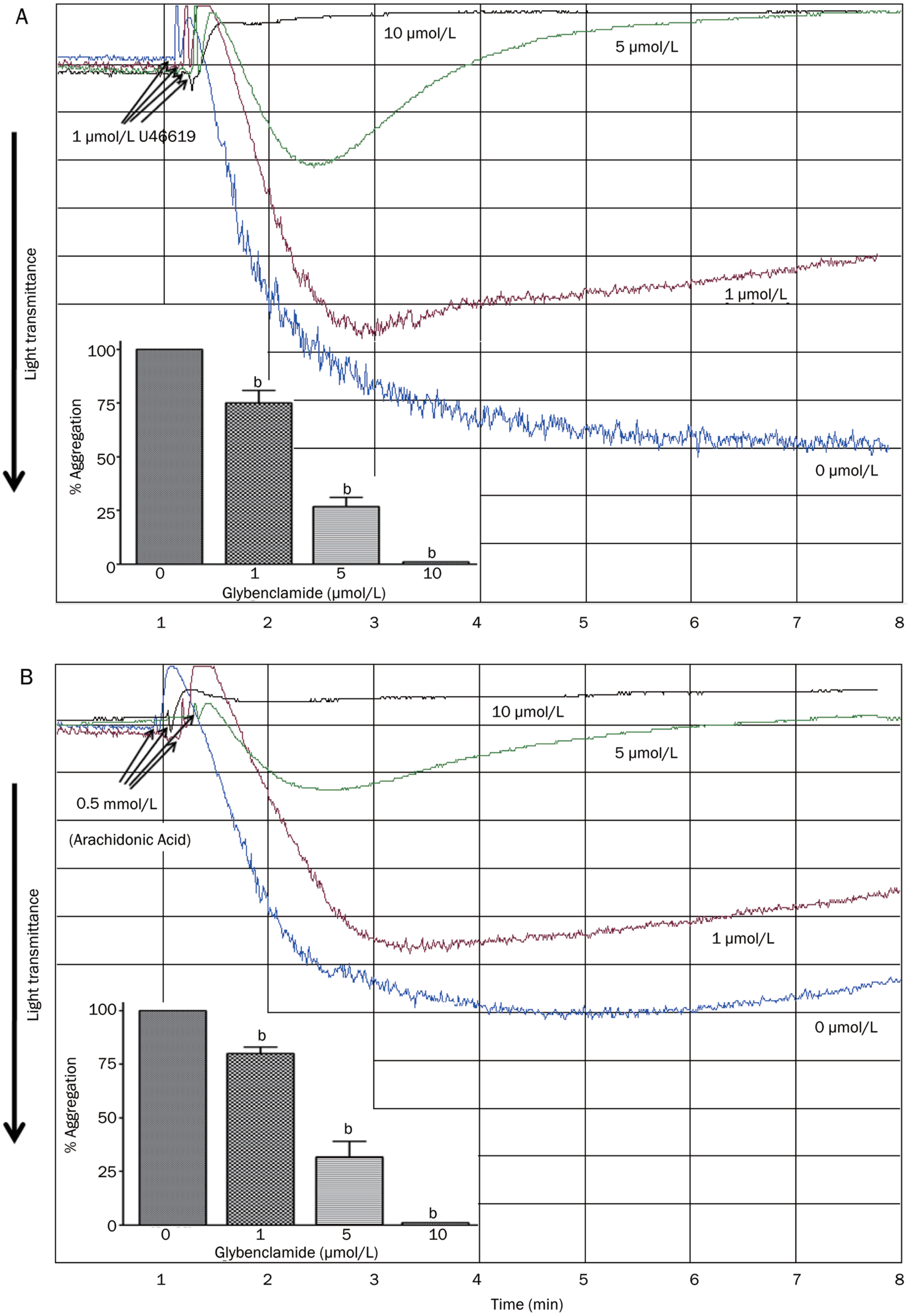

Figure 2. Effect of glybenclamide on human platelet aggregation stimulated by the TPR agonist U46619, and the TXA_2 precursor arachidonic acid. (A) Indomethacin-treated PRP was stimulated with 1 μmol/L U46619 in the absence or presence of increasing concentrations of glybenclamide (1–10 μmol/L) to generate a concentration-dependent inhibition curve (inset shows quantification of the glybenclamide concentration-dependent inhibition curve of U46619-induced aggregation response). (B) PRP was stimulated with 0.5 mmol/L arachidonic acid in the absence or presence of increasing concentrations of glybenclamide (1–10 μmol/L) to generate a concentration-dependent inhibition curve (inset shows quantification of the glybenclamide concentration-dependent inhibition curve of arachidonic acid-induced aggregation response). Each aggregation curve is representative of multiple traces obtained from three separate platelet preparations, from three different blood donors ($^{b}P<0.05$, $n=3$).

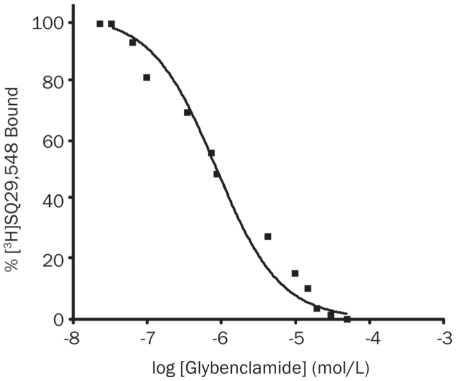

Figure 3. Displacement binding curve of [^{3}H]SQ29,548 by glybenclamide in intact platelets. Binding displacement of 1 nmol/L [^{3}H]SQ29,548 with increasing concentrations of glybenclamide (0.035–30 μmol/L). Results are the average of at least three different experiments, from blood obtained from three separate donors.

This was further confirmed by determining whether glybenclamide inhibits aggregation induced by TRAP4.

Glybenclamide is devoid of inhibitory effects on TRAP4-induced platelet aggregation

As was the case with the platelet agonist ADP, our results revealed that glybenclamide, even at high concentrations (10 μmol/L) did not exhibit any detectable effects on platelet aggregation triggered by 40 μmol/L TRAP4 (Figure 4B). These data indicate that glybenclamide does not produce broad-spectrum inhibition of platelet aggregation, which is consistent with cAMP-independent mechanisms. To directly examine this notion, we next investigated whether glybenclamide raises platelet cAMP levels.

Glybenclamide does not raise platelet cAMP levels

The finding that glybenclamide exerts inhibitory effects on platelet activation that are specific to TPRs argues against a cAMP-dependent mechanism. This conclusion was confirmed by measuring cAMP levels in response to glybenclamide treatment. Our data indicates that even at 10 μmol/L, glybenclamide did not elevate platelet cAMP levels, as opposed to 1 nmol/L of the control PGI$_2$ (Figure 5A). Furthermore, while the adenylyl cyclase inhibitor SQ22536 (300 μmol/L) did not produce any detectable effects on glybenclamide blockade of U46619- or arachidonic acid-stimulated aggregation (Figure 5B and 5C, respectively), it completely reversed the inhibitory effects of PGI$_2$ on aggregation induced by U46619 (Figure 5D). These data demonstrate that the underlying mechanism of inhibition of platelet activation by glybenclamide does not involve cAMP. We next examined the effect of glybenclamide on calcium mobilization in response to TPR activation.

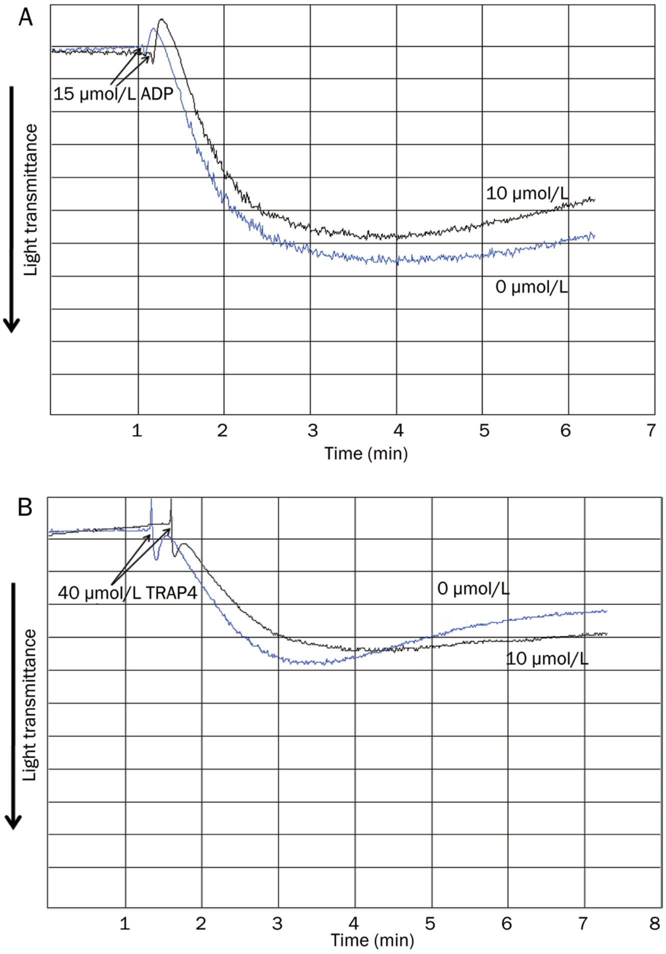

Figure 4. Effect of glybenclamide on human platelet aggregation stimulated by ADP, and the thrombin receptor activating peptide 4 (TRAP4). (A) Indomethacin-treated PRP was stimulated with 15 μmol/L ADP in the absence or presence of 10 μmol/L glybenclamide. (B) Indomethacin-treated PRP was stimulated with 40 μmol/L TRAP4 in the absence or presence of 10 μmol/L glybenclamide. Each aggregation curve is representative of multiple traces obtained from three separate platelet preparations, from three different blood donors.

Glybenclamide inhibits calcium mobilization induced by TPR/U46619 but not by ADP

Since calcium plays a central role in platelet aggregation downstream of TPR and other G-protein coupled receptors, it is expected that glybenclamide would also inhibit calcium mobilization. Indeed, it was found that glybenclamide (10 μmol/L) abolished calcium mobilization in response to 1 μmol/L U46619 and 0.5 mmol/L arachidonic acid (Figure 6A and not shown, respectively). On the other hand, 10 μmol/L glybenclamide did not produce any effects on calcium mobilization in response to 15 μmol/L ADP or 40 μmol/L TRAP4 (Figure 6B, and not shown, respectively). These data are consistent with glybenclamide's inhibitory effects that are selective for TPR-dependent platelet function. Finally, we sought to compare the inhibitory profile of glybenclamide with that for the classical TPR antagonist SQ29,548.

Glybenclamide exhibits a platelet-function inhibitory profile that is comparable to that of the classical TPR antagonist SQ29,548

Similar to glybenclamide's effects, it was found that the selective TPR antagonist SQ29,548 (at 150 nmol/L or 1 μmol/L) blocked platelet aggregation stimulated by 1 μmol/L U46619

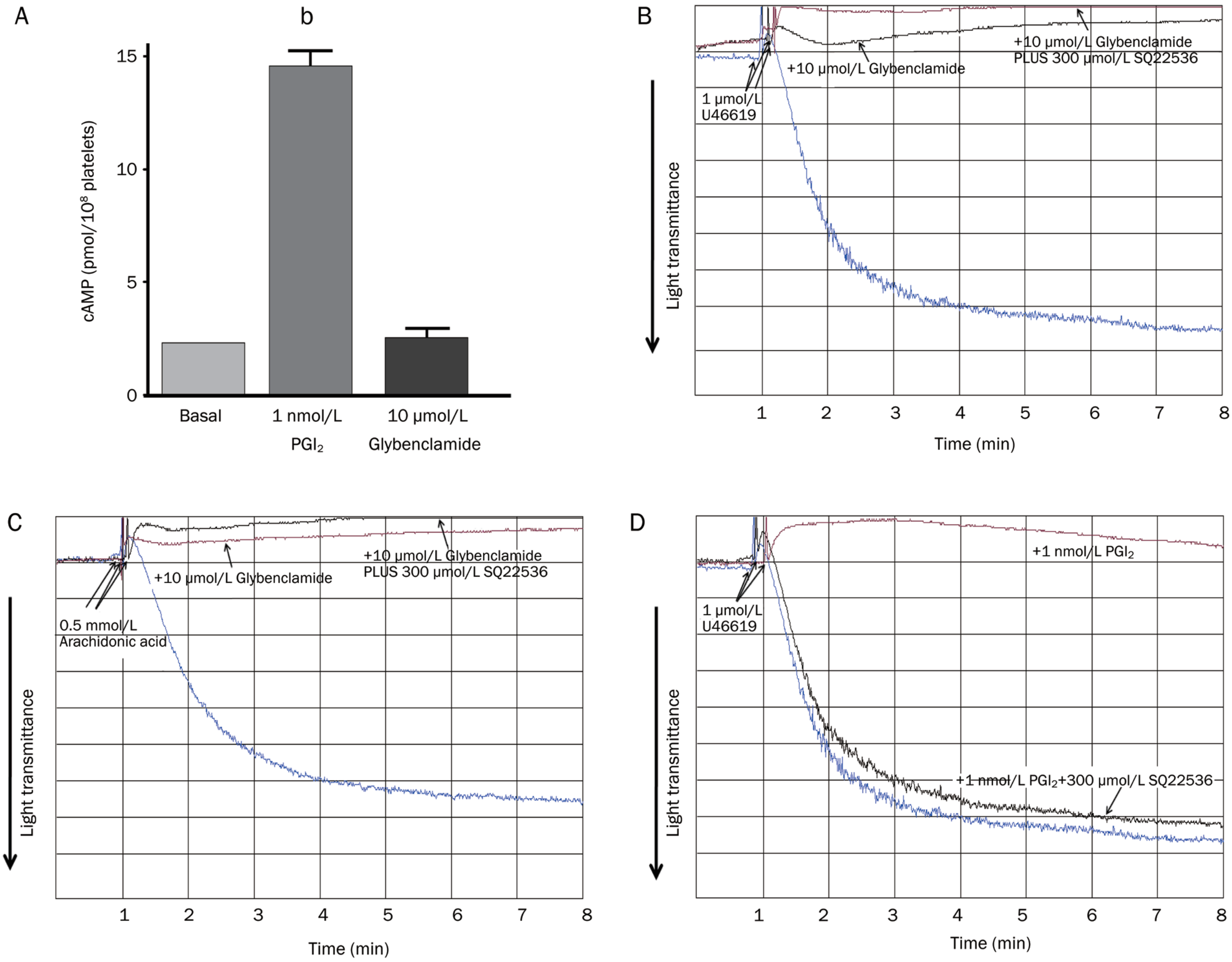

Figure 5. Effects of glybenclamide and PGI_2 on basal platelet cAMP levels; and effects of glybenclamide on human platelet aggregation induced by U46619 or arachidonic acid (compared to the effects of PGI_2 on human platelet aggregation induced by U46619) in the presence or absence of the AC inhibitor SQ22536. A) PRP was treated with 10 μmol/L glybenclamide or 1 nmol/L of the control PGI_2 before cAMP levels were measured ($^bP<0.05$, $n=3$). B) PRP was first incubated with or without the AC inhibitor SQ22536 (300 μmol/L) and then stimulated with 1 μmol/L U46619 in the presence or absence of 10 μmol/L glybenclamide. C) PRP was first incubated with or without the AC inhibitor SQ22536 (300 μmol/L) and then stimulated with 0.5 mmol/L arachidonic acid in the presence or absence of 10 μmol/L glybenclamide. D) PRP was first incubated with or without the AC inhibitor SQ22536 (300 μmol/L) and then stimulated with 1 μmol/L U46619 in the presence or absence of 1 nmol/L PGI_2. Each aggregation curve is representative of multiple traces obtained from three separate platelet preparations, from three different blood donors.

or 0.5 mmol/L arachidonic acid (Figure 7A, 7B, 7C, and not shown). On the other hand, SQ29,548 (at 150 nmol/L or even 1 μmol/L) was found to be devoid of any inhibitory effects on platelet aggregation triggered by 15 μmol/L ADP, or 40 μmol/L TRAP4 (Figure 7D, 7E, 7F, and not shown). Thus, the inhibitory profile exhibited by glybenclamide on platelet function appears to be identical to that of the classical TPR antagonist SQ29,548, which is in agreement with a TPR-dependent mechanism of action.

In summary, the present studies demonstrate that glybenclamide has the capacity to exert TPR-specific inhibitory effects on human platelet function, as demonstrated by selective blockade of aggregation (and calcium mobilization) by the classical agonists U46619 and arachidonic acid, and displacement of binding of a classical TPR ligand. Our results also provide evidence that cAMP is not involved in the mechanism of inhibition, since glybenclamide lacked any inhibition on aggregation mediated by the agonists ADP and TRAP4, nor did it increase platelet cAMP levels.

Discussion

Given the clear involvement of TXA_2/TPR signaling in the pathogenesis of multiple disease processes (*eg*, thrombosis and asthma)[10–12, 39], the limitations of aspirin therapy[15, 16], and evidence that antagonists are superior to aspirin in certain disease states[40], there is an increasing interest in the development of TPR antagonists. Of note, due to a host of reasons, the use of antagonists developed (which were not rationally designed)

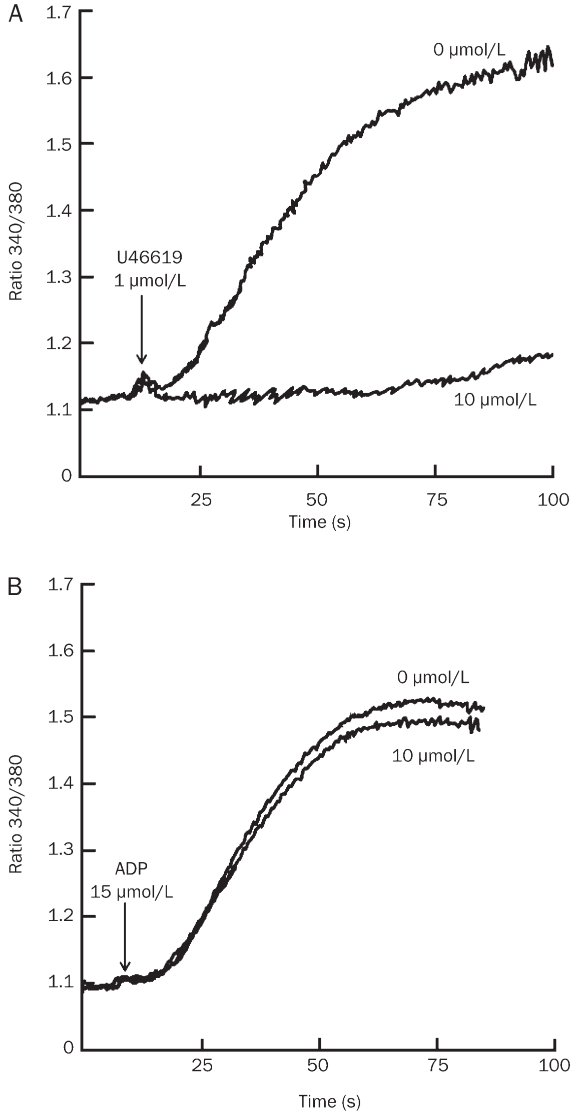

Figure 6. Effect of glybenclamide on human platelet calcium mobilization stimulated by the TPR agonist U46619, and ADP. (A) Indomethacin-treated PRP was stimulated with 1 μmol/L U46619 in the absence or presence of 10 μmol/L glybenclamide. (B) Indomethacin-treated PRP was stimulated with 15 μmol/L ADP in the absence or presence of 10 μmol/L glybenclamide. Each calcium trace is representative of multiple traces obtained from three separate platelet preparations, from three different blood donors.

thus far, has been experimental[18–21, 41]. Nonetheless, it is anticipated that recent literature regarding the ligand-binding domain of TPR will aid the discovery of TPR antagonists[42, 43].

Historically, conventional drug discovery takes one of two routes[44], either the target-centered or compound-centered approach, and each route may take around 15 years. Consequently, there is growing interest in an approach that focuses on investigating new indications for drugs that have already been approved by the FDA (*ie*, "drug rediscovery")[24–26]. Aside from their well-characterized pharmacology, such drugs would have a safety profile that has been well defined through many years of clinical experience. To this end, we decided to undertake a similar approach (*ie*, repurpose a currently approved drug) in our pursuit of agents that possess antagonistic activity against platelet TPRs. Specifically, we searched for drugs that share structural similarity with TPR antagonists. We selected the experimental TPR antagonist with the highest affinity (*ie*, SQ29,548), and we were particularly interested in compounds that share similarity with the pharmacophores of SQ29,548[28]. We found that the antidiabetic agent glybenclamide meets this structural requirement as follows (see Figure 1): 1) the functional groups which are anionic at physiological pH (7.4); these are the carboxylic acid group of SQ29,548 and the sulfonylurea of glybenclamide (indicated by the red fonts in the structures); 2) the amide groups (indicated by the pink fonts in the structures); and 3) the aromatic rings (indicated in blue fonts in the structures). On the other hand, glybenclamide appears to lack a chemical group equivalent to the fourth SQ29,548 pharmacophore, *ie*, the 14-position nitrogen indicated by the grey font in SQ29,548 structure (see Figure 1). Nonetheless, we believe that there is sufficient similarity in their chemistry to confer glybenclamide with the capacity to interact with TPRs. In order to test this notion and to address previous inconsistencies regarding its biological activity, we evaluated the effects of glybenclamide on platelet aggregation mediated via TPR activation. Interestingly, it was found that pre-treating platelets with glybenclamide resulted in significant inhibition in their aggregation response to the agonist U46619, in a concentration dependent manner. Glybenclamide also inhibited the calcium mobilization response triggered by U46619. These findings demonstrate that this antidiabetic drug does indeed have the capacity to block platelet function, presumably via interacting with TPRs. To further test this notion, we examined the effects of glybenclamide on aggregation triggered by the TXA_2 precursor arachidonic acid. Our results showed that glybenclamide exerted a concentration-dependent inhibitory effect on aggregation triggered by arachidonic acid. Given the chemical similarity between glybenclamide and the antagonist SQ29,548, this finding appears to be consistent with a TPR-dependent mechanism of action. This notion was further supported by the finding that glybenclamide completely displaced the radiolabeled antagonist SQ29,548 from its platelet TPR binding sites. In addition, these data suggest that glybenclamide does in fact contain a "minimum" number of pharmacophores that are required for interacting with TPR, and possess a three dimensional orientation that allows for this interaction. Nevertheless, without performing molecular modeling studies, it will be difficult to accurately predict which of the proposed chemical groups of glybenclamide serve as pharmacophores, and thereby participate in its interaction process with the ligand binding pocket of TPR. Notably, the concentration needed to produce complete inhibition of platelets by glybenclamide is higher than those for SQ29,548, which suggests that the former has lower affinity for the receptor. It is tempting to speculate that the apparent low affinity of glybenclamide for platelet TPRs is due to: 1 lack of one or more of the established pharmacophores of SQ29,548 (*eg*, the 14-position nitrogen), which means lower

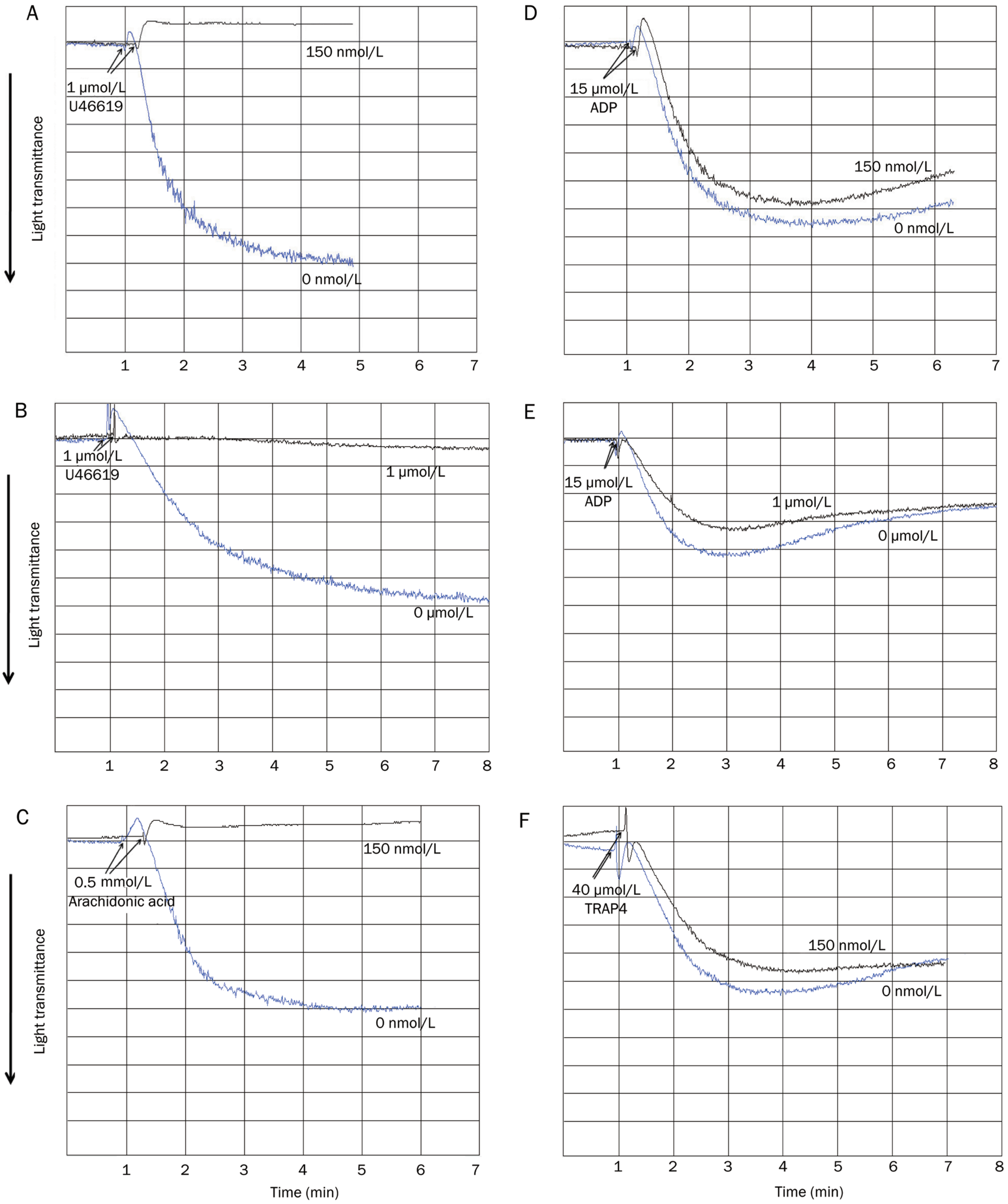

Figure 7. Effect of SQ29,548 on human platelet aggregation stimulated by the TPR agonist U46619, the TXA_2 precursor arachidonic acid, ADP, and the thrombin receptor activating peptide 4 (TRAP4). A) Indomethacin-treated PRP was stimulated with 1 μmol/L U46619 in the absence or presence of 150 nmol/L SQ29,548. B) Indomethacin-treated PRP was stimulated with 1 μmol/L U46619 in the absence or presence of 1 μmol/L SQ29,548. C) PRP was stimulated with 0.5 mmol/L arachidonic acid in the absence or presence of 150 nmol/L SQ29,548. D) Indomethacin-treated PRP was stimulated with 15 μmol/L ADP in the absence or presence of 150 nmol/L SQ29,548. E) Indomethacin-treated PRP was stimulated with 15 μmol/L ADP in the absence or presence of 1 μmol/L SQ29,548. F) Indomethacin-treated PRP was stimulated with 40 μmol/L TRAP4 in the absence or presence of 150 nmol/L SQ29,548. Each aggregation curve is representative of multiple traces obtained from three separate platelet preparations, from three different blood donors.

number of TPR amino acid recognition/interaction sites; and/or 2 possessing a three dimensional conformation that is somewhat different from SQ29,548; especially, since glybenclamide is a flexible compound whereas SQ29,548 has a rigid chemistry, and this would impact the manner by which it docks onto the binding pocket; and/or 3 differences in the bonding energies of the two molecules. Therefore, to guide the repurposing of drugs, one should make similar structural comparisons, especially for experimental drugs with well-defined pharmacophores[45]. Based on these considerations, we believe this may represent a general paradigm that may be extended to other targets/drugs.

In summary, our data thus far provide evidence that glybenclamide exhibits inhibitory effects on platelet function, and indicate that the underlying mechanism is mediated, at least in part, via TPR blockade. However, our data does not exclude the possibility that cAMP, a common inhibitor of platelet function, may contribute to the antiplatelet effects of glybenclamide. If this were the case, then glybenclamide would be expected to also produce inhibitory effects on platelet activation triggered by mechanisms independent of TPRs (*eg*, ADP or TRAP4). However, our experiments revealed that even when used at a concentration that completely blocked TPR-mediated aggregation, glybenclamide produced no apparent effects on aggregation or calcium mobilization induced by ADP, or TRAP4, nor did it cause cAMP increases. Also, the adenylyl cyclase inhibitor SQ22536 did not reverse the inhibitory effects that glybenclamide exerted on platelet activation by TPRs, whereas it completely reversed those by the control PGI_2. These findings further demonstrate that the inhibitory effects exerted by glybenclamide are limited to TPR antagonism. Consistent with our conclusions, control experiments revealed that glybenclamide exhibited a platelet-function inhibitory profile that is similar to that for the TPR antagonist SQ29,548, i.e., selective blockade of platelet aggregation mediated by activation of TPRs, but not by ADP or TRAP4 receptors.

Collectively, our results obtained using human platelets provide evidence that glybenclamide exerts antiplatelets effects that are TPR dependent. Consequently, glybenclamide has the potential to serve as a therapeutic agent, and can be added to the arsenal of interventions available for treating thrombotic disease. Furthermore, based on recent evidence[46] of a novel inhibitory function for isoprostanes in platelets, which was shown to prevail under conditions of TPR antagonism, concurrent therapy of a TPR antagonist (*eg*, glybenclamide) and aspirin might be superior to either therapy alone. Thus, glybenclamide may prove beneficial in combination therapy approaches.

Even if this newly identified biological activity is not adequate for therapy or if the hypoglycemia that may be induced by glybenclamide is an issue, novel glybenclamide derivatives, with antithromboxane receptor activity, may be rationally-designed; as was previously done were a TPR antagonist was derived from the loop diuretic torasemide; which is also a sulfonylurea[47]. Nevertheless, our findings suggest that the use of glybenclamide should be encouraged in the treatment of diabetic patients with enhanced platelet functions; especially since hypoglycemia would not be a limiting factor. Finally, consistent with our findings, a study on patients diagnosed with type II Diabetes Millets, and treated with glybenclamide for 4 months, revealed that they were protected against thrombosis formation[48]. Thus, while hypoglycemia could be a limiting factor, glybenclamide appears to produce its protective effects against thrombosis development, at concentrations that are effective for managing Diabetes Millets[48]. This is an important consideration given the established link between diabetes and thrombotic disorders.

Non standard abbreviations

PRP, platelet rich plasma; PPP, platelet poor plasma; TXA_2, thromboxane A_2; TPR, thromboxane A_2 receptor; TRAP4, thrombin receptor-activating peptide 4; PAR, protease activated receptor.

Acknowledgments

This work was supported by Intramural Funding Support from the College of Pharmacy at Western University of Health Sciences (to FTK). The authors would like to thank Dr Daniel PEARCE for assistance with blood draws. The authors have no conflicting financial interests.

Author contribution

Fadi T KHASAWNEH: Experimental design, data interpretation/analysis and prepared the manuscript; Wallace J MURRAY: data interpretation/analysis and participated in manuscript preparation; Harold J TING: Performed experiments and manuscript preparation.

References

1 Baglia FA, Shrimpton CN, Emsley J, Kitagawa K, Ruggeri ZM, Lopez JA, *et al*. Factor XI interacts with the leucine-rich repeats of glycoprotein Ibalpha on the activated platelet. J Biol Chem 2004; 279: 49323–9.

2 Born GV. Aggregation of blood platelets by adenosine diphosphate and its reversal. Nature 1962; 194: 927–9.

3 Brisson C, Azorsa DO, Jennings LK, Moog S, Cazenave JP, Lanza F. Co-localization of CD9 and GPIIb-IIIa (alpha IIb beta 3 integrin) on activated platelet pseudopods and alpha-granule membranes. Histochem J 1997; 29: 153–65.

4 Du X. Signaling and regulation of the platelet glycoprotein Ib-IX-V complex. Curr Opin Hematol 2007; 14: 262–9.

5 Landis RC. Protease activated receptors: clinical relevance to hemostasis and inflammation. Hematol Oncol Clin North Am 2007; 21: 103–13.

6 Reilly M, Fitzgerald GA. Cellular activation by thromboxane A2 and other eicosanoids. Eur Heart J 1993; 14 Suppl K: 88–93.

7 Halushka PV, Mais DE, Mayeux PR, Morinelli TA. Thromboxane, prostaglandin and leukotriene receptors. Annu Rev Pharmacol Toxicol 1989; 29: 213–39.

8 Hirata M, Hayashi Y, Ushikubi F, Yokota Y, Kageyama R, Nakanishi S, *et al*. Cloning and expression of cDNA for a human thromboxane A_2 receptor. Nature 1991; 349: 617–20.

9 Kim SO, Lim CT, Lam SC, Hall SE, Komiotis D, Venton DL, *et al*. Purification of the human blood platelet thromboxane A_2/prostaglandin H_2 receptor protein. Biochem Pharmacol 1992; 43: 313–22.

10 Oates JA, FitzGerald GA, Branch RA, Jackson EK, Knapp HR, Roberts LJ 2nd. Clinical implications of prostaglandin and thromboxane A_2 formation (2). N Engl J Med 1988; 319: 761–7.
11 Patrono C, Ciabattoni G, Davi G. Thromboxane biosynthesis in cardiovascular diseases. Stroke 1990; 21 (12 Suppl): IV130–3.
12 Ogletree ML. Overview of physiological and pathophysiological effects of thromboxane A2. Fed Proc 1987; 46: 133–8.
13 Clarke RJ, Mayo G, Price P, FitzGerald GA. Suppression of thromboxane A2 but not of systemic prostacyclin by controlled-release aspirin. N Engl J Med 1991; 325: 1137–41.
14 Patrono C. Aspirin as an antiplatelet drug. N Engl J Med 1994; 330: 1287–94.
15 Meijer K, Schulman S. Determinants of bleeding risk in patients on antithrombotic and antifibrinolytic drugs. Semin Thromb Hemost 2008; 34: 762–71.
16 Schlansky B, Hwang JH. Prevention of nonsteroidal anti-inflammatory drug-induced gastropathy. J Gastroenterol 2009; 44 Suppl 19: 44–52.
17 Pusch G, Feher G, Kotai K, Tibold A, Gasztonyi B, Feher A, *et al*. Aspirin resistance: focus on clinical endpoints. J Cardiovasc Pharmacol 2008; 52: 475–84.
18 Le Breton GC, Venton DL, Enke SE, Halushka PV. 13-Azaprostanoic acid: a specific antagonist of the human blood platelet thromboxane/endoperoxide receptor. Proc Natl Acad Sci U S A 1979; 76: 4097–101.
19 Nicolaou KC, Magolda RL, Smith JB, Aharony D, Smith EF, Lefer AM. Synthesis and biological properties of pinane-thromboxane A2, a selective inhibitor of coronary artery constriction, platelet aggregation, and thromboxane formation. Proc Natl Acad Sci USA 1979; 76: 2566–70.
20 Ogletree ML, Harris DN, Greenberg R, Haslanger MF, Nakane M. Pharmacological actions of SQ 29,548, a novel selective thromboxane antagonist. J Pharmacol Exp Ther 1985; 234: 435–41.
21 Patscheke H, Stegmeier K, Muller-Beckmann B, Sponer G, Staiger C, Neugebauer G. Inhibitory effects of the selective thromboxane receptor antagonist BM 13.177 on platelet aggregation, vasoconstriction and sudden death. Biomed Biochim Acta 1984; 43: S312–8.
22 DiMasi JA, Hansen RW, Grabowski HG. The price of innovation: new estimates of drug development costs. J Health Econ 2003; 22: 151–85.
23 Cohen FJ. Macro trends in pharmaceutical innovation. Nat Rev Drug Discov 2005; 4: 78–84.
24 Aronson JK. Old drugs--new uses. Br J Clin Pharmacol 2007; 64: 563–5.
25 Chong CR, Sullivan DJ Jr. New uses for old drugs. Nature 2007; 448: 645–6.
26 McPhie DC. Old drugs, new uses: solving a Hatch-Waxman patent predicament. Food Drug Law J 2004; 59: 155–68.
27 Dessi P. [Basic pharmacological research on the hypoglycemic action of N-4-[beta-(2-methoxy-5-chlorbenzamide)-ethyl]-benzosulfonyl-N′-cyclohexylu rea (Glybenclamide)]. Acta Diabetol Lat 1969; 6: 206–21.
28 Jin B, Hopfinger AJ. A proposed common spatial pharmacophore and the corresponding active conformations of some TXA_2 receptor antagonists. J Chem Inf Comput Sci 1994; 34: 1014–21.
29 Ozaki Y, Yatomi Y, Kume S. Effects of oral hypoglycaemic agents on platelet functions. Biochem Pharmacol 1992; 44: 687–91.
30 Dubois C, Panicot-Dubois L, Gainor JF, Furie BC, Furie B. Thrombin-initiated platelet activation *in vivo* is vWF independent during thrombus formation in a laser injury model. J Clin Invest 2007; 117: 953–60.
31 Satoh K, Ozaki Y, Yatomi Y, Kume S. Effects of sulfonylurea agents on platelet arachidonic acid metabolism; study on platelet homogenates. Biochem Pharmacol 1994; 48: 1053–5.
32 Pfister SL, Pratt PE, Kurian J, Campbell WB. Glibenclamide inhibits thromboxane-mediated vasoconstriction by thromboxane receptor blockade. Vascul Pharmacol 2004; 40: 285–92.
33 Eagle E, Carlson AJ. Toxicity, antipyretic and analgesic studies on 39 compounds including aspirin, phenacetin and 27 derivatives of carbazole and tetrahydrocarbazole. J Pharmacol Exp Ther 1950; 99: 450–7.
34 Steiner TJ, Voelker M. Gastrointestinal tolerability of aspirin and the choice of over-the-counter analgesia for short-lasting acute pain. J Clin Pharm Ther 2009; 34: 177–86.
35 Michal F, Born GV. Effect of the rapid shape change of platelets on the transmission and scattering of light through plasma. Nat New Biol 1971; 231: 220–2.
36 Hung SC, Ghali NI, Venton DL, Le Breton GC. Specific binding of the thromboxane A2 antagonist 13-azaprostanoic acid to human platelet membranes. Biochim Biophys Acta 1983; 728: 171–8.
37 Kattelman EJ, Venton DL, Le Breton GC. Characterization of U46619 binding in unactivated, intact human platelets and determination of binding site affinities of four TXA2/PGH2 receptor antagonists (13-APA, BM 13.177, ONO 3708 and SQ 29,548). Thromb Res 1986; 41: 471–81.
38 Gilman AG. A protein binding assay for adenosine 3':5'-cyclic monophosphate. Proc Natl Acad Sci U S A 1970; 67: 305–12.
39 Dahlen SE, Kumlin M, Granstrom E, Hedqvist P. Leukotrienes and other eicosanoids as mediators of airway obstruction. Respiration 1986; 50 Suppl 2: 22–9.
40 Cayatte AJ, Du Y, Oliver-Krasinski J, Lavielle G, Verbeuren TJ, Cohen RA. The thromboxane receptor antagonist S18886 but not aspirin inhibits atherogenesis in apo E-deficient mice: evidence that eicosanoids other than thromboxane contribute to atherosclerosis. Arterioscler Thromb Vasc Biol 2000; 20: 1724–8.
41 Ghali NI, Kattelman EJ, Hung SC, Schnorf KE, Le Breton GC, Venton DL. Synthesis of [17,18-^{3}H] *trans*-13-azaprostanoic acid. A labeled probe for the PGH2/TXA2 receptor. Prostaglandins 1984; 27: 865–76.
42 Khasawneh FT, Huang JS, Turek JW, Le Breton GC. Differential mapping of the amino acids mediating agonist and antagonist coordination with the human thromboxane A2 receptor protein. J Biol Chem 2006; 281: 26951–65.
43 Turek JW, Halmos T, Sullivan NL, Antonakis K, Le Breton GC. Mapping of a ligand-binding site for the human thromboxane A2 receptor protein. J Biol Chem 2002; 277: 16791–7.
44 Drews J. Drug discovery: a historical perspective. Science 2000; 287: 1960–4.
45 Guner OF. History and evolution of the pharmacophore concept in computer-aided drug design. Curr Top Med Chem 2002; 2: 1321−32.
46 Khasawneh FT, Huang JS, Mir F, Srinivasan S, Tiruppathi C, Le Breton GC. Characterization of isoprostane signaling: evidence for a unique coordination profile of 8-iso-PGF(2alpha) with the thromboxane A(2) receptor, and activation of a separate cAMP-dependent inhibitory pathway in human platelets. Biochem Pharmacol 2008; 75: 2301–15.
47 Rolin S, Dogne JM, Michaux C, Delarge J, Masereel B. Activity of a novel dual thromboxane A(2)receptor antagonist and thromboxane synthase inhibitor (BM-573) on platelet function and isolated smooth muscles. Prostaglandins Leukot Essent Fatty Acids 2001; 65: 67–72.
48 Shi MZ, Feng JG, Zheng JJ. A comparison between glibenclamide and glipizide in the treatment of type II diabetes. Zhonghua Nei Ke Za Zhi 1991; 30: 94–7, 126.

npg
Acta Pharmacologica Sinica (2010) 31: 160–164
© 2010 CPS and SIMM All rights reserved 1671-4083/10 $32.00
www.nature.com/aps

Original Article

Hydrogen peroxide stress stimulates phosphorylation of FoxO1 in rat aortic endothelial cells

Ye-yu WANG, Si-min CHEN, Hao LI*

Department of Pathophysiology, Nanjing Medical University, Nanjing 210029, China

Aim: To examine whether the phosphorylation of the O subfamily of forkhead transcription factors (FoxO) is involved in response to oxidative stress in rat aortic endothelial cells (RAECs).
Methods: RAECs were treated with H_2O_2 and phosphorylation status of proteins were evaluated by Western blot analysis. The subcellular localization of FoxO1 was determined by nuclear and cytosolic fractionation followed by Western blot analysis as well as immunocytochemistry. The transcriptional activity of FoxO1 in H_2O_2 stress was assessed by luciferase reporter assay. Expression of FoxO1 target gene was determined by real-time PCR analysis.
Results: H_2O_2 stress stimulated phosphorylation of FoxO1 at Thr24 and Ser256 in a concentration and time dependent manner in RAECs. Pretreatment of RAECs with PI-3K inhibitors abolished the activation of Akt and prevented the phosphorylation of FoxO1. Akt-mediated phosphorylation promoted nuclear exclusion of FoxO1. An IRS-driven luciferase activity transactivated by exogenous FoxO1 was modestly suppressed by hydrogen peroxide stress. The expression of Bim, a target gene of FoxO factors, was negatively regulated by Akt-mediated phosphorylation in response to hydrogen peroxide stimulation.
Conclusion: Our data demonstrate that phosphorylation of FoxO1 by PI-3K/Akt signaling is implicated in response to oxidative stress in vascular endothelial cells.

Keywords: oxidative stress; FoxO; endothelial cells; phosphorylation

Acta Pharmacologica Sinica (2010) 31: 160–164; doi: 10.1038/aps.2009.201

Introduction

Intracellular reactive oxygen species (ROS) have been linked to aging; neurodegenerative diseases such as Alzheimer disease and Parkinson disease; cancer; and vascular disease. In the vasculature, oxidative stress is associated with metabolic alterations (diabetes, obesity, and high cholesterol) and results in endothelial dysfunction. Endothelial dysfunction is the initial step in the pathogenesis of atherosclerosis and its clinical complications (coronary disease, hypertension, and heart failure) and is thus considered a common risk factor for many cardiovascular diseases[1, 2].

One of the key determinants of ROS homeostasis and endothelial function is the O subfamily of forkhead transcription factors (FoxO). Consisting of the functionally related proteins FoxO1, FoxO3a, and FoxO4 (also known as FKHR, FKHRL1, and AFX, respectively), FoxO factors regulate hormonal, nutrient, and stress responses and play a key role in endothelial homeostasis[3]. A major regulator of FoxO activity is protein kinase B (Akt), which directly phosphorylates and inactivates FoxO factors, triggering their translocation from the nucleus to the cytoplasm[4]. In addition to phosphorylation, FoxOs are also regulated through other post-translational modifications including acetylation and ubiquitination[5].

Several lines of evidence suggest a role for FoxO factors in ROS homeostasis. FoxO-deficient hematopoietic stem cells contain high concentrations of ROS and show reduced expression of genes involved in ROS detoxification[3]. In particular, Foxo3a has been shown to directly activate transcription of three important antioxidant enzymes: MnSOD, catalase, and Prx3 and protects quiescent cells in vitro from oxidative stress[6–8]. Interestingly, FoxO itself is also regulated by ROS. Treatment of cells with hydrogen peroxide, which increases cellular oxidative stress, results in acetylation or deacetylation of FoxO proteins[9, 10]. FoxO4 is monoubiquitinated under conditions of oxidative stress and results in nuclear translocation[11]. FoxO proteins are also phosphorylated by other protein kinases, including JNK or Mst1 in response to oxidative stress and translocate to the nucleus[12].

The role of FoxO factors in endothelial function is an active area of research. However, despite the well-established physi-

---

* To whom correspondence should be addressed.
E-mail haoli@njmu.edu.cn
Received 2009-09-16 Accepted 2009-12-22

ological relevance of ROS production to vascular function, the regulation of FoxO factors in endothelial oxidative stress has not been characterized. Here, we show that H_2O_2 activates PI-3K/Akt signaling and stimulates phosphorylation of FoxO1, which negatively regulates forkhead transcriptional activity in rat aortic endothelial cells (RAECs). Our results indicate that phosphorylation of FoxO by its major regulator Akt is implicated in response to oxidative stress in vascular endothelial cells.

Materials and methods

Cell isolation and culture

Male Sprague-Dawley rats were anesthetized and the thoracic aortas of rats were rapidly removed and collected in Dulbecco's Modified Eagle's Medium (Invitrogen, USA) and cleaned carefully of connective tissue and adherent fat. Isolated aorta was longitudinally cut open and cut into approximately 1 mm^2 sections and placed intimal side down into T25 flasks. DMEM containing 20% fetal bovine serum (HyClone, USA), 100 U/mL penicillin and 100 μg/mL streptomycin (Gibco,USA) was gently added to cover the tissues without disturbing the orientation of the explants and cultured at 37 °C in a humidified atmosphere of 5% CO_2. RAECs were allowed to grow out from the explants after 7−10 d, after which the tissues were removed. The cell culture purity (90%) was assessed by staining for factor VIII antigen, as previously described[13]. Confluent cells were passaged by trypsinization with 0.25 trypsin-0.02% EDTA (Gibco, USA) and replated at a 1:3–1:4 dilution. Passages between 3 and 10 were used for all experiments. The study was approved by the Ethics Committee of nanjing medical University. Animal handling followed the Declaration of Helsinki and the Guiding Priciples in the Care and Use of Animals.

Western blot analysis

80%−90% confluent RAECs were serum-starved overnight in DMEM medium before incubation with H_2O_2 at concentration and time as indicated. LY294002 was preincubated 1 h and wortmannin was preincubated 30 min before hydrogen peroxide stimulation. RIPA buffer containing protease inhibitors (Roche Diagnostics, Swiss) was added to RAECs to generate whole cell lysates. The samples were heated at 95 °C for 5 min and loaded on a 8% SDS-polyacrylamide gel. Protein extracts (50 μg) were separated by 8% SDS-PAGE gel and then transferred onto a methanol-activated PVDF membrane using a Bio-Rad transfer blotting system. Non-specific binding was blocked with 5% skim milk for 1 h at room temperature. Blots were incubated overnight with antibodies against phospho-FoxO1 (Thr24), phospho-FoxO1 (Ser256), phospho-Akt(Ser473), FoxO1, and Akt, respectively (Cell Signaling, USA). β-actin (Sigma, USA) was used as internal control. Membranes were incubated for 1 h at room temperature with a HRP-conjugated corresponding secondary antibodies after washing. Antigen detection was performed with an enhanced chemiluminescence detection system FluorChem (Alpha Innotech, USA).

Cytosolic and Nuclear fractionation

After stimulation with or without H_2O_2 for 20 min, RAECs (5×10^{6}cells) were suspended in buffer A (10 mmol/L Hepes, pH 7.9, 10 mmol/L KCl, 0.1 mmol/L EDTA, 1 mmol/L DTT, 0.5 mmol/L PMSF , 0.4% NP-40, protease inhibitors), swollen for 10 min on ice, and centrifuged at 10000×*g* for 5min. Supernatant was collected as a cytoplasmic extract. The pellet was washed, resuspended in buffer B (20 mmol/L Hepes, pH 7.9, 400 mmol/L NaCl, 1 mmol/L EDTA, 10% glycerol, 1 mmol/L DTT, 0.5 mmol/L PMSF, protease inhibitors), and vortexed for 20 min at 4 °C. The supernatant after centrifugation was used as nuclear extract. Proteins from cytosol and nuclear extract were subjected to immunoblotting.

Immunocytochemistry

RAECs were grown on glass slides and serum-starved overnight in DMEM medium. Cells were then treated with H_2O_2 (500 μmol/L, 20 min), fixed and washed twice with ice-cold PBS. Immunofluorescence staining using a primary antibody against phospho-FoxO1 (Thr24) and FITC-conjugated secondary antibody was performed. Samples were mounted with mounting medium and observed with a Nikon imaging system (Yokohama, Japan).

Plasmids, transfections and luciferase assay

Plasmid DNAs for FoxO1 and an IRS-driven luciferase (3xIRS-luc) reporter containing canonical insulin-responsive sequences were kindly provided from Dr Zhi-ping LIU (University of texas southwestern medical center at Dallas, USA). RAECs were transfected with reporter plasmid and plasmid encoding FoxO1 using Lipofectamine 2000 (Invitrogen, USA) according to the manufacturer's instructions. At 24 h after transfection, cells were either untreated or stimulated with 200 μmol/L H_2O_2 for 12 h. Cell extracts were assayed for luciferase expression, using a luciferase assay kit (Promega, USA). Relative promoter activities were expressed as luminesence relative units normalized for cotransfected-Renilla luciferase expression in the cell extracts.

RNA and real-time PCR analysis

Total celluar RNA was extracted using Trizol reagent (Takara, Otsu, Japan) according to the manufacturer's instructions. The total RNA (2 μg) was reverse transcribed using PrimeScript^{TM} RT reagent Kit (Takara, Otsu, Japan). Real-time PCR was performed with Power SYBR Green PCR Master Mix (Applied Biosystems, USA) using a Applied Biosystems 7500 Real-Time PCR System. The primer sequences used for Bim were: 5′-AAACGATTACCGAGAGGCGGAAGA-3′ (sense), 5′-AATGCCTTCTCCATACCAGACGGA-3′ (antisense). All primers were synthesized by shanghai invitrogen corporation. The relative quantities of mRNA were determined using comparative cycle threshold methods and normalized against GAPDH (glyceraldehyde-3-phosphate dehydrogenase) mRNA.

Statistical analysis

Statistical analysis was performed using functions from Microsoft Excel. Student's *t* test was used to assay the statistical significance.

Results

H_2O_2 stimulates phosphorylation of FoxO1 in RAECs via PI-3K/Akt signaling

Similar with human umbilical vein endothelial cells, FoxO1 and FoxO3a are the predominant FoxO factors in RAECs. The expression pattern of the forkhead factors FoxO1, FoxO3a, and FoxO4 in RAECs were characterized (data not shown). As reported previously with other types of endothelial cells, the available phosphospecific antibodies to FoxO3a yielded nonspecific signals in Western blot analyses of RAECs, therefore we focused our study on FoxO1. Treatment of RAECs with H_2O_2 significantly enhanced phosphorylation of endogenous FoxO1 at Thr24 and Ser256 in a concentration-dependent manner (Figure 1A). Maximal phosphorylation of FoxO1 was observed at 20 min incubation with H_2O_2 (Figure 1B). In agreement with the known role of Akt in forkhead protein phosphorylation, exogenous hydrogen peroxide also resulted in a concentration- and time-dependent activation of Akt (Figure 1A&1B). Pretreatment of RAECs with LY294002 and wortmannin, two selective inhibitors of PI-3K , abolished the activation of Akt and prevented the phosphorylation of FoxO factors induced by H_2O_2, suggesting a PI-3K/Akt-dependent phosphorylation of FoxO1 was implicated in response to hydrogen peroxide stress in RAECs.

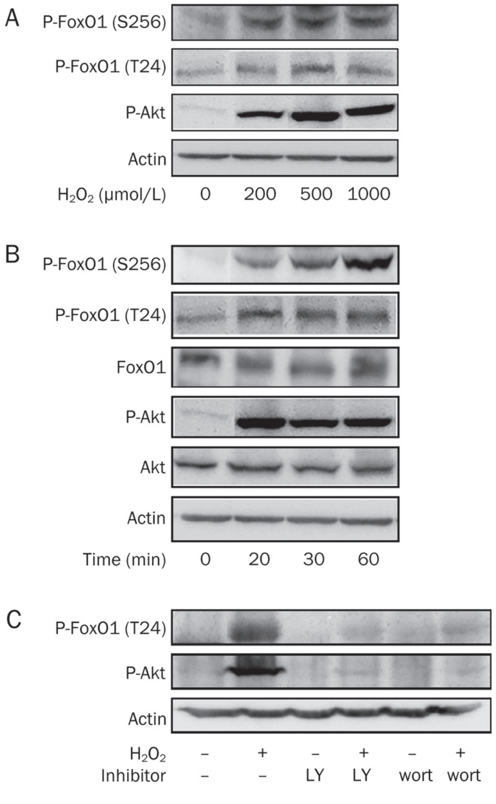

Figure 1. H_2O_2 stimulates phosphorylation of FoxO1 in rat aortic endothelial cells (RAECs) in a concentration- and time-dependent manner. RAECs were incubated with H_2O_2 for the indicated concentration for 20 min (A) or with 500 μmol/L H_2O_2 for the indicated time (B). Whole cell lysates were immunoblotted to detect endogenous expression of phosphorated and total FoxO1 or Akt, respectively. (C) RAECs were treated with 500 μmol/L H_2O_2 for 20 min in the presence or absence of pretreatment with the PI-3K inhibitor LY294002 (10 μmol/L) or wortmannin (500 nmol/L) and phosphorylation of FoxO1 and Akt were determined by Western Blot analysis.

H_2O_2 treatment promotes nuclear exclusion of FoxO1 in RAECs

Akt-mediated phosphorylation of FoxO factors is thought to inhibit FoxOs function by promoting their export from the nucleus. To test whether H_2O_2-induced phosphorylation of FoxOs is accompanied by a change in FoxOs localization, nuclear and cytoplasmic fractions were prepared from H_2O_2-treated RAECs and subjected to immunoblot with phospho-specific FoxO antibodies. As shown in Figure 2A, a 20-min

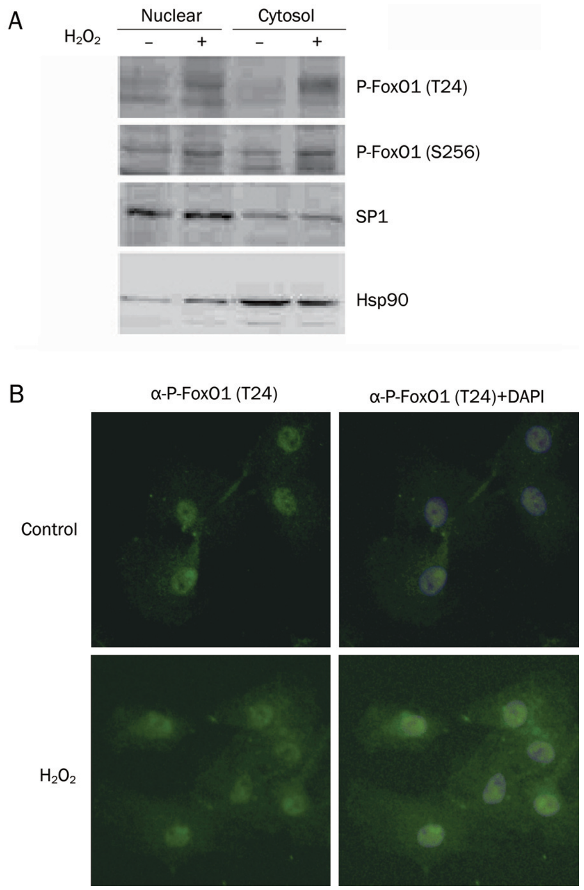

Figure 2. H_2O_2 promotes nuclear exclusion of FoxO1 in RAECs. (A) RAECs were serum-starved overnight and then either untreated or stimulated with 500 μmol/L H_2O_2 for 20 min. Cytoplasmic and nuclear fractions were prepared and subjected to Western blot with antibodies as indicated. Antibodies against SP1 and Hsp90 were used to validate the fractionation procedure. (B) Serum-starved RAECs were treated with vehicle or 500 μmol/L H_2O_2 for 20 min. Cells were immunostained with anti-phospho-FoxO1 antibody (left panels). Co-staining of the same cells with 4,6-diamidino-2-phenylindole (DAPI) is shown in the right panels. (×400)

treatment with 500 μmol/L H_2O_2 induced a significant increase in the amount of phosphorylated FoxO1 in the cytoplasm. Immunostaining of RAECs with antibody against phospho-FoxO1 (Thr24) confirmed this result (Figure 2B). Certain amount of phosphorylated FoxO1 resided in the nucleus, suggesting that other modifications such as monoubiqitination or phosphorylation of other residues, which usually result in nuclear localization of forkhead factors, may also be present in these molecules simultaniously. We also tested the subcellular localization of total FoxO1 upon H_2O_2 treatment, but did not find detectable change with Western blot analysis and immunocytochemistry (data not shown), suggesting that phosphorylation of FoxO1 by Akt is minor fraction of total forkhead proteins, or other modifications may exist that affect the final distribution of FoxO1 in hydrogen peroxide stress.

Akt-mediated phosphorylation of FoxO1 negatively regulates forkhead transcriptional activity in hydrogen peroxide stress in RAECs

The transcriptional activity of exogenous FoxO1 in hydrogen peroxide stress was assessed by reporter assay using an IRS-driven luciferase construct. RAECs were transfected with luciferase reporter plasmid carrying IRS promoter and plas—mid encoding FoxO1 as indicated. Twenty-four hours after transfection, cells were exposed to 200 μmol/L H_2O_2 for 12 h, and were harvested for luciferase assay. Consistent with nuclear exclusion of FoxO1 shown above, IRS promoter activity transactivated by exogenous FoxO1 was modestly suppessed in response to hydrogen peroxide stress (Figure 3A).

To assess the effect of Akt-mediated phosphorylation on the transcriptional activity of endogenous FoxO factors in hydrogen peroxide stress, mRNA was extracted from RAECs after H_2O_2 stimulation. As known, one of the major roles of FoxO factors is the regulation of apoptosis. The pro-apoptotic gene Bim is suggested as one of target genes of FoxO transactivation and posttranslational modification of FoxOs, especially phosphorylation, is considered to play an important role in activating Bim. Therefore, we examined the effect of Akt-mediated phosphorylation of forkhead proteins on the transcription of Bim by real-time PCR. Consistent with previous reports, the level of Bim transcript was increased in 4 h of H_2O_2 treatment (Figure 3B). Pretreatment of RAECs with PI3K/Akt inhibitor LY294002 increased the induction of Bim in response to H_2O_2 stimulation, suggesting that Akt-mediated phosphorylation of FoxOs contributes, at least in part, to the negative regulation of forkhead transcriptional activity in oxidative stress.

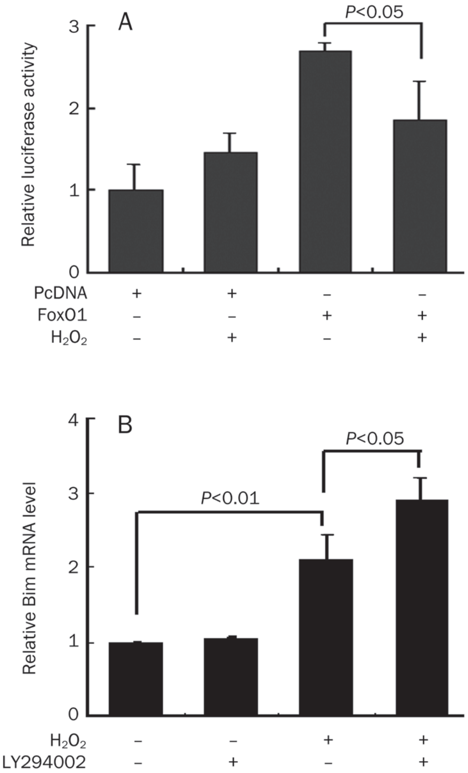

Figure 3. Akt-mediated phosphorylation of FoxO1 negatively regulates forkhead transcriptional activity. (A) RAECs were transfected with 3xIRS-luc reporter plasmid and plasmid encoding FoxO1 and pcDNA. At 24 h after transfection, cells were either untreated or stimulated with 200 μmol/L H_2O_2 for 12 h. Cell extracts were assayed for luciferase expression and luciferase activity was normalized to Renilla activity for each well to control for transfection efficiency. Data shown are averages±standard deviations for three independent experiments. (B) RAECs were incubated with 200 μmol/L H_2O_2 for 4 h in the presence or absence of pretreatment with the PI-3K inhibitor LY294002 (10 μmol/L). Total RNA was prepared for real-time PCR. The data are shown as means of fold-induction of each group over the control group. Data shown are averages±standard deviations for four independent experiments.

Discussion

The function of FoxO proteins is controlled by different post-translational modifications that include phosphorylation, acetylation and ubiquitylation. The serine/threonine kinase Akt is one mediator of phosphorylation of FoxO factors and negatively regulates forkhead transcriptional activity. Previous studies have shown that various extracellular stimuli such as vascular endothelial growth factor (VEGF), angiopoietin-1, shear stress, and 11,12-epoxyeicosatrienoic acid activated PI3K/Akt signaling and promoted the phosphorylation and transcriptional inactivation of FoxO factors in endothelial cells[14–17]. Here, we demonstrated that ROS generation by exogenous sources such as H_2O_2 treatment also induced the phosphorylation and nuclear exclusion of FoxO1 through activation of Akt signaling in RAECs. As reported previously, Akt may be activated in EGF receptor-dependent manner upon ROS treatment[18]. Hence, Our findings indicate that PI3K/Akt-mediated phosphorylation of FoxO factors contributes to the response to oxidative stress in endothelial cells.

Although little is known as to the regulation of FoxO factors in endothelial oxidative stress, several studies have focused on the regulation of FoxO factors in other cell types upon hydrogen peroxide stress. It has been reported that in PC12 cells FoxO3 was phosphorylated after exposure to hydrogen peroxide for 20 min and resulted in the redistribution of the protein to the cytosol[19]. However, another study in human colon carcinoma cell DLD1 demonstrated that H_2O_2 treatment induced the nuclear translocation and activation of FoxO4 by the activation of the small GTPase Ral, which results in a JNK-dependent phosphorylation of FoxO4 on threonine 447 and threonine 451[12]. Our data indicated that although H_2O_2 induced a significant increase in the amount of phosphorylated FoxO1 in the cytoplasm, no detectable change in the distribution of total FoxO1 was observed upon H_2O_2 treament. The distinct subcellular locolization may result from a difference in cell types used or the specific FoxO factor studied. Since no conserved T447/451 phosphorylation sites are revealed by alignment of FoxO4 with FoxO1 and FoxO3a, whether FoxO1 and FoxO3a are potential substrates for JNK still needs to be determined. Therefore, our data extend understanding of the distribution of FoxO factors in response to oxidative stress in vascular endothelial cells.

In this study, we focused on the phosphorylation of FoxO factors. In fact, FoxOs are also regulated through other posttranslational modifications such as acetylation and ubiquitination. Studies have shown that the acetylations of FoxO3 and FoxO4 are increased in response to hydrogen peroxide[9, 10]. FOXO4 is also reported to be regulated by mono-ubiquitination after increased cellular oxidative stress, which increased nuclear localization of FOXO and hence increased transcriptional activity[11]. Whether FoxO1 is acetylated or mono-ubiquitinated needs to be further investigated. Thus the regulation of FoxO in oxidative stress is complex, and different degrees of phosphorylation or other posttranslational modifications may confer distinct effects. Furthermore, the interaction of FoxO with other transcription factors such as nuclear factor-B (NF-κB) would likely contribute to this complexity.

In summary, our data demonstrated that hydrogen peroxide strss activates PI-3K/Akt signaling and stimulates phosphorylation of FoxO1, which negatively regulates forkhead transcriptional activity in endothelial cells. Our results indicate that phosphorylation of FoxO by its major regulator Akt is implicated in response to oxidative stress in vascular endothelial cells.

Acknowledgments

This study was supported by National Natural Science Foundation of China (No 30700302) to Hao LI.

Author contribution

Hao LI designed research; Ye-yu WANG and Si-min CHEN performed research; Ye-yu WANG analyzed data; Hao LI wrote the paper.

References

1 Finkel T. Redox-dependent signal transduction. FEBS Lett 2000; 476: 52–4.
2 Maulik N. Redox signaling of angiogenesis. Antioxid Redox Signal 2002; 4: 805–15.
3 Paik JH, Kollipara R, Chu G, Ji H, Xiao Y, Ding Z, *et al*. FoxOs are lineage-restricted redundant tumor suppressors and regulate endothelial cell homeostasis. Cell 2007; 128: 309–23.
4 Huang H, Tindall DJ. Dynamic FoxO transcription factors. J Cell Sci 2007; 120 (Pt 15): 2479–87.
5 Greer EL, Brunet A. FOXO transcription factors at the interface between longevity and tumor suppression. Oncogene 2005; 24: 7410–25.
6 Kops GJ, Dansen TB, Polderman PE, Saarloos I, Wirtz KW, Coffer PJ, *et al*. Forkhead transcription factor FOXO3a protects quiescent cells from oxidative stress. Nature 2002; 419: 316–21.
7 Chiribau CB, Cheng L, Cucoranu IC, Yu YS, Clempus RE, Sorescu D. FOXO3A regulates peroxiredoxin III expression in human cardiac fibroblasts. J Biol Chem 2008; 283: 8211–7.
8 Alcendor RR, Gao S, Zhai P, Zablocki D, Holle E, Yu X, *et al*. Sirt1 regulates aging and resistance to oxidative stress in the heart. Circ Res 2007; 100: 1512–21.
9 Brunet A, Sweeney LB, Sturgill JF, Chua KF, Greer PL, Lin Y, *et al*. Stress-dependent regulation of FOXO transcription factors by the SIRT1 deacetylase. Science 2004; 303: 2011–5.
10 van der Horst A, Tertoolen LG, de Vries-Smits LM, Frye RA, Medema RH, Burgering BM. FOXO4 is acetylated upon peroxide stress and deacetylated by the longevity protein hSir2(SIRT1). J Biol Chem 2004; 279: 28873–9.
11 Brenkman AB, de Keizer PL, van den Broek NJ, Jochemsen AG, Burgering BM. Mdm2 induces mono-ubiquitination of FOXO4. PLoS One 2008; 3: e2819.
12 Essers MA, Weijzen S, de Vries-Smits AM, Saarloos I, de Ruiter ND, Bos JL, *et al*. FOXO transcription factor activation by oxidative stress mediated by the small GTPase Ral and JNK. EMBO J 2004; 23: 4802–12.
13 Chen ZY, Feng GG, Nishiwaki K, Shimada Y, Fujiwara Y, Komatsu T, *et al*. Possible roles of neuropeptide Y Y3-receptor subtype in rat aortic endothelial cell proliferation under hypoxia, and its specific signal transduction.Am J Physiol Heart Circ Physiol 2007; 293: H959–67.
14 Abid MR, Guo S, Minami T, Spokes KC, Ueki K, Skurk C, *et al*. Vascular endothelial growth factor activates PI3K/Akt/forkhead signaling in endothelial cells. Arterioscler Thromb Vasc Biol. 2004; 24: 294–300.
15 Papapetropoulos A, Fulton D, Mahboubi K, Kalb RG, O'Connor DS, Li F, *et al*. Angiopoietin-1 inhibits endothelial cell apoptosis via the Akt/survivin pathway. J Biol Chem 2000; 275: 9102–5.
16 Dimmeler S, Assmus B, Hermann C, Haendeler J, Zeiher AM. Fluid shear stress stimulates phosphorylation of Akt in human endothelial cells: involvement in suppression of apoptosis. Circ Res 1998; 83: 334–41.
17 Potente M, Fissllthaler B, Busse R, Fleming I. 11,12-Epoxyeicosatrienoic acid-induced inhibition of FOXO factors promotes endothelial proliferation by down-regulating p27Kip1. J Biol Chem 2003; 278: 29619–25.
18 Wang X, McCullough KD, Franke TF, Holbrook NJ. Epidermal growth factor receptor-dependent Akt activation by oxidative stress enhances cell survival. J Biol Chem 2000; 275: 14624–31.
19 Nemoto S, Finkel T. Redox regulation of forkhead proteins through a p66shc-dependent signaling pathway. Science 2002; 295(5564): 2450–2.

Acta Pharmacologica Sinica (2010) 31: 165–174
© 2010 CPS and SIMM All rights reserved 1671-4083/10 $32.00
www.nature.com/aps

Original Article

CPU86017, a berberine derivative, attenuates cardiac failure through normalizing calcium leakage and downregulated phospholamban and exerting antioxidant activity

Min-you QI[#], Yu FENG[#], De-zai DAI*, Na LI, Yu-si CHENG, Yin DAI

Research Division of Pharmacology, China Pharmaceutical University, Nanjing 210009, China

---

Aim: To investigate whether CPU86017, a berberine derivative, attenuates heart failure by blocking calcium influx and exerting its antioxidant activity.
Methods: Myocardial infarction was induced in male Sprague-Dawley rats for 17 d followed by isoproterenol (ISO) (5 mg/kg, sc) treatment for 5 d to reduce cardiac function. The rats were divided into 5 groups: sham operation, myocardial infarction (MI), MI plus ISO, and co-treated (in mg/kg, *po*) with either propranolol (PRO, 10) or CPU86017 (80). Hemodynamic measurements were conducted, and measurements of the redox system, calcium handling proteins and endothelin (ET) system *in vivo* were done. Furthermore, calcium flux studies and PLB immunocytochemistry were conducted *in vitro*.
Results: Compared to sham operation, HF was evident following MI and further worsened by ISO treatment. This occurred in parallel with downregulated mRNA and protein production of SERCA2a, PLB, and FKBP12.6, and was associated with upregulation of pre-proET-1, endothelin converting enzyme, and PKA mRNA production in the myocardium *in vivo*. Calcium leakage was induced by ISO treatment of isolated beating myocytes *in vitro*. These changes were attenuated by treatment with either PRO or CPU86017. PLB fluorescence in myocytes was downregulated by ISO treatment, and was relieved significantly by treatment with antioxidant aminoguanidine, ascorbic acid or CPU86017 *in vitro*.
Conclusion: HF, calcium leakage, downregulated PLB, FKBP12.6, SERCA2a production, and upregulated PKA were caused by ISO treatment, and were abolished by CPU86017 treatment. The beneficial effects of CPU86017 are attributable to its antioxidant and calcium influx blocking effects.

Keywords: berberine; FKBP12.6; SERCA2a; heart failure; calcium leakage; endothelin; oxidative stress; phospholamban; Sprague-Dawley rats

---

Acta Pharmacologica Sinica (2010) 31: 165–174; doi: 10.1038/aps.2009.180

Introduction

Heart failure (HF) is a progressive clinical syndrome with high mortality. Despite significant advances in understanding the mechanisms underlying this disease, current treatments for HF have not been satisfied. Calcium homeostasis is essential for maintaining normal cardiac performance, and relies on the balance of calcium influx via *L*-type calcium channels with calcium release via the activity of the ryanodine receptor type 2 (RyR2) in the sarcoplasmic reticulum[1]. RyR2 responds to small influxes of calcium, and triggers a relatively large amount of calcium to be released into the cytosol, thereby eliciting calcium excitation coupling for contractility[2]. The Ca^{2+} releasing channel is tightly closed in diastole due to modulation by the protein calstabin 2 (FKBP12.6), which associates with RyR2[3]. The process of calcium homeostasis, however, is critically impaired due to hyperphosphorylation of protein kinase A (PKA)[4]. PKA hyperphosphorylated exists in a hyperadrenergic state[5] elicited by isoproterenol (ISO) treatment, resulting in both arrhythmogenesis and HF[1]. Impaired calcium homeostasis may not be due solely to the effects of the RyR2-FKBP12.6 complex and the impact of hyperphosphorylation of PKA. Calcium homeostasis in the cardiac cycle requires appropriate activity of a pair of Ca^{2+} modulating proteins: SERCA2a (sarcoplasmic reticulum Ca^{2+} ATPase), and its regulator PLB (phospholamban). These proteins are respon-

---

[#] The two authors contributed equally to this work.
[*] To whom correspondence should be addressed.
E-mail dezaidai@vip.sina.com
Received 2009-07-29 Accepted 2009-11-16

sible for swiftly pumping an excess of calcium back into the calcium store of the sarcoplasmic reticulum during diastole. Emerging data have shown that SERCA2a[6] and PLB[7] may be actively involved in the pathogenesis of HF. In addition to PKA, hyperphosphorylated PKCε may also play an important role in this process[8, 9].

A growing body of evidence has shown that dysfunction of calcium handling proteins is mainly due to the abnormal formation of the RyR2-FKBP12.6 complex[1], and may also be due to the downregulation of SERCA2a and PLB, as demonstrated by the pivotal role of cardiac insufficiency in diabetic cardiomyopathy[10] and arrhythmogenesis[11, 12]. Downregulation of FKBP12.6 found in failing hearts facilitates Ca^{2+} leakage at diastole, leaving more Ca^{2+} behind, resulting in depletion of Ca^{2+} stores in the sarcoplasmic reticulum. This impairs calcium excitation-coupling in the cardiac cycle, and is the basic mechanism underlying the pathologies of failing hearts[12, 13]. Under the hyperadrenergic state, SERCA2a and PLB expression could also contribute to excess cytosolic Ca^{2+} at diastole. However, the relationship of PLB with HF has not been fully evaluated, and has only been described in a limited number of studies[14, 15].

CPU86017 is derived from berberine and contains chemical modifications that result in an improvement in water solubility, calcium channel blocking activity, and antioxidative activity[16]. We have shown that CPU86017 is effective in relieving pulmonary hypertension induced by either hypoxia[17] or monocrotaline[18]. Interestingly, a recent study demonstrated a novel clinical use of the drug verapamil to prolong survival of patients suffering from CPVT (catecholaminergic polymorphism ventricular tachycardia). CPVT is due to a mutation in RyR2[19], which leads to defective association with FKBP12.6. CPVT is triggered by physical exercise, and is related to leakiness of RyR2 channels and defective/downregulated FKBP12.6[20]. This condition can also be produced by ISO treatment[5]. This is likely due to an activated endothelin-1 (ET-1) system and oxidative stress[8]. As a result, abnormal FKBP12.6 can be ameliorated significantly by the endothelin receptor antagonists darusentan, a selective ETA (endothelin receptor A) blocker, or CPU0213, a dual ETA/B blocker[7]. Myocardium infarction (MI) stimulated by ISO administration to rats showed an increased tendency for exacerbated VF relative to MI alone, and this phenomenon was associated with a more depressed expression of RyR2 and SERCA2a in the left ventricle. Expression was recovered by CPU86017 treatment[6]. These results indicate that excessive ISO treatment produces a state of hyperadrenergic activity and impairs a family of calcium-modulating proteins. This disturbs Ca^{2+} homeostasis during the cardiac cycle, in which oxidative stress and an abnormal ET pathway are implicated. Oxidative stress plays a role in the downregulation of FKBP12.6, increasing the vulnerability for developing HF and arrhythmogenesis[21, 22]. However, it is unclear whether these changes are causal factors to exacerbate HF by causing calcium leakage.

Here, we hypothesize that an infarcted rat heart stimulated by ISO could exaggerate cardiac dysfunction in parallel with reduced function of calcium handling proteins and the redox system *in vivo*, and that calcium leakage caused by ISO administration correlates with downregulation of PLB *in vitro*. Furthermore, we propose that these abnormalities could be recovered by CPU86017 treatment, mainly due to its antioxidative and calcium antagonist activity. In the present study, we determined the ability of CPU86017 to attenuate these abnormalities at the molecular level with implications towards HF *in vivo* and *in vitro*.

Materials and methods

Animals

Our study conforms to the Guide for the Care and Use of Laboratory Animals published by the US National Institutes of Health (NIH Publication No 85–23, revised 1996). Male Sprague-Dawley rats (250–280 g) were used for *in vivo* experiments, and neonatal rats were used to isolate cardiomyocytes for *in vitro* experiments.

Experimental protocol

Rats were randomly divided into 5 groups: sham operation (Sham), myocardial infarction (MI) by coronary artery ligation, MI plus injection of ISO, and MI+ISO treated with either propranolol (PRO), or CPU86017. Rats were subjected to left coronary ligation, and were allowed to recover from the operation[6]. HF developed chronically following MI for 17 d. Treatment with ISO (5 mg/kg, sc) was continued for 5 d to exacerbate congestive cardiac failure. From the 18th day, cotreatment with either propranolol (10 mg/kg, *po*) or CPU86017 (80 mg/kg, *po*) was continued for 5 d, whereas rats in the sham, MI, and MI+ISO groups received the same volume of normal saline.

Hemodynamics

Rats were anesthetized with urethane (1.5 g/kg, ip), and a left ventricular cannulation was performed via the left common carotid, according to previously described methods[10]. The intracardiac pressure recordings for the left ventricular systolic pressure (LVSP), left ventricular end-diastolic pressure (LVEDP), maximum velocity of left ventricular systole (LV+dp/dt_{max}), and maximum velocity of left ventricular diastolic pressure (LV-dp/dt_{max}) were measured by a real-time hemodynamic analyzer (MPA2000, Shanghai Secondary Military Medical University)[10].

Heart weight index

Weights of the whole heart (HW), the left ventricle (LVW) and right ventricle (RVW) were measured and used to calculate the ratio to body weight (HW/BW, LVW/BW, and RVW/BW), respectively, and compared among the groups[10].

RT-PCR

The mRNA levels for SERCA2a, PLB, RyR2, FKBP12.6, ECE (endothelin converting enzyme), preproET-1 (preproendothelin-1), and PKA were measured by semi-quantitative RT-PCR[10]. Briefly, RNA was extracted from cardiac tissue by TRIzol, and was reverse transcribed into cDNA by MMLV RT with a profile of 10 min at 25 °C, 30 min at 48 °C and 2 min at 95 °C. One microgram of cDNA was used for PCR in a 25 μL final reaction volume. PCR products were stained with ethidium bromide and visualized under UV light (GDS8000, Sygene, England). The density of each band was measured using professional image analysis software. The ratio of the mRNA of the gene of interest against an internal standard GAPDH oxidase was calculated. The nucleotide sequences of primers chosen are listed in Table 1.

Table 1. Oligonucleotide primers used for reverse transcript-polymerase chain reactions.

	Oligonucleotide primers
SERCA2a	Sense: 5′-CCGTATCCGATGACAATG-3′
	Antisense: 5′-CCAGGCTCCAGGTAGTTT-3′
PLB	Sense: 5′-TACCTTACTCGCTCGGCTATC-3′
	Antisense: 5′-CAGAAGCATCACAATGATGCAG-3′
RyR2	Sence: 5′-GAATCAGTGAGTTACTGGGCATGG-3′
	Antisense: 5′-CTGGTCTCTGAGTTCTCCAAAAGC-3′
FKBP12.6	Sense: 5′-GTGAAGGCAGGAAGGAA-3′
	Antisense: 5′-GCAGCCAACAGAAGATAAG-3′
ECE	Sense: 5′-GGACTTCTTCAGCTACGCCTGT-3′
	Antisense: 5′-CTAGTTTCGTTCATACACGCACG-3′
PreproET-1	Sense: 5′-AGCAATAGCATCAAGGCATC-3′
	Antisense: 5′-TCAGACACGAACACTCCCTA-3′
PKA	Sense: 5′-CAAGAGAGTCAAGGGCAGGAC-3′
	Antisense: 5′-CAACCTTTCTCGGTAAATCGC-3′
GAPDH	Sense: 5′-GCTGGGGCTCACCTGAAGG-3′
	Antisense: 5′-GGATGACCTTGCCCACAGCC-3′

Western blot

Quantitative analysis of SERCA2a, PLB, and FKBP12.6 protein levels was performed as previously described[10]. Briefly, a portion of cardiac tissue was homogenized in 4 volumes of extraction buffer and centrifuged at 10 000×*g* for 10 min at 4 °C. After determining the protein concentration, supernatants were stored at -20 °C before use. The samples were heated at 95 °C in loading buffer and fractionated by sodium dodecyl sulfate polyacrylamide gel electrophoresis (SDS-PAGE) on a 10% gel. Following transfer to a nitrocellulose membrane and blocking with nonfat milk (5% *w/v*), the blot was incubated with primary antibody overnight at 4 °C. After washing, the blot was then incubated with horseradish peroxidase conjugated goat immunoglobulin (IgG) for 2 h at room temperature. Antigen was detected with a 3,3′-diaminobenzidine (DAB) kit, and visualized by an imaging acquisition instrument (Labwork, England) and quantified by densitometry. The ratio of tested protein against the sham was calculated quantitatively.

Biochemistry assay

A portion of cardiac mass was homogenized in normal saline, and the levels of nitric oxide (NO), malondialdehyde (MDA), superoxide dismutase (SOD), glutathione peroxidase (GSH-px) and the activities of induced NOS (iNOS) were determined following the instructions of the reagent kits (Nanjing Jiancheng Bioengineering Institute, China)[10].

Calcium transients

Single cardiac myocytes were enzymatically isolated from whole ventricles of adult rats as described before with some modifications[23]. In brief, male rats (250±50 g), were heparinized and anaesthetized with ethylurethane (1.5 g/kg, ip). The heart was quickly excised and retrogradely perfused through the aortic cannula mounted on a Langendorff apparatus at 37 °C with a Ca^{2+}-free Tyrode solution for about 5 min. This was then switched to the same solution containing 0.33 mg/mL type II collagenase (Worthington, USA) for 12±2 min. The ventricles were dissected and cardiac myocytes were collected and dispersed and stored in a high-K^+, low-Cl^- Kraft-Brühe (KB) solution.

Measurements of cytosolic $[Ca^{2+}]_i$ were performed as described previously[23, 24], with some modifications. Briefly, cardiomyocytes loaded with Fluo-3 were transferred to a 300-μL perfusion chamber, placed on an inverted microscope (Olympus IX71, Japan), perfused with compounds of interest or vehicle, and gassed with 95% O_2+5% CO_2 at room temperature. Cyclic contractions of cardiomyocyte were paced by square wave pulses of 40 V, with a 5-ms duration at 0.5 Hz in a field of electric stimulation. Imaging of Fluo-3 fluorescence within cardiac cycles was recorded 5 min after perfusion of tested compounds or vehicle, and the signals were converted into absolute $[Ca^{2+}]_i$ by the calibration formula, $[Ca^{2+}]_i=K_d*(F-F_{min})/(F_{max}-F)$. Here, K_d represents the dissociation constant for Ca^{2+}-bound Fluo-3, F was obtained from $F=F_{cell}-F_{bak}$, where F_{cell} is the mean fluorescent intensity measured in myocytes, and F_{bak} is the fluorescent intensity of the background. F_{max} represented the maximum fluorescence of cells permeable to Ca^{2+}, and was obtained by adding 5 mmol/L A23187 to Tyrode's solution containing 10 mmol/L Ca^{2+}. F_{min} was calculated from $F_{min}=1.25*F_{Mn}-0.25*F_{max}$, where F_{Mn} was obtained by adding 5 mmol/L $MnCl_2$ to 5 mmol/L A23187-treated myocytes[24].

Solutions Normal

Tyrode's solution contained (in mmol/L): 135 NaCl, 5.4 KCl, 1.8 $CaCl_2$, 2 $MgSO_4$, 0.33 NaH_2PO_4, 10 glucose and 10 HEPES (pH adjusted to 7.4 with NaOH). The Ca^{2+}-free Tyrode's solution used for the cell isolation procedure was prepared by simply omitting $CaCl_2$ from the normal Tyrode's solution. The KB solution for cell preparation contained (in mmol/L): 40 KCl, 3 $MgCl_2$, 20 KH_2PO_4, 50 *L*-glutamic acid, 20 taurine, 70 KOH, 10 glucose, 0.5 EGTA and 10 HEPES (pH adjusted to 7.3 with KOH). All solutions used during the procedure were oxygenated and maintained at 37 °C. ISO (100 nmol/L) was directly added to normal Tyrode's solution. Propranolol at 10^{-6} mol/L or CPU86017 at 10^{-7}, 10^{-6}, and 10^{-5} mol/L was coincubated with ISO. Peak (systolic), variant (difference between systolic and diastolic) and trough (diastolic) concentrations of

$[Ca^{2+}]_i$ were calculated.

Immunocytochemistry of phospholamban

The procedure was conducted as previously described[7]. Briefly, ventricular myocytes were isolated from adult rats, plated onto laminin-coated slip chambers, and cultured at 37 °C in MEM/EBSS serum-free medium. Four hours later, test drugs were added to chambers for 8 groups: (1) Control; (2) ISO (10^{-6} mol/L); (3 and 4) ISO+aminoguanidine (Ami, 10^{-5} or 10^{-6} mol/L), a blocker for iNOS, with potent antioxidant activity; (5 and 6) ISO+ascorbic acid (VC, 10^{-4} or 10^{-5}), a typical antioxidant ; and (7 and 8) ISO+CPU86017 (10^{-5} or 10^{-6}).

Immunocytochemistry assay for PLB[7]

Briefly, 24 h after drug incubation, the ventricular myocytes were fixed using 4% paraformaldehyde for 15 min at 37 °C and were rinsed and then incubated for 30 min with 2% bovine serum albumin in PBS to reduce nonspecific binding. After overnight incubation at 5 °C with the primary antibody, cells were rinsed and incubated with the secondary antibody conjugated with fluorescent isothiocyanate (FITC), for 2 h at room temperature. Stained cells were imaged by fluorescence and were photographed. The fluorescence image was converted into gray density in the accumulated data to be compared among groups.

Statistics

All the data are expressed as mean±SD. The differences between groups are compared with ANOVA, and $P<0.05$ is considered statistically significant.

Results

Cardiac dysfunction

Cardiac function was depressed following myocardial infarction, and was further worsened by injection of ISO. Compared to the sham group, the systolic and diastolic functions were compromised significantly in the ISO group, with declines in LVSP by -30.2% ($P<0.01$), LV+dp/dt_{max} by -46.7% ($P<0.01$), and LV-dp/dt_{max} by -53.3% ($P<0.01$). LVEDP was elevated by +786.8% ($P<0.01$), relative to normal (Figure 1A–1D). An impairment in cardiac function was demonstrated by MI, and was further compromised by ISO administration ($P<0.05$), compared to MI alone. Medication with either propranolol or CPU86017 for 5 d significantly reversed cardiac dysfunction, where CPU86017 preserved LVSP by 66.5% ($P<0.01$), LVEDP by 90.5% ($P<0.01$), LV+dp/dt_{max} by 83.7% ($P<0.01$), and LV-dp/dt_{max} by 84.7% ($P<0.01$) relative to the ISO group.

Cardiac hypertrophy

Myocardium hypertrophy was found following MI and ISO medication, demonstrating an increase in the heart weight

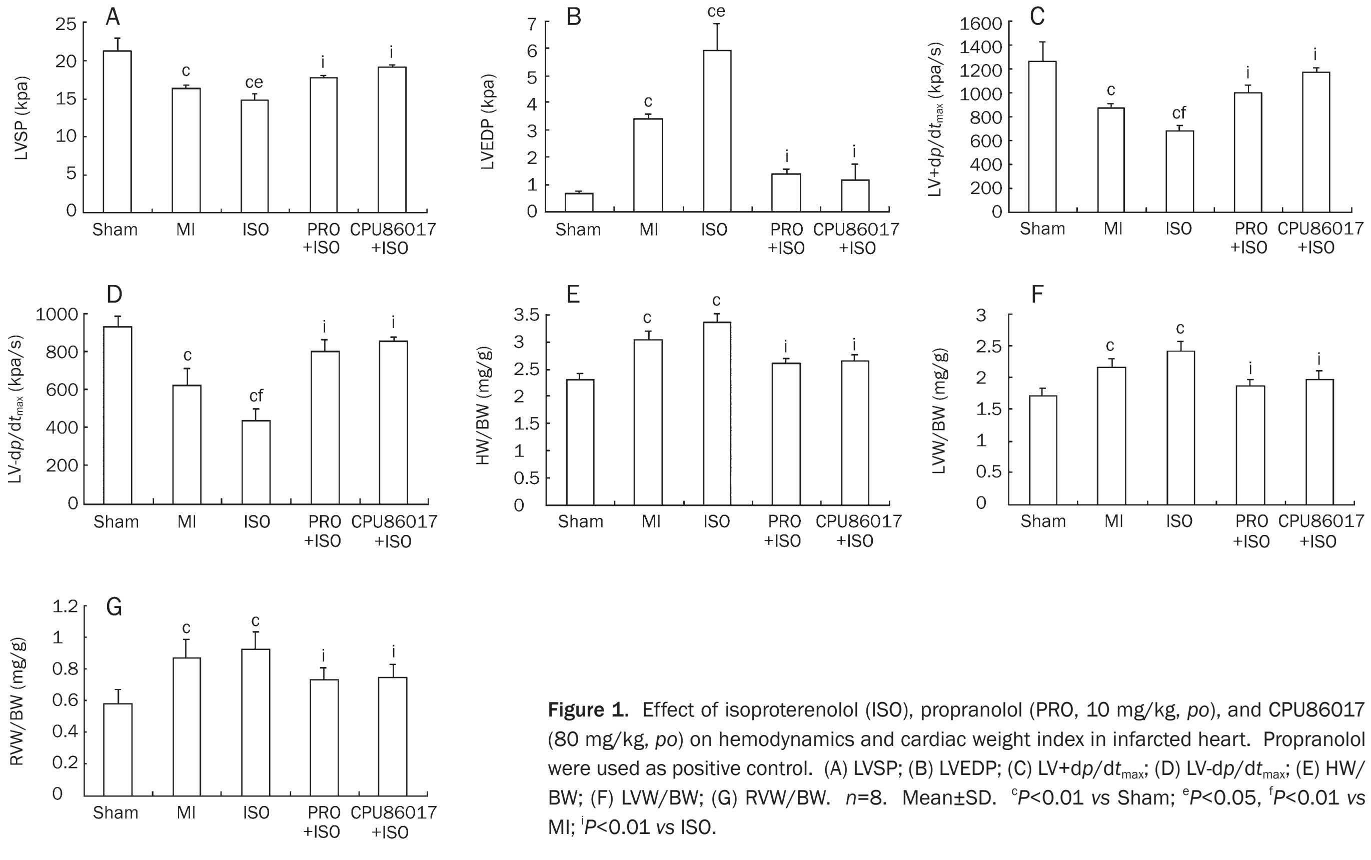

Figure 1. Effect of isoproterenolol (ISO), propranolol (PRO, 10 mg/kg, *po*), and CPU86017 (80 mg/kg, *po*) on hemodynamics and cardiac weight index in infarcted heart. Propranolol were used as positive control. (A) LVSP; (B) LVEDP; (C) LV+dp/dt_{max}; (D) LV-dp/dt_{max}; (E) HW/BW; (F) LVW/BW; (G) RVW/BW. n=8. Mean±SD. $^{c}P<0.01$ *vs* Sham; $^{e}P<0.05$, $^{f}P<0.01$ *vs* MI; $^{i}P<0.01$ *vs* ISO.

indexes HW/BW, LVW/BW, and RVW/BW by 46.1%, 41.3% and 60.3% ($P<0.01$) respectively (Figure 1E–1G). Both propranolol and CPU86017 were able to significantly reverse hypertrophy.

Abnormal calcium handling molecules

To characterize the beginning of cardiac dysfunction initiated by MI and worsened in the presence of ISO, we focused our attention on measuring the changes in the expression of SERCA2a and PLB. Downregulation of the two molecules was significant in the MI group, and further downregulation was achieved by ISO treatment ($P<0.05$, Figure 2). In the MI heart, mRNA levels of SERCA2a (Figure 2A) and PLB (Figure 2C) in the left ventricle decreased, in agreement with a reduction in the respective protein levels. These were found to be reduced by 48.8% and 56.7%, respectively, (both $P<0.01$), relative to the sham operation group (Figure 2B, 2D). Further reduction in mRNA and protein levels ($P<0.05$), was seen in the MI+ISO group, compared to MI alone with exception of the SERCA2a protein. Both propranolol and CPU86017 were effective to the same extent in abolishing the abnormalities.

Expression of RyR2 and FKBP12.6 in the myocardium was

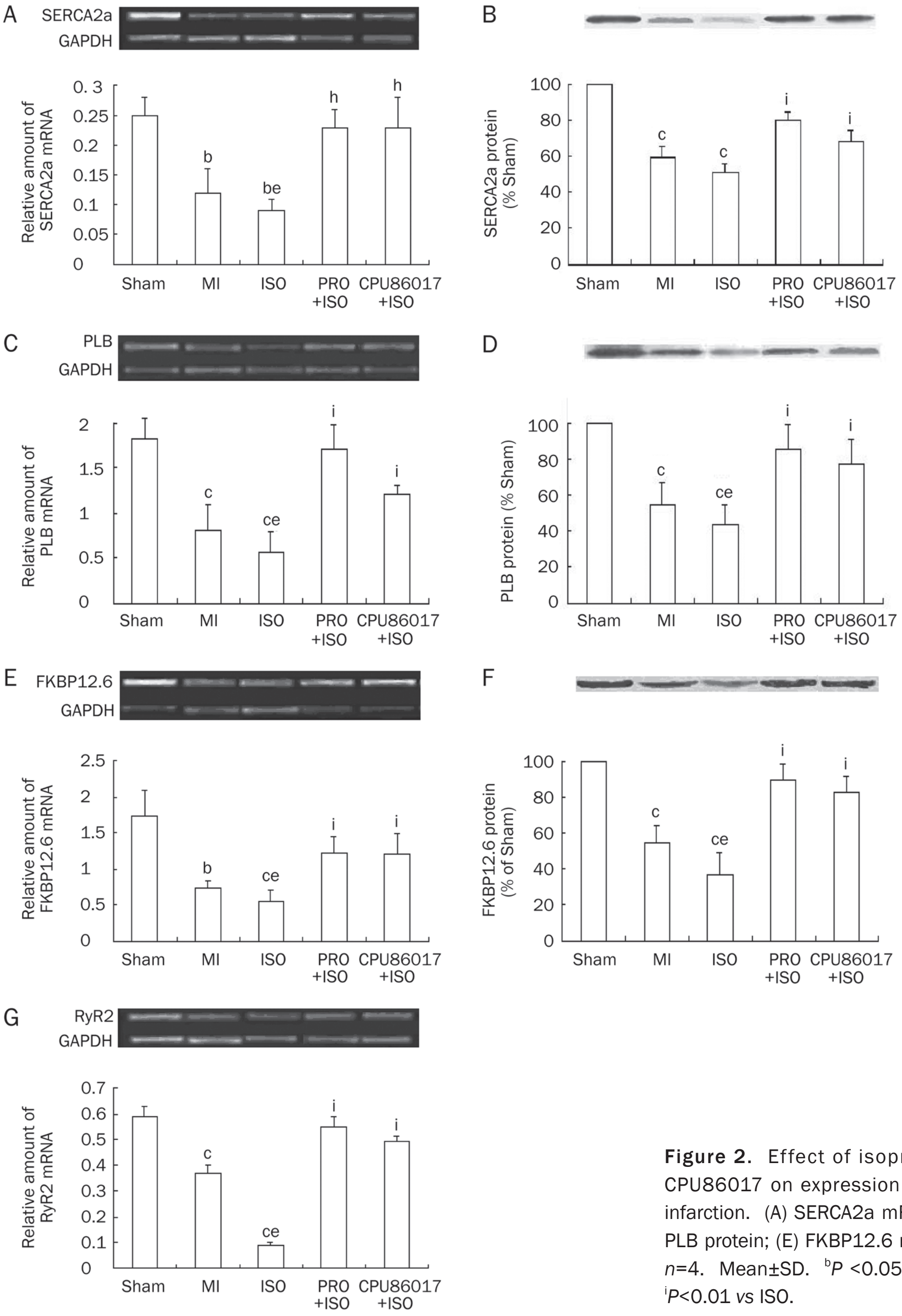

Figure 2. Effect of isoproterenolol (ISO), propranolol (PRO), and CPU86017 on expression of calcium handing proteins in myocardial infarction. (A) SERCA2a mRNA; (B) SERCA2a protein; (C) PLB mRNA; (D) PLB protein; (E) FKBP12.6 mRNA; (F) FKBP12.6 protein; (G) RyR2 mRNA. *n*=4. Mean±SD. $^bP<0.05$, $^cP<0.01$ *vs* Sham; $^eP<0.05$ *vs* MI; $^hP<0.05$, $^iP<0.01$ *vs* ISO.

depressed in response to MI combined with ISO administration. Expression of these proteins was significantly depressed in response to MI (P<0.05) relative to the sham, and worsened by ISO (P<0.05), as compared to MI alone (Figure 2E, 2G). Levels of the FKBP12.6 protein were decreased in parallel with the changes in cardiac dysfunction (P<0.01) (Figure 2F). Intervention with propranolol and CPU86017 was successful in significant reversal of the abnormalities.

Calcium transient activity and calcium leakage

Calcium transient studies in rat ventricular myocytes were carried out to show cyclic changes in traces of Fluo-3 in regular beating cardiomyocytes elicited by electrical field stimulation. The peak, variance (difference between peak and end-of-diastolic value), and trough values at diastole were calculated. After application of 100 nmol/L isoproterenol, calcium transients were significantly augmented in the three values. An increment in diastolic levels over the normal level was recognized as calcium leakage. Changes in $[Ca^{2+}]_i$ induced by ISO were respectively reversed by either treatment with propranolol at 1 μmol/L or CPU86017 at 10 μmol/L. CPU86017 was mild in inhibiting these changes, and no effect was found at 0.1 μmol/L (Figure 3).

Upregulation of ECE, preproET-1 and PKA mRNA

We were next interested in investigating whether cardiac dysfunction in MI followed by activation of the β-adrenoceptor by ISO medication was related to an activated ET system in the myocardium. Upregulation of the myocardial ET system was reflected by escalating mRNA levels of ECE and preproET-1 (Figure 4A, 4B) in the infarcted left ventricle (P<0.01) compared to the sham. A further increase in pp-ET-1 was caused by ISO administration, relative to MI rats (P<0.05). Treatment with propranolol and CPU86017 remarkably decreased these changes (P<0.01).

PKA is considered an important downstream effector, subsequent to β-adrenoceptor activation. Expression of PKA mRNA appeared to be upregulated significantly (P<0.01) in MI, and further escalation in PKA mRNA by ISO was substantial, in parallel to changes in cardiac function (P<0.05) (Figure 4C). PKA upregulation was markedly inhibited by either propranolol or CPU86017 (P<0.01, Figure 4).

Oxidative stress

Oxidative stress was evident in the myocardium found in both the MI alone group and the combined ISO injection groups, with an elevation of MDA content by 107% (P<0.01),

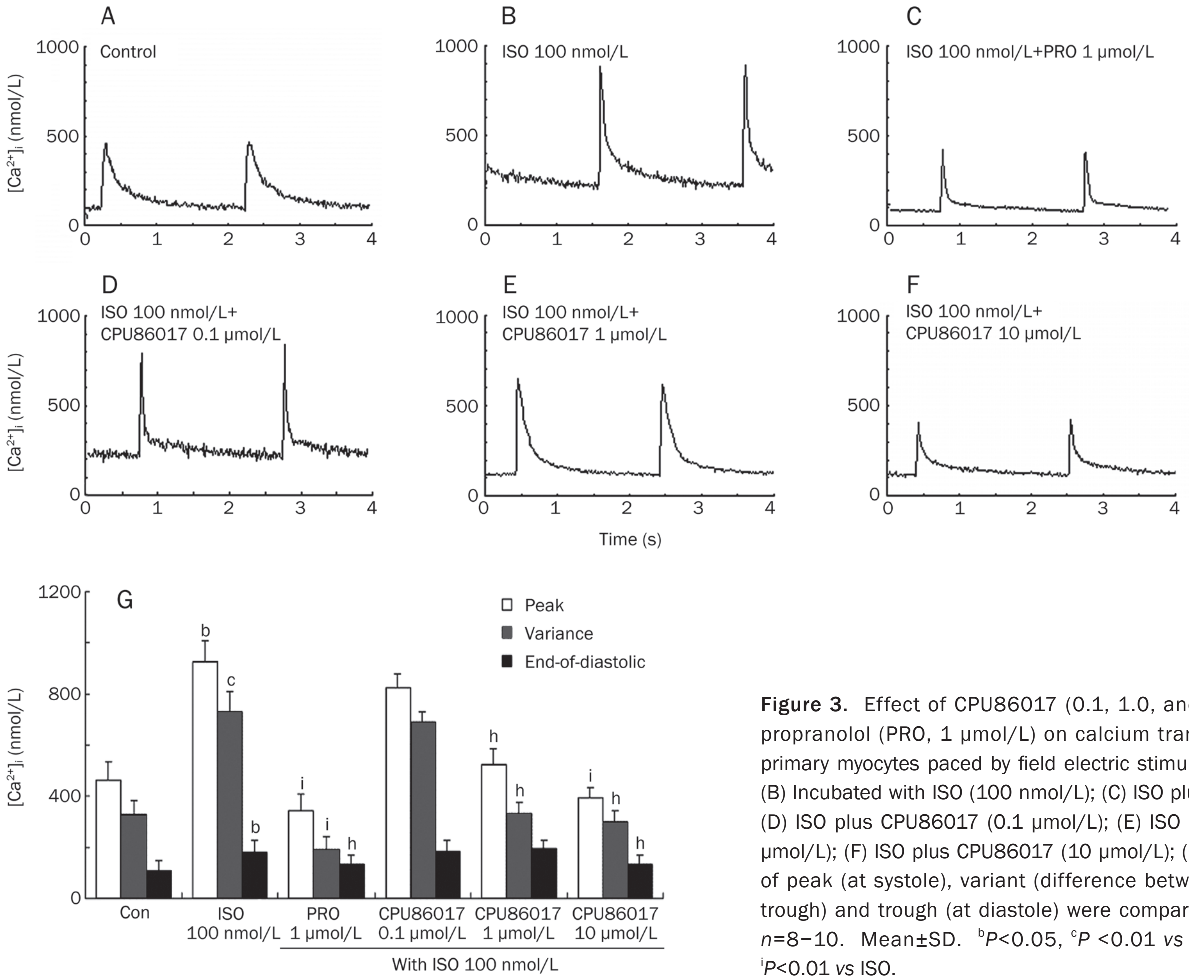

Figure 3. Effect of CPU86017 (0.1, 1.0, and 10 μmol/L) and propranolol (PRO, 1 μmol/L) on calcium transients in beating primary myocytes paced by field electric stimulation. (A) Control; (B) Incubated with ISO (100 nmol/L); (C) ISO plus PRO (1 μmol/L); (D) ISO plus CPU86017 (0.1 μmol/L); (E) ISO plus CPU86017 (1 μmol/L); (F) ISO plus CPU86017 (10 μmol/L); (G) Cumulated data of peak (at systole), variant (difference between the peak and trough) and trough (at diastole) were compared among groups. n=8–10. Mean±SD. ^bP<0.05, ^cP <0.01 *vs* Control; ^hP<0.05, ^iP<0.01 *vs* ISO.

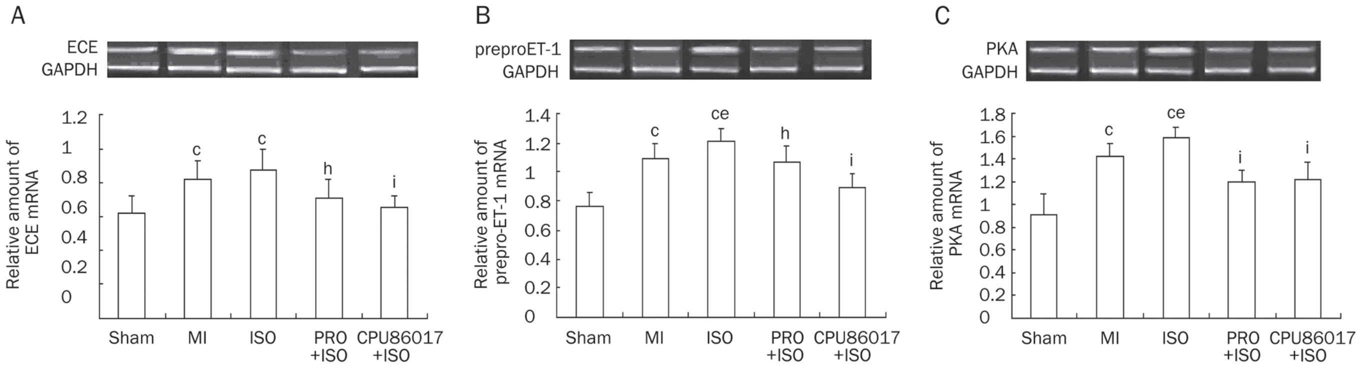

Figure 4. Effect of isoproterenolol (ISO), propranolol (PRO), and CPU86017 on up-regulation of mRNA expression of ECE (A), prepro-ET-1 (B), and PKA (C) in the failing heart caused by infarction. *n*=4. Mean±SD. $^c P<0.01$ *vs* Sham; $^e P<0.05$ *vs* MI; $^h P<0.05$, $^i P<0.01$ *vs* ISO.

and decreased SOD and GSH-px content by 40.3% and 48.2% ($P<0.01$), respectively, in the ISO group relative to the sham group. A further significant decline in SOD activity was observed following ISO medication (Figure 5A–5C).

Activity of iNOS and NO content: Cytokines are frequently involved in failing hearts, and the activity of iNOS was measured, showing enhanced iNOS activity following the MI procedure ($P<0.01$) relative to the sham group. An excess of NO content was the product of activated iNOS, and served as an oxidant, contributing adversely to cardiac function and further elevating NO levels ($P<0.05$) during ISO administration, compared to the MI group. These changes play a large role in oxidative stress, and were attenuated by either propranolol or CPU86017 treatment (Figure 5D, 5E).

Immunocytochemistry of phospholamban

Phospholamban (PLB) is a critical modulator of SERCA2a, and modulates the uptake process of Ca^{2+} into the Ca^{2+} store of the sarcoplasmic reticulum. We found that PLB was downregulated by ISO medication, as seen by a loss of fluorescence in these treated myocytes relative to normal myocytes (Figure 6). Aminoguanidine, a specific inhibitor of iNOS[25] was sufficient for recovering the fluorescence image of PLB protein, as was the antioxidant ascorbic acid[26] (but at higher concentrations). Recovery of fluorescence of PLB was also achieved by an application of CPU86017 to levels comparable to those of antioxidants (Figure 6).

Discussion

There are four major findings emanating from the present study: 1) Compromised cardiac function and hypertrophy were caused by MI and worsened by ISO medication *in vivo*; 2) Changes in cardiac function by MI combined with ISO stimulation occurred in parallel with changes in FKBP12.6, SER-

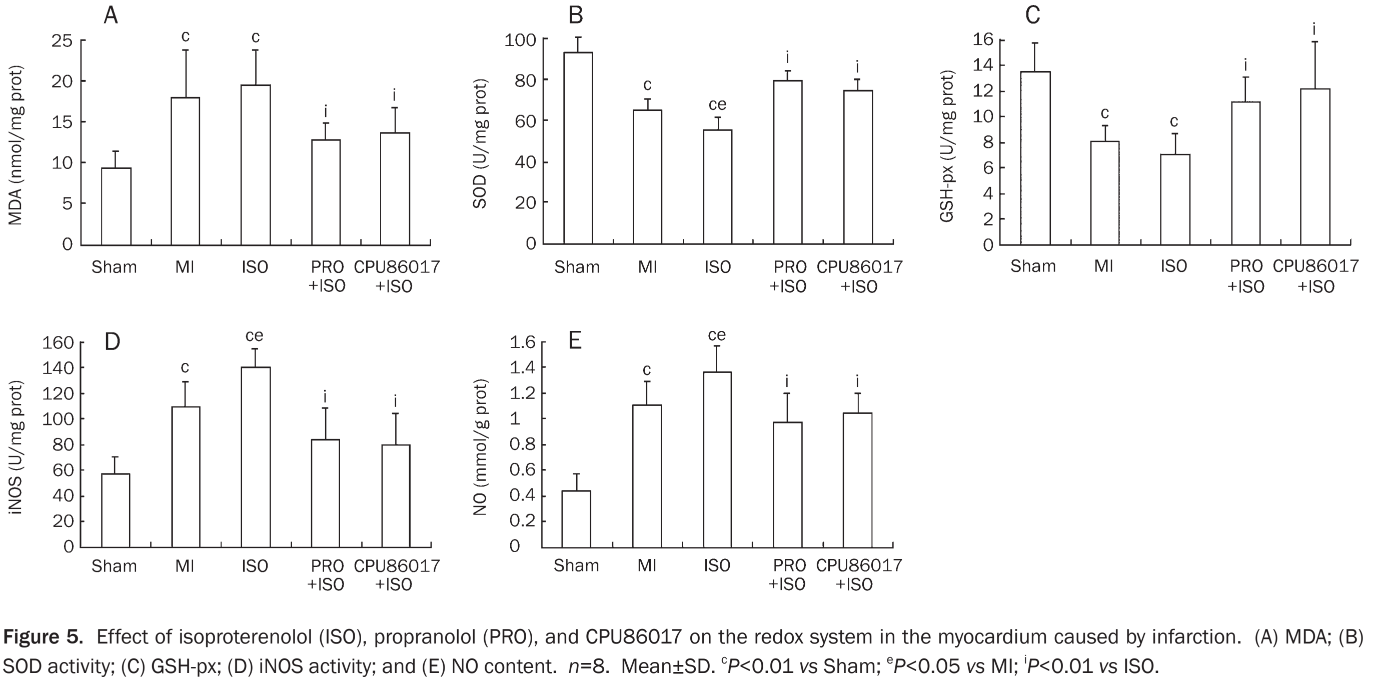

Figure 5. Effect of isoproterenolol (ISO), propranolol (PRO), and CPU86017 on the redox system in the myocardium caused by infarction. (A) MDA; (B) SOD activity; (C) GSH-px; (D) iNOS activity; and (E) NO content. *n*=8. Mean±SD. $^c P<0.01$ *vs* Sham; $^e P<0.05$ *vs* MI; $^i P<0.01$ *vs* ISO.

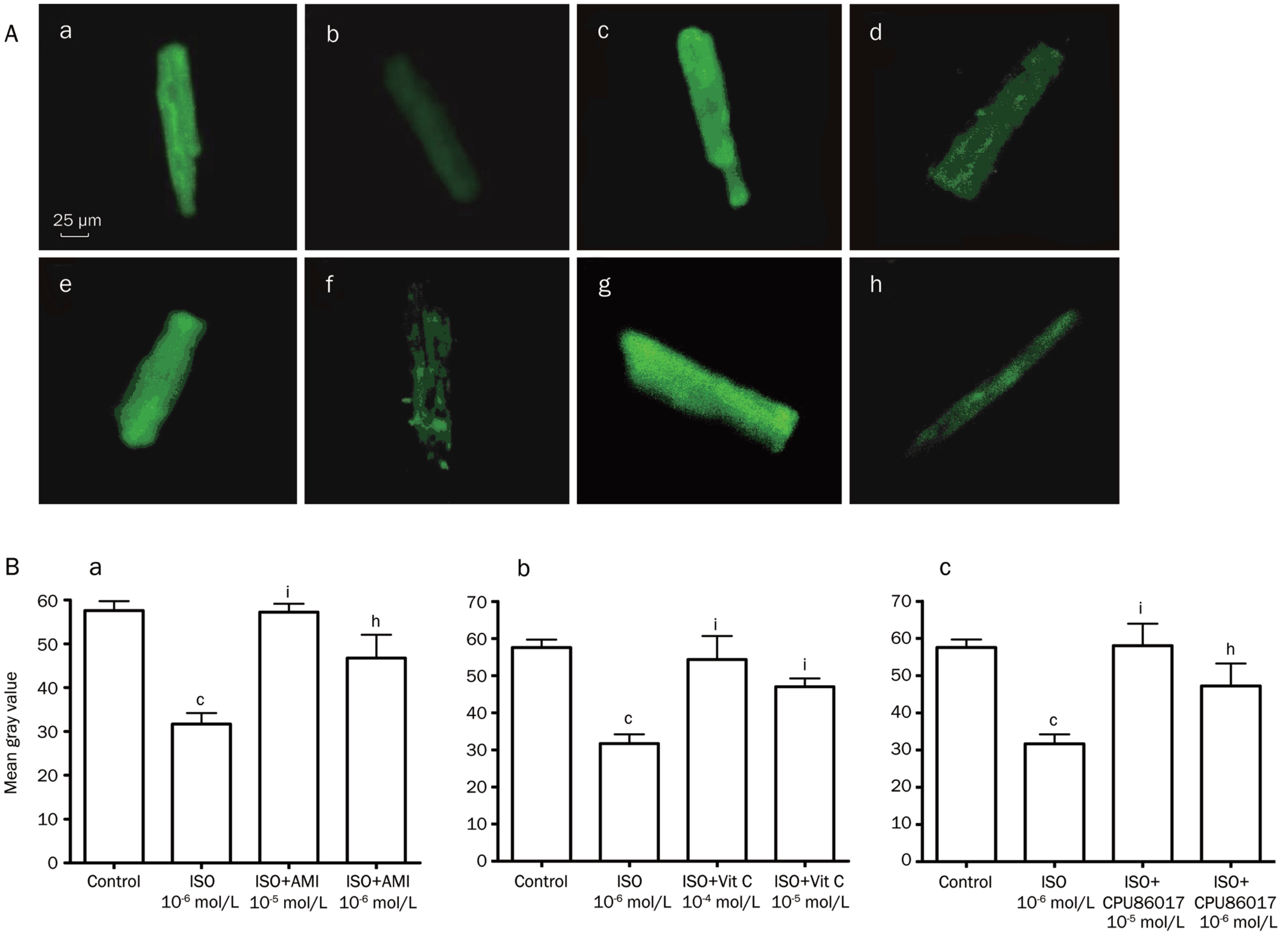

Figure 6. Effect of antioxidants aminoguanidine (AMI), ascorbic acid (Vit C), and CPU86017 on downregulation of phospholamban (PLB) in the primary rat myocytes induced by isoproterenolol (ISO). (A) Fluorescent image: a, Control; b, ISO 1 μmol/L; c, ISO+AMI 10 μmol/L; d, ISO+AMI 1 μmol/L; e, ISO+Vit C 100 μmol/L; f, ISO+Vit C 10 μmol/L; g, ISO+CPU86017 10 μmol/L; h, ISO+CPU86017 1 μmol/L; (B) Gray density in cumulated data: a, AMI; b, Vit C; c, CPU86017. *n*=8. Mean±SD. $^{c}P<0.01$ *vs* Control; $^{h}P<0.05$, $^{i}P<0.01$ *vs* ISO.

CA2a, PLB, RyR2, and PKA levels, and overt oxidative stress in the myocardium; 3) Ca^{2+} leakage was elicited in the presence of ISO, and responded to CPU86017 treatment *in vitro*; 4) Calcium leakage caused by ISO is related to the downregulation of PLB due to the activity of oxidants, and can be reversed by CPU86017 treatment.

With regards to the treatment of HF, more attention should be paid to the biomarkers of calcium homeostasis in the cardiac cycle[27]. The elevated Ca^{2+} levels at the end of diastole that result from calcium leakage are major factors in the pathogenesis of failing hearts. This leakage is due to an unstable and defective RyR2 caused by the dissociation of FKBP12.6[1, 8]. In addition, other factors, including downregulation of SERCA2a and PLB expression, are of interest because of their contribution to calcium leakage by less efficient Ca^{2+} uptake into the pool of the sarcoplasmic reticulum. Defective SERCA2a disturbs intracellular calcium regulation, adversely affecting excitation-contraction coupling in cardiac myocytes, and consequently impairs the systolic and diastolic functions of the heart[28]. Thus, exacerbated cardiac dysfunction by ISO medication may be the result of two factors: abnormal calcium releasing activity and abnormal calcium uptake behavior at the sarcoplasmic reticulum. Changes in cardiac function by the two steps coincided with changes in biomarkers including RyR2 and its modulator FKBP12.6, as well as SERCA2a and its modulator PLB. This is in line with other published findings on aggravating cardiac failure by ISO injection[5, 29-31] .

Hyperphosphorylation of the calcium handling proteins, including those such as RyR2, in the hyperadrenergic state is mainly caused by PKA. However, calmodulin kinase II is also implicated in this process[32]. In addition, the effects of ISO treatment may be partly mediated by PKCε phosphorylation[8] to downregulate RyR2, FKBP12.6, SERCA2a, and PLB, with involvement of oxidative stress and related ET pathways[7]. Ca^{2+} released into the cytosol requires an equal amount of Ca^{2+} uptake in the sarcoplasmic reticulum during diastole, and is essential in maintaining Ca^{2+} homeostasis and normal relaxation[33]. An excess of ROS mediates downregulation of

FKBP12.6, and the antioxidative activity of tocopherol sufficiently mitigates ISO-induced downregulation of calcium handling proteins as well as hyperphosphorylation of PKCε[8]. Thus, an attenuation of the hyperadrenergic state induced by downregulation of FKBP12.6 by CPU86017 is possibly the consequence of its antioxidative activity.

SERCA2a activity positively correlates with cardiac performance, and downregulation of SERCA2a is frequently associated with downregulation of PLB[34]. A clinically applicable, high-efficiency, percutaneous means of therapeutic gene delivery with adenovirus expressing a pseudophosphorylated mutant AdS16E recovers the phosphorylation of PLB, resulting in an improvement of HF in large animals[35]. With downregulated SERCA2a and PLB, the speed and amount of calcium uptake into the sarcoplasmic reticulum are reduced, rendering high diastolic Ca^{2+} levels at diastole. This is critical to developing cardiac insufficiency. Downregulated PLB as seen by immunohistochemistry after ISO treatment correlates with cardiac dysfunction. We showed that CPU86017 was sufficient to mitigate these changes to the same extent as other antioxidants such as ascorbic acid and aminoguanidine (a specific blocker for iNOS), and consequently reduces the damage to the myocardium by attenuating the genesis of NO and possibly the potent oxidant ONOO· in the presence of ISO.

CPU86017, derived from berberine[16], reduced ISO elevated diastolic Ca^{2+} in a concentration-dependent way that was at least partially attributed to its antioxidant activity. This resembled the activity of ascorbic acid in the present study and that of tocopherol[7]. In contrast, PKA phosphorylation by ISO medication is markedly suppressed by a blockade on endothelin receptors[7, 8] and an activated ET system typically found in pulmonary artery hypertension is sufficiently suppressed by CPU86017[17, 18]. The antioxidant activity of CPU86017 provides relief to arrhythmogenesis in thyroxin-induced cardiomyopathy in rats[36] and reduces calcium leakage in isolated myocytes from thyroxin-induced arrhythmic rat hearts[37]. These results indicate that CPU86017 initiates beneficial effects on both HF and cardiac dysrhythmia related to normalized PLB expression, likely stemming from its antioxidative properties. Propanolol used in conjunction with verapamil, a classic calcium antagonist, has been proven to be more effective in prolonging the survival of patients with mutated RyR2 presenting CPVT[38] than propranolol alone. Thus, a restriction of calcium influx by the calcium antagonism of CPU86017 contributes in part to attenuating ISO-induced HF and arrhythmogenesis. Furthermore, calcium leakage can be blocked by intervention with compound JTV519[39] , which shares a similar profile of multi-channel blocking activity including an inhibitory effect on Ca^{2+} influx with CPU86017[40]. Furthermore, an antioxidative activity is effective in ameliorating abnormal PLB and calcium leakage during septic shock due to improved mitochondria activity[41].

Limitations: Concerning activated PKA in the presence of β-adrenoceptor stimulation by ISO, we did not directly observe hyperphosphorylated PKA protein, but upregulated PKA mRNA only. However, following β-receptor activation in our previous reports we found that that besides phosphorylation of PKA, ISO induced hyperphosphorylation of PKCε. This could be reproduced by H_2O_2, and is suppressed by propranolol, endothelin receptor antagonist, or the antioxidant tocopherol[8]. Thus, both PKA and PKCε are involved in ISO induced hyperphosphorylation and are responsible for downregulation of calcium handling proteins. Furthermore, this process is likely mediated by ROS.

In conclusion, cardiac dysfunction was deteriorated in two steps by MI and ISO stimulation in parallel with changes in downregulation of calcium handling proteins (PLB, SERCA2a, FKBP12.6, and RyR2) leading to calcium leakage. These abnormalities are likely to be related to the genesis of ROS. The antioxidative activity of CPU86017 contributes to relieving HF via normalizing downregulation of PLB and calcium leakage. CPU86017 therefore has the potential to treat stress-related exacerbation of HF and arrhythmias in clinical practice.

Acknowledgements

This project was supported by the National Natural Foundation of China No 30670760 and the Major State Basic Research Development Program of the People's Republic of China (No 2006CB503807).

Author contribution

Min-you QI and Yu FENG conducted the project and data processing. Na LI and Yu-si CHENG assisted with data processing and manuscript preparation. De-zai DAI and Yin DAI designed the research project by setting up hypotheses, raised suitable targets for investigation and revised the manuscript.

References

1 Wehrens XH, Lehnart SE, Reiken S, Vest JA, Wronska A, Marks AR. Ryanodine receptor/calcium release channel PKA phosphorylation: a critical mediator of heart failure progression. Proc Natl Acad Sci USA 2006; 103: 511–8.

2 Lehnart SE, Wehrens XH, Kushnir A, Marks AR. Cardiac ryanodine receptor function and regulation in heart disease. Ann NY Acad Sci 2004; 1015: 144–59.

3 Lehnart SE. Novel targets for treating heart and muscle disease: stabilizing ryanodine receptors and preventing intracellular calcium leak. Curr Opin Pharmacol 2007; 7: 225–32.

4 Reiken S, Gaburjakova M, Guatimosim S, Gomez AM, D'Armiento J, Burkhoff D, *et al*. Protein kinase A phosphorylation of the cardiac calcium release channel (ryanodine receptor) in normal and failing hearts. Role of phosphatases and response to isoproterenol. J Biol Chem 2003; 278: 444–53.

5 Ellison GM, Torella D, Karakikes I, Purushothaman S, Curcio A, Gasparri C, *et al*. Acute beta-adrenergic overload produces myocyte damage through calcium leakage from the ryanodine receptor 2 but spares cardiac stem cells. J Biol Chem 2007; 282: 11397–409.

6 Wang HL, Dai DZ, Gao E, Zhang YP, Lu F. Dispersion of ventricular mRNA of RyR2 and SERCA2 associated with arrhythmogenesis in rats. Acta Pharmacol Sin 2004; 25: 738–43.

7 Feng Y, Tang XY, Dai DZ, Dai Y. Reversal of isoproterenol induced downregulation of phospholamban and FKBP12.6 is mediated by antagonism of endothelin receptors of CPU0213. Acta Pharmacol

Sin. 2007; 28: 1746–54.

8 Li N, Jia N, Dai DZ, Dai Y. Endothelin receptor antagonist CPU0213 and vitamin E reverse downregulation of FKBP12.6 and SERCA2a: a role of hyperphosphorylation of PKC epsilon. Eur J Pharmacol 2008; 591: 211–8.

9 Cheng YS, Dai DZ, Dai Y. Isoproterenol disperses distribution of NADPH oxidase, MMP-9, and pPKCepsilon in the heart, which are mitigated by endothelin receptor antagonist CPU0213. Acta Pharmacol Sin 2009; 30: 1099-106.

10 Qi MY, Xia HJ, Dai DZ, Dai Y. A novel endothelin receptor antagonist CPU0213 improves diabetic cardiac insufficiency attributed to upregulation of the expression of FKBP12.6, SERCA2a, and PLB in rats. J Cardiovasc Pharmacol 2006; 47: 729–35.

11 Phrommintikul A, Chattipakorn N. Roles of cardiac ryanodine receptor in heart failure and sudden cardiac death. Int J Cardiol 2006; 112: 142–52.

12 Marks AR. Novel therapy for heart failure and exercise-induced ventricular tachycardia based on 'fixing' the leak in ryanodine receptors. Novartis Found Symp 2006; 274: 132–47.

13 Gyorke S, Terentyev D. Modulation of ryanodine receptor by luminal calcium and accessory proteins in health and cardiac disease. Cardiovasc Res 2008; 77: 245–55.

14 Shattock MJ. Phospholemman: its role in normal cardiac physiology and potential as a druggable target in disease. Curr Opin Pharmacol 2009; 9: 160–6.

15 Gao MH, Tang T, Guo T, Miyanohara A, Yajima T, Pestonjamasp K, *et al*. Adenylyl cyclase type VI increases Akt activity and phospholamban phosphorylation in cardiac myocytes. J Biol Chem 2008; 283: 33527–35.

16 Dai DZ. CPU86017: a novel Class III antiarrhythmic agent with multiple actions at ion channels. Cardiovasc Drug Rev 2006; 24: 101–15.

17 Zhang TT, Cui B, Dai DZ, Tang XY. Pharmacological efficacy of CPU 86017 on hypoxic pulmonary hypertension in rats: mediated by direct inhibition of calcium channels and antioxidant action, but indirect effects on the ET-1 pathway. J Cardiovasc Pharmacol 2005; 46: 727–34.

18 Zhang TT, Cui B, Dai DZ, Su W. CPU 86017, p-chlorobenzyltetrahyd roberberine chloride, attenuates monocrotaline-induced pulmonary hypertension by suppressing endothelin pathway. Acta Pharmacol Sin 2005; 26: 1309–16.

19 Sumitomo N, Harada K, Nagashima M, Yasuda T, Nakamura Y, Aragaki Y, *et al*. Catecholaminergic polymorphic ventricular tachycardia: electrocardiographic characteristics and optimal therapeutic strategies to prevent sudden death. Heart 2003; 89: 66–70.

20 Kontula K, Laitinen PJ, Lehtonen A, Toivonen L, Viitasalo M, Swan H. Catecholaminergic polymorphic ventricular tachycardia: recent mechanistic insights. Cardiovasc Res 2005; 67: 379–87.

21 Nakamura R, Egashira K, Machida Y, Hayashidani S, Takeya M, Utsumi H, *et al*. Probucol attenuates left ventricular dysfunction and remodeling in tachycardia-induced heart failure: roles of oxidative stress and inflammation. Circulation 2002; 106: 362–7.

22 Brigadeau F, Gelé P, Marquié C, Soudan B, Lacroix D. Ventricular arrhythmias following exposure of failing hearts to oxidative stress *in vitro*. J Cardiovasc Electrophysiol 2005; 16: 629–36.

23 Kao JP, Harootunian AT, Tsien RY. Photochemically generated cytosolic calcium pulses and their detection by fluo-3. J Biol Chem 1989; 264: 8179–84.

24 Huang ZJ, Dai DZ, Li N, Na T, Ji M, Dai Y. Calcium antagonist property of CPU228, a dofetilide derivative, contributes to its low incidence of torsades de pointes in rabbits. Clin Exp Pharmacol Physiol 2007; 34: 310–7.

25 Ishibashi Y, Takahashi N, Tokumaru A, Karino K, Sugamori T, Sakane T, *et al*. Activation of inducible NOS in peripheral vessels and outcomes in heart failure patients. J Card Fail 2008; 14: 724–31.

26 Han JM, Chang BJ, Li TZ, Choe NH, Quan FS, Jang BJ, *et al*. Protective effects of ascorbic acid against lead-induced apoptotic neurodegeneration in the developing rat hippocampus *in vivo*. Brain Res 2007; 1185: 68–74.

27 Minamisawa S, Sato Y, Cho MC. Calcium cycling proteins in heart failure, cardiomyopathy and arrhythmias. Exp Mol Med 2004; 36: 193–203.

28 Lokuta AJ, Maertz NA, Meethal SV, Potter KT, Kamp TJ, Valdivia HH, *et al*. Increased nitration of sarcoplasmic reticulum Ca^{2+}-ATPase in human heart failure. Circulation 2005; 111: 988–95.

29 Du XJ, Cox HS, Dart AM, Esler MD. Sympathetic activation triggers ventricular arrhythmias in rat heart with chronic infarction and failure. Cardiovasc Res 1999; 43: 919–29.

30 Elhendy A, Sozzi FB, van Domburg RT, Bax JJ, Geleijnse ML, Roelandt JR. Relation among exercise-induced ventricular arrhythmias, myocardial ischemia, and viability late after acute myocardial infarction. Am J Cardiol 2000; 86: 723–9.

31 Priori SG, Napolitano C, Memmi M, Colombi B, Drago F, Gasparini M, *et al*. Clinical and molecular characterization of patients with catecholaminergic polymorphic ventricular tachycardia. Circulation 2002; 106: 69–74.

32 Currie S. Cardiac ryanodine receptor phosphorylation by CaM Kinase II: keeping the balance right. Front Biosci 2009; 14: 5134–56.

33 Chakraborti S, Das S, Kar P, Ghosh B, Samanta K, Kolley S, *et al*. Calcium signaling phenomena in heart diseases: a perspective. Mol Cell Biochem 2007; 298: 1–40.

34 Vittone L, Mundina-Weilenmann C, Mattiazzi A. Phospholamban phosphorylation by CaMKII under pathophysiological conditions. Front Biosci 2008; 13: 5988–6005.

35 Kaye DM, Preovolos A, Marshall T, Byrne M, Hoshijima M, Hajjar R, *et al*. Percutaneous cardiac recirculation-mediated gene transfer of an inhibitory phospholamban peptide reverses advanced heart failure in large animals. J Am Coll Cardiol 2007; 50: 253–60.

36 Hao JM, Dai DZ, Yu F. The exaggerated oxidative stress developed in cardiomyopathy by over-doses of thyroxin and these were reversed partly by CPU86017, a derivative of tetra-hydro-berberine. J Advan Pharm Sci 2005; 29: 417–21.

37 Na T, Huang ZJ, Dai DZ, Zhang Y, Dai Y. Abrupt changes in FKBP12.6 and SERCA2a expression contribute to sudden occurrence of ventricular fibrillation on reperfusion and are prevented by CPU86017. Acta Pharmacol Sin 2007; 28: 773–82.

38 Rosso R, Kalman JM, Rogowski O, Diamant S, Birger A, Biner S, *et al*. Calcium channel blockers and beta-blockers versus beta-blockers alone for preventing exercise-induced arrhythmias in catecholaminergic polymorphic ventricular tachycardia. Heart Rhythm 2007; 4: 1149–54.

39 Yano M, Kobayashi S, Kohno M, Doi M, Tokuhisa T, Okuda S, *et al*. FKBP12.6-mediated stabilization of calcium-release channel (ryanodine receptor) as a novel therapeutic strategy against heart failure. Circulation 2003; 107: 477–84.

40 Yamamoto T, Yano M, Xu X, Uchinoumi H, Tateishi H, Mochizuki M, *et al*. Identification of target domains of the cardiac ryanodine receptor to correct channel disorder in failing hearts. Circulation 2008; 117: 762–72.

41 Hassoun SM, Marechal X, Montaigne D, Bouazza Y, Decoster B, Lancel S, *et al*. Prevention of endotoxin-induced sarcoplasmic reticulum calcium leak improves mitochondrial and myocardial dysfunction. Crit Care Med 2008; 36: 2590–6.

Acta Pharmacologica Sinica (2010) 31: 175–183
© 2010 CPS and SIMM All rights reserved 1671-4083/10 $32.00
www.nature.com/aps

Original Article

Protective role of PI3-kinase/Akt/eNOS signaling in mechanical stress through inhibition of p38 mitogen-activated protein kinase in mouse lung

Xin-qi PENG[1,#,*], Mahendra DAMARLA[2,#], Jarrett SKIRBALL[2], Stephanie NONAS[5], Xiao-ying WANG[7], Eugenia J HAN[2], Emile J HASAN[2], Xuan CAO[2], Adel BOUEIZ[2], Rachel DAMICO[2], Rubin M TUDER[4], Alfred M SCIUTO[1], Dana R ANDERSON[1], Joe GN GARCIA[6], David A KASS[3], Paul M HASSOUN[2], Jun-tian ZHANG[7,*]

[1]Division of Analytical Toxicology, US Army Medical Research Institute of Chemical Defense, Aberdeen Proving Ground, MD, USA; [2]Division of Pulmonary & Critical Care Medicine, [3]Division of Cardiology, Department of Medicine, Johns Hopkins University School of Medicine, Baltimore, MD, USA; [4]Division of Pulmonary Sciences and Critical Care Medicine, Department of Medicine, University of Colorado Denver School of Medicine, Denver, CO, USA; [5]Oregon Health & Science University, Division of Pulmonary and Critical Care Medicine, Portland, OR, USA; [6]Department of Medicine, University of Chicago Pritzker School of Medicine, Chicago, IL, USA; [7]Department of Pharmacology, Institute of Materia Medica, Chinese Academy of Medical Sciences, Beijing 100050, China

---

Aim: To test the hypothesis that PI3K/Akt/eNOS signaling has a protective role in a murine model of ventilation associated lung injury (VALI) through down-regulation of p38 MAPK signaling.
Methods: Male C57BL/J6 (wild-type, WT) or eNOS knockout mice (eNOS$^{-/-}$) were exposed to mechanical ventilation (MV) with low (LV$_T$, 7 mL/kg) and high tidal volume (HV$_T$, 20 mL/kg) for 0–4 h. A subset of WT mice was administered the specific inhibitors of PI3K (100 nmol/L Wortmannin [Wort], ip) or of p38 MAPK (SB203580, 2 mg/kg, ip) 1 h before MV. Cultured type II alveolar epithelial cells C10 were exposed to 18% cyclic stretch for 2 h with or without 20 nmol/L Wort pretreatment. At the end of the experiment, the capillary leakage *in vivo* was assessed by extravasation of Evans blue dye (EBD), wet/dry weight ratio and lung lavage protein concentration. The lung tissue and cell lysate were also collected for protein and histological review.
Results: MV decreased PI3K/Akt phosphorylation and eNOS expression but increased phospho-p38 MAPK expression along with a lung leakage of EBD. Inhibitions of phospho-Akt by Wort worsen the lung edema, whereas inhibition of p38 MAPK kinase restored activation of Akt together with alleviated capillary leakage. eNOS$^{-/-}$ mice showed an exacerbated lung edema and injury. The stretched C10 cells demonstrated that Wort diminished the activation of Akt, but potentiated phosphorylation of MAPK p38.
Conclusion: Our results indicate that PI-3K/Akt/eNOS pathway has significant protective effects in VALI by preventing capillary leakage, and that there is a cross-talk between PI3K/Akt and p38 MAPK pathways in vascular barrier dysfunction resulting from VALI.

Keywords: mechanical stress; ventilator-associated lung injury; pulmonary capillary leakage; PI3K/Akt/eNOS; p38 MAPK signalings; signals cross-talk; pulmonary edema; wortmannin

---

Acta Pharmacologica Sinica (2010) 31: 175–183; doi: 10.1038/aps.2009.190

Introduction

Acute lung injury (ALI) is a complex syndrome marked by increased vascular permeability resulting in tissue edema and profound hypoxia[1, 2]. Mechanical ventilation (MV) is often a necessary treatment for respiratory failure and a supportive measure in critically ill patients. However, it is well known that ventilation with high tidal volume (HV$_T$ MV) or pressure may be harmful, causing damage to previously healthy lungs or worsening already injured ones. This is especially the case for permeability whereby exacting mechanical stress on various components of the respiratory system can lead to ventilation associated lung injury (VALI). We performed the study described herein in an effort to elucidate the underlying mechanisms of VALI and investigate potential therapies against VALI.

Akt (protein kinase B), a multifunctional serine-threonine protein kinase, is a major downstream signaling molecule of phosphoinositide 3-kinase (PI3K). It is also an upstream

---

[#] These authors contributed equally to this work.

[*] To whom correspondence should be addressed.

E-mail xinqipeng@gmail.com (Xin-qi PENG)
zhangjt@imm.ac.cn (Jun-tian ZHANG)

Received 2009-09-25 Accepted 2009-12-03

enzyme of eNOS. Its activation has been implicated in various endothelial functions, including cell survival, migration, and activation of nitric oxide synthase[3–5]. Studies *in vitro* have shown that Akt can directly phosphorylate endothelial nitric oxide (NO) synthase (eNOS) and activate the enzyme, leading to NO production[6]. Thus the PI3K/Akt/eNOS signaling pathway is critical for maintenance of endothelial vascular tone, and integrity[7, 8]. We have previously demonstrated that NOS signaling and p38 MAPK are significantly implicated in the development of acute lung injury[9, 10]. Though the PI3K/Akt and MAPKs, which include the ERK1/2, JNK, and p38 MAPK subgroups, are probably the best-characterized survival-related or death-associated signaling pathways[11–15] respectively, their functional roles in the VALI, especially the interplay between these two pathways, have not yet been elucidated. The emerging evidence has triggered interest on the crosstalk link between PI3K/Akt and MAPKs signaling[16–19].

The purpose of this study is to identify the protective role of PI3K/Akt/eNOS signaling in the context of the lung vascular permeability in response to mechanical stress and to ascertain if this protective effect occurs via p38 MAPK signaling in murine HV_T MV and cyclic stretch models. Our results indicate that the PI3K/Akt/eNOS pathway is involved in the process of HV_T MV with a change in phosphorylated forms in intact lungs. Furthermore, genetic deletion of eNOS exacerbates vascular dysfunction as assessed by Evans Blue Dye (EBD). Finally, the findings that pharmacologic antagonism of PI3K with Wort potentiates phosphorylation of p38 MAPK in response to cyclic stretch in C10 epithelial cells and that inhibition of p38 MAPK facilitates the activation of Akt, a survival signaling protein, suggest interplay between the Akt and p38 MAPK pathways in vascular barrier dysfunction[20].

Materials and methods

Materials

CMRL 1066 medium was purchased from Invitrogen (Carlsbad, CA), and fetal bovine serum was obtained from Hyclone (Logan, UT) and Invitrogen (Carlsbad, CA). Wortmannin was obtained from Calbiochem (San Diego, CA). Phospho-specific antibodies of PI3K, Akt, and eNOS as well as p38 MAP kinase were obtained from Cell Signaling Technology (Beverly, MA). SB203580 and other reagents used in this study were obtained from Sigma (St Louis, MO).

Animal model of VILI and drug administration

Male C57BL/6J mice aged 10 weeks (23−25 g, Jackson Laboratory, Bar Harbor, ME) were studied in a pathogen-free facility under a protocol approved by the Johns Hopkins University Department of Laboratory Animal Medicine. Anesthesia was induced with sodium pentobarbital (50 mg/kg, ip). Animals then underwent tracheotomy and intubation prior to exposure to MV (Harvard Apparatus, Boston, MA) with room air for 0 (Control, Cont), 2, or 4 h with either 7 mL/kg or 20 mL/kg tidal volume (LV_T or HV_T). The respiratory rate was set at 160 breaths per minute for all tidal volumes together with an adjustment of the dead space to maintain arterial pH between 7.35 and 7.45. Airway pressures were continuously measured and remained around 0−2 cm H_2O. A 500-μL bolus of lactated Ringer's solution was given intravenously at the initiation of MV to maintain adequate mean arterial blood pressure (about 80 Torr) during 4 h of ventilation. The adequacy of MV settings on gas exchange was evaluated according to the mean blood pressure (MBP) and the arterial blood gases obtained via catheterization of a femoral artery. Rectal temperature was maintained near 37 °C using a heating lamp and pad. At the end of MV, the animals were administered an intraperitoneal lethal dose of the anesthetic agent before the lungs were harvested.

To assess the effect of MV on the signaling of PI3K/Akt/eNOS and p38 MAPK, mice were treated with either a specific inhibitor of p38 MAPK, SB203580 (2 mg/kg, ip), or a specific inhibitor of PI3K, Wort (100 nmol/L, ip)[21], 1 h before exposure to MV. SB203580 and Wort were dissolved in DMSO first and then diluted further by saline. All doses, route of administration, and timing of delivery of pharmacological agents as well as the solvent were based on known half-life of agents and preliminary experiments that demonstrated efficacy[22, 23].

Assessment of pulmonary capillary permeability

Acute changes in vascular permeability were evaluated by using bronchoalveolar lavage (BAL) fluid albumin concentrations and EBD assay in intact mice. Pulmonary edema formation was also assessed using lung wet-to-dry weight (W/D) ratios. EBD (20 mg/kg) was injected into the external jugular vein 60 min prior to termination of the experiment to determine vascular leak as previously described[24, 25]. To determine wet-to-dry lung weight ratio, as a separate measure of pulmonary edema, briefly the left lung was excised and immediately weighed on pre-tared dishes for determination of wet lung weight. The samples were then dried in an oven (Fisher Isotemp) of 60 °C for 7 d and weighed several times until the weight became consistent[26].

Cyclic stretch (CS) and C10, epithelial cell culture

C10, a murine nonmalignant alveolar type II–like epithelial cell line, was cultured in CMRL 1066 medium supplemented with 10% fetal bovine serum (FBS) and antibiotics. Cells were seeded at standard densities (8×10^5 cells/well) onto collagen I–coated BioFlex plates, and once confluence was reached, the plates were mounted onto the FX-4000T Flexercell Tension Plus system (Flexercell International, McKeesport, PA) equipped with a 25-mm BioFlex loading station. This system provides uniform radial and circumferential strain across a membrane surface along all radii. Cells were subjected to 18% elongation for the desired time at 25 cycles per minute. Cells grown on BioFlex plates and simultaneously placed in a cell culture incubator were considered as static controls. At the end of the experiment, the cells were harvested for protein analysis.

SDS-PAGE and immuno-blotting analysis

Aliquots from cell lysates and tissue homogenates were immunoblotted using native and phosphospecific antibodies as previously described[9]. The blots were then visualized with the ECL Western Blot Detection Kit (Amersham, Piscataway, NJ, USA).

Statistics

Data are shown as mean±standard deviation (SD), for each experimental condition. Comparisons between groups were performed using *t*-tests or one-way ANOVA with Bonferroni correction. Analysis of variance for comparison of the different groups was used with significance set at $P<0.05$.

Results

The signaling pathway of PI3K/Akt/eNOS in response to MV

Immunoblot analysis for phospho-specific (active) and total isoforms of PI3K, Akt and eNOS was performed on lung tissue homogenates obtained from wild type mice subjected to MV with HV_T for 0 (Control), 15, 30, 60, or 120 min. As demonstrated in Figure 1A, MV at HV_T induced a decrease in PI3K, Akt and eNOS phosphorylation as early as 30 min after initiation of MV. Figures 1B, 1C and 1D show the densitometry of phospho-PI3K, phopho-Akt, and phospho-eNOS normalized to total Akt. When we extended the experiment to 4 h HV_T MV, a consistent change of phosphor-Akt was observed (Figure 2).

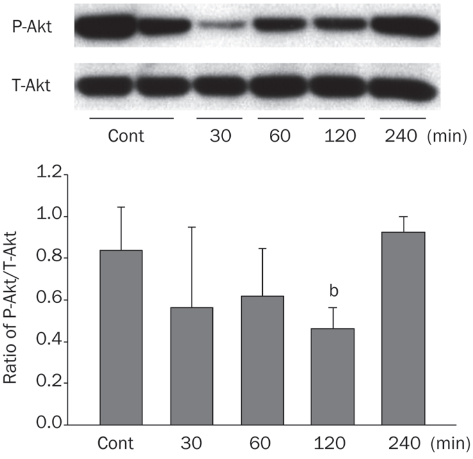

Figure 2. Down-regulation of phospho-Akt in response to mechanical stress in a time-dependent fashion. (A) In a separate experiment of 4 h HV_T MV, we observed that phospho-Akt at its serine residue 473 decreased most noticeably at 30 min and then gradually returned to control level at 2 h. (B) shows the densitometry of phopho-Akt normalized to total Akt. n=3–4 mice per condition, $^bP<0.05$.

eNOS signaling is required for maintaining the integrity of the pulmonary vasculature

To define the role of eNOS in pulmonary permeability associated with VALI, we obtained eNOS$^{-/-}$ mice from the same strain background as its wild type and exposed both to MV for up to 4 h at LV_T (7 mL/kg) or HVT (20 mL/kg) at 160 BPM. Peak airway pressure was monitored continuously as detailed in Methods. Pulmonary vascular leakage was assessed by the extravasation of EBD into lung parenchyma. MV with LV_T caused no change in extravasation of EBD in WT mice, but caused a remarkable increase of EBD leakage in eNOS$^{-/-}$ mice lungs. HV_T MV caused a 50% increase of EBD in WT mice lungs and a further increase of about 100% in eNOS$^{-/-}$ mice (Figure 3).

Wet/dry lung weight ratios, a separate measure of pulmonary edema, showed that 4 h of LV_T MV increased this ratio, but not significantly. HV_T MV caused more remarkable lung water retention in eNOS$^{-/-}$ mice than in WT mice (Figure 4). No difference was observed between WT and eNOS$^{-/-}$ mice at the control condition (results not shown).

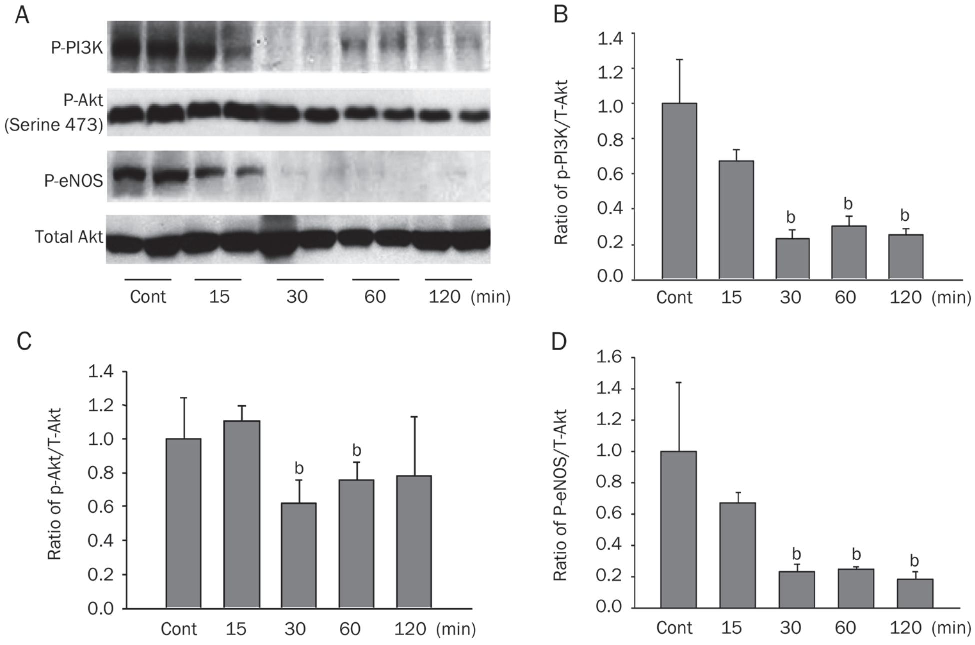

Figure 1. The signaling pathway of PI3K/Akt/eNOS in response to MV. C57BL/6J mice were randomly exposed to spontaneous breathing (Control, Cont) or HV_T (20 mL/kg) for 2 h. (A) Immunoblotting of WT mouse lung homogenates shows a decrease in PI3K, Akt, and eNOS phosphorylation after initiation of HV_T MV detected by their active forms of antibody. (B), (C), and (D) show the densitometry of phospho-PI3K, phopho-AKT, and phospho-eNOS normalized to total Akt. n=3–4 mice per condition, $^bP<0.05$ *vs* control. Note: the Figure 1A P-Akt bands represented a combination of the results came from several experiments.

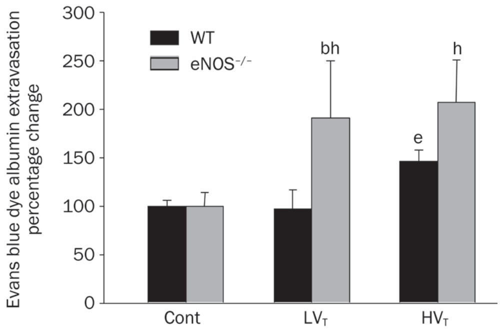

Figure 3. eNOS defective mice are less tolerant than WT mice in response to high amplitude mechanical stress featured with severe lung edema. Pulmonary vascular leakage was assessed at 4 h by the extravasation of evans blue dye(EBD) albumin in the lung parenchyma. MV with LV$_T$ caused no change in EBD influx in C57BL/6J mouse lungs, but caused a marked increase of EBD extravasation in eNOS$^{-/-}$ mouse lungs. In addition, HV$_T$ MV caused a 100% increase of EBD in eNOS$^{-/-}$ mouse lung in comparison with a 50% increase of EBA in WT mice. *n*=4 mice/experimental condition. ^{b}*P*<0.05 *vs* Control; ^{e}*P*<0.05 *vs* LV$_T$; ^{h}*P*<0.05 *vs* WT vent-exposed mice.

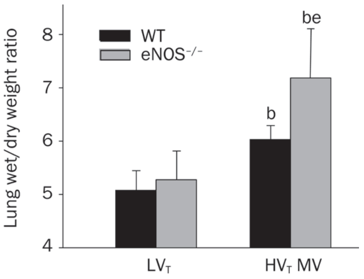

Figure 4. Effects of eNOS deficiency on pulmonary vascular leakage during mechanical ventilation. As a separate measure of pulmonary edema, wet/dry lung weight ratios were determined at the end of 4 h HV$_T$ MV. HV$_T$ MV caused an increase of the lung wet-dry weight ratio especially in eNOS-deficient mice. *n*=4 mice/experimental condition. ^{b}*P*<0.05 *vs* LV$_T$ exposed animals; ^{e}*P*<0.05 compared with WT mice exposed to HV$_T$ MV.

PI3K/Akt regulates the protective role of eNOS in reducing the lung edema

To ascertain its upstream regulation of eNOS, we examined the expression of phospho-Akt in WT and eNOS$^{-/-}$ mice after MV stress. We found that phospho-Akt declined more dramatically in eNOS$^{-/-}$ mice in comparison with WT. In addition, there was a lower level of phospho-Akt in eNOS$^{-/-}$ mice when exposed to LV$_T$ (Figure 5). To further explore the effect of this pathway on the vascular leakage associated with HV$_T$ MV, we then administered the PI3K inhibitor Wortmannin (Wort, 100 nmol/L, ip) 1 h prior to HV$_T$ MV exposure. At the end of the experiment, EBD assay was performed as mentioned above. As shown in Figure 6, Wort pre-treatment significantly worsened EBD lung accumulation in WT mice triggered by 4 h HV$_T$ MV in comparison with the non-treated group. The morphology of the lungs demonstrated a consistent finding with EBD assay that Wort treatment exacerbated neutrophil infiltration and lung edema (Figures 7A, 7B). There were no striking histologic changes in lungs of C57BL/6J mice exposed to LV$_T$ as compared with control animals (results not shown).

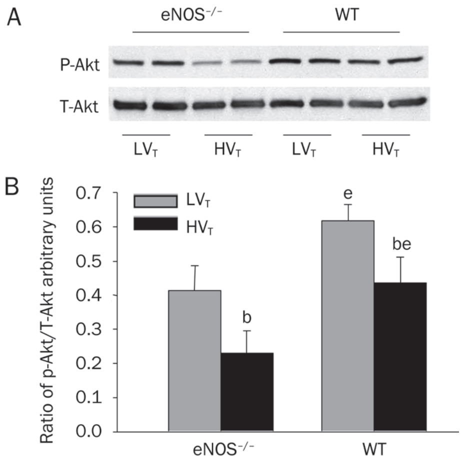

Figure 5. Lower levels of phosph-Akt expression in eNOS$^{-/-}$ mice compared with WT mice after exposure to mechanical stress. We specifically evaluated the level of phosphor-Akt, a survivor signal in response to a variety of stresses, in our 4-h VALI model by immunoblotting. (A) Consistent with our data above, decreased phopho-Akt was blunted in WT mice at the end of 4 h HV$_T$ MV, while eNOS$^{-/-}$ mice showed a significant further decrease of phosphorylated Akt in response to 4 h HV$_T$ over the attenuated expression of phospho-Akt when exposed to LV$_T$. (B) Densitometry of phopho-Akt normalized to total Akt. *n*=3–4 mice per condition. ^{b}*P*<0.05 *vs* LV$_T$; ^{e}*P*<0.05 *vs* eNOS$^{-/-}$ mice.

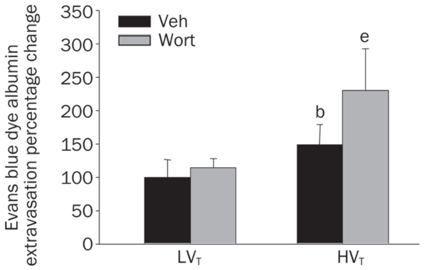

Figure 6. Wortmannin (Wort) pretreatment aggravates the pulmonary vascular leakage in WT mice induced by 4 h HV$_T$ MV. C57BL/6J mice (WT) were pretreated with Wort (100 nmol/L, given intraperitoneally), a selective PI3Kase inhibitor, 1 h prior to exposure to MV. Wort itself dose not have effect on EBD assay (data not shown). Exposure of animals to LV$_T$ on the other hand caused no changes in these values as compared to controls (data not shown). However, Wort pretreatment significantly enhanced EBD lung accumulation in C57BL/6J mice caused by 4 h HV$_T$ MV. *n*=4–6 mice/experimental condition. ^{b}*P*<0.05 vs LV$_T$; ^{e}*P*<0.05 *vs* HV$_T$ MV.

Cross-talk between p38 MAPK and PI3K/Akt/eNOS

Given the evidence of up-regulation of p38 MAPK contributing to VALI in our murine model[10, 22], we sought to determine

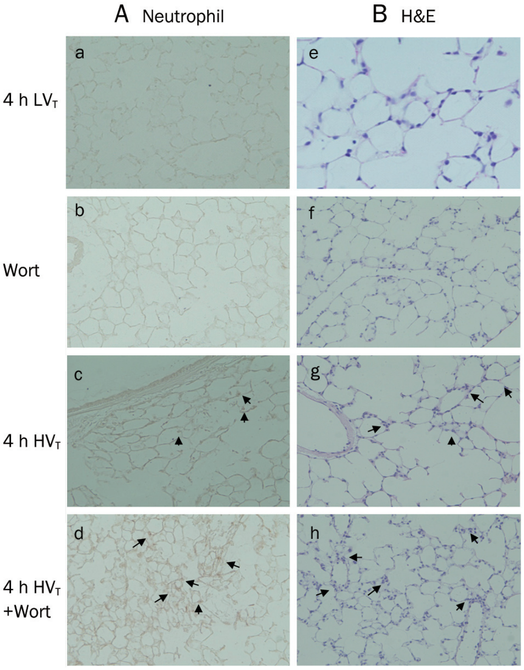

Figure 7. The morphological review of the lungs after pretreatment with Wort and mechanical ventilation. (A) Neutrophil immunostaining: the presence of parenchymal neutrophil was assessed using specific anti-neutrophil antibody. Exposure to 4 h HV_T MV produced an increased staining of neutrophils in the interstitium and alveolus in WT mice (c, arrow) compared to LV_T and Wort only (a and b). However, Wort — a specific inhibitor of PI3K--pretreatment exacerbated this effect (d, arrow). (B) Hematoxyline and eosin stain of lung tissue (×40): the presence of neutrophil infiltration in WT mice lungs when exposed to HV_T for 4 h is similar as seen on the neutrophil immuno-staining but with occasional alveolar hemorrhage (g, arrow) compared to LV_T and Wort only (e and f); Wort worsened the lung injury compared to that in animals ventilated alone (h, arrow). There were no striking histological changes in lungs of C57BL/6J mice exposed to LV_T as compared with control animals (results not shown).

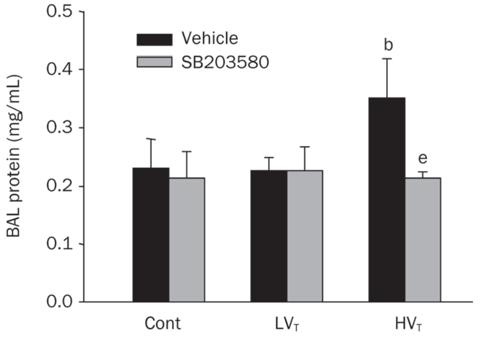

Figure 8. Inhibition of p38 MAP kinase prevents protein leakage in response to HV_T MV. Mice were treated with the p38 MAP kinase inhibitor SB203580 (2 mg/kg, ip) 1 h prior to exposure to 1–2 h HV_T MV. The data showed that the lung capillary leakage was attenuated by using the index of BAL protein at the end of 2 h HV_T MV. *n*=4. ${}^bP<0.05$ *vs* LV_T; ${}^eP<0.05$ *vs* 2 h HV_T MV.

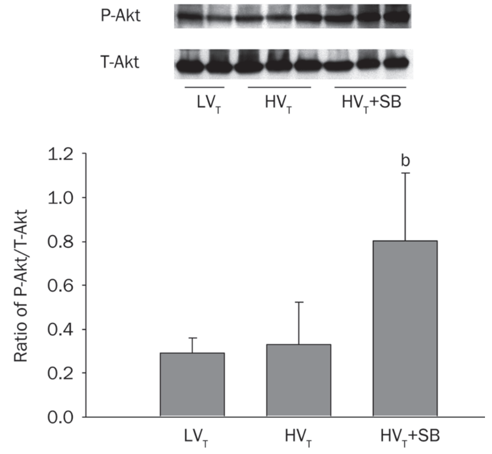

Figure 9. The effect of SB203580(SB) on the activation of Akt in WT mice exposed to 4 h mechanical ventilation. Western blotting on the mice lung exposed to HV_T MV for 4 h demonstrated that the inhibition of p38 MAPK with SB203580 increased the activation of Akt (serine 473 phosphorylation), indicating interplay between these two signal pathways. *n*=3–4 mice per condition. ${}^bP<0.05$.

the possible involvement of p38 MAPK in the pathway of PI3K/Akt/eNOS. We found that pretreatment of WT mice with SB203580 (2 mg/kg, ip) 1 h prior to HV_T MV attenuated lung capillary leakage as measured by the index of BAL protein at the end of 2 h HV_T MV (Figure 8). Recently, using the index of wet/dry lung weight ratio and EBD, we demonstrated that inhibition of the p38 MAP kinase pathway with SB203580 reduces pulmonary capillary permeability in response to high tidal volume mechanical ventilation[22]. More strikingly, at 4 h we found that inhibition of p38 MAPK with SB203580 treatment increased the activation of Akt in response to HV_T MV, possibly indicating interplay between these two signaling pathways (Figure 9). To further confirm the overlapping of these two signals, we observed the effect of the PI3K inhibitor, 20 nmol/L Wort[27], on the expression of phospho-Akt and phospho-p38 MAPK on C10 alveolar epithelial cells when exposed to 18% elongation of CS for 1−2 h. This data demonstrated that pharmacologic antagonism of PI3K with Wort diminished the activation of Akt, but potentiated phosphorylation of MAPK p38 in response to mechanical stress in cultured epithelial cells (Figure 10).

Discussion

In this study, we demonstrated that eNOS signaling is required for maintaining the integrity of the pulmonary vasculature in response to mechanical stress, and that this effect is modulated by its upstream pathway of PI3K/Akt. More importantly, we provide evidence for the first time about the existence of cross-talk of PI3K/Akt/eNOS and the p38 MAP kinase pathways in a mechanical stretch model. We demonstrate that inhibition of PI3-kinase/Akt potentiates p38 MAPK activation, while inhibition of p38 MAPK results in an increased phosphorylation of

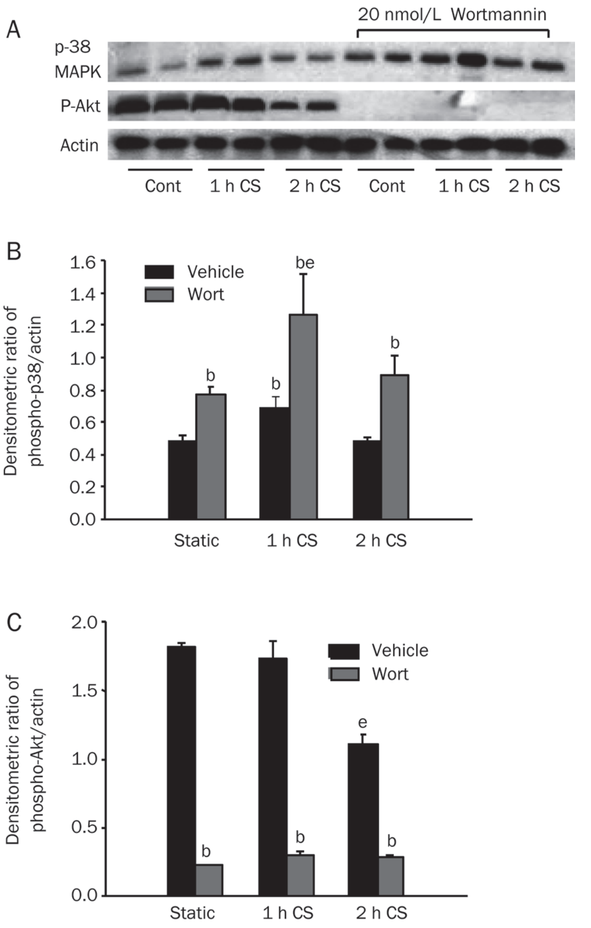

Figure 10. The effect of PI3K inhibitor, 20 nmol/L Wort, on the expression of phospho-Akt and phospho-p38 MAPK. Pharmacologic antagonism of PI3K with Wort diminished the activation of Akt, but potentiated phosphorylation of MAPK p38 in C10, type II alveolar epithelial cells when exposed to 18% cyclic stretch (CS) from 1–2 h. A) the representative blotting; B and C) the densitometric ratio of phospho-p38/actin and phospho-Akt/actin. *n*=3–4. $^b P<0.05$ *vs* Vehicle; $^e P<0.05$ *vs* static. Note: the P-Akt bands represented a combination of the results came from several experiments.

Akt, which regulates the protective effect of eNOS against the pulmonary vascular edema associated with mechanical stress. In summary, this work, coupled with results from prior studies, demonstrates that the protective role of PI3K/Akt/eNOS signaling in mechanical stress is mediated in part via inhibition of p38 mitogen-activated protein kinase signaling.

The signaling pathway of PI3K/Akt/eNOS in response to MV

In this work, we investigated the role of PI3-kinase/Akt/eNOS in ventilator-associated alveolar-capillary injury and dysfunction in a murine model by using eNOS$^{-/-}$ mice together with WT mice, and by using a pharmacological inhibitor of PI3-kinase. We found in our previous study that total eNOS signaling in intact mice lung decreased after animals were exposed to HV$_T$ MV[9]. In the present VALI study we measured the active forms of PI3K/Akt/eNOS. We found initially that not only the phospho-eNOS signal would decrease as early as 15 min, but also that the phosphorylation of PI3 kinase and Akt declined in the same time-dependent pattern after initiation of HV$_T$ MV up to 2 h in WT mice lungs. This indicated that the PI3K/Akt pathway is involved in this event (Figure 1). We then extended ventilating stress to 4 h. Immunoblotting showed the same trend of the decline in phospho-Akt as seen during the first 2 h of HV$_T$ MV. This change gradually returned toward baseline at the end of 4 h HV$_T$ MV (Figure 2). Given that the total Akt did not changed and all the signals were detected on the same blotting, we quantified the expression of phosphorylated PI3K/Akt/eNOS based on total Akt.

eNOS signaling is required for maintaining the integrity of the pulmonary vasculature

We further explored the role of eNOS in the pulmonary micro-vascular leakage. We found that genetic deletion of eNOS reduced the tolerance of the pulmonary endothelium to mechanical stress. MV with LV$_T$ caused no change of extravasation of EBD in wild type mice, but caused remarkable increase of EBD leakage in eNOS$^{-/-}$ mice lungs. HV$_T$ MV caused a 50% increase of EBD influx in the WT mice lungs and a further increase of about 100% in EBD lung accumulation in eNOS$^{-/-}$ mice (Figure 3). This result was consistent with our previously published work that a declined expression of eNOS protein was associated with VALI in C57BL/6J mice, and that an increased eNOS activity was correlated with the tolerance of iNOS deficient mice to ventilator-induced pulmonary capillary leakage[9]. This finding was also in agreement with the work of Takenaka *et al*, in which overexpressed eNOS in the lung could reduce VALI[28, 29].

We also observed wet/dry lung weight ratios as a separate measure of pulmonary edema to confirm the effect of eNOS influencing vascular barrier function. As shown in Figure 4, HV$_T$ MV for 4 h caused more profound lung edema in eNOS$^{-/-}$ mice than in WT mice. According to our data, the enhanced pulmonary permeability in response to mechanical stress can be explained in part by defects in eNOS signaling, a finding similar to that of a previous report in which eNOS or Akt1 deficient mice exhibited impaired blood flow recovery and neovascularization following arterial occlusion[30] and a suppressed VEGF-induced angiogenesis and vascular permeability[13]. Chen *et al* also showed that impaired vascular maturation due to loss of the gene of Akt1 (Akt1$^{-/-}$) in mice may be attributed to reduced activation of endothelial nitric oxide synthase (eNOS)[7].

Lungs from eNOS-deficient animals showed less change in the index of wet/dry weight ratio compared to wild-type (WT) controls than would be expected based on the Evans blue dye assay (EBD). Pharmacokinetic analysis demonstrated that 87% of the decline in intravascular Evans blue during the first 3 h after administration was a result of transvascular flux to tissue compartments. Thus, the initial accrual of Evans blue in the lung and heart may be used as a marker of transcapillary macromolecular flux in those tissues[26].

EBD mainly measures the condition of capillary permeability detected by albumin leaking from vasculature to the interstitial compartment. The initial decline in intravascular content of EBD corresponds to the intercompartmental clearance and to transcapillary macromolecular flux. While the wet/dry lung weight ratios measure whole lung water accumulation, this includes the three fluid compartments (vascular, interstitial and alveolar). The measurement not only reflects vascular and pulmonary permeability, but also the hydraulic pressure of the capillaries and fluid clearance of the airways.

The differences observed between the wet/dry ratio and EBD indicate that the wet/dry weight ratio is not as sensitive as the EBD assay for the evaluation of vasculature leakage. This may be due to a number of factors. First, it is likely that mechanical stretch may have non-uniform effects on protein permeability, hydraulic conductivity and fluid clearance[31]. Also, many studies showed that hydraulic conductivity increased without changes in protein permeability[32]. Furthermore, it is possible that water flux across the vascular barrier is increased with eNOS deficiency, but that edema clearance mechanisms are unaltered or in a compensatory condition, thus attenuating any differences in lung wet/dry weight between knockout and WT animals. These three factors may blunt the change of vascular permeability caused by mechanical stress, especially at the condition of LV_T MV. We did not show the data for the spontaneously breathing in the animals because we repeatedly demonstrated in our preliminary experiments and published works that there is no difference between the control and LV_T MV.

There is now compelling evidence supporting that endothelial NO is a barrier-tightening factor in modulating thrombin, cytokine and H_2O_2-induced endothelial permeability[33, 34]. Electron microscopic analyses revealed an intercellular junction opening in lung microvasculature in $eNOS^{-/-}$ mice[35]. In eNOS transgenic mice there is a remarkable resistance to ventilator-induced lung injury and to bacterial lipopolysaccharide induced septic shock (with attenuated hypotension, pulmonary leukocyte infiltration and lung water content), as well as an enhanced survival rate over control mice[28, 29]. Therefore, eNOS-derived nitric oxide is believed to be a determinant of endothelial junctional integrity, and eNOS will be a beneficial signaling protein protecting the vessel from leakage.

PI3K/Akt regulates the protective role of eNOS in reducing the lung edema

Recent studies indicated that Akt1 deficiency, the predominant isoform of Akt, could cause an immature development of the vasculature that is prone to leak[7, 13]. In the vessel wall, the loss of Akt1 increases inflammatory mediators and reduces eNOS phosphorylation, suggesting that Akt1 exerts vascular protection against atherogenesis, in part, through the action of eNOS[12].

Considering the link between PI3K/Akt and eNOS, eNOS signaling is necessary for maintaining the integrity of the lung vasculature after exposure to mechanical ventilation. Given that PI3K/Akt *in vivo* roles and the interactions with other signaling are not yet explicitly defined, we investigated the expression of phospho-Akt on the lungs of both $eNOS^{-/-}$ and WT mice after 4 h HV_T MV. As shown in Figure 5, there was a lower level of phosphorylated-Akt detected at the residue of serine 473 respond to both LV_T and HV_T MV in $eNOS^{-/-}$ mice compared to WT mice. This may suggest a mechanism related to a vulnerability of $eNOS^{-/-}$ mice in response to mechanical stress. In addition, these data may suggest a possible feedback role of eNOS deficiency on Akt activation.

Chen and colleagues reported a modest decrease in the basal levels of active eNOS in endothelial cells isolated from $Akt1^{-/-}$ mice when compared to wild-type mice[7]. Interestingly, our experimental data demonstrated that deletion of the eNOS gene could decrease the activation of Akt both at the physiological condition and when the animal responds to high tidal volume mechanical stretch.

The direct role of Akt in the maintenance of vascular permeability was further supported by our observation that pretreatment with Wort, a pharmacological inhibitor of PI3K, significantly worsened EBD lung accumulation in WT mice induced by 4 h HV_T MV (Figure 6). In addition, H&E staining and neutrophil immunostaining in the lungs showed an enhanced interstitial and alveolar infiltration of neutrophils in WT mice pretreated with Wort and exposed to 4 h HV_T MV compared with vehicle (Figures 7A, 7B). These findings indicate that phospho-Akt plays an essential role in modulating eNOS-regulated vascular permeability and suggest an upstream regulatory role of PI3K/Akt on eNOS in our model.

Cross-talk between p38 MAPK and PI3K/Akt/eNOS

In recent years, the emerging evidence has triggered the interests on the crosstalk between PI3K/Akt and MAPKs signalings[18, 19, 36, 37]. The important reason for elucidating the interplay of the PI3K/Akt and p38 MAPK pathways is that the former pathway is the best-characterized survival-related system and the latter is a death-associated signaling pathway[13]. Many studies have suggested a close relationship between NOS/NO expression and p38 phosphorylation[17, 38, 39]. Data from our study shows that inhibition of p38 MAPK by SB203580 increased the activation of Akt in response to HV_T MV and decreased the lung edema. Our recently published work demonstrated that inhibition of the p38 MAP kinase pathway prevents EBD extravasations and water retention in mice lungs in response to high tidal volume mechanical ventilation[22]. Thus, in this study, we mainly focused on the signaling pathway PI3K/Akt /eNOS using Wort on EBD and wet/dry ratio observations instead of inhibition of both pathways. Furthermore, given the awareness that phosphorylation of Akt triggered by HV_T MV has resolved by 4 h ventilation and the evidence of the severe lung edema and injury at this time point, we observed the interaction between the two signals by applying the PI3K inhibitor, Wort, to evaluate p38 MAPK change. The PI3K inhibitor, Wort, potentiated phosphorylation of p38 MAPK in response to mechanical stretch, suggesting a possible mechanism of modulation between parallel signaling pathways at this time point[40]. Based on the results we published before that the peak of phosphorylated P38 MAPK expression is around 60 min before it returns back during the 2 h HV_T MV and the lung injuries were seen at either 2 h or 4 h HV_T MV, we believe that the suppressed protective pathway of PI3K/Akt/eNOS in the 4 h HV_T MV was mediated by up-regulation of p38 MAPK. Thus, maintaining a normal level of PI3K/Akt/eNOS may negate the p38 MAPK role attributed to VALI.

Our results are in agreement with the report that PI3-kinase/Akt signaling promotes endothelial cell survival by inhibiting p38 MAPK-dependent apoptosis, because Akt may cause MEKK3 phosphorylation, an upstream regulator of p38 MAPK. The phosphorylated form of MEKK3 decreases MEKK3 kinase activity leading to down-regulation of MKK3/6 and p38 MAPK activation[21].

Therefore, we conclude that protection of capillary leakage was associated with activation of Akt and attenuation of p38 MAPK expression. In addition, eNOS deficient mice were prone to HV_T MV-mediated injury. The crosstalk between the two signaling pathways shown above may govern the differential effects of PI3K/Akt/eNOS and p38 MAPK on vascular barrier function in our experimental setting. The finding that PI3K/Akt/eNOS has a critical role in maintaining the integrity of vasculature through inhibition of p38 MAPK deepens our insight and has potential therapeutic implications.

Acknowledgements

This work was supported by grants from American Heart Association (Mid-Atlantic, Beginning Grant-in-Aid #0765286U), American Lung Association of Maryland (Biomedical Research Grant, 2006) and the National Heart, Lung and Blood Institute (NIH R01 HL049441; P50 HL 73994).

The authors thank Drs Hunter C CHAMPION, Allan CHESLEY and Michael T CROW for helpful consultation and technical assistance. We thank CPT Gleeson MURPHY and Ms Cindy A KRONMAN for critical reading.

Finally, I give heartfelt love and gratitude to my father, Mr Yun-xiang PENG, for his unconditional love and support on my effort to get funding for this work.

Author contribution

Xin-qi PENG is responsible for the overall administration and direction of the project,who contributed to the design, conducting, data assessment, and the publication of the results for this study; Jun-tian ZHANG contributed to the conducting and the publication of the work; Mahendra DAMARLA and Stephanie NONAS helped with the project funding and provided comments as well as assisted in the interpretation of the research; Jarrett SKIRBALL, Emile J HASAN, Xuan CAO and Adel BOUEIZ helped on performing the research; Eugenia J HAN helped on the writing for the project funding and performed the research; Xuan CAO, Xiao-ying WANG, Dana R ANDERSON and Alfred M SCIUTO helped on the paper writing; Rubin M TUDER helped on reviewing the results of the morphology and immuno-histochemistry; Rachel DAMICO provided comments on this study; David A KASS, Joe GN GARCIA and Alfred M SCIUTO contributed as consultants on this study; Paul M HASSOUN provided part of funding for this study and assisted the first author in interpretation of the data as well as contributed as a consultant.

References

1 Ware LB, Matthay MA. The acute respiratory distress syndrome. N Engl J Med 2000; 342: 1334–49.

2 Peng X, Hassoun PM, Sammani S, McVerry BJ, Burne MJ, Rabb H, *et al*. Protective effects of sphingosine 1-phosphate in murine endotoxin-induced inflammatory lung injury. Am J Respir Crit Care Med 2004; 169: 1245–51.

3 Miyahara T, Hamanaka K, Weber DS, Drake DA, Anghelescu M, Parker JC. Phosphoinositide 3-kinase, Src, and Akt modulate acute ventilation-induced vascular permeability increases in mouse lungs. Am J Physiol Lung Cell Mol Physiol 2007; 293: L11–21.

4 Dimmeler S, Fleming I, Fisslthaler B, Hermann C, Busse R, Zeiher AM. Activation of nitric oxide synthase in endothelial cells by Akt-dependent phosphorylation. Nature 1999; 399: 601–5.

5 Go YM, Boo YC, Park H, Maland MC, Patel R, Pritchard KA Jr, *et al*. Protein kinase B/Akt activates c-Jun NH2-terminal kinase by increasing NO production in response to shear stress. J Appl Physiol 2001; 91: 1574–81.

6 Iwakiri Y, Tsai MH, McCabe TJ, Gratton JP, Fulton D, Groszmann RJ, *et al*. Phosphorylation of eNOS initiates excessive NO production in early phases of portal hypertension. Am J Physiol Heart Circ Physiol 2002; 282: H2084–90.

7 Chen J, Somanath PR, Razorenova O, Chen WS, Hay N, Bornstein P, *et al*. Akt1 regulates pathological angiogenesis, vascular maturation and permeability *in vivo*. Nat Med 2005; 11: 1188–96.

8 Yu J, deMuinck ED, Zhuang Z, Drinane M, Kauser K, Rubanyi GM, *et al*. Endothelial nitric oxide synthase is critical for ischemic remodeling, mural cell recruitment, and blood flow reserve. Proc Natl Acad Sci USA 2005; 102: 10999–1004.

9 Peng X, Abdulnour RE, Sammani S, Ma SF, Han EJ, Hasan EJ, *et al*. Inducible nitric oxide synthase contributes to ventilator-induced lung injury. Am J Respir Crit Care Med 2005; 172: 470–9.

10 Abdulnour RE, Peng X, Finigan JH, Han EJ, Hasan EJ, Birukov KG, *et al*. Mechanical stress activates xanthine oxidoreductase through MAP kinase-dependent pathways. Am J Physiol Lung Cell Mol Physiol 2006; 291: L345–53.

11 Dimmeler S, Zeiher AM. Nitric oxide-an endothelial cell survival factor. Cell Death Differ 1999; 6: 964–8.

12 Fernández-Hernando C, Ackah E, Yu J, Suárez Y, Murata T, Iwakiri Y, *et al*. Loss of Akt1 leads to severe atherosclerosis and occlusive coronary artery disease. Cell Metab 2007; 6: 446–57.

13 Ackah E, Yu J, Zoellner S, Iwakiri Y, Skurk C, Shibata R, *et al*. Akt1/protein kinase Balpha is critical for ischemic and VEGF-mediated angiogenesis. J Clin Invest 2005; 115: 2119–27.

14 Kim HJ, Lee HS, Chong YH, Kang JL. p38 Mitogen-activated protein kinase up-regulates LPS-induced NF-kappaB activation in the development of lung injury and RAW 264.7 macrophages. Toxicology 2006; 225: 36–47.

15 Morrell ED, Tsai BM, Wang M, Crisostomo PR, Meldrum DR. p38 mitogen-activated protein kinase mediates the sustained phase of hypoxic pulmonary vasoconstriction and plays a role in phase I vasodilation. J Surg Res 2006; 134: 335–41.

16 Lee ER, Kim JY, Kang YJ, Ahn JY, Kim JH, Kim BW, *et al*. Interplay between PI3K/Akt and MAPK signaling pathways in DNA-damaging drug-induced apoptosis. Biochim Biophys Acta 2006; 1763: 958–68.

17 Xing F, Jiang Y, Liu J, Zhao K, Mo Y, Liu Z, *et al*. Downregulation of

human endothelial nitric oxide synthase promoter activity by p38 mitogen-activated protein kinase activation. Biochem Cell Biol 2006; 84: 780–8.

18 Kristof AS, Fielhaber J, Triantafillopoulos A, Nemoto S, Moss J. Phosphatidylinositol 3-kinase-dependent suppression of the human inducible nitric-oxide synthase promoter is mediated by FKHRL1. J Biol Chem 2006; 281: 23958–68.

19 Liagre B, Leger DY, Vergne-Salle P, Beneytout JL. MAP kinase subtypes and Akt regulate diosgenin-induced apoptosis of rheumatoid synovial cells in association with COX-2 expression and prostanoid production. Int J Mol Med 2007; 19: 113–22.

20 Peng X, Damarla M, Damico R, Hasan H, Boueiz A, Pae HH, *et al*. Protective role of PI3-kinase/akt signaling in mechanical stress through inhibition of p38 mitogen-activated protein kinase signaling. Am J Respir Crit Care Med 2008; 177(Abstracts issue): A760.

21 Gratton JP, Morales-Ruiz M, Kureishi Y, Fulton D, Walsh K, Sessa WC. Akt down-regulation of p38 signaling provides a novel mechanism of vascular endothelial growth factor-mediated cytoprotection in endothelial cells. J Biol Chem 2001; 276: 30359–65.

22 Damarla M, Hasan E, Boueiz A, Le A, Pae HH, Montouchet C, *et al*. Mitogen activated protein kinase activated protein kinase 2 regulates actin polymerization and vascular leak in ventilator associated lung injury. PLoS One 2009; 4: e4600.

23 Le A, Damico R, Damarla M, Boueiz A, Pae HH, Skirball J, *et al*. Alveolar cell apoptosis is dependent on p38 MAP kinase-mediated activation of xanthine oxidoreductase in ventilator-induced lung injury. J Appl Physiol 2008; 105: 1282–90.

24 Green TP, Johnson DE, Marchessault RP, Gatto CW. Transvascular flux and tissue accrual of Evans blue: effects of endotoxin and histamine. J Lab Clin Med 1988; 111: 173–83.

25 Rossner W, Tempel K. Quantitative determination of the permeability of the so-called blood-brain barrier of Evans blue (T 1824). Med Pharmacol Exp Int J Exp Med 1966; 14: 169–82.

26 Becker PM, Kazi AA, Wadgaonkar R, Pearse DB, Kwiatkowski D, Garcia JG. Pulmonary vascular permeability and ischemic injury in gelsolin-deficient mice. Am J Respir Cell Mol Biol 2003; 28: 478–84.

27 Peng X, Haldar S, Deshpande S, Irani K, Kass DA. Wall stiffness suppresses Akt/eNOS and cytoprotection in pulse-perfused endothelium. Hypertension 2003; 41: 378–81.

28 Yamashita T, Kawashima S, Ohashi Y, Ozaki M, Ueyama T, Ishida T, *et al*. Resistance to endotoxin shock in transgenic mice overexpressing endothelial nitric oxide synthase. Circulation 2000; 101: 931–7.

29 Takenaka K, Nishimura Y, Nishiuma T, Sakashita A, Yamashita T, Kobayashi K, *et al*. Ventilator-induced lung injury is reduced in transgenic mice that overexpress endothelial nitric oxide synthase. Am J Physiol Lung Cell Mol Physiol 2006; 290: L1078–86.

30 Emanueli C, Monopoli A, Kraenkel N, Meloni M, Gadau S, Campesi I, *et al*. Nitropravastatin stimulates reparative neovascularisation and improves recovery from limb Ischaemia in type-1 diabetic mice. Br J Pharmacol 2007; 150: 873–82.

31 Vincent PA, Kreienberg PB, Minnear FL, Saba TM, Bell DR. Simultaneous measurement of fluid and protein permeability in isolated rabbit lungs during edema. J Appl Physiol 1992; 73: 2440–7.

32 Ehrhart IC, Hofman WF. Pressure-dependent increase in lung vascular permeability to water but not protein. J Appl Physiol 1992; 72: 211–8.

33 Draijer R, Atsma DE, van der Laarse A, van Hinsbergh VW. cGMP and nitric oxide modulate thrombin-induced endothelial permeability. Regulation via different pathways in human aortic and umbilical vein endothelial cells. Circ Res 1995; 76: 199–208.

34 Wong D, Dorovini-Zis K, Vincent SR. Cytokines, nitric oxide, and cGMP modulate the permeability of an in vitro model of the human blood-brain barrier. Exp Neurol 2004; 190: 446–55.

35 Predescu D, Predescu S, Shimizu J, Miyawaki-Shimizu K, Malik AB. Constitutive eNOS-derived nitric oxide is a determinant of endothelial junctional integrity. Am J Physiol Lung Cell Mol Physiol 2005; 289: L371–81.

36 Lee ER, Kim JY, Kang YJ, Ahn JY, Kim JH, Kim BW, *et al*. Interplay between PI3K/Akt and MAPK signaling pathways in DNA-damaging drug-induced apoptosis. Biochim Biophys Acta 2006; 1763: 958–68.

37 Xing F, Jiang Y, Liu J, Zhao K, Mo Y, Liu Z, *et al*. Downregulation of human endothelial nitric oxide synthase promoter activity by p38 mitogen-activated protein kinase activation. Biochem Cell Biol 2006; 84: 780–8.

38 Gao X, Wang H, Sairenji T. Inhibition of Epstein-Barr virus (EBV) reactivation by short interfering RNAs targeting p38 mitogen-activated protein kinase or c-myc in EBV-positive epithelial cells. J Virol 2004; 78: 11798–806.

39 Brahmbhatt S, Gupta A, Sharma AC. Bigendothelin-1 (1–21) fragment during early sepsis modulates tau, p38-MAPK phosphorylation and nitric oxide synthase activation. Mol Cell Biochem 2005; 271: 225–37.

40 Lv GF, Chen B, Zhang WF, Wang YC, Zhu XX, Hu DH. Study on crosstalk between phosphatidylinositol 3-kinase/Akt pathway and p38 mitogen-activated protein kinase pathway in cardiomyocyte with challenge of burn serum. Zhonghua Shao Shang Za Zhi 2008; 24: 263–7.

npg
Acta Pharmacologica Sinica (2010) 31: 184–190
© 2010 CPS and SIMM All rights reserved 1671-4083/10 $32.00
www.nature.com/aps

Original Article

SLC22A2 gene 808 G/T variant is related to plasma lactate concentration in Chinese type 2 diabetics treated with metformin

Qing LI, Fang LIU*, Tai-shan ZHENG, Jun-ling TANG, Hui-juan LU, Wei-ping JIA

Department of Endocrinology and Metabolism, Shanghai Jiaotong University affiliated Sixth People's Hospital; Shanghai Clinical Center of Diabetes, Shanghai Institute for Diabetes, Shanghai Key Laboratory of Diabetes, Shanghai 200233, China

Aim: To investigate the potential relationship between the *SLC22A2* gene polymorphism and blood lactate concentration in Shanghai Hans suffering from type 2 diabetes mellitus (T2DM).
Methods: The *SLC22A2* single nucleotide polymorphism (SNP) 808G/T was genotyped in 400 T2DM patients, including a metformin-treated group (n=200) and a non-metformin-treated group (n=200). Fasting plasma lactic acid levels were measured with an enzyme-electrode assay. Biochemical indexes, including plasma alanine aminotransferase (ALT), creatinine (Cr), and glycolated hemoglobin (HbA1c), were also measured.
Results: The fasting plasma lactate concentration in the metformin-treated group was significantly higher than that in the non-metformin-treated group (1.29±0.45 mmol/L *vs* 1.18±0.44 mmol/L, P=0.015). Additionally, the ratio of patients with hyperlactacidemia was 8% (16/200) for the metformin-treated group and 5.5% (11/200) for the non-metformin-treated group, with no lactic acidosis found in either group. The frequency of the SLC22A2 808G/T T allele was 12.9%. Patients with the mutant genotype (TT) had a higher blood lactate concentration in the metformin-treated group than those in the non-metformin-treated group (t=2.492, P=0.013). This trend was not observed in the GG and GT genotypes when compared with metformin-treated and non-metformin-treated groups. Patients with the mutant genotype (TT) in the metformin-treated group also had a higher incidence of hyperlactacidemia compared with the GG genotype (40.0% *vs* 6.9%, P=0.050) in the metformin-treated group and the GG (6.0%, P=0.042) or GT (4.3%, P=0.043) genotypes in the non-metformin-treated group. In the metformin-treated group, there were significant gender differences in lactate concentrations in the TT (2.18±0.15 *vs* 1.04±0.27 mmol/L, P=0.008) and GG genotypes (1.40±0.51 *vs* 1.19±0.35 mmol/L, P=0.004). The lactate levels of women with the TT genotype were the highest in the metformin-treated group, but differences in lactate levels among the genotypes were not observed in the non-metformin-treated group.
Conclusion: There is an 808G/T polymorphism in the *SLC22A2* gene in Chinese Hans with T2DM. The 808G>T variance in the *SLC22A2* gene can affect the plasma lactate level and the incidence of hyperlactacidemia in T2DM patients undergoing metformin therapy. Additionally, the female patients carrying the TT genotype are prone to lactatemia.

Keywords: ASP-PCR; metformin; *SLC22A2* gene; organic cation transporter 2; lactate; single nucleotide polymorphism; type 2 diabetes mellitus

Acta Pharmacologica Sinica (2010) 31: 184–190; doi: 10.1038/aps.2009.189

Introduction

Metformin is one of the most commonly used drugs for the treatment of type 2 diabetes mellitus (T2DM). It also has beneficial effects in cardiovascular disease, impaired glucose tolerance and polycystic ovary syndrome through an insulin-sensitizing effect[1]. However, metformin therapy is characterized by considerable inter-individual variability in clinical efficacy[2]. Some studies have shown that metformin is not metabolized but is transported by at least two organic cation transporters (OCTs), OCT1 and OCT2[3, 4]. The human OCT1 transporter (*SLC22A1*) is primarily expressed in the liver and is not detected in the kidney. Furthermore, OCT2 (*SLC22A2*) has been found to be the most abundant organic cation transporter in the basolateral membranes of human kidney[5, 6]. A kinetic analysis of metformin transport and its distribution in rats suggested that metformin is a superior substrate for renal OCT2 rather than hepatic OCT1, and renal OCT2 plays a dominant role in metformin pharmacokinetics[4]. In addition, OCT2 is responsible for the observed gender differences in

---

* To whom correspondence should be addressed.
E-mail liufangstar@163.com
Received 2009-08-27 Accepted 2009-12-04

renal basolateral membrane organic cation transporting activity[7–9]; however, to date no studies related to human OCT2 and its relevance to metformin-treatment in diabetic populations have been reported.

Genetic factors have been estimated to account for 64% to 94% of individual variations in renal clearance of various drugs, including metformin, amoxicillin, and ampicillin[10]. In Chinese people in particular, genetic factors have been shown to account for up to 75% of the inter-individual variability in drug disposition and its effects[11]. The existence of genetic polymorphisms in the human OCT2 gene has been previously reported in some populations. A total of 28 genetic variations in the OCT2 gene have been identified in non-Asian American populations, as reported by Leabman. Among those variants, three non-synonymous SNPs (T199I, T201M, and A270S) in the SLC22A2 gene decreased the renal clearance of metformin compared to the reference genotype [12]. The non-synonymous SNP, 808G>T (Ala270Ser), was found to be present in 13.3% of individuals from a healthy population of Chinese from Hong Kong. Subjects who are homozygous for 808G>T tend to have higher plasma exposure to metformin, and this can be further enhanced in elderly patients or those with renal dysfunction [13]; however, other variations in the OCT2 gene were rare (less than 3%) in the Chinese population. Thus, the variant that is the most likely to be related to metformin sensitivity and plasma lactate in Chinese Hans with T2DM may be the 808G/T transversion in the SLC22A2 gene.

Serum lactate level is a balance between its synthesis and elimination. Lactate, which is produced in the gut, liver, and peripheral tissues, such as erythrocytes and the skin, is utilized to form glucose in the liver[14]. The portion of lactate that is not metabolized is excreted almost completely in the urine by the kidney. Two possible mechanisms for raised lactate levels due to metformin have been proposed: 1) increases in glycolytic lactate production in peripheral tissues[15] and 2) inhibition of lactate metabolism/transport in the liver and other tissues such as heart and muscle. Wang DS reported that the plasma lactate concentrations of metformin-treated wild-type mice were 2.5-fold greater than that in metformin-treated OCT (-/-) mice[16]. However, prospective large-scale studies in patients with diabetes still lack the necessary evaluation of the clinical relevance of the SLC22A2 genetic polymorphisms and their impact on the beneficial and adverse effects of metformin.

The allele-specific primer polymerase chain reaction (ASP-PCR) assay is a method used to determine SNPs based on DNA amplification, and the SNPs can be determined by whether the primers anneal to the target DNA[17, 18]. The present study was designed to determine SNPs at position 808 of the *SLC22A2* gene using ASP-PCR and to investigate the potential relationship between *SLC22A2* gene polymorphisms and blood lactate concentrations in Shanghai Hans with T2DM.

Materials and methods

Subjects

A total of 400 patients with T2DM [diagnosed according to 1999 World Health Organization (WHO) and American Diabetes Association standards] were enrolled in the study between April 2007 and October 2008 from the Shanghai Diabetes Center, including a group receiving metformin treatment (n=200) and another group with no metformin treatment (n=200). The patients had a male: female ratio of 200:200 and a median age of 60 years (range 35–77 years). All participants with predisposing conditions, such as congestive heart failure, renal insufficiency, chronic lung disease with hypoxia, history of alcohol use, or aged older than 80 years, were excluded from the study. These conditions were determined from their medical history, physical examination, electrocardiographic evaluation, and routine laboratory tests (blood chemistry evaluation, hematologic testing, and urinalysis). The patients did not take any medications other than hypoglycemic agents (sulfonylureas and glitazones) starting three days before being admitted to the hospital.

Measurement of plasma lactate concentrations and biochemical indexes

After taking metformin [500 mg three times daily (tid)] at least three days from the first day of admission to the hospital, blood samples from metformin-treated and non-metformin-treated groups were collected in the morning of the fourth day after an overnight fast and without any physical activity. The fasting venous plasma glucose (FPG), creatinine (Cr), urea nitrogen (BUN), alanine aminotransferase (ALT), and HbA1c were determined on the same morning with lactate. FPG was determined with the glucose oxidase method. Kidney and liver function was measured on an automatic analyzer (Hitachi 7180 biochemistry automatic analyzer, Japan). HbA1c was measured with a high-performance liquid chromatography (HPLC). Body mass index (BMI) was calculated by dividing body weight in kg divided by the square of the height in m. The glomerular filtration rate (GFR) was detected by a Technetium-99 isotope scan. The total GFR was calculated as the sum of the left and right kidneys. If GPT>60 U/L or Cr>110 μmol/L or GFR<60 mL/min, the patient was excluded from the study. A total of 400 patients satisfied the above criteria and were recruited into this study. Written informed consent was obtained from all subjects.

SNP determination (808G>T) in the *SLC22A2* gene using the ASP-PCR method

The genomic sequence of *SLC22A2* exon4 was obtained using the BLAST program(accession number: rs316019) (http://www.ncbi.nlm.nih.gov/SNP). The genotyping of the SNP (808G>T) of *SLC22A2* was performed using the ASP-PCR method according to previous reports[18]. The primer set (forward primer: 5′-AAAGGTTCTACCGTCCAA-3′; reverse primer for 808G: 5′-GTGGTTGCAGTTCACAGTAGC-3′; reverse primer for 808T: 5′-GGTGGTTCCAGTTCACAGTATC-3′) was designed to amplify a 359-bp and 360-bp portion of the *SLC22A2* gene encoding the SNP. ASP-PCR was carried out in 20 μL reaction volumes consisting of 2*reaction buffer, 4 mmol/L dNTPs, 15 pmol primer mixture, 2U *Taq*

DNA polymerase (5 U/μL), and 25 ng genomic DNA (20 ng/μL) (Sai Bai Sheng (sbs) gene company, Shanghai, China). The reaction mixtures were placed in an ABI 9700 thermal cycler (Applied Biosystems) that was programmed for touchdown PCR to improve the specificity of PCR amplification[19]. For this procedure, the annealing temperature was 57 °C for two PCR cycles and decreased by 1 °C per two cycles for the next 4 cycles until an optimal annealing temperature of 55 °C was reached. Then, there were 35 PCR cycles at the annealing temperature of 55 °C with a final extension at 72 °C for 10 min. PCR products were analyzed by electrophoresis on 3% agarose gels followed by ethidium bromide staining and inspection under UV light.

Direct sequencing of the *SLC22A2* gene in randomly selected individuals with and without the 808G/T mutation

To confirm the results of the ASP-PCR-based determination of the 808G>T SNP in the *SLC22A2* gene, exon4 of the *SLC22A2* gene, including site 808, was sequenced using DNA samples from randomly selected individuals diagnosed to be wt (wild-type), heterozygote or mutant homozygote.

Statistical analyses

All numerical values are expressed as the mean±SD, and the count data are expressed as percentages. The Hardy-Weinberg equilibrium was tested by SHEsis. The plasma lactate concentration between different groups and different genders of the three genotypes was compared by factorial design variance analysis. The blood lactate concentration of the three genotypes was compared by one-way analysis of variance (ANOVA) followed by Fisher's exact test to find statistically significant differences in the frequency of genotypes of *SLC22A2* (808G>T) between the two groups. Whether Cr, ALT, or GFR values and plasma lactate concentration differed among genders and groups was tested using Student's *t* test or Chi-square test. Finally, the incidence of hyperlactacidemia in different genotypes was compared using Fisher's exact test. All analyses were performed with SPSS software (version 16.0; SPSS, Chicago, Illinois, USA). All *P*-values were two-sided and a *P* value of <0.05 was considered significant.

Results

Identification of organic cation transporter 2 genetic polymorphisms

The results of ASP-PCR showed that there were three genotypes of the *SLC22A2* gene at position 808: GG (*n*=308), GT (*n*=81) and TT (*n*=11) in 400 T2DM patients of Chinese Hans (Table 1 and Figure 1), and this was confirmed by direct sequencing (Figure 2A−2C). The gene distributions were consistent with Hardy-Weinberg equilibrium in all of the groups. In short, the frequencies of the GT genotype and the TT genotype in all patients were 20.2% and 2.8%, respectively, and the T allele frequency was 12.9%.

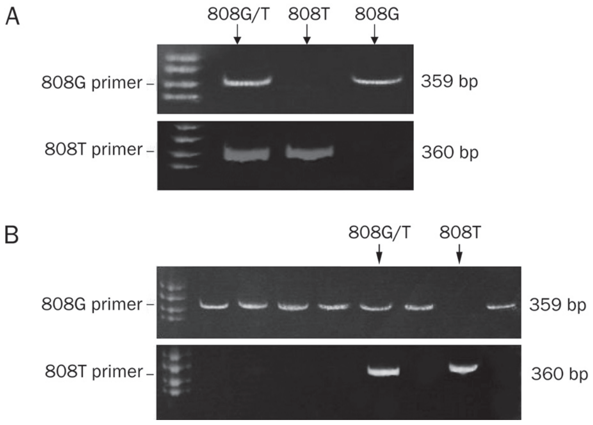

Figure 1. Representative patterns of electrophoresis of allele specific primer-polymerase chain reaction (ASP-PCR) products with different primers for determination of 808G/T genotypes of the *SLC22A2* gene. When the PCR products were observed in the lanes of 808G primers and no PCR products were observed in lanes for 808T primers (359 bp and 360 bp, respectively) , the strain was diagnosed as wild-type (wt) (A). When the PCR products were observed in the lanes of 808G and 808T primers (359 bp and 360 bp, respectively), the strain was considered as heterozygote (A). When the PCR products were observed in the lanes of 808T and no PCR products were observed in lanes for 808G primers, the strain was diagnosed as mutant homozygotes. (B) Applying the clear genotype of 8 samples as control for each test.

The general biochemical characteristics in different genotypes of the two groups

Table 2 shows the clinical characteristics of patients (*n*=400) in this study. The patients with the TT genotype in the metformin-treated group (*n*=200) had significantly lower HbA1c compared to the GG or GT genotypes in the metformin-treated group (*P*=0.022 and *P*=0.033, respectively). There were no differences in age, BMI, duration of diabetes, FPG and BUN,

Table 1. The numbers and frequencies of three genotypes and alleles in groups with and without metformin therapy.

Exon	Subjects	Metformin (*n*=200)		Non-metfromin (*n*=200)		Total (*n*=400)	
		Genotypes *n* (%)	Allele *n* (%)	Genotypes *n* (%)	Allele *n* (%)	Genotypes *n* (%)	Allele *n* (%)
Exon4	808G/T	GG 160 (80)	G 355 (88.7)	GG 148 (74)	G 342 (85.5)	GG 308 (77)	G 697 (87.1)
		GT 35 (17.5)	T 45 (11.3)	GT 46 (23)	T 58 (14.5)	GT 81 (20.2)	T 103 (12.9)
		TT 5 (2.5)		TT 6 (3)		TT 11 (2.8)	

Hardy-Weinberg balance test; Fisher's exact test, *P*=0.383 *vs* non-metformin group.

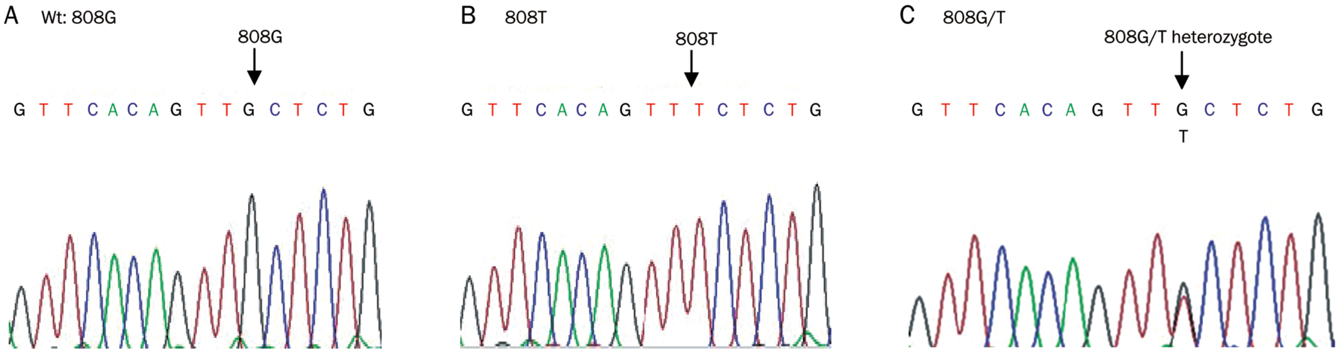

Figure 2. Direct sequence results of sense strands of *SLC22A2* genotypes of (A) wildtype (wt), (B) 808T, (C) 808G/T strains. In the strains with wt, the sense base at position 808 was G (A). In the strain with 808T mutation, the sense base at position 808 was T (B). In the strain with 808G/T, the sense bases at position 808 were G and T, respectively.

Cr, ALT, or GFR between different genotypes both in the metformin-treated and the non-metformin-treated groups ($P>0.05$; Table 2).

Plasma lactate concentration in different genotypes of the two groups

Of these 400 cases, the fasting plasma lactate concentration in the metformin-treated group (1.29±0.45 mmol/L) was higher than in the non-metformin-treated group (1.18±0.44 mmol/L, $P=0.015$), and the ratio of patients with hyperlactacidemia in the metformin-treated group was slightly higher than in the non-metformin-treated group (8% *vs* 5.5%, $P=0.58$), but no lactic acidosis was found in any of the patients. Figure 3 indicates that the patients in the metformin-treated group that carried the mutant homozygote genotype (TT) had higher lactate concentrations than patients in the non-metformin-treated group with the TT genotype ($P=0.013$); however, the difference in blood lactate concentration between the two groups with GG and GT genotypes was not significant ($P=0.053$, $P=0.344$,

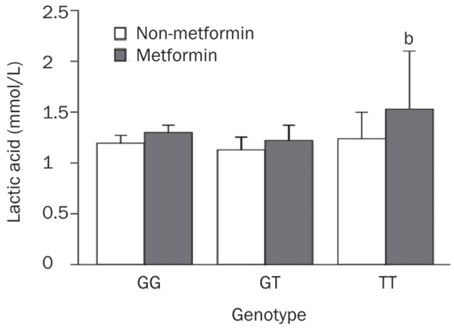

Figure 3. The plasma lactate levels of three genotypes in two groups with and without metformin treatment. By the method of analysis of variance of factorial design, there was no significant difference in the blood lactate levels of GG and GT genotypes in two groups ($P=0.053$, $P=0.344$). The plasma lactate level of metformin group carried TT genotype was higher obviously than that of non-metformin group with TT ($t=2.492$, $P=0.013$). Each column represents as mean±SEM. ${}^{b}P=0.013$, compared with non-metformin group with TT genotype.

Table 2. Comparison of the clinical characteristics and biochemical indexes between subjects with and without metformin treatment.

	Metformin group			Non-metformin group		
	GG	GT	TT	GG	GT	TT
N	160	35	5	148	46	6
Age	57.24±11.22	59.91±12.07	59.20±12.23	63.21±11.83	63.32±11.31	64.5±9.79
BMI	25.99±3.22	26.76±3.89	25.79±4.40	24.04±3.12	23.11±3.17	24.73±2.88
DUR	7.11±6.37	6.93±6.46	8.2±5.4	8.06±7.53	8.07±7.05	10.66±11.41
FPG	8.76±2.81	8.48±2.10	8.11±1.92	7.99±2.59	7.61±2.29	6.80±1.11
HbA1c	8.97±2.03	8.88±1.75	7.70±0.84^{be}	9.01±2.23	8.93±2.32	8.36±0.76
BUN	5.50±1.47	5.46±1.54	6.06±2.69	6.24±2.01	6.22±1.76	5.72±0.81
Cr	70.78±16.30	68.03±17.83	74.70±22.56	79.57±17.97	75.28±15.34	74.00±12.14
ALT	29.60±17.16	25.57±14.83	28.00±15.60	26.17±16.27	20.86±11.68	22.83±13.22
GFR	97.93±21.03	93.43±17.96	99.28±25.60	84.00±21.91	85.25±20.25	86.65±16.19

Data were expressed as mean±SD (range). Student's *t* test and Chi-square test were used. BMI: body mass index; DUR: duration after diabetes onset; FPG: fasting plasma glucose; HbA1c: glycosylated hemoglobin; BUN: urea nitrogen; Cr: creatinine; ALT: alanine transferase. GFR: glomerular filtration rate; ${}^{b}P=0.022$, ${}^{e}P=0.033$, compared to GG or GT genotype in metformin group.

respectively). Furthermore, the incidence of hyperlactacidemia among the three genotypes in both groups is shown in Table 3. The results reveal that patients carrying the TT genotype in the metformin-treated group had a higher incidence of hyperlactacidemia compared to patients with the GG genotype (40.0% *vs* 6.9%, *P*=0.050) in the metformin-treated group and with the GG (6.0%, *P*=0.042) or GT (4.3%, *P*=0.043) genotype in the non-metformin-treated group. In contrast, the difference in lactatemia in patients with the TT genotype between the two groups was not significant.

Gender differences in lactate concentrations

The ANOVA of factorial design indicated that the blood lactate concentration in women who carried the GG and TT genotype in the *SLC22A2* gene was significantly higher than that of men (*P*=0.001, *P*=0.025, respectively), but the difference in lactate concentrations in the GT genotype was not significant (*P*=0.529, Figure 4). In the metformin-treated group, the blood lactate concentration in women who carried the GG or TT genotypes in the *SLC22A2* gene was significantly higher than that of men (*P*=0.004, *P*=0.008, respectively) and that of women who carried the TT genotype was significantly higher than that of women with the GG or GT genotypes (*P*=0.045, *P*=0.041, respectively, Figure 5). However, the levels of plasma Cr in women were significantly lower than those in men (*P*=0.000). In the non-metformin-treated group, there was no significant relationship between lactate concentrations and any of the three genotypes.

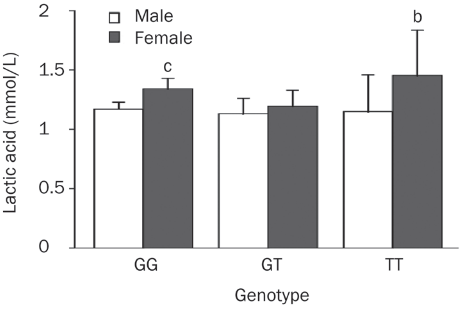

Figure 4. The plasma lactate levels of three genotypes in different genders. In 400 subjects, the blood lactate concentration in women carried GG and TT genotype of *SLC22A2* gene was higher significantly than that of men, and the difference of lactate concentration in GT genotype was no significance by the analysis of variance of factorial design. [b]*P*=0.025, [c]*P*=0.001, compared to lactate levels of males.

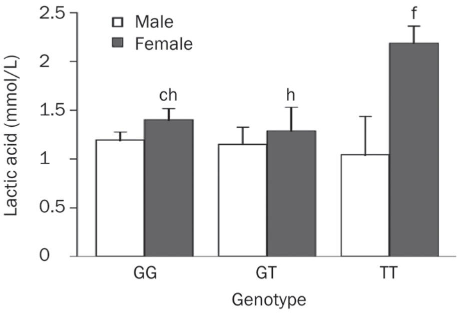

Figure 5. The plasma lactate levels of three genotypes between different genders in metformin group. The blood lactate concentration in women carried GG and TT genotype of *SLC22A2* gene was higher significantly than that of men. The blood lactate concentration in women carried TT genotype of *SLC22A2* gene was higher significantly than those with GG or GT genotypes. [c]*P*=0.004, [f]*P*=0.008, compared to lactate levels of males; [h]*P*<0.05 (*P*=0.045 for GG genotype, *P*=0.041 for GT genotype) compared to lactate levels of females with TT genotype.

Discussion

In the present study, the ASP-PCR method was performed to detect the 808G>T SNP in the *SLC22A2* gene, which encodes OCT2. By applying touchdown PCR conditions, better specificity was achieved, and the results were reliable. This analysis showed that there were three genotypes (GG, GT, and TT) at position 808 in the *SLC22A2* gene in Chinese Hans with T2DM. The genotype in the two groups and the total group were in accordance with Hardy-Weinberg equilibrium, and the T allele frequency was 12.9%, which was similar to the data in healthy populations from Hong Kong (13.3%), Japan (16.8%), and Korea (11%)[13, 20, 21].

This research further investigated the relationship between the SLC22A2 808G>T polymorphism and plasma lactate levels in these T2DM patients treated with or without metformin. The results reveal that the mean lactate level of patients with the mutant homozygote genotype (TT) was the highest in all groups, especially in patients treated with metformin; however, the HbA1c level was the lowest. In other words, the *SLC22A2* gene (808G>T) variation can affect the plasma lactic acid and HbA1c levels of T2DM patients receiving metformin

Table 3. The number of cases and the incidence of hyperlactacidemia of three genotyps in groups treated with or without metformin.

	Metformin (*n*=200)			Non-metformin (*n*=200)		
	GG *n* (%)	GT *n* (%)	TT *n* (%)	GG *n* (%)	GT *n* (%)	TT *n* (%)
hLA	11 (6.9%)	3 (8.6%)	2 (40%[beh])	9 (6.0%)	2 (4.3%)	0 (0%)
nLA	149 (93.1%)	32 (91.4%)	3 (60%)	139 (94.0%)	44 (95.7%)	6 (100%)

hLA: hyperlactacidemia, nLA: nomal lactate concentration. The lactate level higher than 1.96 mmol/L was defined as hyperlactacidemia. Fisher's exact test, [b]*P*=0.042, [e]*P*=0.043 compared to GG or GT genotype in non-metformin group; [h]*P*=0.05, compared with GG genotype in metformin group.

therapy. To date, a few studies examining the relevance of the 808G/T gene polymorphism and metformin pharmacokinetics have been reported, but studies about these polymorphisms and their association with blood lactate concentration are rare. The above-mentioned Hong Kong study in the general population demonstrated that the *SLC22A2* (808G>T) polymorphism influenced metformin metabolism *in vivo* and that the discharge of metformin was reduced in subjects with the TT genotype[14]. Similarly, the present study indicates that the incidence of lactatemia in T2DM patients carrying the TT genotype in the metformin-treated group increased and their HbA1c decreased significantly compared to the non-metformin-treated group. However, no marked difference was found in patients with the GG or GT genotypes. Thus, it is likely that a metformin concentration in the plasma clears more glucose, decreasing the level of HbA1c and increasing the plasma lactate level by inhibiting lactate metabolism in the liver. That is to say, *SLC22A2* gene (808G>T) polymorphisms increase the plasma lactate level by elevating the circulating concentration of metformin.

Earlier studies have demonstrated that OCT1-mediated hepatic uptake of guanides play an important role in lactic acidosis[16, 22]. However, an animal study revealed that metformin is a superior substrate for renal OCT2 rather than hepatic OCT1, and renal OCT2 plays the dominant role in metformin pharmacokinetics[4]. From the results of this study, we can infer that OCT2 also takes part in the occurrence of hyperlactacidemia. After administration of metformin, the OCT2 transporter of T2DM patients carrying allele T at position 808 of the *SLC22A2* gene could not bind with the drug and subsequently excrete the drug into the urine. This escalated the blood concentration of metformin, which caused the production of lactate. Therefore, this study proved the relevance of the *SLC22A2* 808 G/T polymorphism and the raised blood lactate concentration/hyperlactacidemia in the metformin-treated group and supplied a possible explanation for the decreased excretion of metformin. However, in this study, there were no obvious differences between patients with the GG and TT genotypes, which may be the result of the small sample size. Thus, it is necessary to expand the sample size to further prove these findings in the future.

The study additionally showed that compared to the non-metformin-treated group, there was a gender difference in plasma lactate levels. The plasma lactate concentrations in females were higher than in males with the same SLC22A2 808G/T genotype in the metformin-treated group, and women carrying the TT genotype had significantly higher plasma lactate levels than those with the GG or GT genotypes. Diabetic patients recruited in this study had normal liver and renal function. In addition, Cr, BUN, and ALT levels of women in the metformin-treated group were not higher, and their Cr levels were lower than in men. Thus, it is unlikely that abnormal liver production or renal excretion of lactate caused this result. Therefore, the gender differences in lactate levels are more likely related to the fundamental difference in sex hormone levels in males and females. Urakami demonstrated in rats that OCT2 is responsible for the gender differences in renal basolateral membrane OCT activity, and OCT2, but not OCT1, is sexually up-regulated by testosterone and down-regulated by estradiol in the kidney[8–10]. In our clinical study of 1021 patients with T2DM, we observed that blood lactate levels were due to gender differences, with females having significantly higher blood lactate levels than males treated with metformin (unpublished data). Until now, no related study has reported the relationship between OCT2 gene polymorphisms and gender. From the results of this study and previous animal experiments, we speculate that the gender differences in blood lactate concentration might be due to differential OCT2 expression in males and females. Specifically, the low expression of OCT2 in females may reduce the renal excretion of metformin, cause its accumulation, and induce a higher level of lactic acid. The in-depth mechanisms of metformin metabolism and excretion need to be confirmed by further studies. Even so, this study may have important clinical meaning for metformin therapy. Because of the relatively high frequency of G808T in the diabetic population, we can use ASP-PCR to rapidly detect the highest allele frequency (A270S) and predict the risk of lactatemia in patients carrying the T allele, especially in females with the TT genotype, which may prevent the occurrence of lactic acidosis.

Limitations of this study include the indirect measurement of blood metformin concentrations and the lack of control of other hypoglycemic agents in these patients. These may limit the significance of this study, and we cannot certify the speculation directly. Another limitation of the present research was small sample size, and therefore more studies with larger sample sizes should be done to further prove these findings.

In summary, our results demonstrate that there is an 808G/T polymorphism in the *SLC22A2* gene in Chinese Hans with T2DM. The 808G>T variance in the *SLC22A2* gene can increase plasma lactate levels and the incidence of hyperlactacidemia in T2DM patients undergoing metformin therapy. Female patients carrying the TT genotype are prone to lactatemia.

Acknowledgements

We thank the individuals who participated in the present study and Doctor Cheng HU for his excellent suggestions during the writing of this paper. This work was supported by grants from Shanghai Key Laboratory of Diabetes Mellitus (08DZ2230200) and the Shanghai Municipal Health Bureau (054012).

Author contribution

Fang LIU and Wei-ping JIA designed the research; Qing LI and Tai-shan ZHENG performed the research; Jun-ling TANG and Hui-juan LU contributed new analytical reagents and tools; Qing LI analyzed the data; Qing LI and Fang LIU wrote the paper.

References

1 Hundal RS, Inzucchi SE. Metformin: new understandings, new uses.

Drugs 2003; 63: 1879–94.

2 Hermann LS, Scherstén B, Bitzén PO, Kjellström T, Lindgärde F, Melander A. Therapeutic comparison of metformin and sulfonylurea, alone and in various combinations, a double- blind controlled study. Diabetes Care 1994; 17: 1100–9.

3 Dresser MJ, Xiao G, Leabman MK, Gray AT, Giacomini KM. Interactions of N-tetraalkylammonium compounds and biguanides with a human renal organic cation tranporter (hOCT2). Pharm Res 2002; 19: 1244–7.

4 Kimura N, Masuda S, Tanihara Y, Ueo H, Okuda M, Katsura T, Inui K, *et al*. Metformin is a superior substrate for renal organic cation tranporter OCT2 rather than hepatic OCT1. Drug Metab Pharmacokinet 2005; 20: 379–86.

5 Motohashi H, Sakurai Y, Saito H, Masuda S, Urakami Y, Goto M, *et al*. Gene expression levels and immunolocalization of organic ion transproters in the human kidney. J Am Soc Nephrol 2002; 13: 866–74.

6 Gorboulev V, Ulzheimer JC, Akhoundova A, Ulzheimer-Teuber I, Karbach U, Quester S, *et al*. Cloning and characterization of two human polyspecific organic cation transporters. DNA Cell Biol 1997; 16: 871–81.

7 Urakami Y, Nakamura N, Takahashi K, Okuda M, Saito H, Hashimoto Y, *et al*. Gender differences in expression of organic cation transporter OCT2 in rat kidney. FEBS Letters 1999; 461: 339–42.

8 Urakami Y, Okuda M, Saito H, Inui K. Hormonal regulation of organic cation transporter OCT2 expression in rat kidney. FEBS Letters 2000; 473: 173–6.

9 Asaka J, Terada T, Okuda M, Katsura T, Inui K. Androgen receptor is responsible for rat organic cation transporter 2 gene regulation but not for rOCT1 and rOCT3. Pharm Res 2006; 23: 697–704.

10 Leabman MK, Giacomini KM. Estimating the contribution of genes and environment to variation in renal drug clearance. Pharmacogenetics 2003; 13: 581–4.

11 Yin OQ, Tomlinson B, Chow M. Variability in renal clearance of substrates for renal transporters in Chinese subjects. J Clin Pharmacol 2006; 46: 157–63.

12 Leabman MK, Huang CC, Kawamoto M, Johns SJ, Stryke D, Ferrin TE, *et al*. Polymorphisms in a human kidney xenobiotic transporter, OCT2, exhibit altered function. Pharmacogenetics 2002; 12: 395–405.

13 Wang ZJ, Yin OQ, Tomlinson B, Chow MS. The polymorphisms and *in-vivo* renal functional consequence: studies with metformin and cimetidine. Pharmacogenet Genomics 2008; 18: 637–45.

14 Radziuk J, Pye S. Hepatic glucose uptake, gluconeogenesis and the regulation of glycogen synthesis. Diabetes Metab Res Rev 2001; 17: 250–72.

15 Borst SE, Snellen HG, Lai HL. Metformin treatment enhances insulin-stimulated glucose transport in skeletal muscle of Sprague-Dawley rats. Life Sci 2000; 67: 165–74.

16 Wang DS, Kusuhara H, Kato Y, Jonker JW, Schinkel AH, Sugiyama Y. Involvement of organic cation transporter 1 in the lactic acidosis caused by metformin. Mol Pharmacol 2003; 63: 844–8.

17 Nakamura A, Furuta T, Shirai N, Sugimoto M, Kajimura M, Soya Y, *et al*. Determination of mutations of the 23S rRNA gene of Helicobacter pylori by allele specific primer-polymerase chain reaction method. J Gastroenterol Hepatol 2007; 22: 1057–63.

18 Ishiguro A, Kubota T, Soya Y, Sasaki H, Yagyu O, Takarada Y, *et al*. High-throughput detection of multiple genetic polymorphisms influencing drug metabolism with mismatch primers in allele-specific polymerase chain reaction. Anal Biochem 2005; 337: 256–61.

19 Korbie DJ, Mattick JS. Touchdown PCR for increased specificity and sensitivity in PCR amplification. Nat Protoc 2008; 3: 1452–6.

20 Fukushima-Uesaka H, Maekawa K, Ozawa S, Komamura K, Ueno K, Shibakawa M, *et al*. Fourteen novel single nucleotide polymorphisms in the SLC22A2 gene encoding human organic cation transporter (OCT2). Drug Metab Pharmacokinet 2004; 19: 239–44.

21 Kang HJ, Song IS, Shin HJ, Kim WY, Lee CH, Shim JC, *et al*. Identification and functional characterization of genetic variants of human organic cation transporters in a Korean population. Drug Metab Dispositon 2007; 35: 667–75.

22 Hayer-Zillgen M, Brüss M, Bönisch H. Expression and pharmacological profile of the human organic cation transporters hOCT1, hOCT2 and hOCT3. Br J Pharmacol 2002; 136: 829–36.

Acta Pharmacologica Sinica (2010) 31: 191–201
© 2010 CPS and SIMM All rights reserved 1671-4083/10 $32.00
www.nature.com/aps

Original Article

Immunomodulatory activity of andrographolide on macrophage activation and specific antibody response

Wei WANG[1,2,#], Jing WANG[2,#], Sheng-fu DONG[2], Chun-hong LIU[2], Paola ITALIANI[3], Shu-hui SUN[2], Jing XU[4], Diana BORASCHI[3], Shi-ping MA[1,*], Di QU[2,*]

[1]Department of Pharmacology of Chinese Materia Medica, China Pharmaceutical University, Nanjing 210038, China; [2]Key Laboratory of Medical Molecular Virology of Ministries of Education and Health, Institute of Medical Microbiology and Institutes of Biomedical Sciences, Shanghai Medical College of Fudan University, Shanghai 200032, China; [3]Laboratory of Cytokines, Unit of Immunobiology, Institute of Biomedical Technologies, National Research Council, Pisa 56124, Italy; [4]Beijing Institute of Biological Products, Beijing 100024, China

Aim: To investigate the immunomodulatory effects of andrographolide on both innate and adaptive immune responses.
Methods: Andrographolide (10 μg/mL *in vitro* or 1 mg/kg *in vivo*) was used to modulate LPS-induced classical activated (M1) or IL-4-induced alternative activated (M2) macrophages *in vitro* and humor immune response to HBsAg *in vivo*. Cytokine gene expression profile (M1 *vs* M2) was measured by real-time PCR, IL-12/IL-10 level was detected by ELISA, and surface antigen expression was evaluated by flow cytometry, whereas phosphorylation level of ERK 1/2 and AKT was determined by Western blot. The level of anti-HBs antibodies in HBsAg immunized mice was detected by ELISA, and the number of HBsAg specific IL-4-producing splenocyte was enumerated by ELISPOT.
Results: Andrographolide treatment *in vitro* attenuated either LPS or IL-4 induced macrophage activation, inhibited both M1 and M2 cytokines expression and decreased IL-12/IL-10 ratio (the ratio of M1/M2 polarization). Andrographolide down-regulated the expression of mannose receptor (CD206) in IL-4 induced macrophages and major histocompability complex/costimulatory molecules (MHC I, CD40, CD80, CD86) in LPS-induced macrophages. Correspondingly, anti-HBs antibody production and the number of IL-4-producing splenocytes were reduced by *in vivo* administration of andrographolide. Reduced phosphorylation levels of ERK1/2 and AKT were observed in macrophages treated with andrographolide.
Conclusion: Andrographolide can modulate the innate and adaptive immune responses by regulating macrophage phenotypic polarization and Ag-specific antibody production. MAPK and PI3K signaling pathways may participate in the mechanisms of andrographolide regulating macrophage activation and polarization.

Keywords: macrophages; cytokines; antibodies; immunomodulator; andrographolide

Acta Pharmacologica Sinica (2010) 31: 191–201; doi: 10.1038/aps.2009.205

Introduction

Andrographis paniculata is an herb used in Chinese traditional medicine as recorded in Chinese Pharmacopoeia[1], and a common remedy for anti-infection treatment[2]. Andrographolide, a bicyclic diterpenoid lactone, 3-[2-[decahydro-6-hydroxy-5-(hydroxylmethyl)-5,8a-dimethyl-2-methylene-1-napthalenyl] ethylidene]-dihydro-4-hydroxy-2(3*H*)-furanone, is the major active constituent and has various pharmacological effects, including anti-inflammation[3], anti-tumor[4], antidiabetic[5] and cardioprotective activities[6]. In clinic, andrographolide has being applied as an anti-inflammatory remedy for upper respiratory tract infection and bacterial dysentery. Andrographolide was reported to have immunoregulatory activities. In tumor-bearing mice it enhanced natural killer cell activity[7], increased secretion of IL-2 and IFN-γ by T cells and thereby inhibited the tumor growth[8]. In autoimmune encephalomyelitis mice it interfered with maturation of dendritic cells[9], induced antigen-specific tolerance and thus prevented detrimental autoimmune responses[10]. It suggests that androgra-

---

[#] These two authors contributed equally to this work.
[*] To whom correspondence should be addressed.
E-mail dqu@shmu.edu.cn (Di QU)
spma@cpu.edu.cn (Shi-ping MA)
Received 2009-06-29 Accepted 2009-12-24

pholide can have different effects in different immune disease models, playing a role as a modulator of altered immune responses rather than a sole immunostimulatory or immunosuppressive agent. Considering that macrophages are widely distributed immune cells that play an indispensable role in homeostasis and defense, we investigated the immunomodulatory effect of andrographolide on the alteration of macrophage phenotype and function.

Macrophages can be activated and phenotypically polarized by different stimuli and microenvironment[11]. In general, activated and polarized macrophages can be broadly classified into two main groups: classically activated inflammatory macrophages (M1), which produce large amount of inflammatory cytokines like TNF-α, IL-1β, IL-6, IL-12, IL-18, and IL-23; and alternatively activated macrophages (M2) that produce other cytokines as IL-10, IL-1Ra, and IL-18BP[12]. M1 participate in polarized Th1 responses as inducers and effectors, while M2 support Th2-associated effects and functions[13]. Macrophages exhibit phenotypic plasticity to control immunological balance in the microenvironment[14]. However, the immunomodulatory effect of andrographolide on the alteration of macrophage phenotype has not been investigated. We studied how andrographolide altered macrophage phenotype in naïve and LPS/IL-4 activated macrophages by comparing the expression of activation-relevant M1 *vs* M2 cytokines.

Macrophages not only serve as the primary defense barrier in the innate immune response, but also act as important accessory cells in the adaptive immune response[15]. Activated macrophages phagocytose antigens by pattern recognition receptors (such as mannose receptor)[16], and provided signals to mediate T cells activation. One signal is the major histocompatibility antigen complex binding to T cell receptor (TCR), the other is the interaction of co-stimulatory molecules with their respective ligands on T cells[17]. We observed effects of andrographolide on the antigen uptake and presenting capacity of macrophages by measuring mannose receptor (CD206), MHC I/II and co-stimulatory molecules (CD40, CD80, CD86) on naïve and LPS/IL-4 activated macrophages. In addition, yeast-derived recombinant HBsAg (vaccine qualified) was used as an antigen to induce Ag-specific antibody in a Th2/M2-dependent mouse model of adaptive responses[18, 19], and effects of andrographolide on humor immune responses were evaluated by the levels of serum antibodies and the number of IL-4 producing splenocytes.

Studies on the signal transduction mechanism of macrophage activation have indicated that stimuli, such as LPS or IL-4, trigger the mitogenactivated protein kinase (MAPK) and phosphoinositol-3-kinase (PI3K) signaling pathways[20, 21]. MAPK pathway positively regulated the expression of pro-inflammatory cytokines (TNF-α, IL-1β, IL-6 *etc*), whereas PI3K pathway conversely inhibits MAPK pathway activation and induced anti-inflammatory cytokines (IL-10 *etc*)[22, 23]. To investigate the mechanisms of andrographolide regulating macrophage activation and polarization, the effects of andrographolide on phosphorylation level of ERK 1/2 (MAPK pathway) and AKT (PI3K pathway) were analyzed.

Materials and methods

Reagents

Andrographolide was kindly provided by Chong Yuan Biology Science Co, Ltd (Nanjing, China), and it was dissolved in dimethyl sulfoxide (Sigma-Aldrich, St Louis, MO, USA) at 10 mg/mL as a stock solution. LPS from *E coli* strain 055:B5 was purchased from Sigma-Aldrich. Recombinant murine IL-4 and IL-13 were purchased from Pepro Tech Inc (Rocky Hill, NJ, USA). Human hepatitis B surface antigen (yeast-derived recombinant HBsAg, vaccine qualified) was kindly provided by Beijing Institute of Biological Products (Beijing, China). Fluorochrome-labeled monoclonal antibodies to surface antigens on murine macrophages were purchased from eBioscience (San Diego, CA, USA). Antibodies against phospho-ERK, ERK, phospho-AKT, AKT and β-actin were purchased from Cell Signal Technology (Beverly, MA, USA).

Endotoxin detection

Contamination of endotoxin in andrographolide was assessed by the Limulus Amoebocyte Lysate (LAL) colorimetric assay (QCL-1000® Endpoint LAL Assay; Lonza, Walkersville, MD, USA), according to the manufacturer's instructions. The absorbance at 405 nm is linear in the concentration range of 0.1–1.0 EU/mL endotoxin. The endotoxin concentration in diluted andrographolide was calculated with the absorbance from the standard curve by linear regression.

Peritoneal macrophage isolation

Primary mouse peritoneal macrophages were obtained from C57BL/6 mice (SPF, aged 6–8 weeks, SIPPR-BK Experimental Animal Ltd Co, Shanghai, China) 4 days after intraperitoneal injection of 1.5 mL 3% Brewer thioglycollate medium (Kang Run Biology Science Co Ltd, Shanghai, China). Peritoneal exudate cells were harvested from the peritoneal cavity of mice by lavage, washed with ice-cold RPMI-1640 medium (Invitrogen, Carlsbad, CA, USA) containing 1% fetal bovine serum (FBS; Invitrogen), resuspended in pre-warmed RPMI-1640 containing 10% FBS and supplemented with 100 mg/L streptomycin and 10^5 U/L penicillin (Invitrogen), and distributed in wells of the BD Falcon™ culture plates (BD Biosciences, San Jose, CA, USA). Macrophages were allowed to adhere for 2–3 h at 37 °C in humidified atmosphere containing 5% CO_2, and non-adherent cells were removed by washing twice with PBS. Cell number and viability was assessed using trypan blue exclusion under microscope. Thioglycollate-treated mice will yield about 10^7 peritoneal macrophages per mouse. Pooled macrophages were cultured and treated with andrographolide (10 μg/mL) and/or LPS/IL-4 (100 ng/mL). The purity of isolated mouse peritoneal macrophages pooled from five mice was greater than 95%, as determined by staining with fluorescein isothiocyanate (FITC)-conjugated anti-mouse F4/80 and flow cytometric analysis.

Macrophage viability

Macrophage viability was assessed by the mitochondria-dependent reduction of MTT, 3-(4,5-dimethyl-thiazol-2-yl)-2,5-

diphenyltetrazolium bromide (Amresco, Solon, Ohio, USA) to formazan. In 96-well plates, 2×10^4 cells/well were treated with andrographolide and/or LPS/IL-4 for 24 h, then MTT solution was added to a final concentration of 0.5 g/L and further incubated for 4 h at 37 °C, 5% CO_2. The culture medium was dumped off and 200 μL DMSO was added to resuspend formazan into the solvent. The absorbance was measured at the test wavelength of 570 nm (670 nm as the reference wavelength) by the DTX Series Multimode Detectors (Beckman, Fullerton, CA, USA), and the percentage of viable cells was calculated versus untreated cell control.

Macrophage cytokine gene expression

Cytokine gene transcription of mouse peritoneal macrophages was measured by reverse transcription and real-time PCR. In 6-well plates, 4×10^6 cells/well were treated with andrographolide and/or LPS/IL-4 for 4 h or 24 h. Total RNA was extracted using TRIzol reagent (Invitrogen) according to the manufacture's instruction, and treated with RNase-free DNase-I (Takara, Otsu, Shiga, Japan) for removal of potentially contaminating DNA. First-strand cDNA was synthesized from 2 μg total RNA with random hexamer primer (Takara) and M-MLV reverse transcriptase (RT) (Promega, Madison, WI, USA) for 30 min at 37 °C. PCR amplification was performed using ABI PRISM® 7500 real time PCR system (Applied Biosystems, Foster City, CA, USA), and reactions were carried out with SYBR® Premix Ex Taq™ (2×mixture) (Takara) and specific primers for mouse cytokines according to the sequences in GenBank (Table 1). Primers were designed using Beacon Designer 6.0 (PREMIER Biosoft International, Palo Alto, CA, USA) and synthesized by Sangon Biology Science Co, Ltd (Shanghai, China). Amplification conditions were: (1) 95 °C/10 s, 1 cycle, for hot-start; (2) 95 °C/5 s, 60 °C/34 s, 40 cycles, for PCR and data collection; (3) dissociation stage: 0.1 °C/ s from 60 to 95 °C, for melting curve analysis. Relative quantification of gene expression in treatment groups *vs* control (freshly isolated cells before culture) was calculated using the comparative threshold cycle method $2\^[(Ct_{GAPDH}-Ct_{Gene})_{treatment}-(Ct_{GAPDH}-Ct_{Gene})_{control}]$ where GAPDH is the housekeeping gene[24].

Table 1. Primer sequences for detecting mouse cytokine mRNA expression.

Cytokine	Accession number (mRNA)	Primer sequence (5'→3')
TNF-α	NM_013693	f: GTG GAA CTG GCA GAA GAG r: CCA TAG AAC TGA TGA GAG G
IL-1β	NM_008361	f: TGG GAA ACA ACA GTG GTC AG r: CCA TCA GAG GCA AGG AGG A
IL-1Ra	NM_031167	f: ACA GTA GAA GGA GAC AGA AG r: GGT GGT AGA GCA GAA GAC
IL-6	NM_031168	f: TGC CTT CTT GGG ACT GAT G r: ACT CTG GCT TTG TCT TTC TTG T
IL-10	NM_010548	f: GAA GAC CCT CAG GAT GCG r: CCA AGG AGT TGT TTC CGT TA
IL-12	NM_008352	f: AGA TGA AGG AGA CAG AGG AG r: GCA CGA GGA ATT GTA ATA GC
IL-18	NM_008360	f: GAC TCT TGC GTC AAC TTC r: GAT CAA TAT CAG TCA TAT CCT C
IL-18BP	NM_010531	f: ACT TCT CCT GTT TGT TTG TG r: TCT GGA TAC TGG GCT GTG
GAPDH	NM_008084	f: GGT GAA GGT CGG TGT GAA CG r: CTC GCT CCT GGA AGA TGG TG

f: forward primer; r: reverse primer.

Macrophage cytokine production

Mouse peritoneal macrophages (4×10^6 cells/well in 6-well plate) were treated with andrographolide and/or LPS/IL-4/IL-13 for 48 h. Culture supernatants were collected, IL-12p40 and IL-10 concentrations were determined using specific ELISA kits (eBioscience), according to the manufacturer's instructions.

Macrophage surface antigen expression

Flow cytometry was used to determine the surface antigen expression (F4/80, MHC-I, MHC-II, CD40, CD80, CD86, and CD206) in mouse peritoneal macrophages. Briefly, 4×10^6 cells/well in 6-well plates treated with andrographolide and/or LPS/IL-4 for 24 h were stained with fluorochrome-labeled mAbs (30 min on ice), washed with FACScan buffer (PBS containing 2% FBS and 0.1% Sodium Azide), and fixed with 4% paraformaldehyde. Flow cytometry acquisition was performed on FACScan® flow cytometer and data were analyzed using CellQuest™ software (BD Biosciences). The percentage of cells positive for each surface protein was determined based upon isotype control staining, and the amount of surface antigen expression of all cells counted was calculated by the following equation:

Expression Index (EI)=% positive cells×Mean Fluorescence Intensity[25].

Mice immunization and andrographolide administration

Inbred female BALB/c mice (SPF, aged 6–8 weeks) were purchased from SIPPR-BK Lab Animal Co, Ltd (Shanghai, China) and housed under pathogen-free conditions. All animal studies were performed in accordance to national and international laws and policies. Mice were grouped as indicated in the experiments described below, each group consisting of 6 mice. Two groups of mice were immunized intramuscularly twice over a 4-week period with HBsAg alone (1 μg/mouse) or followed by intraperitoneal administration of andrographolide ($1\ mg\cdot kg^{-1}\cdot d^{-1}$, 7 d). Another group of mice received HBsAg admixed with $Al(OH)_3$ adjuvant [1 μg HBsAg+50 μg $Al(OH)_3$/mouse] as a positive control. Naïve mice were used as a negative control.

Detection of anti-HBsAg antibodies

Sera were collected from the retroorbital plexuses of individual mice at 2, 4, and 6 weeks after the first HBsAg immunization. Anti-HBsAg antibodies were detected by anti-HBs ELISA kit (Diagnostic Reagent Center of Shanghai Municipal

Infectious Diseases Hospital, Shanghai, China) according to the manufacturer's instruction. Each serum was diluted by serial threefold dilution and incubated in a 96-well plate precoated with HBsAg for 1 h at 37 °C. Plates were washed and horseradish peroxidase (HRP)-conjugated goat anti-mouse IgG (Huamei Bioengineering Co, Ltd, Shanghai) was added and further incubated for 1 h at 37 °C. After washing, the substrate (tetramethyl benzidine) was added and incubated for 15 min at 37 °C. The absorbance was measured at 450 nm with the reference wavelength of 630 nm in a 96-well plate spectrophotometer. Antibody titers are presented as the reciprocal of the highest dilution showing a positive reaction.

Detection of IL-4-producing splenocytes

After mice were sacrificed at 6 week after the first HBsAg immunization, spleens were removed and dissociated on 200-gauge nylon mesh. Splenocytes were treated with lysis buffer (0.15 mol/L NH_4Cl, 0.01 mol/L $KHCO_3$, 0.1 mol/L Na_2EDTA, pH 7.4) at room temperature for 1.5 min to lyse red cells, washed with RPMI-1640 and resuspended in RPMI-1640 with 10% FBS. IL-4-producing cells in spleens from immunized mice were detected by the enzyme-linked immunospot (ELISPOT) assay. Briefly, 96-well multiscreen filtration plates (Millipore, Billerica, MA, USA) were coated with anti-mouse IL-4 capture antibody (5 μg/mL; BD Biosciences) overnight and blocked with culture medium for 1.5 h. Spleen cells (5×10^5) were added to wells and stimulated with 0.5 μg/mL HBsAg at 37 °C for 48 h. Plates were washed, and biotinylated anti-mouse IL-4 detection antibodies (2 μg/mL) were added and incubated for 2 h at room temperature. After washing, streptavidin–HRP was added and incubated for 1 h at room temperature, and 3-amino-9-ethylcarbazole was used as substrate. Spots were developed for about 30 min and the reaction was stopped by washing with deionized water. Spots were enumerated manually by inspection under a dissecting microscope, and automatically using an ImmunoSpot Analyzer-BioReader 4000 Pro-X (BIO-SYS GmbH, Karben, Germany).

Detection of ERK 1/2 and AKT phosphorylation

The phosphorylation level of ERK 1/2 and AKT proteins in mouse peritoneal macrophages was measured by Western blot assay. Briefly, in 6-well plates, 4×10^6 cells/well were treated with andrographolide and/or LPS/IL-4/IL-13 for 2 h or 12 h. After washing with PBS, cells were lyzed in the lysis buffer (20 mmol/L Tris, pH 7.5, 150 mmol/L NaCl, 1 mmol/L Na_2EDTA, 2.5 mmol/L sodium pyrophosphate, 1% Triton X-100, 1 mmol/L β-glycerophosphate, 1 mmol/L Na_3VO_4, 1 μg/mL Leupeptin, 1 mmol/L PMSF) on ice and centrifuged (14000×*g*, 5 min, 4 °C). The lysate of cells (mixed with 5×protein loading buffer and boiled for 5 min at 100 °C) were analyzed by 12% SDS-PAGE, transferred to PVDF membrane (Millipore, Bedford, MA, USA) and blocked with 5% nonfat milk in TBST buffer (20 mmol/L Tris, pH 8.0, 150 mmol/L NaCl and 0.1% Tween-20) for 2 h at room temperature. The membranes were incubated with the primary antibody overnight at 4 °C, then with a horseradish peroxidase-conjugated secondary antibody 1 h at room temperature, and detected by enhanced chemiluminescence kit (Thermo scientific, Waltham, MA, USA) according to the manufacturer's instructions. Protein molecular weight was estimated by Prestained Protein Ladder (Fermentas, Glen Burnie, MD, USA). For repeated immunoblotting, membranes were incubated in the stripping buffer (62.5 mmol/L Tris, pH 6.7, 20% SDS and 100 mmol/L 2-mercaptoethanol) for 30 min at 50 °C.

Statistical analysis

Experimental data obtained were analyzed with the SPSS software. Variance between groups was analyzed by ANOVA, means of groups were compared by *t*-test. Differences with $P<0.05$ were considered statistically significant.

Results

Endotoxin contamination of the andrographolide preparation

The presence of endotoxin contamination in the preparations of test molecules is a major source of false results, in particular in assays on macrophages which are exquisitely sensitive to endotoxin stimulation. Thus, the presence of endotoxin in the andrographolide preparation was checked, by using a quantitative chromogenic LAL assay. Three concentrations of andrographolide were assayed (10, 50, and 100 μg/mL). At each of these concentrations the endotoxin contamination was below the detection limit of the assay (0.1 EU/mL). To make sure that andrographolide did not interfere with the enzymatic reaction at the basis of endotoxin detection, or with the optical reading of the yellow color developed by liberation of para-nitroaniline, the reaction developed by known concentration of standard LPS (0.5 EU/mL) was compared with that developed by LPS in the presence of andrographolide. Addition of andrographolide does not affect in any way the detection of standard endotoxin, as shown in Figure 1.

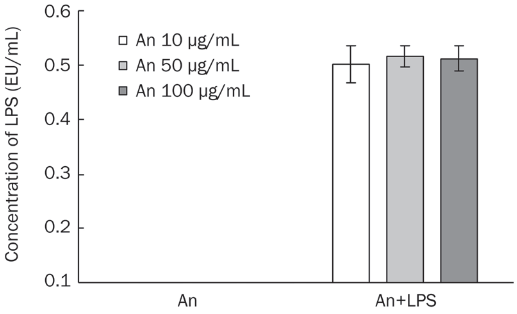

Figure 1. No endotoxin contamination in preparation of andrographolide (An). The An batch used for the experimental procedures was assessed at different concentrations (10−100 μg/mL) for endotoxin contamination (left part of the figure). As control of possible interference of An with the endotoxin-induced reaction, an dilutions were added to a fixed concentration of LPS (0.5 EU/mL) and tested in the LAL assay (right part of the figure). The lower detection limit of the assay is 0.1 EU/mL. Endotoxin was not detected in An alone, and An did not inhibit detection of 0.5 EU/mL of standard LPS.

Effects of andrographolide on murine macrophages viability

The *in vitro* toxicity of andrographolide and/or LPS or IL-4 on mouse peritoneal macrophages was assessed by MTT assay. At the concentration of 2.5–10 μg/mL, andrographolide did not affect the viability of macrophages, but at the concentration of 40 μg/mL, cell viability was inhibited by 50% versus the control (Figure 2). Therefore, the concentration of 10 μg/mL was used for *in vitro* studies on macrophages.

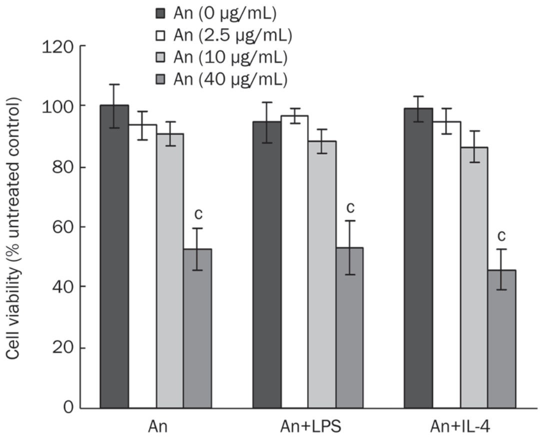

Figure 2. Effects of andrographolide (An) on macrophage viability. Mouse peritoneal macrophages (2×10^4 cells/well, 96-well plate) were incubated for 24 h with different concentrations of An (0–40 μg/mL) alone or together with LPS or IL-4 (both at 100 ng/mL). Cell viability was determined using the MTT method, as described. Values are the mean±SD of eight replicate wells from one experiment, representative of three performed. $^cP<0.01$ *vs* no treatment control.

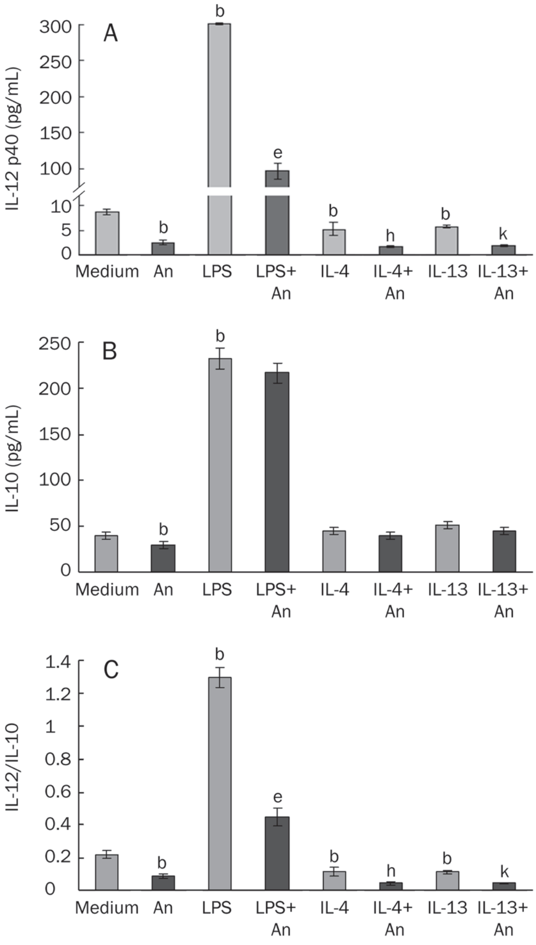

Figure 3. Effects of andrographolide (An) on IL-12 and IL-10 productions. Mouse peritoneal macrophages were incubated with An (10 μg/mL) alone or together with LPS, IL-4, or IL-13 (100 ng/mL) for 48 h. IL-12 (A) and IL-10 (B) concentration in the supernatant were detected by ELISA, and the ratio of IL-12/IL-10 was calculated (C). Values are the mean±SD of three replicate wells from one experiment, representative of three performed. $^bP<0.05$ *vs* no treatment control; $^eP<0.05$ *vs* LPS treatment control; $^hP<0.05$ *vs* IL-4 treatment control; $^kP<0.05$ *vs* IL-13 treatment control.

Effects of andrographolide on cytokine expression in naive murine macrophages

The effect of andrographolide on naive murine macrophage activation was evaluated by measuring expression of M1/M2 cytokine with quantitative real-time RT-PCR and ELISA assay (for IL-12 and IL-10). TNF-α, IL-12, IL-1β, IL-18, and IL-6 mRNA were measured as M1-related inflammatory cytokines, while IL-10, IL-1Ra, and IL-18BP were assessed as M2 activation cytokines. Treated with andrographolide for 24 h, the mRNA level of both M1 and M2 cytokines in macrophages was decreased as compared to untreated cells: TNF-α, 25% of control; IL-12, 5%; IL-1β, 33%; IL-10, 35%; IL-1Ra, 25% (Table 2). The results of M1/ M2 cytokine genes transcription were confirmed by IL-12 and IL-10 cytokine productions detected by ELISA, as shown in Figure 3.

Effects of andrographolide on cytokine expression in LPS/IL-4 activated murine macrophages

Murine macrophages were activated by LPS or IL-4 for M1 or M2 polarization. In LPS-activated macrophages, transcription of the cytokine genes detected as above was increased after 4 h of stimulation, while induced cytokine expression was partially restored upon longer stimulation time (24 h). In contrast, the expression of the M1 cytokine (TNF-α) was decreased and that of the M2 cytokine (IL-10) was increased in IL-4-activated macrophages (Table 2).

The effect of andrographolide on LPS/IL-4 activated murine macrophages was evaluated by measuring expression of activation relevant cytokines. When andrographolide was added along with LPS or IL-4, it down-regulated expression of both M1 and M2 cytokines in activated macrophages, shown in Table 2.

It is important to note that the most important parameters for discriminating between M1 and M2 polarization are the relative levels of IL-12 *vs* IL-10 expression. M1 macrophages typically express high level of IL-12 and low level of IL-10, and M2 cells vice versa. Thus, the IL-12/IL-10 ratio has been calculated for untreated macrophages (0.488 at 4 and 0.789 at 24 h), for cells treated with LPS (31.0 at 4 h and 9.02 at 24 h,

Table 2. The effects of andrographolide (An) on cytokine mRNA expression level in naive and activated macrophages.

Stimulation time		Cytokines detected	Mean (range) values of cytokine mRNA expression ratio (cultured *vs* fresh cells) Medium	An	LPS	LPS+An	IL-4	IL-4+An
4 h	M1	TNF-α	1.02	**0.245↓**	**112↑**	**35.9↓**[a]	**0.461↓**	**0.169↓**[b]
			(0.92–1.1)	(0.22–0.27)	(106–118)	(30–43)	(0.44–0.48)	(0.15–0.19)
		IL-12	0.398	0.321	**1450↑**	**197↓**[a]	0.266	0.265
			(0.35–0.45)	(0.21–0.49)	(1310–1590)	(142–273)	(0.22–0.33)	(0.19–0.36)
		IL-1β	0.293	0.277	**789↑**	**115↓**[a]	0.318	**0.128** [b]
			(0.26–0.32)	(0.22–0.35)	(750–829)	(76.8–173)	(0.28–0.36)	(0.10–0.16)
		IL-18	0.985	0.769	**5.98↑**	**2.50↓**[a]	0.75	0.65
			(0.87–1.1)	(0.68–0.87)	(5.6–6.4)	(2.0–3.1)	(0.65–0.84)	(0.57–0.72)
		IL-6	0.418	0.300	**2097↑**	**413↓**[a]	**0.958↑**	**0.488↓**[b]
			(0.37–0.47)	(0.24–0.37)	(1880–2330)	(307–556)	(0.85–1.1)	(0.36–0.58)
	M2	IL-10	0.815	0.572	**46.7↑**	**18.3↓**[a]	**4.55↑**	**2.00↓**[b]
			(0.67–0.99)	(0.43–0.74)	(43–51)	(13–26)	(4.1–5.1)	(1.7–2.3)
		IL-1Ra	1.13	0.867	**9.15↑**	**4.50↓**[a]	0.828	0.712
			(1.0–1.2)	(0.73–1.02)	(8.6–9.9)	(3.8–4.9)	(0.80–0.85)	(0.57–0.89)
		IL-18BP	1.25	1.67	**7.00↑**	8.79	1.57	1.94
			(1.1–1.4)	(1.5–1.9)	(6.7–7.3)	(6.2–13)	(1.4–1.8)	(1.6–2.2)
Ratio IL-12/IL-10			0.488	0.561	**31.0**	**10.8**	**0.059**	**0.135**
IL-1β/IL-1Ra			0.257	0.322	**86.2**	**25.6**	0.386	0.366
IL-18/IL-18BP			0.792	0.461	0.854	**0.284**	0.478	0.335
24 h	M1	TNF-α	0.847	**0.211↓**	**2.92↑**	4.34	0.734	**0.183↓**[b]
			(0.74–0.94)	(0.20–0.22)	(2.3–3.8)	(3.8–4.9)	(0.67–0.80)	(0.17–0.20)
		IL-12	0.557	**0.029↓**	**7.85↑**	**1.83↓**[a]	0.807	**0.087↓**[b]
			(0.36–0.84)	(0.01–0.08)	(5.7–11)	(1.7–2.0)	(0.67-1.0)	(0.08–0.10)
		IL-1β	0.06	**0.019↓**	**5.31↑**	**0.526↓**[a]	0.10	0.020↓[b]
			(0.05–0.08)	(0.018–0.020)	(3.7–7.6)	(0.47–0.59)	(0.09–0.1)	(0.016–0.025)
		IL-18	1.09	0.573	0.630	0.492	0.804	0.734
			(0.93–1.3)	(0.50–0.66)	(0.47–0.85)	(0.46–0.53)	(0.73–0.89)	(0.69–0.79)
		IL-6	0.144	0.31	**2.77↑**	**1.03↓**[a]	**1.55↑**	**0.621↓**[b]
			(0.12–0.18)	(0.28–0.34)	(2.1–3.6)	(0.92–1.1)	(1.4–1.7)	(0.58–0.66)
	M2	IL-10	0.708	**0.248↓**	0.870	**0.385↓**[a]	**2.53↑**	**0.804↓**[b]
			(0.62–0.81)	(0.19–0.31)	(0.67-1.1)	(0.38–0.41)	(2.4–2.6)	(0.68–0.94)
		IL-1Ra	1.62	**0.396↓**	2.81	**0.865↓**[a]	1.77	**0.226↓**[b]
			(1.4–1.9)	(0.39–0.42)	(2.2–3.6)	(0.81–0.92)	(1.6–1.9)	(0.19–0.26)
		IL-18BP	2.23	1.89	**19.2↑**	10.6	**5.16↑**	4.16
			(1.9–2.6)	(1.8–2.0)	(15–25)	(9.7–12)	(5.0–5.3)	(3.8–4.6)
Ratio IL-12/IL-10			0.789	**0.120**	**9.02**	**4.69**	**0.320**	**0.113**
IL-1β/IL-1Ra			0.037	0.050	**1.89**	**0.608**	0.056	0.087
IL-18/IL-18BP			0.489	0.302	0.033	0.046	**0.155**	0.175

Data are shown in the table as $2^{-\Delta\Delta Ct_{mean}}$ [$2^{-(\Delta\Delta Ct+SD)}$, $2^{-(\Delta\Delta Ct-SD)}$], $\Delta\Delta Ct=(Ct_{Gene}-Ct_{GAPDH})_{treatment}-(Ct_{Gene}-Ct_{GAPDH})_{control}$.
Data in bold are those with >2-fold difference. ↑up-regulation (>2-fold increase *vs* medium control), ↓down-regulation (>2-fold decrease *vs* medium control),
↓[a] down-regulation (>2-fold decrease *vs* LPS-treated control), ↓[b] down-regulation (>2-fold decrease *vs* IL-4-treated control).

indicating strong M1 polarization), and for IL-4-treated cells (0.059 and 0.320 at 4 and 24 h *ie* distinctly M2). Treatment with andrographolide could polarize M2 direction in the control cells after 24 h of exposure (IL-12/IL-10 ratio from 0.789 to 0.120), strongly decrease M1 polarization of LPS-treated cells (from 31.0 to 10.8) at 4 h, and further increase M2 phenotype in IL-4 treated cells (from 0.320 to 0.113) (Table 2). The results of M1/M2 cytokine genes transcription were confirmed by IL-12 and IL-10 cytokine productions detected by ELISA, as shown in Figure 3.

Effects of andrographolide on surface antigen expression in murine macrophages

To evaluate the effect of andrographolide on the antigen uptake and presenting capacity of macrophages, modulation of mannose receptor (CD206), MHC class I/II and co-stimulating molecules (CD40, CD80, CD86) was assessed by flow cytometry in naïve macrophages or cells activated with LPS or IL-4 in the presence or in the absence of andrographolide.

When murine macrophages were treated by andrographolide alone, the expression of MHC-I (EI 24.9) was down-regulated comparing with basal antigen expression in naïve macrophages (MHC-I: 47.5; MHC-II: 0.157; CD40: 9.86; CD80: 9.90; CD86: 3.57; CD206: 4.25). Activation with LPS increased the expression of MHC-I (189), CD40 (60.3), CD80 (18.3) and CD86 (10.8). However, activation with IL-4 increased the expression of CD40 (17.4) and CD206 (19.7), as shown in Figure 4.

When andrographolide was added along with LPS, it down-regulated the LPS-induced increase of MHC-I (from 189 to 103), CD40 (from 60.3 to 27.1), CD80 (from 18.3 to 6.94) and CD86 (from 10.8 to 4.23). Andrographolide treatment along with IL-4 down-regulated IL-4-induced expression of CD40

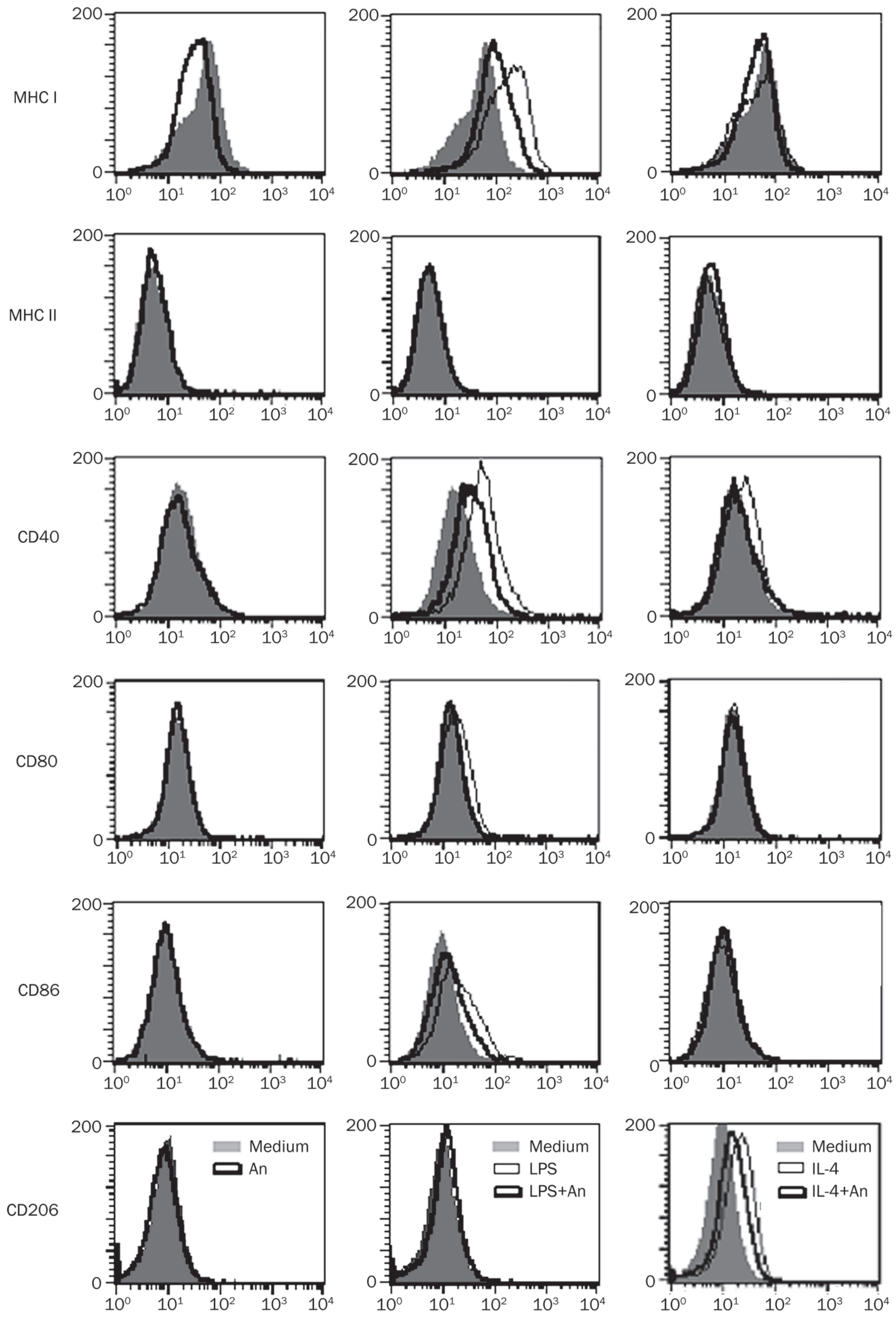

Figure 4. Effect of andrographolide (An) on macrophage surface antigen expression. Macrophages (4×10^6 cells/well, 6-well plate) were incubated for 24 h with An (10 μg/mL) alone or together with LPS or IL-4 (both at 100 ng/mL). Expression of surface antigens was tested by flow cytometric analysis, as described. Data were analysed by CellQuest^{TM} software. Data from one experiment representative of three performed.

(from 17.4 to 14.2) and CD206 (from 19.7 to 11.6), as shown in Figure 4.

Effects of andrographolide on specific antibody response

To determine whether andrographolide can regulate the adaptive immune response *in vivo*, its effect on specific antibody response was tested in mice vaccinated with HBsAg. Mice were primed intramuscularly with HBsAg (1 μg/mouse), and andrographolide was administered intraperitoneally for 7 consecutive days starting from the day of priming. After 4 weeks the mice were boosted with the same dose of HBsAg. Mice immunized with HBsAg plus alum was used as control. Anti-HBsAg antibody titers were determined at 2 and 4 weeks after priming, and 2 weeks after boosting (*ie*, 6 weeks after priming). Treatment of andrographolide resulted in decreased anti-HBs titers at all time tested (Figure 5A). At 2 weeks after boosting, splenocytes were isolated from immunized mice, stimulated *in vitro* with HBsAg (0.5 μg/mL), and IL-4-producing cells were measured by ELISPOT. The number of IL-4-producing cells in the spleen of HBsAg-immunized mice (23/10^6 spleen cells) was decreased by 40% in mice immunized with HBsAg plus andrographolide, while in mice immunized with HBsAg plus alum IL-4-producing cells increased about 2 fold (Figure 5B).

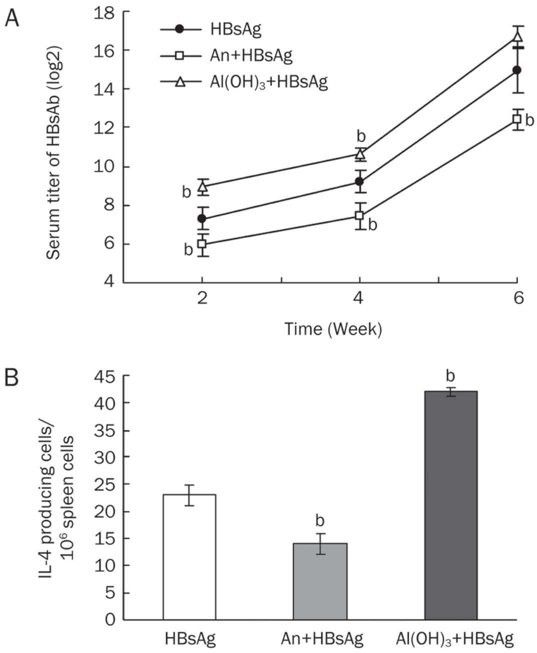

Figure 5. Andrographolide (An) inhibits serum anti-HBsAg antibody titers and reduces the numer of IL-4-producing cells. Mice were immunized with HBsAg as described. The first group received HBsAg alone (two administrations of 1 μg/mouse 4 weeks apart). The second group received HBsAg and repeated administrations of An (1 mg·kg^{-1}·d^{-1}, 7 d). The last group received HBsAg plus Al(OH)$_3$ adjuvant (50 μg/mouse). (A) Serum anti-HBsAg antibodies were measured by ELISA after 2, 4, and 6 weeks from the first antigen inoculum. Antibody titers are presented as the reciprocal of the highest dilution showing a positive reaction. (B) At 6 weeks (2 weeks after the second antigen inoculum) mice were sacrificed, spleen cells isolated and challenged in culture with HBsAg (0.5 μg/mL). The number of IL-4-producing cells/10^6 spleen cells was measured by mouse IL-4 ELISPOT. Data are presented as the mean±SD of values from 6 mice/group in one experiment, representative of three performed. $^b P<0.05$ *vs* the control group of HBsAg.

Effects of andrographolide on ERK 1/2 and AKT phosphorylation

As MAPK and PI3K signaling pathway are involved in the macrophage activation, the effects of andrographolide on phosphorylation level of ERK 1/2 (MAPK pathway) and AKT (PI3K pathway) were analyzed by Western blot assay in naïve macrophages or cells activated with LPS or IL-4/IL-13 in the presence or in the absence of andrographolide. Activation by LPS or IL-4/IL-13 increased ERK 1/2 and AKT phosphorylation. Treatment with andrographolide for 2 h exerted an apparent inhibitory effect on phosphorylation of ERK 1/2 and AKT in both M1 and M2 activated macrophages. However, this modulatory effect of andrographolide was reversed or restored after 12 h treatment (Figure 6, 7).

Discussion

Macrophages have remarkable heterogeneity and plasticity that allows them to efficiently respond to exogenous and endogenous signals by changing their functional phenotype[11, 14]. In this study, thioglycollate-elicited mouse peritoneal macrophage (F4/80$^+$ population)[26] have been used to investigate the immunomodulatory activities of andrographolide on the innate immune response *in vitro*. Our results indicated that andrographolide showed potent immunoregulatory properties in murine macrophages. Andrographolide reduced expression of inflammatory cytokines (TNF-α, IL-12, IL-1β, IL-18, and IL-6) in LPS activated macrophages, which is consistent with a previous report that andrographolide decreased TNF-α and IL-12 mRNA expression and cytokine production in murine peritoneal macrophages, although they did not detect IL-1β, IL-18, and IL-6[27].

The response of macrophages to the microenvironment changes is of key importance in the ability of the organism to cope with dangers (*eg* an infection). For example, at the acute stage of an infection, macrophages respond to microbial exogenous signals such as LPS (a structural component of Gram-negative bacteria) and produce pro-inflammatory cytokines (classical inflammatory activation). This reaction is important for the efficient control of growth and dissemination of invading pathogens. At later times, other signals such as the endogenous anti-inflammatory cytokine IL-4/IL-13 can re-direct macrophage activation into an alternative regulatory pathway (alternative M2 activation) that promotes the resolution of inflammation by reducing inflammatory cytokine production and inducing synthesis of anti-inflammatory and tissue repairing factors[12, 28]. We observed the phenomenon in this study that LPS induced a rapid and significant increase of cytokines gene transcription at the early time (4 h), which returns toward background at 24 h. On the other hand IL-4 did not up-regulate inflammatory cytokine expression but was able to induce expression of regulatory molecules IL-10 and IL-18BP also at the late time, and this tendency was also observed in IL-13 treated macrophages (Supplementary Table 1).

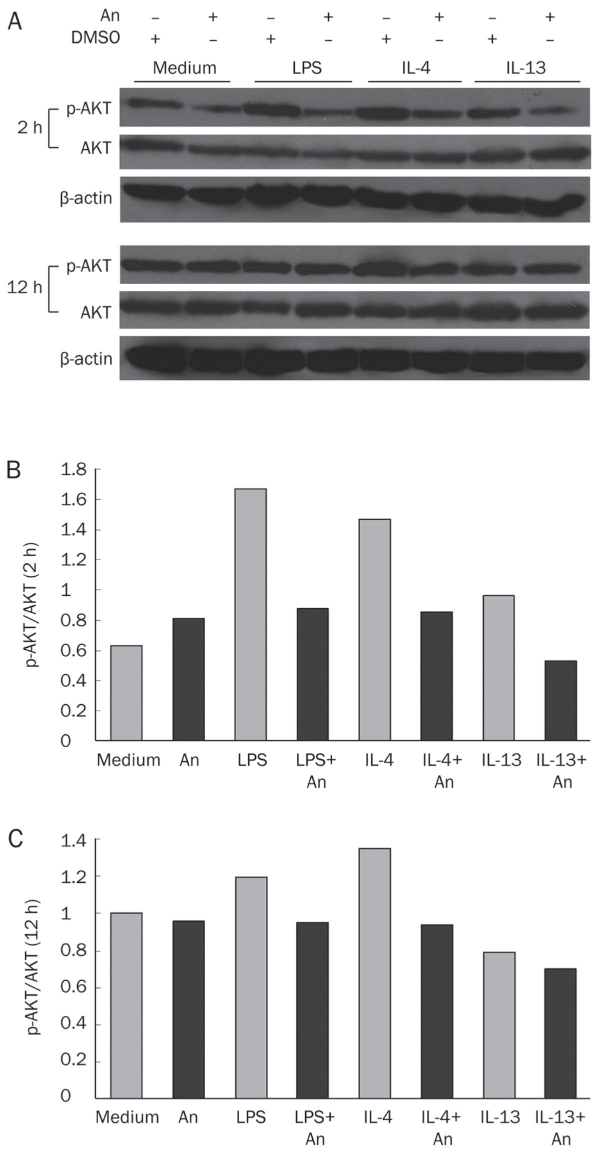

Figure 6. Andrographolide (An) modulates the PI3K signalling pathway activation. Macrophages were incubated with An (10 μg/mL) alone or together with LPS, IL-4 or IL-13 for 2 h/ 12 h. (A) AKT phosphorylation and total ERK 1/2 expression were detected by Western Blot. β-actin was used as a protein loading control. (B, C) The densitometric analysis of band intensity in (A) is analyzed by Quantity One software (Bio-Rad).

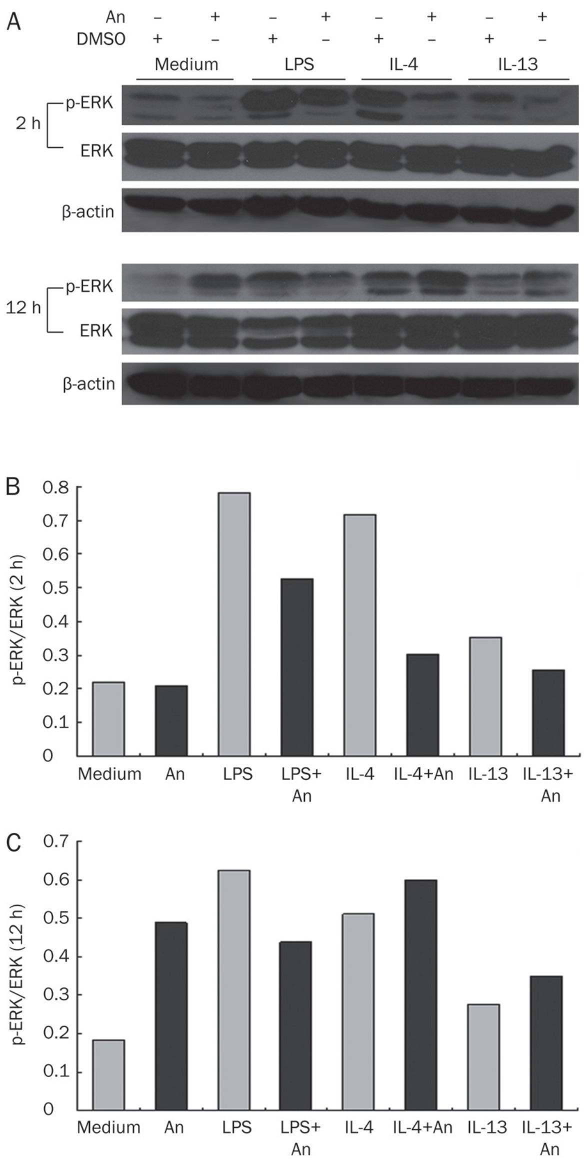

Figure 7. Andrographolide (An) modulates the MAPK signalling pathway activation. Macrophages were incubated with An (10 μg/mL) alone or together with LPS, IL-4 or IL-13 for 2 h/ 12 h. (A) ERK 1/2 phosphorylation and total AKT expression were detected by Western Blot. β-actin was used as a protein loading control. (B, C) The densitometric analysis of band intensity in (A) is analyzed by Quantity One software (Bio-Rad).

It has been described that a phenotypic switch in the macrophage population occurs over time in some cases and is associated with immune mediated pathology[11]. On one hand, over-production of inflammatory cytokines can lead to chronic inflammation and a variety of autoimmune diseases, including inflammatory bowel disease, rheumatoid arthritis, asthma and even atherosclerosis. On the other hand, over-production of anti-inflammatory cytokines can lead to persistent infection and tumor tolerance[29, 30]. Regulation of macrophage activation by immunomodulatory drugs at specific stage of different diseases can be of important therapeutic benefit. In the present study, LPS or IL-4 activated mouse peritoneal macrophages were treated with andrographolide, to assess the effect of the agent in regulating macrophage activation. It showed that andrographolide significantly down regulated the expression of both M1- and M2-related cytokines in macrophages activated with either LPS or IL-4. As both inflammatory and anti-inflammatory cytokine genes are triggered by LPS and IL-4 (as prototypes of type 1 and type 2 inflammation), the relative activation of inflammatory *vs* anti-inflammatory genes is a better estimate of M1 *vs* M2 polarization as compared to assessement of single genes. The ratio of M1:M2 cells may be more important than the absolute number of cells[31]. M1 macrophage cells usually have the phenotype showing IL-12 high, IL-10 low, IL-23 high, and M2 cells vice versa[32]. The ratio between IL-12 and IL-10 production is indicative of classical *vs* alternative activation. We found that treatment of andrographolide for 4 h significantly decreased the LPS-induced M1 polarization (IL-12/IL-10 ratio from 31.0 to 10.8) and slightly reversed the IL-4-induced M2 polarization (from 0.059 to 0.135). After 24 h of treatment andrographolide showed anti-inflammatory effect on LPS-stimulated cells (IL-12/IL-10 ratio from 9.02 to 4.69), but tended toward the M2-like phenotype of IL-4-activated cells (from 0.320 to 0.113). The inhibitory activity of andrographolide on IL-23 was also observed in LPS-induced macrophages (Supplementary Table 2). Correspondingly, IL-12 production and the ratio of IL-12/IL-10 were reduced by andrographolide after 48 h of treatment. Thus andrographolide acted as a modulator in macrophage activation depending on the initial microenvironment.

Cytokine environment and cell-cell interaction are important factors in the adaptive immune response. As professional antigen-presenting cells, macrophages not only respond to Th1 and Th2 cytokines and alter their functional phenotypes, but also secrete different amounts of M1 and M2 cytokines and express antigen uptake and presenting related surface markers (such as mannose receptor, MHC and costimulatory molecules) to present antigen protein and activate T/B cells[13, 33]. The effects of andrographolide were thus investigated on the antigen-uptake and presenting capacity related suface markers of macrophages *in vitro* and specific antibody response *in vivo*. Andrographolide inhibited LPS-induced expression of class I MHC and costimulatory molecules (CD40, CD80, and CD86), and inhibited IL-4 induced expression of mannose receptor. Similar effects have been observed in dendritic cells, in which andrographolide inhibited LPS-induced up-regulation of the maturation markers CD40 and CD86[9]. Administration of andrographolide to mice immunized with HBsAg (vaccine quality) significantly down-regulated anti-HBs production. The capacity of andrographolide to reduce macrophage expression of pattern recognition receptor (mannose receptor, CD206) and MHC/costimulatory molecules indicated that andrographolide may inhibit the antigen uptake and presentation and result in reduced specific antibody production. HBsAg induces Th2 biased response and increases specific IL-4-producing splenocytes after immunization of mice[19]. Treatment with andrographolide decreased the number of HBsAg specific IL-4-producing cells in parallel to the decrease of anti-HBs production.

MAPK and PI3K signaling pathway have been reported to be involved in macrophage activation[22, 23], the effects of andrographolide on the signaling pathway activation were analyzed by detecting phosphorylation level of ERK 1/2 (MAPK pathway) and AKT (PI3K pathway). Andrographolide exerted an apparent inhibitory effect on phosphorylation of ERK 1/2 and AKT at the early time (2 h) and reversed or restored them after 12 h, suggesting that ERK 1/2 and AKT pathways may contribute to the regulatory activity of andrographolide on macrophage activation. The inhibitory effect of andrographolide on PI3K and MAPK pathway may indicate that the mechanism of andrographolide modulating macrophage polarization is not the direct activation of naïve macrophages but an inhibitory effect on already activated macrophages.

The results indicate that andrographolide is able to modulate the innate immune response by regulating both classical and alternative activation of macrophages, and regulate specific antibody production as well as antigen-specific IL-4 producing splenocytes. Our study provides more evidences for using andrographolide as an immunomodulatory drug in the therapy for immune disorders.

Acknowledgements

This work was supported by the Program of Ministry of Science and Technology of China (S2010GR0385, 2008ZX10004-014, and 2008ZX10002-002), the International Science and Technology Cooperation Program of Shanghai Science and Technology Commission (074307038) and PhD student visiting scholarship of Fudan University for 2008-2009.

Author contribution

Prof Di QU and Prof Shi-ping MA designed the project and edited the manuscript. Prof Diana BORASCHI made suggestions for the project and manuscript. Wei WANG and Jing WANG designed and performed and analyzed most of the studies and wrote the manuscript. Sheng-fu DONG and Chun-hong LIU performed the research and analysis of experiments with mice immunization and antibody detection. Paola ITALIANI performed the research and analysis of experiments with endotoxin detection. Shu-hui SUN and Jing XU contributed new reagents and analytical performance of flow cytometry.

Supplementary informaiton

Supplementary Table 1 show the effects of andrographolide (An) on M1/ M2 cytokines mRNA expression level in IL-13 activated macrophages. Supplementary Table 2 show the effects of andrographolide (An) on IL-23 mRNA expression level in naive and activated macrophages. Supplementary data associated with this article can be found in the online version.

References

1 State Pharmacopoeia Committee. Chinese Pharmacopoeia. Beijing: Chemical Industry Press; 2005. p 189−190.
2 Kligler B, Ulbricht C, Basch E, Kirkwood CD, Abrams TR, Miranda M, *et al.* *Andrographis paniculata* for the treatment of upper respiratory infection: A systematic review by the natural standard research collaboration. Explore-Ny 2006; 2: 25−9.
3 Abu-Ghefreh AA, Canatan H, Ezeamuzie CI. *In vitro* and *in vivo* anti-inflammatory effects of andrographolide. Int Immunopharmacol 2009; 9: 313−8.
4 Zhou J, Lu GD, Ong CS, Ong CN, Shen HM. Andrographolide sensitizes cancer cells to TRAIL-induced apoptosis via p53-mediated death receptor 4 up-regulation. Mol Cancer Ther 2008; 7: 2170−80.
5 Yu BC, Chang CK, Su CF, Cheng JT. Mediation of beta-endorphin in

andrographolide-induced plasma glucose-lowering action in type I diabetes-like animals. Naunyn-Schmiedeberg's Arch Pharmacol 2008; 377: 529–40.

6 Woo AY, Waye MM, Tsui SK, Yeung ST, Cheng CH. Andrographolide up-regulates cellular-reduced glutathione level and protects cardiomyocytes against hypoxia/reoxygenation injury. J Pharmacol Exp Ther 2008; 325: 226−35.

7 Sheeja K, Kuttan G. Modulation of natural killer cell activity, antibody-dependent cellular cytotoxicity, and antibody-dependent complement-mediated cytotoxicity by andrographolide in normal and Ehrlich ascites carcinoma-bearing mice. Integr Cancer Ther 2007; 6: 66−73.

8 Sheeja K, Kuttan G. Activation of cytotoxic T lymphocyte responses and attenuation of tumor growth *in vivo* by *Andrographis paniculata* extract and andrographolide. Immunopharmacol Immunotoxicol 2007; 29: 81−93.

9 Iruretagoyena MI, Tobar JA, Gonzalez PA, Sepulveda SE, Figueroa CA, Burgos RA*, et al.* Andrographolide interferes with T cell activation and reduces experimental autoimmune encephalomyelitis in the mouse. J Pharmacol Exp Ther 2005; 312: 366−72.

10 Iruretagoyena MI, Sepulveda SE, Lezana JP, Hermoso M, Bronfman M, Gutierrez MA*, et al.* Inhibition of nuclear factor-kappa B enhances the capacity of immature dendritic cells to induce antigen-specific tolerance in experimental autoimmune encephalomyelitis. J Pharmacol Exp Ther 2006; 318: 59−67.

11 Mosser DM, Edwards JP. Exploring the full spectrum of macrophage activation. Nat Rev Immunol 2008; 8: 958−69.

12 Martinez FO, Sica A, Mantovani A, Locati M. Macrophage activation and polarization. Front Biosci 2008; 13: 453−61.

13 Mills CD, Kincaid K, Alt JM, Heilman MJ, Hill AM. M-1/M-2 macrophages and the Th1/Th2 paradigm. J Immunol 2000; 164: 6166−73.

14 Zhang X, Mosser DM. Macrophage activation by endogenous danger signals. J Pathol 2008; 214: 161−78.

15 Bowdish DM, Loffredo MS, Mukhopadhyay S, Mantovani A, Gordon S. Macrophage receptors implicated in the "adaptive" form of innate immunity. Microbes Infect 2007; 9: 1680−7.

16 Gazi U, Martinez-Pomares L. Influence of the mannose receptor in host immune responses. Immunobiology 2009; 214: 554−61.

17 Crow MK. Modification of accessory molecule signaling. Springer Semin Immunopathol 2006; 27: 409−24.

18 Jafarzadeh A, Zarei S, Shokri F. Low dose revaccination induces robust protective anti-HBs antibody response in the majority of healthy non-responder neonates. Vaccine 2008; 26: 269−76.

19 Dong SF, Chen JM, Zhang W, Sun SH, Wang J, Gu JX*, et al.* Specific immune response to HBsAg is enhanced by beta-glucan oligosaccharide containing an alpha-(1-->3)-linked bond and biased towards M2/Th2. Int Immunopharmacol 2007; 7: 725−33.

20 Gwinn MR, Vallyathan V. Respiratory burst: role in signal transduction in alveolar macrophages. J Toxicol Environ Health B Crit Rev 2006; 9: 27−39.

21 Varin A, Gordon S. Alternative activation of macrophages: Immune function and cellular biology. Immunobiology 2009; 214: 630−41.

22 Rao KM. MAP kinase activation in macrophages. J Leukoc Biol 2001; 69: 3−10.

23 Fukao T, Koyasu S. PI3K and negative regulation of TLR signaling. Trends Immunol 2003; 24: 358−63.

24 Livak KJ, Schmittgen TD. Analysis of relative gene expression data using real-time quantitative PCR and the 2(-Delta Delta C(T)) method. Methods 2001; 25: 402−8.

25 D'Anto V, Eckhardt A, Hiller KA, Spagnuolo G, Valletta R, Ambrosio L*, et al.* The influence of Ni(II) on surface antigen expression in murine macrophages. Biomaterials 2009; 30: 1492−501.

26 Gordon S. The macrophage: past, present and future. Eur J Immunol 2007; 37 Suppl 1: S9−17.

27 Qin LH, Kong L, Shi GJ, Wang ZT, Ge BX. Andrographolide inhibits the production of TNF-alpha and interleukin-12 in lipopolysaccharide-stimulated macrophages: role of mitogen-activated protein kinases. Biol Pharm Bull 2006; 29: 220−4.

28 Bouhlel MA, Derudas B, Rigamonti E, Dievart R, Brozek J, Haulon S*, et al.* PPARgamma activation primes human monocytes into alternative M2 macrophages with anti-inflammatory properties. Cell Metab 2007; 6: 137−43.

29 Mosser DM. The many faces of macrophage activation. J Leukoc Biol 2003; 73: 209−12.

30 Mora AL, Torres-Gonzalez E, Rojas M, Corredor C, Ritzenthaler J, Xu J*, et al.* Activation of alveolar macrophages via the alternative pathway in herpesvirus-induced lung fibrosis. Am J Respir Cell Mol Biol 2006; 35: 466−73.

31 Brown BN, Valentin JE, Stewart-Akers AM, McCabe GP, Badylak SF. Macrophage phenotype and remodeling outcomes in response to biologic scaffolds with and without a cellular component. Biomaterials 2009; 30: 1482−91.

32 Mantovani A, Sica A, Locati M. Macrophage polarization comes of age. Immunity 2005; 23: 344−6.

33 Ma J, Chen T, Mandelin J, Ceponis A, Miller NE, Hukkanen M*, et al.* Regulation of macrophage activation. Cell Mol Life Sci 2003; 60: 2334−46.

npg
Acta Pharmacologica Sinica (2010) 31: 202–210
© 2010 CPS and SIMM All rights reserved 1671-4083/10 $32.00
www.nature.com/aps

Original Article

Downregulation of Dickkopf-1 is responsible for high proliferation of breast cancer cells via losing control of Wnt/β-catenin signaling

Xiao-lei ZHOU[1], Xiao-ran QIN[1], Xiao-dong ZHANG[2, *], Li-hong YE[1, *]

Departments of [1]Biochemistry and [2]Cancer Research, Key Laboratory of Molecular Microbiology and Technology of Ministry of Education, Institute for Molecular Biology, College of Life Sciences, Nankai University, Tianjin 300071, China

Aim: To investigate the role of DKK-1/Wnt/β-catenin signaling in high proliferation of LM-MCF-7 breast cancer cells, a sub-clone of MCF-7 cell line.
Methods: Two cell lines (MCF-7 and LM-MCF-7) with different proliferation abilities were used. LM-MCF-7 cells were transiently transfected with the pcDNA3-DKK-1 plasmid encoding the DKK-1 gene (or MCF-7 cells were transfected siRNA targeting DKK-1 mRNA). Flow cytometry analysis and 5-bromo-2′-deoxyuridine (BrdU) incorporation assay were applied to detect the cell proliferation. The expression levels of β-catenin, phosphorylated β-catenin, c-Myc, cyclin D1 and Survivin were examined by Western blot analysis. The regulation of Survivin was investigated by Luciferase reporter gene assay.
Results: Western blot and RT-PCR analysis showed that the expression level of DKK-1 was downregulated in LM-MCF-7 relative to MCF-7 cells. Flow cytometry and BrdU incorporation assay showed DKK-1 could suppress growth of breast cancer cells. Overexpression of DKK-1 was able to accelerate phosphorylation-dependent degradation of β-catenin and downregulate the expression of β-catenin, c-Myc, cyclin D1 and Survivin. Luciferase reporter gene assay demonstrated that Survivin could be regulated by β-catenin/TCF4 pathway.
Conclusion: We conclude that the downregulation of DKK-1 is responsible for the high proliferation ability of LM-MCF-7 breast cancer cells via losing control of Wnt/β-catenin signaling pathway, in which c-Myc, cyclinD1 and Survivin serve as essential downstream effectors. Our finding provides a new insight into the mechanism of breast cancer cell proliferation.

Keywords: Dickkopf-1; Wnt/β-catenin; breast cancer; cell proliferation; MCF-7 cell line; survivin

Acta Pharmacologica Sinica (2010) 31: 202–210; doi: 10.1038/aps.2009.200

Introduction

Breast cancer is a very common tumor worldwide, and its metastasis is a major cause of death. Our laboratory previously established a metastatic subclone from the MCF-7 breast cancer cell line, called LM-MCF-7, derived from a lung metastasis of a severe combined immunodeficient (SCID) mouse[1]. Both in vivo and in vitro experiments, our results showed that LM-MCF-7 had high malignant phenotype in cell proliferation. Results of gene chips assay, containing 21,329 kinds of human genes, demonstrated that 67 kinds of genes were markedly different between LM-MCF-7 cells and MCF-7 cells[2], suggesting that the two cell lines were remarkably different in molecular events associated with malignance. Therefore, the two cell lines, having the similar genetic background, are ideal parallel cell lines to investigate the mechanism of proliferation of breast cancer cells[1, 3, 4]. However, the endogenous signal pathways which are responsible for the high proliferation ability of LM-MCF-7 cells remain unclear.

The aggressive nature of malignant cancer cells is determined by complex signaling pathways that regulate key functions including cell proliferation, survival, migration, and invasion. The enhanced and independent cell proliferation is an essential step in tumor metastasis[5]. Recent studies show that the signal transduction pathways, such as NOTCH3-mediated signaling, ErbB-mediated cascade, serum and glucocorticoid-inducible kinase (SGK)-mediated signaling, G protein-coupled receptor GPR40-mediated signaling and ERK/MAPK signaling, are involved in the regulation of breast cancer cell proliferation[6–8]. It has been reported that Wnt signaling plays an important role in regulation of cell proliferation in several cancers, such as prostate cancer, lung cancer, myeloma and

---

* To whom correspondence should be addressed.
E-mail yelihong@nankai.edu.cn (Prof Li-hong YE)
zhangxd@nankai.edu.cn (Prof Xiao-dong ZHANG)
Received 2009-10-22 Accepted 2009-12-22

colon cancer[9–12].

Dickkopf-1 (DKK-1) was first identified as a secreted inhibitor of the canonical Wnt signaling pathway[13]. DKK-1 mediates its inhibitory effects on Wnt signaling by binding to the Kremen receptor. Frizzled, the receptor for Wnt, and Kremen both use LRP5/6 as a co-receptor. As a result DKK-1 can sequester LRP5/6 away from Frizzled, thereby inhibiting Wnt signaling[14–16]. An increasing number of studies have indicated that the members of the DKK gene family are involved in a variety of carcinomas, such as colon cancer, colorectal cancer and melanoma[17–21]. DKK-1 mediated inhibition of TCF/Lef transcription can inhibit ovarian carcinoma cell proliferation[19]. Our previous study showed that DKK-1 secreted by mesenchymal stem cells could inhibit the growth of tumor cells via depressing Wnt signaling[22]. However, the role of DKK-1 in the growth of LM-MCF-7 breast cancer cells remains unclear.

In the present study, we investigated the mechanism of growth of LM-MCF-7 breast cancer cells involving Wnt/β-catenin signal pathway. Our finding shows that DKK-1 is downregulated in LM-MCF-7 cells relative to MCF-7 cells, which is responsible for the high proliferation ability of LM-MCF-7 breast cancer cells via losing control of Wnt/β-catenin signaling pathway.

Materials and methods

Cell culture

MCF-7 and LM-MCF-7 cells were cultured in RPMI 1640 medium (Gibco, USA) supplemented with 10% fetal calf serum, 2 mmol/L *L*-glutamine, and 100 U/mL penicillin/streptomycin in humidified 5% CO_2 at 37 °C.

Cell growth curve analysis

MCF-7cells and LM-MCF-7 cells in exponential growth phase were counted and seeded into flasks (1×10^5 cells/flask, 21 flasks per cell line). Medium was changed every 3 days as usual. Three flasks of cells were harvested daily by trypsinisation and counted using a hemocytometer. Draw the growth curve by using the average number. Tumor cell doubling time: $TD=Tlg2/lg(N/N_0)$ (TD: doubling time; T: time interval, N_0: initial cell number, N: end-point cell number)[23].

RNA isolation and RT-PCR

Extraction of total RNA of the cells and reverse transcription were carried out according to a previously published protocol[24]. The specific primers for DKK-1 were: 5′-TAGCACCTTGGATGGGTATT-3′ (forward) and 5′-ATCCTGAGGCACAGTCTGAT-3′ (reverse). The amplification was done for 25 cycles (94 °C 30 s, 56 °C 30 s, 72 °C 30 s). cDNA synthesis was normalized by PCR with GAPDH primers; 5′-CCAAGGTCATCCATGACAAC-3′ (forward), 5′-AGAGGCAGGGATGATGTTCT-3′ (reverse).

Plasmids and Transfections

pcDNA3-DKK-1 plasmid encoding DKK-1 was a gift from Dr Vincent J HEARING[21]. Plasmids pGL3-sur containing Survivin promoter gene and pcDNA-Tcf4δ containing a dominant-negative Tcf-4 gene lacking the portion responsible for the protein binding to DNA were constructed previously in our lab[3]. Short interfering RNA (siRNA) duplex composed of sense and antisense strands were synthesized (Guangzhou RiboBio Co, Ltd, China). RNA oligonucleotides used for targeting DKK-1 were 5′-AAUGGUCUGGUACUUAUUCCdGdC-3′ (sense) and 3′-dCdGUUACCAGACCAUGAAUAAGG-5′ (antisense). Control siRNA oligonucleotides were 5′-AAUGGUCAUGGUCUUAUUCCdGdC-3′ (sense) and 3′-dCdGUUACCAGUACCAGAAUAAGG-5′ (antisense)[25]. One day before transfection, cells were collected, and seeded into 6-well plates at 1×10^5 cells per well (n=3, each group). LM-MCF-7 cells were transfected with 2 μg plasmids such as pcDNA3 empty vector, pcDNA3-DKK-1 encoding DKK-1, or pcDNA-Tcf4δ respectively (MCF-7 cells were transfected with 20 nmol/L DKK-1 siRNA or control siRNA), using LipofectAMINE 2000 (Invitrogen, Carlsbad, CA, USA) according to the manufacturer's instruction. The transfection mixture was removed after 6 h. Transfection efficiency in the cells was monitored in separated wells which paralleled with experimental group by co-transfection of 0.2 μg pEGFP-C2 plasmid, which expresses green fluorescence protein (GFP).

Flow cytometry analysis

After 48 h of transfection, adherent cells were washed with cold PBS and fixed in 70% ethanol at 4 °C. Cells were pelleted and treated with RNase A (50 μg/mL, Takara, Otsu, Japan) and stained with propidium iodide (50 μg/mL, Sigma-Aldrich, St Louis, MO, USA). The cell cycle was determined by a FACSCalibur™ Flow Cytometer (Becton Dickinson, Bedford, Mass). The proliferation indexes (PIs) were calculated by using the formula[26]:

$$PI=(G_2/M+S)\div(G_0/G_1+S+G_2/M)\times100\%$$

BrdU incorporation assay

5-Bromo-2′-deoxyuridine (BrdU) incorporation assay was performed described as previously[27]. In brief, cells were seeded in 6-well culture plate and were grown overnight prior to transfection. After 48 h transfection, all groups (n=3 in every group) were incubated with fresh medium containing 10 μmol/L BrdU (Sigma-Aldrich, St Louis, MO, USA) for 4 h prior to immunofluorescence staining with mouse anti-BrdU antibody. The cells were fixed for 15 min with 4% paraformaldehyde in phosphate buffered saline (PBS). After 1 h incubation with PBS containing 2 mol/L HCl to denature DNA, cover slips were washed 3 times with 0.5% bovine serum albumin (BSA) and 0.5% Tween 20 in PBS, and incubated overnight (4 °C) with a mouse anti-BrdU antibody (NeoMarkers, Fremont, CA, USA) at 1:300 dilution. Reactions were developed using fluorescein isothiocyanate (FITC)-conjugated goat anti-mouse IgG (Dako, Glostrup, Denmark) at 1:100 dilution for BrdU staining. The BrdU labeling index was assessed by point counting through a Nikon TE200 inverted microscope (Nikon, Tokyo, Japan) using a 40×objective lens. A total of 700–800 nuclei were counted in 6–8 representative fields. The labeling index was expressed as the number of positively-labeled nuclei/total number of nuclei. Propidium iodine (Sigma-Aldrich, St Louis, MO, USA) staining for nuclei in 50 μg/mL was used as the control to all cells in each group.

Western blot analysis

After 48 h of transfection, cells were washed three times with ice-cold PBS and extracted directly in the lysis buffer (20 mmol/L Tris-HCl pH 8.0, 150 mmol/L NaCl, 10 mmol/L EDTA pH 8.0, 1% TritonX-100, 1% DOC, 1 mmol/L DTT, and protein inhibitor cocktails) for 30 min at room temperature. Then, the cell lysates were clarified by centrifugation at 13 000 r/min for 20 min and the supernatants were collected for protein determination by the Bradford assay. Equal amounts of protein were separated using 10%–15% SDS-PAGE. Separated proteins were transferred onto polyvinylidene difluoride (PVDF) membranes. The membranes were blocked in PBS/0.1% Tween 20 containing 5% dry milk and probed with primary antibodies: rabbit anti-human DKK-1 polyclonal antibody (1:400 dilution; Sigma-Aldrich, St Louis, MO, USA), mouse anti-c-Myc antibody (1:500 dilution, Sigma-Aldrich), rabbit anti-β-catenin antibody (1:4000 dilution, Sigma-Aldrich), mouse anti-phospho-β-catenin antibody (1:1000 dilution, Sigma-Aldrich), mouse anti-cyclin D1 antibody (1:1000 dilution, Cell Signaling Technology, Danvers, MA, USA), mouse anti-survivin antibody (1:1000 dilution, Santa Cruz Biotech, Delaware Avenue, Santa Cruz, CA, USA). Protein bands were visualized by using the enhanced chemiluminescence (ECL, Amersham phamacia biotech, Tokyo, Japan) system. For loading control, membranes were stripped and reprobed with mouse anti-human β-actin monoclonal antibody (1:20000 dilution, Sigma-Aldrich). All experiments were repeated 3 times. We further confirmed the results by applying Glyco Band-Scan software (PROZYME®, San Leandro, Calif, USA).

Luciferase reporter gene assay

The cells, such as MCF-7 and LM-MCF-7 were placed into 24-well plate respectively. The plasmids of 0.8 μg pGL3-sur (containing survivin promoter), 0.5 μg pcDNA3-Tcf4δ (or 0.5 μg pcDNA3-DKK-1) and 0.1 μg pRL-TK (containing renilla luciferase gene) were co-transfected into the LM-MCF-7 cells in triplicate by using lipofectAMINE 2000 according to the manufacture's recommendation. In MCF-7 cells, plasmids of 0.8 μg pGL3-sur, 20 nmol/L DKK-1 siRNA and 0.5 μg pcDNA3-Tcf4δ were co-transfected into the MCF-7 cells in triplicate. After 48 h transfection, the dual luciferase reporter gene assay was performed by Dual-Glo luciferase Assay kit (Promega, WI, USA). The intensity of luminescence was measured by a TD-20/20 luminometer (Turner Biosystems, Sunnyvale, CA). Data were normalized by Renilla luciferase luminescence intensity.

Statistical analysis

All data are presented as mean±standard error of the mean and were analyzed by ANOVA or Student's *t* test using Prism 4.0 (GraphPad Software, CA). A *P* value of <0.05 was considered statistically significant. All statistical tests were two-sided.

Results

DKK-1 is downregulated in LM-MCF-7 breast cancer cells

Malignant breast cancer cells require an independent proliferation signal pathway to adapt foreign microenvironment for survival. Recent studies show that DKK-1 is involved in regulation of a variety of tumor cells growth[17–21]. Our laboratory previously established a metastatic subclone from the MCF-7 breast cancer cell line, called LM-MCF-7, derived from a lung metastasis of a severe combined immunodeficient (SCID) mouse. Our previous results showed that LM-MCF-7 had high malignant phenotype in cell proliferation[1]. In this study, we showed that the population doubling time *in vitro* was estimated as 34.3 h and 40.0 h in the exponential phase of LM-MCF-7 cells and MCF-7 cells, respectively (Figure 1A). To identify the role of DKK-1 in LM-MCF-7 breast cancer cell proliferation, we investigated the expression of DKK-1 at the levels of mRNA and protein in MCF-7 and LM-MCF-7 cells. RT-PCR and Western blot analysis showed that the expression of DKK-1 at the levels of mRNA and protein was downregulated in LM-MCF-7 cells relative to MCF-7 cells (Figures 1B and 1C), suggesting that DKK-1 may be involved in the high proliferation of LM-MCF-7 breast cancer cells.

DKK-1 suppresses the growth of LM-MCF-7 breast cancer cells

Accordingly, we examined the role of DKK-1 in proliferation of breast cancer cells by transfection. Transfection efficiency revealed that approximately 70%–80% of cells showed green fluorescence (Figure 2A). BrdU incorporation analysis showed that the downregulation of expression of DKK-1 by RNA interference led to the percentage of BrdU-positive MCF-7 cells increased significantly ($P<0.05$, *vs* control, Student's *t* test, Figure 2B). However, the percentage of BrdU-positive LM-MCF-7cells reduced significantly when overexpressing DKK-1 in LM-MCF-7 cells by transfecting with pcDNA3-DKK-1 plasmids ($P<0.05$, *vs* control, Student's *t* test, Figure 2B). Flow cytometry analysis showed that the downregulation of DKK-1 by RNA interference led to the increase of cell proliferation index (PI) of MCF-7 cells from 30.87% to 41.44% ($P<0.05$, *vs* control, Student's *t* test). However, the PI of LM-MCF-7 declined from 50.61% to 32.99% after overexpressing DKK-1 by transfecting pcDNA3-DKK-1 plasmids ($P<0.05$, *vs* control, Student's *t* test, Figure 2C). Thus, our finding suggests that the DKK-1 is involved in proliferation of breast cancer cells.

β-catenin, c-Myc, cyclin D1, and Survivin serve as downstream effectors of DKK-1

Our previous results showed that β-catenin, c-Myc, cyclin D1, and Survivin were upregulated in LM-MCF-7 cells by cDNA microarray[2]. Therefore, we further examined the protein expression levels of them in the cells. Western blot analysis showed that β-catenin, c-Myc, cyclin D1, and Survivin were highly expressed in LM-MCF-7 cells relative to MCF-7cells, while the phosphorylation level of β-catenin was decreased

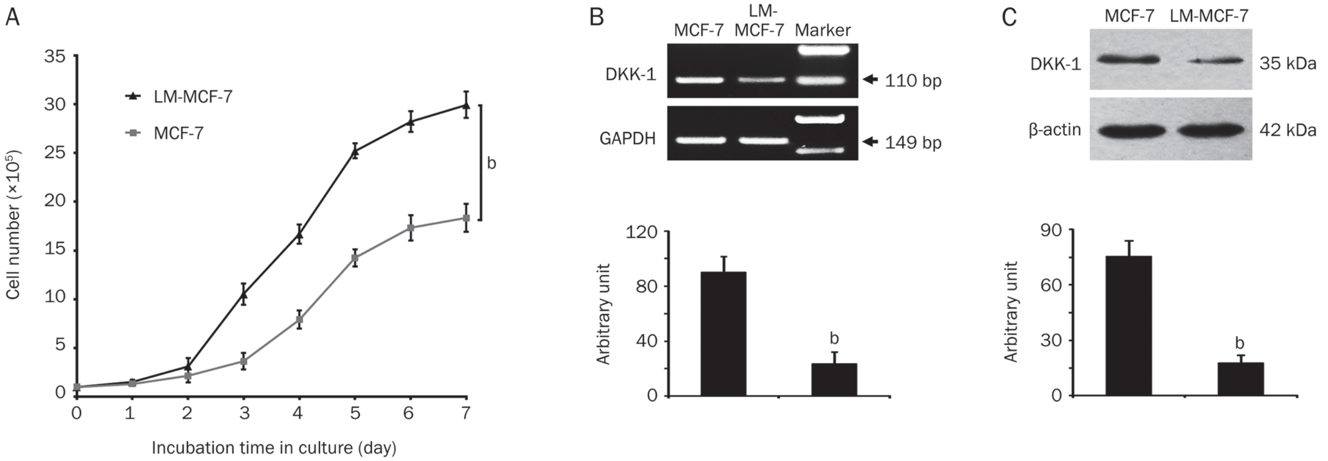

Figure 1. DKK-1 is downregulated in LM-MCF-7 breast cancer cells. (A) Cell growth curve of MCF-7 cells and LM-MCF-7 cells was measured, respectively ($^{b}P<0.05$, Student's *t* test). (B) RT-PCR showed the mRNA expression level of DKK-1 in MCF-7 and LM-MCF-7 cells. Histogram shows the results by applying Glyco Band-Scan software ($^{b}P<0.05$, Student's *t* test). (C) Western blot analysis showed the expression level of DKK-1 in MCF-7 and LM-MCF-7 cells. Histogram shows the results by applying Glyco Band-Scan software ($^{b}P<0.05$, Student's *t* test).

in LM-MCF-7 cells (Figure 3A, 3B), suggesting that β-catenin, c-Myc, cyclin D1, and Survivin may serve as downstream effectors of DKK-1 in the cells. Then, we found that the downregulation of DKK-1 in MCF-7 cells by RNA interference could lead to the upregulation of β-catenin, c-Myc, cyclin D1, and Survivin, and decrease of phosphorylated β-catenin (Figure 3C, 3D). Contrarily, the overexpression of DKK-1 in LM-MCF-7 cells by transfection with pcDNA3-DKK-1 plasmid could result in the opposite results in MCF-7 cells (Figure 3E, 3F). Therefore, we conclude that β-catenin, c-Myc, cyclin D1, and Survivin were downstream effectors of DKK-1 in breast cancer cells.

Survivin is a downstream target gene of β-catenin

To examine whether Survivin is a downstream target gene of β-catenin, we examined the promoter activity of Survivin by luciferase reporter gene assay when co-transfecting with pcDNA-Tcf4δ plasmids. Tcf4δ, containing a dominant-negative Tcf-4 gene lacking the portion that responsible for the Tcf-4 protein binding to DNA, can block β-catenin/Tcf4 signal pathway[24]. Luciferase reporter gene assay showed that the Survivin promoter luciferase activity was higher in LM-MCF-7 cells than in MCF-7 cells ($P<0.05$, Student's *t* test, Figure 4A). Transfection of LM-MCF-7 cells with pcDNA-DKK-1 plasmids or pcDNA-Tcf4δ plasmids could downregulate the Survivin promoter luciferase activity of LM-MCF-7 cells ($P<0.05$, Student's *t* test, *vs* Control, Figure 4A). Meanwhile, downregulation of DKK-1 by RNA interference could enhance Survivin promoter luciferase activity in MCF-7 cells. It failed to change Survivin promoter luciferase activity when DKK-1 RNAi and overexpression of Tcf4δ were performed simultaneously in MCF-7 cells (Figure 4B). Moreover, Western blot assay showed that transfection with pcDNA-Tcf4δ plasmids in LM-MCF-7 cells could efficiently downregulated the expression of Survivin (Figure 4C, 4D), suggesting that Survivin is a downstream target gene of β-catenin.

To further confirm the effect of Wnt/β-catenin on the proliferation of LM-MCF-7 breast cancer cells, we transfected LM-MCF-7 cells with pcDNA-Tcf4δ plasmid for blocking β-catenin/Tcf4 signal pathway. Flow cytometry analysis showed that the overexpression of Tcf4δ could potently inhibit the proliferation of LM-MCF-7 cells, whose proliferation index (PI) of LM-MCF-7 cells declined from 54.57% to 30.54% (Figure 4E, $P<0.05$, *vs* control, Student's *t* test), suggesting that the inhibition of Wnt/β-catenin mediated by DKK-1 is responsible for the high proliferation of breast cancer cells.

Discussion

Breast cancer is the most common malignant disease in women. Our laboratory previously established a metastatic subclone from the MCF-7 breast cancer cell line[1]. We have reported that a positive feedback cascade of Gi/o proteins-PLC-PKC- pERK1/2 mediated by cyclooxygenase (COX) and lipoxygenase (LOX) contributes to the high proliferation of LM-MCF-7 breast cancer cells[4]. Additionally, a cross-talk between myosin light chain kinase (MLCK) and phosphorylated ERK1/2 also leads to the high proliferation of LM-MCF-7 breast cancer cells[3]. In the present study, we investigated the mechanism of high proliferation of LM-MCF-7 cells involving Wnt/β-catenin signaling. The malignant cancer cell growth needs independent signaling pathways which were generated due to the expression levels of certain effectors changes. According to our previous gene chips assay[2], we supposed that an endogenous signaling pathway, such as Wnt/β-catenin, may be responsible for the high proliferation of LM-MCF-7 breast cancer cells. We first examined the expression level of DKK-1 in MCF-7/LM-MCF-7 breast cancer cells. Our data demonstrated that the expression level of DKK-1 was downregulated in LM-MCF-7 cells relative to MCF-7 cells (Figure 1), suggesting that DKK-1 may be involved in the pro-

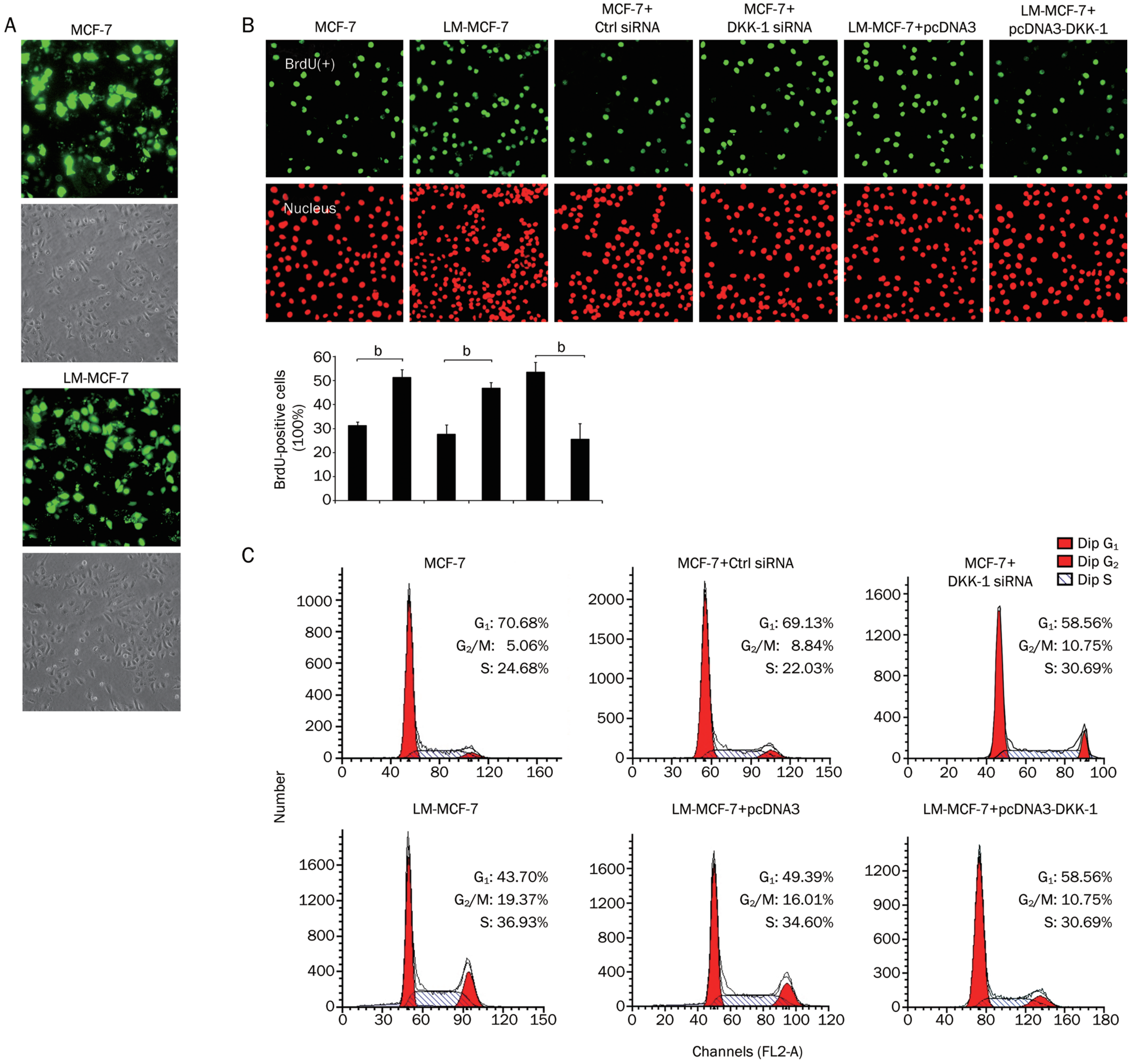

Figure 2. DKK-1 suppresses the growth of LM-MCF-7 breast cancer cells. (A) In transfection efficiency, co-transfection was performed in cells, such as pcDNA3-DKK-1 plasmid and pEGFP-C2 plasmid in LM-MCF-7 cells, and DKK-1 siRNA and pEGFP-C2 plasmid in MCF-7 cells. ×100. (B) Measurement of cell proliferation by BrdU incorporation assay. Positive PI staining is in red in the nucleus, showing the numbers of cells as the control. Green fluorescence shows the number of BrdU-positive cells. ×100. Histogram shows the positive rates of BrdU-positive cells ($^{b}P<0.05$, *vs* control Student's *t* test). (C) Examination of cell cycle by flow cytometry analysis in MCF-7 cells and LM-MCF-7 cells.

liferation of LM-MCF-7 cells. Then, we identified the function of DKK-1 in the growth of LM-MCF-7 cells. Flow cytometry analysis and BrdU incorporation assay showed that elevating expression of DKK-1 could suppress proliferation of breast cancer cells (Figure 2). Our results are consistent with that the expression of DKK family of proteins (DKK-1, -2, and-3) is reduced in most of melanoma cell lines and most of tumor samples[20]. The overexpression of DKK-1 could result in the suppression of tumor growth of human prostate and lung cancers[28, 29]. Previous study also shows ectopic expression of a dominant negative p53 gene in the p53 wild type MCF-7 breast cancer cell line results in a dramatic decrease in levels of DKK-1 mRNA expression[30]. All the data suggest that DKK-1 is a very important factor in tumor cell proliferation.

Next, we try to identify the downstream effectors of DKK-1 in promotion of proliferation of breast cancer cells.

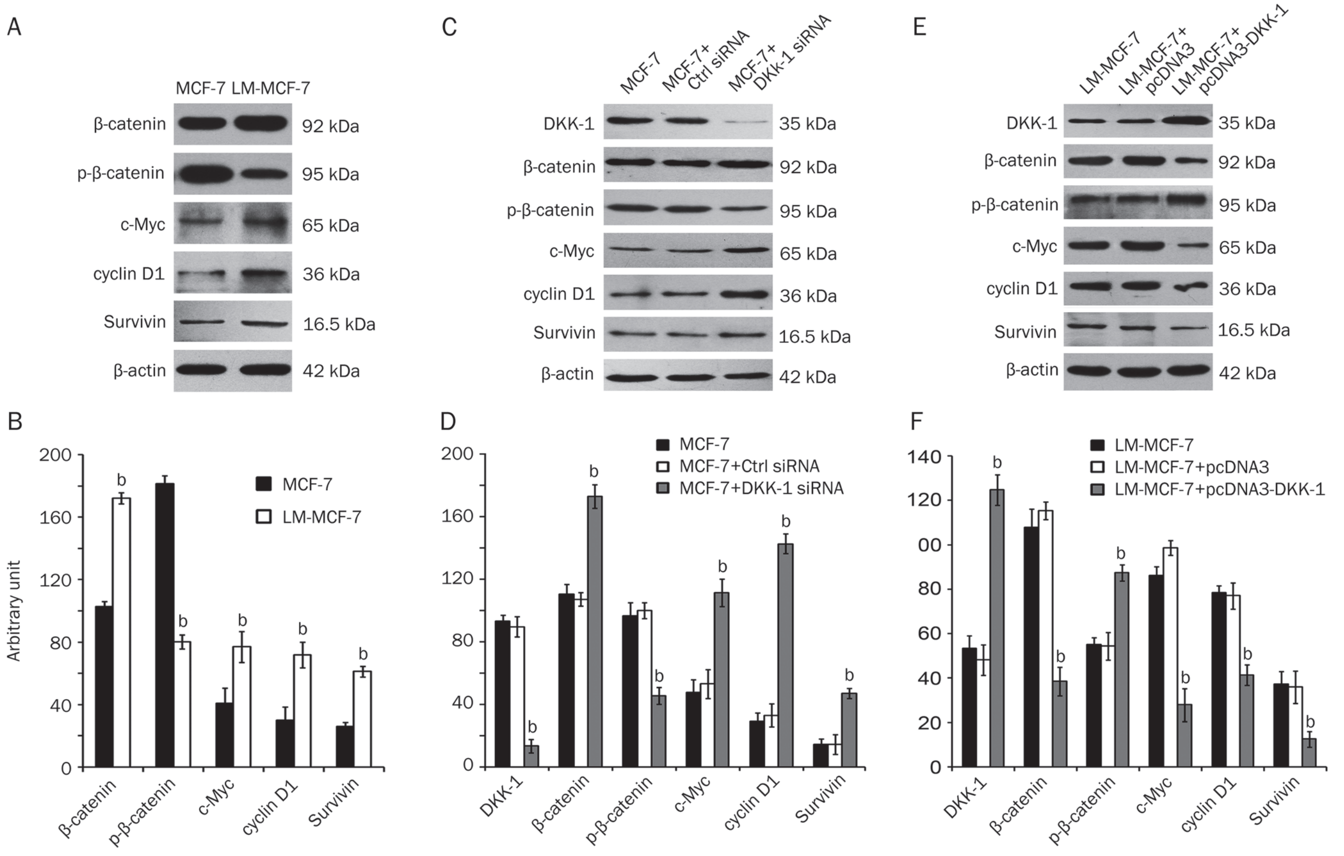

Figure 3. β-Catenin, c-Myc, cyclin D1 and Survivin serve as downstream effectors of DKK-1. (A) Western blot analysis showed the expression level of β-catenin, phosphorylated β-catenin, c-Myc, cyclin D1, and Survivin in MCF-7 and LM-MCF-7 cells. The data are representative of three independent experiments. (B) Histogram shows the results by applying Glyco Band-Scan software ($^{b}P<0.05$, Student's *t* test). (C) Western blot analysis showed the expression level of the proteins when DKK-1 was downregulated by RNA interference in MCF-7 cells. (D) Histogram shows the results by applying Glyco Band-Scan software ($^{b}P<0.05$, *vs* control siRNA, Student's *t* test). (E) Western blot analysis showed the expression level of the proteins when DKK-1 was upregulated by transfection of LM-MCF-7 cells with pcDNA3-DKK-1 plasmid. (F) Histogram shows the results by applying Glyco Band-Scan software ($^{b}P<0.05$, *vs* pcDNA3, Student's *t* test). The data are representative of three independent experiments.

A hallmark of canonical Wnt pathway activation which can enhance proliferation ability of several tumor cell lines shows an increase in β-catenin-dependent transcription, primarily as a result of β-catenin protein stabilization[9, 10, 31, 32]. Thus, we assessed the effects of DKK-1 on the phosphorylation of β-catenin which led to β-catenin degradation. Western blot analysis demonstrated that the expression of DKK-1 could result in declined expression of β-catenin and increased phosphorylation of β-catenin protein (Figure 3), suggesting that the overexpression of DKK-1 in breast cancer cells results in phosphorylation-dependant degradation of β-catenin. This result is consistent with previous study that DKK-1 expression resulted in increased phosphorylation and accelerated half-life of β-catenin protein in T47D carcinoma cells[33]. Next, we examined the expression of β-catenin-dependent transcription effectors[12, 34], such as c-Myc and cyclin D1. c-Myc is a nuclear phosphoprotein that functions as a transcription factor stimulating cell-cycle progression. It responds directly to mitogenic signals and plays a critical role in cell-cycle progression, especially during transition from G_1 to the S phase[35]. cyclin D1 has a rate-limiting role in G_1-S phase transition. Both transgenic mouse models and clinical studies indicate a pivotal role for cyclin D1 in normal and malignant cell growth, particularly in breast cancer[36]. In our experiments, Western blot analysis showed that DKK-1 was able to downregulate the expression of c-Myc and cyclin D1 (Figure 3), suggesting that c-Myc and cyclin D1 are downstream effectors of DKK-1.

We previously showed that Survivin mRNA was upregulated in LM-MCF-7 cells relative to MCF-7 cells by cDNA microarray[2]. Then, we confirmed that at protein level by Western blot analysis (Figure 3A, 3B). Next, we found that DKK-1 could negatively regulate the expression of Survivin (Figure 3D–3F). Luciferase reporter gene assay and Western blot analysis showed that Survivin was a β-catenin/Tcf4 pathway-dependent transcription gene via transfecting breast cancer cells pcDNA-Tcf4δ plasmids which contains a dominant-negative Tcf-4 gene lacking the portion that responsible for the protein binding to DNA (Figure 4). Our results are consistent with previous reports that blockade of Wnt signaling decreased the Survivin protein expression level in melanoma

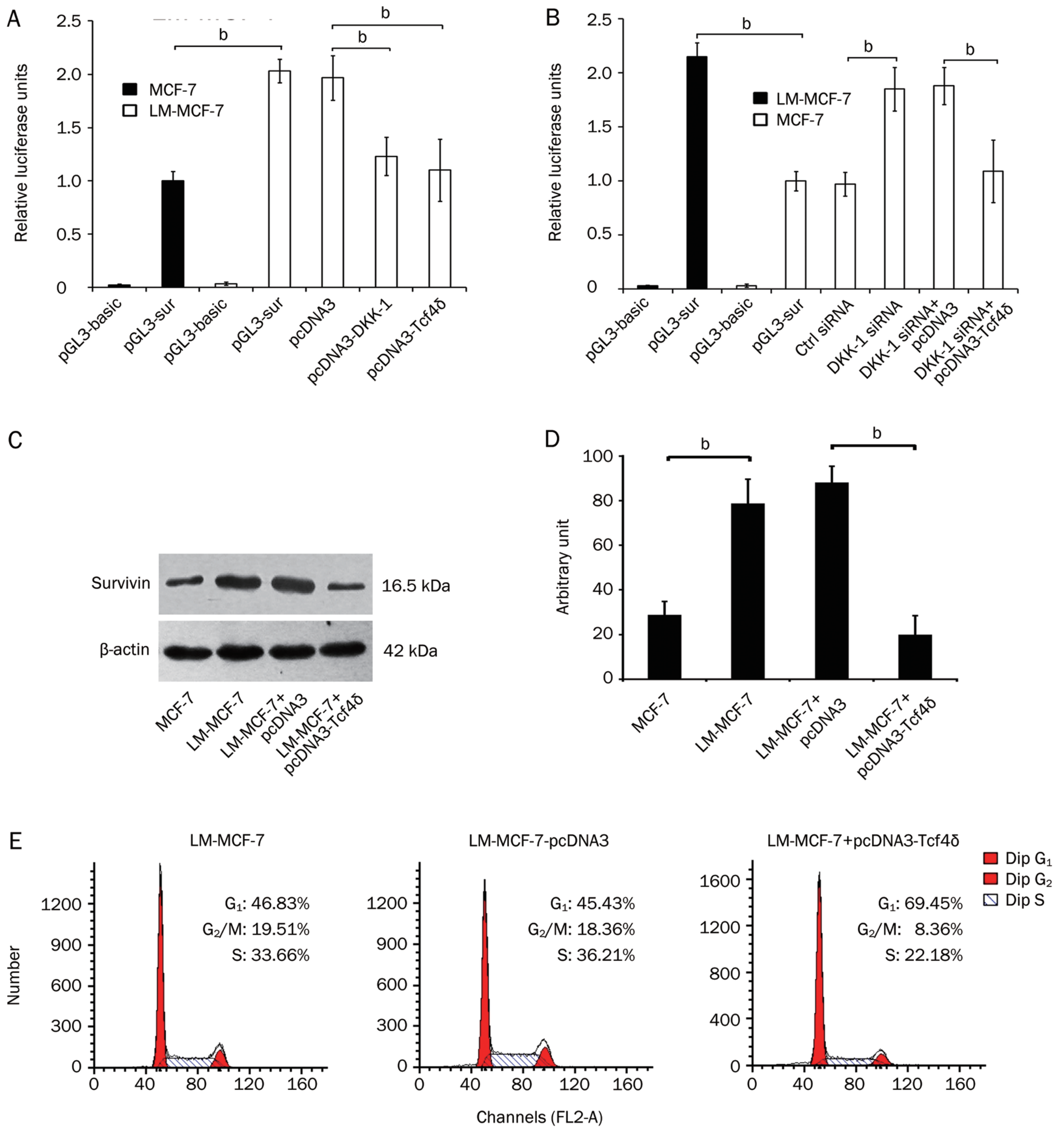

Figure 4. Survivin is a downstream target gene of β-catenin. Effect of DKK-1 (or Tcf4δ) on Survivin promoter was examined by luciferase reporter gene assay. Presented results are relative luciferase activities. (A) Activity of the Survivin promoter could be decreased by the overexpression of DKK-1 (or Tcf4δ) in LM-MCF-7 cells ($^{b}P<0.05$ *vs* pcDNA3, Student's *t* test). (B) Activity of the Survivin promoter could be increased by DKK-1 RNA interference in MCF-7 cells ($^{b}P<0.05$ *vs* control siRNA, Student's *t* test). However, the overexpression of Tcf4δ could abolish the increase ($^{b}P<0.05$ *vs* DKK-1 siRNA+pcDNA3, Student's *t* test). (C) Western blot analysis showed the expression of Survivin could be inhibited by overexpressing Tcf4δ in LM-MCF-7 cells. (D) Histogram shows the results by applying Glyco Band-Scan software ($^{b}P<0.05$ *vs* pcDNA3, Student's *t* test). The data are representative of three independent experiments. (E) Cell cycle of LM-MCF-7 cells and LM-MCF-7 cells transfected with pcDNA-Tcf4δ (or pcDNA3 empty vector) was examined by flow cytometry analysis.

cell lines and colon cancer cells[37, 38]. Survivin is an anti-apoptotic protein which is overexpressed in most human cancers[39]. Therefore, we conclude that DKK-1 can also regulate breast cancer cell proliferation by suppressing Survivin expression via β-catenin.

Our finding provided evidence of correlation between expression levels of DKK-1 and changes of Wnt/β-catenin signal pathway targets (Figure 3 and 4). Moreover, the Wnt signal pathway targets, such as cyclin D1, c-Myc, and Survivin, were all verified as β-catenin/Tcf4 pathway-dependent transcription genes (Figure 4A–4D)[12, 34]. The flow cytometry analysis showed that the blockage of β-catenin/Tcf4 pathway by transfection with pcDNA-Tcf4δ plasmids could potently inhibit the proliferation of LM-MCF-7 cells (Figure 4E). Therefore, we conclude that the downregulation of DKK-1 is responsible for the high proliferation of breast cancer LM-MCF-7 cells via losing control of Wnt/β-catenin signaling. In addition, it has been reported that DKK-1 is able to inhibit tumor growth through noncanonical CamKII pathway in human breast carcinoma cells[33]. DKK-1 mediated activation of the JNK signaling pathway was responsible for inhibition of cell growth in β-catenin-deficient human mesothelioma cells[40]. Thus, it suggests that DKK-1 plays an important role in tumor cell malignance through not only Wnt/β-catenin signal pathway but also other signal pathways.

Taken together, our data demonstrate that the downregulation of DKK-1 is responsible for the high proliferation ability of LM-MCF-7 breast cancer cells via losing control of β-catenin/Tcf transcription cascade, in which c-Myc, cyclinD1, and Survivin serve as essential downstream effectors of β-catenin. Here, our finding provides a new insight into the mechanism of high proliferation of LM-MCF-7 breast cancer cell. Overexpression of DKK-1 may be used in the gene therapy to inhibit the development of breast cancer cells.

Acknowledgments

We thank Prof VJ HEARING from the Laboratory of Cell Biology, National Cancer Institute, National Institutes of Health, USA, for providing pcDNA3-DKK-1 plasmid. The project was supported by grants of National Basic Research Program of China (973 Program, No 2007CB914802, No 2007CB914804, No 2009CB521702), National Natural Scientific Foundation (No 30770826), and Tianjin Natural Scientific Foundation (No 08JCZDJC20700).

Author contribution

Xiao-lei ZHOU, Xiao-dong ZHANG, Li-Hong YE designed research; Xiao-lei ZHOU, Xiao-ran QIN performed research; Xiao-dong ZHANG, Li-Hong YE contributed new reagents or analytic tools; Xiao-lei ZHOU, Xiao-dong ZHANG, Li-Hong YE analyzed data; Xiao-lei ZHOU, Xiao-dong ZHANG, Li-Hong YE wrote the paper.

References

1 Ye L, Wu L, Guo W, Ma H, Zhang X. Screening of a sub-clone of human breast cancer cells with high metastasis potential. Zhonghua Yi Xue Za Zhi 2006; 86: 61–5.

2 Ye L, You J, Qiao L, Cai N, Wang C, Liu Y, *et al*. Screening metastasis-associated genes in breast cancer cells with different matastatic ability by cDNA microarray. Prog Biochem Biophys 2005; 32: 421–8.

3 Zhou X, Liu Y, You J, Zhang H, Zhang X, Ye L. Myosin light-chain kinase contributes to the proliferation and migration of breast cancer cells through cross-talk with activated ERK1/2. Cancer Lett 2008; 270: 312–27.

4 You J, Mi D, Zhou X, Qiao L, Zhang H, Zhang X, *et al*. A positive feedback between activated extracellularly regulated kinase and cyclooxygenase/lipoxygenase maintains proliferation and migration of breast cancer cells. Endocrinology 2009; 150: 1607–17.

5 Yoeli-Lerner M, Yiu GK, Rabinovitz I, Erhardt P, Jauliac S, Toker A. Akt blocks breast cancer cell motility and invasion through the transcription factor NFAT. Mol Cell 2005; 20: 539–50.

6 Yamaguchi N, Oyama T, Ito E, Satoh H, Azuma S, Hayashi M, *et al*. NOTCH3 signaling pathway plays crucial roles in the proliferation of ErbB2-negative human breast cancer cells. Cancer Res 2008; 68: 1881–8.

7 Perez-Nadales E, Lloyd AC. Essential function for ErbB3 in breast cancer proliferation. Breast Cancer Res 2004; 6: 137–9.

8 Sahoo S, Brickley DR, Kocherginsky M, Conzen SD. Coordinate expression of the PI3-kinase downstream effectors serum and glucocorticoid-induced kinase (SGK-1) and Akt-1 in human breast cancer. Eur J Cancer 2005; 41: 2754–9.

9 Lu W, Tinsley HN, Keeton A, Qu Z, Piazza GA, Li Y. Suppression of Wnt/beta-catenin signaling inhibits prostate cancer cell proliferation. Eur J Pharmacol 2009; 602: 8–14.

10 Kim J, You L, Xu Z, Kuchenbecker K, Raz D, He B, *et al*. Wnt inhibitory factor inhibits lung cancer cell growth. J Thorac Cardiovasc Surg 2007; 133: 733–7.

11 Derksen PW, Tjin E, Meijer HP, Klok MD, MacGillavry HD, van Oers MH, *et al*. Illegitimate WNT signaling promotes proliferation of multiple myeloma cells. Proc Natl Acad Sci USA 2004; 101: 6122–7.

12 Clevers H. Wnt breakers in colon cancer. Cancer Cell 2004; 5: 5–6.

13 Fedi P, Bafico A, Nieto Soria A, Burgess WH, Miki T, Bottaro DP, *et al*. Isolation and biochemical characterization of the human Dkk-1 homologue, a novel inhibitor of mammalian Wnt signaling. J Biol Chem 1999; 274: 19465–72.

14 Bafico A, Liu G, Yaniv A, Gazit A, Aaronson SA. Novel mechanism of Wnt signalling inhibition mediated by Dickkopf-1 interaction with LRP6/Arrow. Nat Cell Biol 2001; 3: 683–6.

15 Mao B, Wu W, Davidson G, Marhold J, Li M, Mechler BM, *et al*. Kremen proteins are Dickkopf receptors that regulate Wnt/beta-catenin signalling. Nature 2002; 417: 664–7.

16 Mao B, Wu W, Li Y, Hoppe D, Stannek P, Glinka A, *et al*. LDL-receptor-related protein 6 is a receptor for Dickkopf proteins. Nature 2001; 411: 321–5.

17 Gonzalez-Sancho JM, Aguilera O, Garcia JM, Pendas-Franco N, Pena C, Cal S, *et al*. The Wnt antagonist DICKKOPF-1 gene is a downstream target of beta-catenin/TCF and is downregulated in human colon cancer. Oncogene 2005; 24: 1098–103.

18 Aguilera O, Fraga MF, Ballestar E, Paz MF, Herranz M, Espada J, *et al*. Epigenetic inactivation of the Wnt antagonist DICKKOPF-1 (DKK-1) gene in human colorectal cancer. Oncogene 2006; 25: 4116–21.

19 Bafico A, Liu G, Goldin L, Harris V, Aaronson SA. An autocrine mechanism for constitutive Wnt pathway activation in human cancer cells. Cancer Cell 2004; 6: 497–506.

20 Kuphal S, Lodermeyer S, Bataille F, Schuierer M, Hoang BH, Bosserhoff AK. Expression of Dickkopf genes is strongly reduced in malignant melanoma. Oncogene 2006; 25: 5027–36.

21 Yamaguchi Y, Itami S, Watabe H, Yasumoto K, Abdel-Malek ZA, Kubo T, *et al*. Mesenchymal-epithelial interactions in the skin: increased expression of dickkopf1 by palmoplantar fibroblasts inhibits melanocyte growth and differentiation. J Cell Biol 2004; 165: 275–85.

22 Qiao L, Xu ZL, Zhao TJ, Ye LH, Zhang XD. Dkk-1 secreted by mesenchymal stem cells inhibits growth of breast cancer cells via depression of Wnt signalling. Cancer Lett 2008; 269: 67–77.

23 Li Y, Tang ZY, Ye SL, Liu YK, Chen J, Xue Q, *et al*. Establishment of cell clones with different metastatic potential from the metastatic hepatocellular carcinoma cell line MHCC97. World J Gastroenterol 2001; 7: 630–6.

24 Qin X, Zhang H, Zhou X, Wang C, Zhang X, Ye L. Proliferation and migration mediated by Dkk-1/Wnt/beta-catenin cascade in a model of hepatocellular carcinoma cells. Transl Res 2007; 150: 281–94.

25 Hall CL, Bafico A, Dai J, Aaronson SA, Keller ET. Prostate cancer cells promote osteoblastic bone metastases through Wnts. Cancer Res 2005; 65: 7554–60.

26 Wang FZ, Sha L, Zhang WY, Wu LY, Qiao L, Li N, *et al*. Involvement of

hepatitis B X-interacting protein (HBXIP) in proliferation regulation of cells. Acta Pharmacol Sin 2007; 28: 431–8.

27 Chen Z, Li DQ, Tong L, Stewart P, Chu C, Pflugfelder SC. Targeted inhibition of p57 and p15 blocks transforming growth factor beta-inhibited proliferation of primary cultured human limbal epithelial cells. Mol Vis 2006; 12: 983–94.

28 Kobayashi K, Ouchida M, Tsuji T, Hanafusa H, Miyazaki M, Namba M*, et al.* Reduced expression of the REIC/Dkk-3 gene by promoter-hypermethylation in human tumor cells. Gene 2002; 282: 151–8.

29 Kawano Y, Kitaoka M, Hamada Y, Walker MM, Waxman J, Kypta RM. Regulation of prostate cell growth and morphogenesis by Dickkopf-3. Oncogene 2006; 25: 6528–37.

30 Wang J, Shou J, Chen X. Dickkopf-1, an inhibitor of the Wnt signaling pathway, is induced by p53. Oncogene 2000; 19: 1843–8.

31 Schlange T, Matsuda Y, Lienhard S, Huber A, Hynes NE. Autocrine WNT signaling contributes to breast cancer cell proliferation via the canonical WNT pathway and EGFR transactivation. Breast Cancer Res 2007; 9: R63.

32 Rulifson IC, Karnik SK, Heiser PW, ten Berge D, Chen H, Gu X*, et al.* Wnt signaling regulates pancreatic beta cell proliferation. Proc Natl Acad Sci USA 2007; 104: 6247–52.

33 Mikheev AM, Mikheeva SA, Maxwell JP, Rivo JV, Rostomily R, Swisshelm K*, et al.* Dickkopf-1 mediated tumor suppression in human breast carcinoma cells. Breast Cancer Res Treat 2008; 112: 263–73.

34 He X, Semenov M, Tamai K, Zeng X. LDL receptor-related proteins 5 and 6 in Wnt/beta-catenin signaling: arrows point the way. Development 2004; 131: 1663–77.

35 Spencer CA, Groudine M. Control of c-myc regulation in normal and neoplastic cells. Adv Cancer Res 1991; 56: 1–48.

36 Fernando R, Foster JS, Bible A, Strom A, Pestell RG, Rao M*, et al.* Breast cancer cell proliferation is inhibited by BAD: regulation of cyclin D1. J Biol Chem 2007; 282: 28864–73.

37 You L, He B, Xu Z, Uematsu K, Mazieres J, Fujii N*, et al.* An anti-Wnt-2 monoclonal antibody induces apoptosis in malignant melanoma cells and inhibits tumor growth. Cancer Res 2004; 64: 5385–9.

38 Zhang T, Otevrel T, Gao Z, Ehrlich SM, Fields JZ, Boman BM. Evidence that APC regulates survivin expression: a possible mechanism contributing to the stem cell origin of colon cancer. Cancer Res 2001; 61: 8664–7.

39 Marusawa H, Matsuzawa S, Welsh K, Zou H, Armstrong R, Tamm I*, et al.* HBXIP functions as a cofactor of survivin in apoptosis suppression. EMBO J 2003; 22: 2729–40.

40 Lee AY, He B, You L, Xu Z, Mazieres J, Reguart N*, et al.* Dickkopf-1 antagonizes Wnt signaling independent of beta-catenin in human mesothelioma. Biochem Biophys Res Commun 2004; 323: 1246–50.

Acta Pharmacologica Sinica (2010) 31: 211–218
© 2010 CPS and SIMM All rights reserved 1671-4083/10 $32.00
www.nature.com/aps

Original Article

The epoxyeicosatrienoic acid-stimulated phosphorylation of EGF-R involves the activation of metalloproteinases and the release of HB-EGF in cancer cells

Li-ming CHENG[1,#], Jian-gang JIANG[1,#], Zi-yong SUN[1], Chen CHEN[1], Ryan T DACKOR[2], Darryl C ZELDIN[2], Dao-wen WANG[1,*]

[1]The Institute of Hypertension and Department of Internal Medicine, Tongji Hospital, Tongji Medical College, Huazhong University of Science and Technology, Wuhan 430030, China; [2]Division of Intramural Research, National Institute of Environmental Health Sciences, NIH, Research Triangle Park, NC 27709, USA

Aim: To test the hypothesis that the epoxyeicosatrienoic acid (EET)-induced transactivation of EGF-R depends on the activation of metalloproteinases and the subsequent release of HB-EGF in cancer cells.
Methods: Exogenous 14,15-EET were added to four human-derived cancer cell lines Tca-8113, A549, HepG2, and MDA-MB-231, or these same cell lines were transfected with a mutant CYP epoxygenase (CYP102 F87V, an active 14,15-epoxygenase). The effects of elevated EET levels on the phosphorylation of tyrosine residues in the EGF receptor and on ERK1/2 activation were then assessed.
Results: Both the addition of 14,15-EET and the transfection of cells with CYP102 F87V markedly increased the phosphorylation of the tyrosine residues of EGF-R and ERK1/2, an effect that was blocked by a selective EGF-R tyrosine kinase inhibitor (tyrphostin AG1478), a broad-spectrum metalloproteinase inhibitor (1,10-phenanthroline), and an inhibitor of HB-EGF release (CRM197) in Tca-8113 cells. In addition, AG1478, 1,10-phenanthroline, and CRM197 also inhibited the tyrosine phosphorylation of EGF-R and ERK1/2 that was induced by 14,15-EET in the A549, HepG2, and MDA-MB-231 cell lines.
Conclusion: These results suggest that the EET-induced transactivation of EGF-R depends on activation of metalloproteinases and the subsequent release of HB-EGF in cancer cell lines.

Keywords: arachidonic acid; cytochrome P450 epoxygenase; epoxyeicosatrienoic acids; tumor cell proliferation; EGF-R; ERK1/2; AG1478; phenanthroline; CRM197; metalloproteinase

Acta Pharmacologica Sinica (2010) 31: 211–218; doi: 10.1038/aps.2009.184

Introduction

Arachidonic acid is a polyunsaturated fatty acid that is a component of membrane phospholipids and is acutely released in response to exposure to a number of agonists, including growth factors, cytokines, and hormones, in various cell types. Upon release, it is metabolized via the cyclooxygenase, lipoxygenase, or cytochrome P450 (CYP) monooxygenase pathways, which yield prostaglandins, leukotrienes, and epoxyeicosatrienoic acids (EETs), respectively[1, 2]. When arachidonic acid is metabolized by CYP epoxygenases, it results in the generation of four regioisomeric EETs (5,6-, 8,9-, 11,12-, and 14,15-EET)[3, 4]. We and others have demonstrated that CYP-derived EETs induce changes that have protective effects in endothelial cells, including the upregulation of endothelial nitric oxide synthase (eNOS) expression and activity, the enhancement of angiogenesis, an increase in fibrinolytic activity via the production of tissue plasminogen activator (tPA), and the inhibition of TNF-α-induced apoptosis. Additionally, CYP-derived EETs possess anti-inflammatory properties[3, 5]. Recently, EETs have been implicated in a variety of physiologic processes that are relevant to cancer pathogenesis, including the regulation of intracellular signaling pathways, gene expression, tumor cellular proliferation, and metastasis via the activation of the MAPK and PI3 kinase/Akt pathways as well as via the phosphorylation of EGF-R[6, 7].

In renal proximal tubular epithelial cells, it was found that stable CYP102 F87V expression induced 14,15-EET produc-

---

[#] The first two authors contributed equally to this work.
[*] To whom correspondence should be addressed.

E-mail dwwang@tjh.tjmu.edu.cn

Received 2009-07-18 Accepted 2009-11-19

tion and enhanced cellular proliferation[3]. Further studies in these cells demonstrated that 14,15-EET induced the activation of matrix metalloproteinases (MMPs), which in turn led to the release of heparin-binding epidermal growth factor-like growth factor (HB-EGF), a potent mitogenic EGF-R ligand[3]. In human cancer cells, however, it remains unknown whether the EGF-R phosphorylation and the malignant proliferation induced by CYP epoxygenase-derived EETs involve the activation of MMPs and/or HB-EGF release. A better understanding of the mitogenic signaling events that are initiated by CYP epoxygenase-EET signaling may lead to the development of new anti-cancer therapeutic strategies. Therefore, we investigated the effects that exogenous 14,15-EET and CYP epoxygenase overexpression had on MMP activation and EGF-R phosphorylation in the human cancer cell lines.

Materials and Methods

Materials

Tca-8113 (a human tongue squamous carcinoma cell line), A549 (a human lung cancer cell line), HepG2 (a human liver cancer cell line), MDA-MB-231 (a human breast cancer cell line) were obtained from the American Type Culture Collection (Manassas, VA). Chemicals and reagents were obtained as follows: Cell culture medium were purchased from Hyclone (Logan, UT); antibodies against epidermal growth factor receptor (EGF-R) and phospho-EGF-R from Cell Signaling Technology (Beverly, MA); anti-extracellular signal-regulated kinase (ERK) and anti-phospho-ERK antibodies from New England Biolabs, Inc (Beverly, MA); antibodies against β-actin from Neomarkers (Fremont, CA); horseradish peroxidase-conjugated secondary antibodies (goat anti-rabbit immunoglobulin G and rabbit anti-mouse immunoglobulin G) from KPL (Gaithersburg, MD); enhanced chemiluminescence reagents from Pierce, Inc (Rockford, IL); 14,15-EET from Cayman Chemical Co (Ann Arbor, MI); AG1478 (EGF-R-selective tyrosine kinase inhibitor) from Calbiochem (San Diego, CA); and EGF, 1,10-phenanthroline (a non-specific MMP inhibitor) and CRM197 (an inhibitor of HB-EGF release) from Sigma Chemical Co (St Louis, MO). All other reagents were purchased from standard commercial suppliers.

Adeno-associated virus (AAV)-mediated CYP epoxygenase overexpression

The recombinant adeno-associated virus (rAAV) vector pXXUF1, packaging plasmid pXX2, adenovirus helper plasmid pXX6, and an rAAV plasmid containing the GFP cDNA (GFP-pUF1) were generous gifts from Dr Xiao XIAO (University of Pittsburgh, Pittsburgh, PA). CYP102 F87V is a mutant P450 that is derived from *Bacillus megaterium* ($P450_{BM3}$) in which phenylalanine 87 is replaced with valine, converting it to a highly regio- and stereoselective epoxygenase that biosynthesizes 14(S),15(R)-EET from arachidonic acid. The coding region of the CYP102 F87V mutant was subcloned into pXXUF1 downstream from the cytomegalovirus promoter to produce the construct CYP102 F87V-pUF1. The rAAVs were produced and purified as previously described[3, 8, 9] and their titers were determined by dot blot hybridization. The eluted rAAV was then aliquoted and stored at -80 °C. The resultant rAAVs were designated rAAV-CYP102 F87V and rAAV-GFP. Next, Tca-8113 cells were infected with rAAV-CYP102 F87V or rAAV-GFP (about 50 virions/cell) and cultured for one week to allow them to obtain specifying expression. These cells were used for further experiments as detailed below.

Cell culture and cell proliferation assays

Tca-8113 cells were cultured at 37 °C in DMEM containing 10% (*v/v*) bovine serum, 100 mg/mL streptomycin, and 100 IU/mL penicillin in a humidified atmosphere containing 5% CO_2. The cells were seeded onto 96-well plates (about 1×10^4/well) in DMEM containing 10% bovine serum in a final volume of 0.2 mL. Six parallel wells were set up for control and treated group. Once the cells reached 60% confluence, the medium was changed to serum-free DMEM and the cells were incubated at 37 °C for 12 h to allow for synchronization. Next, 14,15-EET (250 nmol/L) and AG1478 (100 nmol/L) were added to the medium with ethanol used as the vehicle control. After 24 h, 3-(4,5-dimethylthiazol-2-yl)-2,5-diphenyltetrazolium bromide (MTT) (20 μL/well of 5 mg/mL in PBS) was added to the culture medium and the cells were incubated at 37 °C for 4 more hours, at which point the reaction was stopped by the addition of 100 μL DMSO. The reaction product was then quantified by measuring the absorbance at 490 nm using an ELISA reader (Elx800, China).

Immunoblot analysis

Tca-8113, A549, HepG2, and MDA-MB-231 cells were treated with 14,15-EET (250 nmol/L) or EGF (20 ng/mL) with and without various inhibitors, including AG1478 (100 nmol/L), CRM197 (10 μg/mL), and 1,10-phenanthroline (100 μmol/L). The rAAV-infected cells were treated with the inhibitors AG1478 (100 nmol/L), CRM197 (10 μg/mL), and 1,10-phenanthroline (100 μmol/L). Cells were then harvested for Western blot analysis to allow the detection of signaling molecules. Cells were placed on ice, washed twice with ice-cold PBS, and then lysed in RIPA lysis buffer containing 50 mmol/L Tris (pH 8.0), 150 mmol/L NaCl, 0.1% sodium dodecyl sulfate (SDS), 1% Nonidet P-40 (NP-40), 0.5% sodium deoxycholate, 0.02% sodium azide (NaN_3), 1 μg/mL aprotonin, and 1 mmol/L phenylmethylsulfonyl fluoride. Solubilized lysates were centrifuged at 10000×*g* for 15 min. Total protein concentrations were determined by the Bradford assay. After the supernatants were heated to 95 °C for 10 min, they were electrophoresed on SDS-PAGE (8%–12%) gradient gels and transferred to PVDF membranes. Blots were incubated overnight at 4 °C with primary antibodies and washed 4 times with TBST before they were probed with horseradish peroxidase-conjugated secondary antibodies for 2 h at room temperature. Blots were then visualized with enhanced chemiluminescence reagent and the optical densities of the bands were semi-quantified by the Gene Genius Bio Imaging System (SynGene, USA). In some cases, blots were stripped and reprobed with other antibodies.

Statistical analysis

Data were expressed as the mean±SEM for at least three separate experiments. Statistical evaluation was performed using Student's *t*-test or ANOVA, as was appropriate for the situation. *P*-values less than 0.05 were considered to be statistically significant.

Results

14,15-EET induces the phosphorylation of EGF-R and ERK1/2

When cells were incubated with 14,15-EET, there was a dose-dependent increase in the phosphorylation of EGF-R and ERK1/2 observed (Figure 1A and 1B), a finding that had been previously demonstrated by our group[6]. We treated cells with the EGF-R-selective tyrosine kinase inhibitor tyrphostin AG1478 to examine its effect on the EET-induced phosphorylation of EGF-R and ERK1/2. Our results showed that AG1478 attenuated the EET-induced phosphorylation of EGF-R and ERK1/2 (Figure 1C). As expected, AG1478 also attenuated the EGF-induced phosphorylation of EGF-R and ERK1/2 (Figure 1D). These results demonstrate that 14,15-EET enhances the phosphorylation and activation of ERK1/2 in Tca-8113 cells by inducing the transactivation of EGF-R.

14,15-EET promotes cancer cell proliferation via EGF-R activation

We next examined whether 14,15-EET-stimulated proliferation of Tca-8113 cells occurred via the transactivation of EGF-R. The MTT assays showed that 14,15-EET (250 nmol/L) significantly increased Tca-8113 cell proliferation as compared to the vehicle control (26% increase, *P*<0.05). AG1478 completely abolished the proliferative effect induced by 14,15-EET (*P*<0.05, Figure 2). These results suggest that 14,15-EET promotes the proliferation of Tca-8113 cells through transactivation of EGF-R.

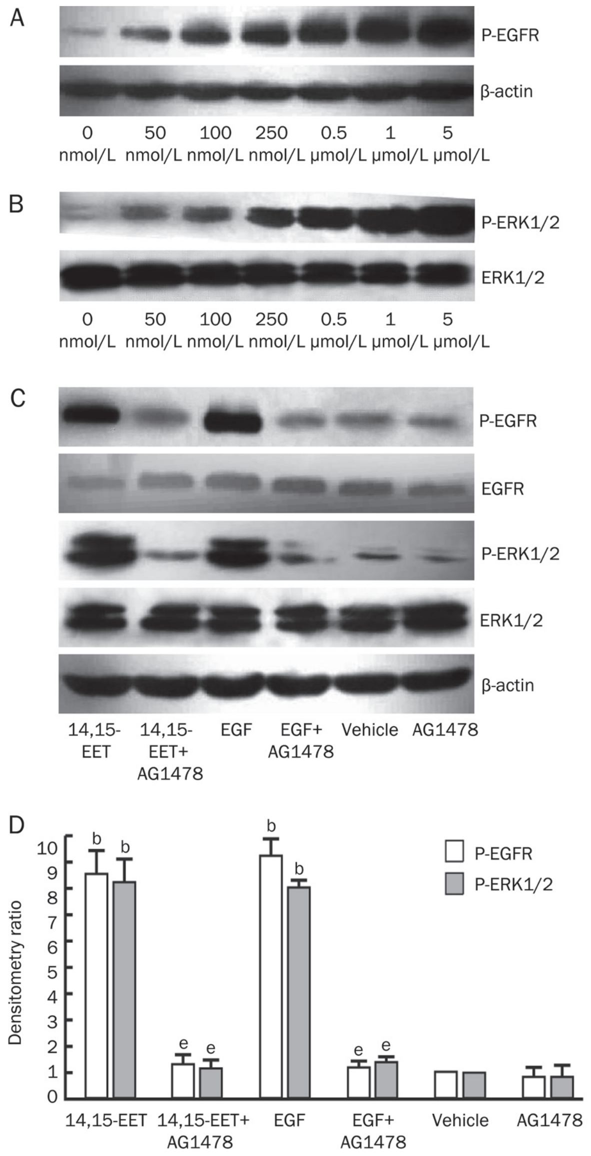

Figure 1. 14,15-EET increases the tyrosine phosphorylation of EGF-R and ERK1/2 in a dose-dependent manner. Serum-deprived Tca-8113 cells were treated with vehicle (ethanol) or different concentrations of 14,15-EET (50, 100, 250, 500 nmol/L, 1, and 5 μmol/L) for 30 min. (A) Phosphorylation of EGF-R was detected using a site-specific tyrosine antibody to EGF-R; β-actin was used as a loading control. (B) Phosphorylated ERK1/2 and total ERK1/2 were analyzed by Western blots. (C) and (D) Effect of tyrphostin AG1478 on EGF-R and ERK1/2 phosphorylation. Serum-deprived Tca-8113 cells were pretreated with or without 100 nmol/L AG1478 for 60 min. They were then stimulated for 30 min with 250 nmol/L 14,15-EET or 20 ng/mL EGF. Phosphorylated EGF-R, total EGF-R, phosphorylated ERK1/2, and total ERK1/2 were detected using appropriate antibodies. (C) Representative Western blots of three separate experiments with similar results. (D) Quantification of three separate experiments by densitometry. ^{b}*P*<0.05 *vs* vehicle control group; ^{e}*P*<0.05 *vs* no signaling pathway inhibitor group.

Effects of 1,10-phenanthroline and diphtheria toxin/CRM197 on 14,15-EET-induced EGF-R activation

To evaluate whether the activation of EGF-R in Tca-8113 cells resulted from the release of HB-EGF due to proteolytic processing by MMPs, we investigated the effects that 1,10-phenanthroline (a non-specific MMP inhibitor) and diphtheria toxin/CRM197 (an inhibitor of HB-EGF release) had on EGF-R and ERK1/2 phosphorylation. The MMP inhibitor 1,10-phenanthroline is a heterocyclic organic compound that forms strong complexes with most metal ions and thus acts as a non-specific metalloproteinases inhibitor[10, 11]. The transmembrane precursor of HB-EGF (pro-HB-EGF) also serves as the unique high-affinity receptor for diphtheria toxin. CRM197, a nontoxic and catalytically inactive (Glu-52) mutant of diphtheria toxin that binds to the extracellular domain of HB-EGF and specifically inhibits the mitogenic activity of HB-EGF[12, 13]. Our results showed that when Tca-8113 cells were treated with 1,10-phenanthroline (100 μmol/L), 14,15-EET-induced EGF-R and ERK1/2 phosphorylation were completely blocked, but that EGF-induced EGF-R and ERK1/2 phosphorylation was not inhibited (Figure 3A and 3B). Furthermore, pretreatment of Tca-8113 cells with CRM197 (10 μg/mL) led to a significant inhibition of the phosphorylation of EGF-R and ERK1/2 by 14,15-EET. However, CRM197 pretreatment had no effect on the EGF-induced phosphorylation of these molecules (Figure

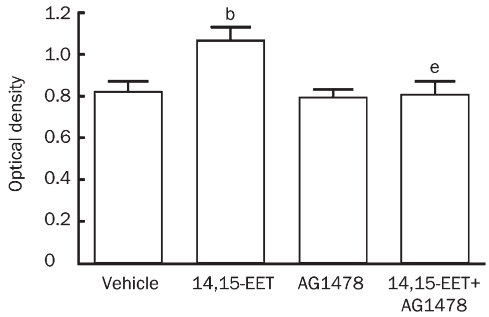

Figure 2. The proliferative effect of 14,15-EET in Tca-8113 cells is abrogated by AG1478. Treatment with 14,15-EET (250 nmol/L) stimulated Tca-8113 cell proliferation. Cell proliferation was 26% higher in the treatment group than in the vehicle control group ($^{b}P<0.05$). Pretreatment with AG1478 completely abolished the proliferative effect induced by 14,15-EET ($^{e}P<0.05$).

3C and 3D). These results are consistent with those obtained with tyrphostin AG1478 and show that the activation of MMPs and subsequent release of HB-EGF are important steps in the phosphorylation of EGF-R and ERK1/2 that is induced by 14,15-EET.

To further investigate the possible mechanism by which 14,15-EET transactivates EGFR, we examined the effects of AG1478, 1,10-phenanthroline, and CRM197 on 14,15-EET-induced EGF-R activation in three other tumor cell lines: A549, HepG2, and MDA-MB-231. As expected, we observed a similar profile to the one we noted in the experiments described above: 14,15-EET increased the levels of phosphorylated EGFR and ERK1/2 in these tumor cells and the 14,15-EET induced-phosphorylation of EGF-R and ERK1/2 was dramatically attenuated by AG1478, 1,10-phenanthroline, and CRM197 (Figure 4). There was no synergistic effect observed when 1,10-phenanthroline and CRM197 were added in combination. These data further indicate that the release of HB-EGF and activation of MMPs both exert regulatory effects on the phosphorylation of EGF-R and ERK1/2 that is induced by 14,15-EET in tumor cells.

Effects of 14,15-epoxygenase CYP102 F87V on the transactivation of EGF-R

We and others have demonstrated that CYP102 F87V is a 14,15-epoxygenase that efficiently metabolizes arachidonic

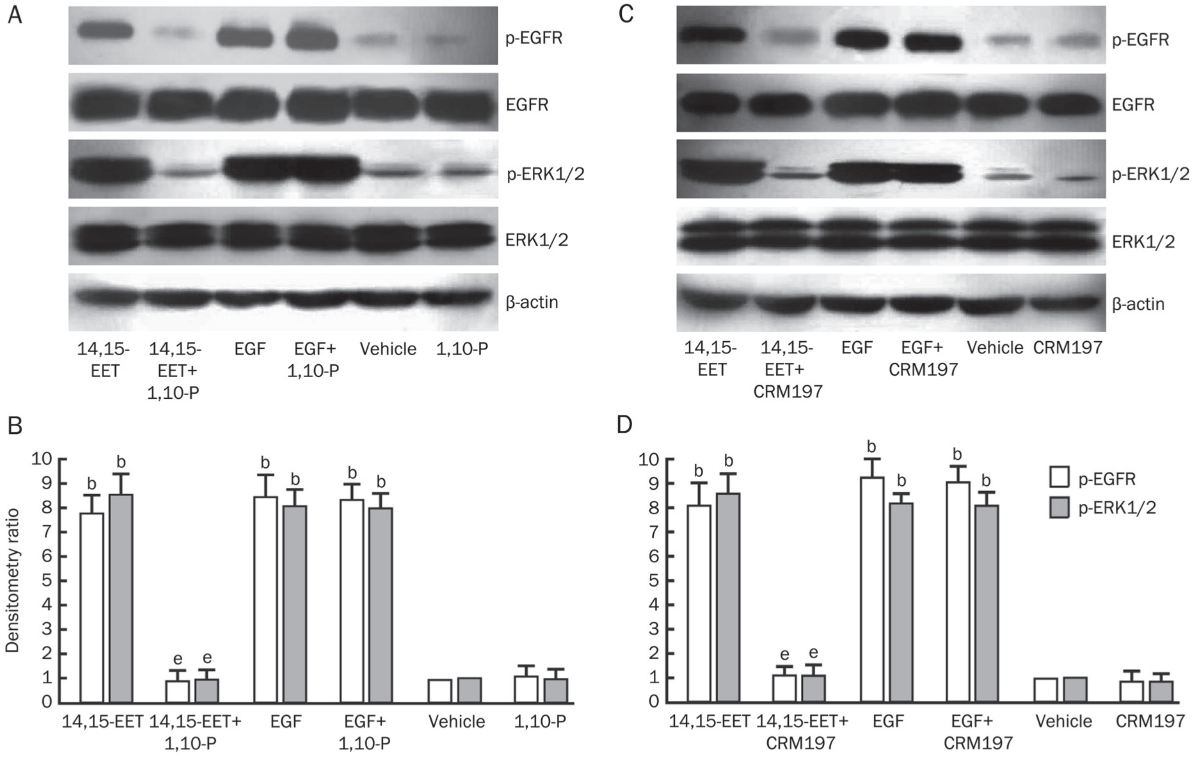

Figure 3. Effects of 1,10-phenanthroline and CRM197 on the 14,15-EET-induced tyrosine phosphorylation of EGF-R and ERK1/2 in Tca-8113 cells. Serum-deprived Tca-8113 cells were incubated with or without 100 μmol/L of 1,10-phenanthroline or 10 μg/mL of CRM197 for 60 min. They were then stimulated for 30 min with 250 nmol/L 14,15-EET or 20 ng/mL EGF. Phosphorylated EGF-R, total EGF-R, phosphorylated ERK1/2, and total ERK1/2 were detected with the corresponding antibodies. (A) Results of incubation with 1,10-phenanthroline. The results shown are representative of three separate experiments with similar results. (B) Densitometric quantification of three separate experiments examining the effects of incubation with 1,10-phenanthroline. (C) Results of incubation with CRM197. The results shown are representative of three separate experiments with similar results. (D) Densitometric quantification of three separate experiments examining the effects of incubation with CRM197. $^{b}P<0.05$ *vs* vehicle control group; $^{e}P<0.05$ *vs* no signaling pathway inhibitor group.

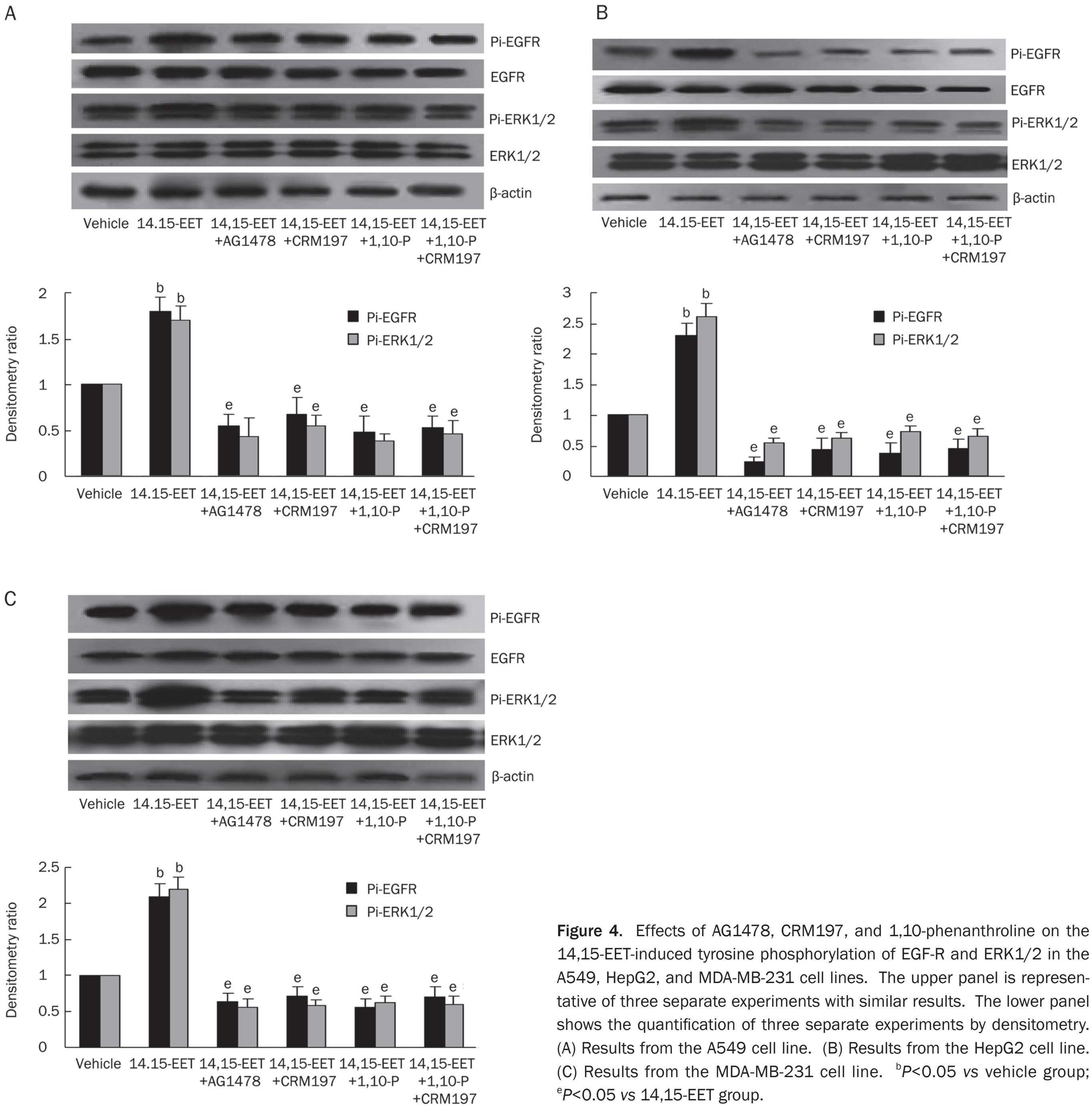

Figure 4. Effects of AG1478, CRM197, and 1,10-phenanthroline on the 14,15-EET-induced tyrosine phosphorylation of EGF-R and ERK1/2 in the A549, HepG2, and MDA-MB-231 cell lines. The upper panel is representative of three separate experiments with similar results. The lower panel shows the quantification of three separate experiments by densitometry. (A) Results from the A549 cell line. (B) Results from the HepG2 cell line. (C) Results from the MDA-MB-231 cell line. $^{b}P<0.05$ *vs* vehicle group; $^{e}P<0.05$ *vs* 14,15-EET group.

acid to 14,15-EET[6]. In this study, we infected Tca-8113 cells with rAAV-CYP102 F87V to determine if CYP epoxygenase overexpression could transactivate EGF-R by activation of the HB-EGF-shedding mechanism. The efficiency of gene transfer was evaluated one week after infection. To assess EET levels, we determined the concentration of its stable metabolites. Western blot analysis revealed robust CYP102 F87V expression in Tca-8113 cells infected with rAAV-CYP102 F87V (Figure 5A). Moreover, we examined the activity of CYP102 F87V in rAAV-CYP102 F87V infected cells. Given the instability of 14,15-EET, the levels of 14,15-DHET(the stable metabolites of 14,15-EET) were assessed using an ELISA assay. The results showed that there was a dramatic increase in 14,15-DHET levels in rAAV-CYP102 F87V infected cells as compared to untreated cells (332±117 pg/250 μg protein *vs* 122±4 pg/250 μg protein, $P<0.05$) (Figure 5B). rAAV-CYP102 F87V infection significantly promoted phosphorylation of EGF-R and ERK1/2, a finding that we had observed previously[6]. Importantly, the induction of phosphorylation conferred by CYP102 F87V overexpression was abolished by the addition of AG1478 2 h before cell harvesting (Figure 6). Furthermore, EGF-R and ERK1/2 phosphorylation were also blocked when CYP102

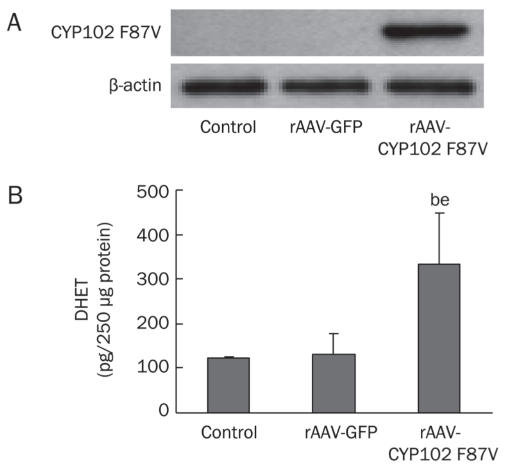

Figure 5. Expression of CYP102 in tumor cells after rAAV-CYP102 F87V gene transfer. (A) CYP102 F87V expression in rAAV-CYP102 F87V-infected cells. (B) CYP102 F87V activity (14,15-DHET production) in rAAV-CYP102 F87V-infected cells. Data are presented as mean±SEM. $^{b}P<0.05$ *vs* control; $^{e}P<0.05$ *vs* rAAV-GFP.

F87V-infected Tca-8113 cells were treated with 1,10-phenanthroline or CRM197 (Figure 6).

Discussion

Multiple studies have shown EETs to be potent mitogens that activate EGF-R and ERKs in various cell types[3, 6]. Previous studies by our group have also demonstrated that EETs increased the expression levels and activity of MMPs in various human cancer cell lines[7]. However, the role of EETs in the activation of EGF-R in human cancer cells remains unclear. In the present study, we found that the addition of 14,15-EET or the overexpression of a selective 14,15-EET epoxygenase can induce the activation of EGF-R and ERK1/2 in multiple human-derived cancer cell lines: Tca-8113, A549, HepG2, and MDA-MB-23. These signaling events were abolished by the addition of the tyrosine kinase inhibitor of EGF-R, AG1478. Interestingly, the addition of 1,10-phenanthroline (a non-specific MMP inhibitor) or diphtheria toxin/CRM197 (an inhibitor of HB-EGF release) also blocked the EET-induced activation of EGF-R and ERK1/2. As expected, neither the inhibition of MMP activity nor the inhibition of HB-EGF cleavage blocked the EGF-induced EGF-R phosphorylation or its downstream activation of ERK1/2 in the cancer cell lines tested. Together, these results demonstrate that MMP activation with subsequent HB-EGF cleavage and release is essential for EET-induced EGF-R activation in human cancer cells.

HB-EGF is synthesized as a type I transmembrane protein in a manner that is similar to the way in which other members of the epidermal growth factor (EGF) family are synthesized. Pro-HB-EGF can be enzymatically shed within the juxtamembrane region, leading to the release of a soluble 14-22 kDa growth factor[13]. The ectodomain shedding of pro-HB-EGF is induced by various stimuli, including phorbol ester 12-O-tetradecanoylphorbol-13-acetate (TPA)[14, 15] and calcium ionophore[16] as well as various growth factors and cytokines[17]. G-protein coupled receptor (GPCR) agonists also stimulate pro-HB-EGF shedding, which in turn mediates EGF-R transactivation via GPCR signaling[18, 19]. Metalloproteinases have been shown to be responsible for the proteolytic cleavage of pro-HB-EGF because the ectodomain shedding of pro-HB-EGF is efficiently inhibited by various metalloproteinase inhibitors. Protein kinase C (PKC) and mitogen-activated protein kinase (MAPK) may be required for the activation of appropriate metalloproteinases as they are known to be involved in the intracellular signaling pathway that leads to pro-HB-EGF shedding[20, 21].

In human colon carcinoma cells, IL-8 promotes cell proliferation and migration via the metalloproteinase-induced cleavage of pro-HB-EGF[22]. Additionally, it has been shown that lysophosphatidic acid (LPA)-induced ectodomain shedding of pro-HB-EGF is critical for tumor formation in ovarian cancer[23], and that the deoxycholic taurine (DCT)-induced transactivation of EGF-R is mediated by the MMP-7-catalyzed release of the EGF-R ligand HB-EGF in H508 human colon cancer cells[24]. In this study, we demonstrated that the addition of 14,15-EET as well as the overexpression of a 14,15-EET-specific epoxygenase leads to EGF-R transactivation via MMP activation and HB-EGF release in four cancer cell lines. However, the specific metalloproteinase responsible for the 14,15-EET-induced cleavage of pro-HB-EGF has not yet been identified and thus requires further study.

The transactivation of EGF-R and the subsequent activation of downstream ERKs by the metalloproteinase-mediated release of soluble HB-EGF plays an important role in EET-stimulated mitogenic signaling. The tyrosine kinase inhibitor of EGF-R, AG1478, may have significant therapeutic value in controlling the malignant growth of various cancers. However, as demonstrated in previous studies, EETs activate the PI3K/Akt signaling pathway in different cell lines and tissues, which can also lead to mitogenic effects[3, 6]. The relative importance that the PI3K/Akt and EGF-R/ERK/MMP signaling pathways have in mediating the mitogenic effects of the products of CYP epoxygenase remains to be determined.

In summary, this study reveals that EGF-R transactivation is a crucial event in the mitogenic signaling pathways initiated by EETs in cancer cells. In addition, the EET-induced transactivation of EGF-R is mediated by the activation of metalloproteinases that cleave pro-HB-EGF from the cell membrane and release active HB-EGF, which subsequently binds to EGF-R and activates downstream ERKs. Thus, CYP epoxygenase-derived EETs may lead to the malignant proliferation of cancer cells as a result of EGF-R transactivation via an MMP-HB-EGF signaling pathway. Further studies will be required to identify the precise metalloproteinases that are activated by EETs in cancer cells and to elucidate the relative importance that EGF-R/ERK/MMP and other signaling pathways have in mediating the mitogenic effects of the products of CYP epoxygenase.

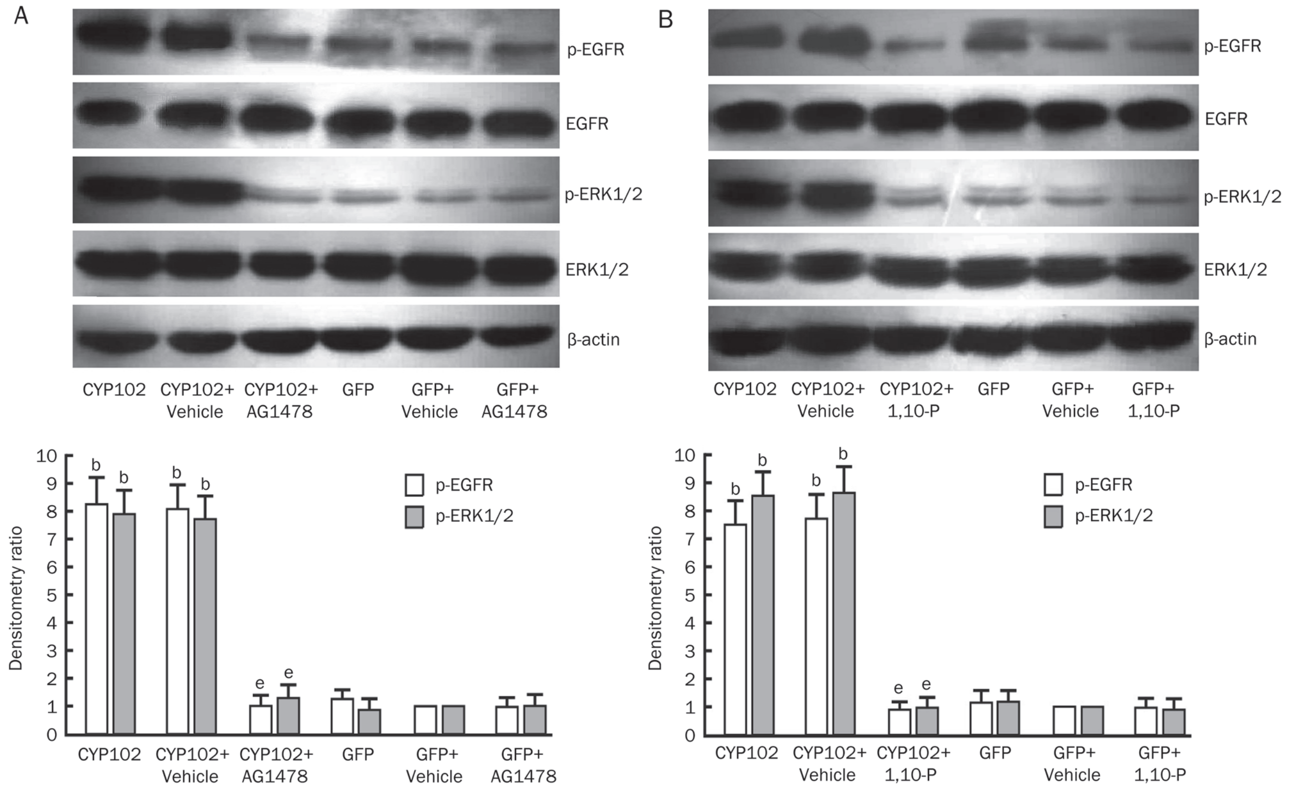

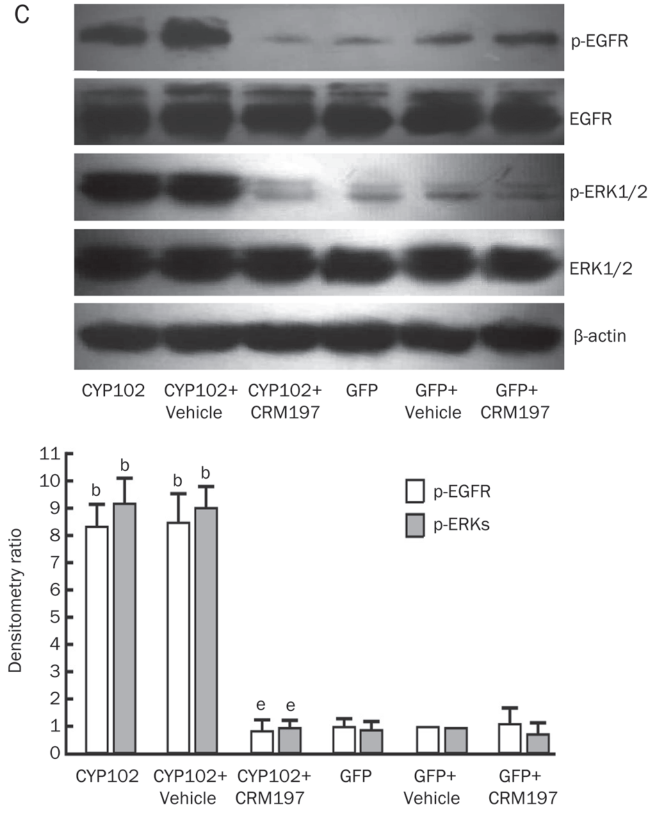

Figure 6. Effects of tyrphostin AG1478, 1,10-phenanthroline, and the nontoxic mutant of diphtheria toxin CRM197 on the activation of EGF-R and ERK1/2 in rAAV-CYP102 F87V-transfected Tca-8113 cells. Tca-8113 cells were transfected with rAAV-CYP102 F87V or rAAV-GFP (GFP) and cultured for one week to allow for maximal expression. Serum-starved cells were treated with the indicated agents and cell lysates were immunoblotted with the indicated antibodies. Upper panels are representative of three separate experiments with similar results. Lower panels show the quantification of three separate experiments by densitometry. (A) Results shown are for tyrphostin AG1478. (B) Results shown are for 1,10-phenanthroline. (C) Results shown are for CRM197. $^{b}P<0.05$ *vs* rAAV-GFP control group; $^{e}P<0.05$ *vs* no signaling pathway inhibitor group.

Acknowledgements

This work was supported by the International Collaboration Project (No̲ 2005DFA30880), the 973 grant (2007CB512004), and two National Natural Science Foundation of China grant (30430320, 30770882). This work was also funded, in part, by the Intramural Research Program of the NIH and the National

Institute of Environmental Health Sciences (Z01 ES025034).

Author contribution

Li-ming CHENG, Dao-wen WANG designed research; Li-ming CHENG, Jian-gang JIANG, Chen CHEN performed research; Zi-yong SUN, Ryan T DACKOR, Darryl C ZELDIN contributed new analytical tools and reagents; Li-ming CHENG, Dao-wen WANG, Ryan T DACKOR, Darryl C ZELDIN analyzed data; Li-ming CHENG, Dao-wen WANG wrote the paper.

Abbreviations

EET, epoxyeicosatrienoic acid; HETE, hydroperoxyeicosatetraenoic acid; CYP, cytochrome P450; EGF-R, epidermal growth factor receptor; p-EGFR, phosphorylated epidermal growth factor receptor; HB-EGF, heparin-binding epidermal growth factor-like growth factor; TNF-α , tumor necrosis factor-α; eNOS, endothelial nitric oxide synthase; tPA, tissue plasminogen activator; MMP, matrix metalloproteinase; ERK, extracellular signal-regulated kinase; p-ERK, phosphorylated extracellular signal-regulated kinase; MAPK, mitogen-activated protein kinase; PI3K, phosphatidylinositol 3-kinase; MTT, 3-(4,5-dimethylthiazol-2-yl)-2,5-diphenyltetrazolium bromide; DMEM, Dulbecco's modified Eagle's medium; DMSO, dimethyl sulfoxide; PBS, phosphate-buffered saline; AG1478, a selective epidermal growth factor receptor blocker; CRM197, an inhibitor of HB- epidermal growth factor release; rAAV, recombinant adeno-associated virus; EGF, epidermal growth factor; SDS, sodium dodecyl sulfate; NP-40, Nonidet P-40; NaN_3, sodium azide; TPA, 12-O-tetradecanoylphorbol-13-acetate; GPCR, G-protein coupled receptor; PKC, protein kinase C; LPA, lysophosphatidic acid; DHET, dihydroxyeicosatrienoic acid; DCT, deoxycholic taurine; Akt, cellular homolog of the v-alt oncogene, an S/T protein kinase; PKB, protein kinase B.

References

1 Funk CD. Prostaglandins and leukotrienes: advances in eicosanoid biology. Science 2001; 294: 1871–5.

2 Kroetz DL, Zeldin DC. Cytochrome P450 pathways of arachidonic acid metabolism. Curr Opin Lipidol 2002; 13: 273–83.

3 Chen C, Li G, Liao W, Wu J, Liu L, Ma D, *et al*. Selective inhibitors of CYP2J2 related to terfenadine exhibit strong activity against human cancers *in vitro* and *in vivo*. J Pharmacol Exp Ther 2009; 329: 908–18.

4 Capdevila JH, Falck JR, Harris RC. Cytochrome P450 and arachidonic acid bioactivation. Molecular and functional properties of the arachidonate monooxygenase. J Lipid Res 2000; 41: 163–81.

5 Node K, Ruan XL, Dai J, Yang SX, Graham L, Zeldin DC, *et al*. Activation of Galpha s mediates induction of tissue-type plasminogen activator gene transcription by epoxyeicosatrienoic acids. J Biol Chem 2001; 276: 15983–9.

6 Jiang JG, Chen CL, Card JW, Yang S, Chen JX, Fu XN, *et al*. Cytochrome P450 2J2 promotes the neoplastic phenotype of carcinoma cells and is up-regulated in human tumors. Cancer Res 2005; 65: 4707–15.

7 Jiang JG, Ning YG, Chen C, Ma D, Liu ZJ, Yang S, *et al*. Cytochrome p450 epoxygenase promotes human cancer metastasis. Cancer Res 2007; 67: 6665–74.

8 Xiao X, Li J, Samulski RJ. Efficient long-term gene transfer into muscle tissue of immunocompetent mice by adeno-associated virus vector. J Virol 1996; 70: 8098–108.

9 Xiao X, Li J, Samulski RJ. Production of high-titer recombinant adeno-associated virus vectors in the absence of helper adenovirus. J Virol 1998; 72: 2224–32.

10 Kiss Z. The zinc chelator 1,10-phenanthroline enhances the stimulatory effects of protein kinase C activators and staurosporine, but not sphingosine and H_2O_2, on phospholipase D activity in NIH 3T3 fibroblasts. Biochem J 1994; 298 (Pt 1): 93–8.

11 Chen J, Chen JK, Neilson EG, Harris RC. Role of EGF receptor activation in angiotensin II-induced renal epithelial cell hypertrophy. J Am Soc Nephrol 2006, 17: 1615–23.

12 Naglich JG, Metherall JE, Russell DW, Eidels L. Expression cloning of a diphtheria toxin receptor: identity with a heparin-binding EGF-like growth factor precursor. Cell 1992; 69: 1051–61.

13 Mitamura T, Higashiyama S, Taniguchi N, Klagsbrun M, Mekada E. Diphtheria toxin binds to the epidermal growth factor (EGF)-like domain of human heparin-binding EGF-like growth factor/diphtheria toxin receptor and inhibits specifically its mitogenic activity. J Biol Chem 1995; 270: 1015–9.

14 Goishi K, Higashiyama S, Klagsbrun M, Nakano N, Umata T, Ishikawa M, *et al*. Phorbol ester induces the rapid processing of cell surface heparin-binding EGF-like growth factor: conversion from juxtacrine to paracrine growth factor activity. Mol Biol Cell 1995; 6: 967–80.

15 Raab G, Higashiyama S, Hetelekidis S, Abraham JA, Damm D, Ono M, *et al*. Biosynthesis and processing by phorbol ester of the cells surface-associated precursor form of heparin-binding EGF-like growth factor. Biochem Biophys Res Commun 1994; 204: 592–7.

16 Dethlefsen SM, Raab G, Moses MA, Adam RM, Klagsbrun M, Freeman MR. Extracellular calcium influx stimulates metalloproteinase cleavage and secretion of heparin-binding EGF-like growth factor independently of protein kinase C. J Cell Biochem 1998; 69: 143–53.

17 Raab G, Klagsbrun M. Heparin-binding EGF-like growth factor. Biochim Biophys Acta 1997; 1333: F179–99.

18 Daub H, Weiss FU, Wallasch C, Ullrich A. Role of transactivation of the EGF receptor in signalling by G-protein-coupled receptors. Nature 1996; 379: 557–60.

19 Prenzel N, Zwick E, Daub H, Leserer M, Abraham R, Wallasch C, *et al*. EGF receptor transactivation by G-protein-coupled receptors requires metalloproteinase cleavage of proHB-EGF. Nature 1999; 402: 884–8.

20 Izumi Y, Hirata M, Hasuwa H, Iwamoto R, Umata T, Miyado K, *et al*. A metalloprotease-disintegrin, MDC9/meltrin-gamma/ADAM9 and PKCdelta are involved in TPA-induced ectodomain shedding of membrane-anchored heparin-binding EGF-like growth factor. EMBO J 1998; 17: 7260–72.

21 Gechtman Z, Alonso JL, Raab G, Ingber DE, Klagsbrun M. The shedding of membrane-anchored heparin-binding epidermal-like growth factor is regulated by the Raf/mitogen-activated protein kinase cascade and by cell adhesion and spreading. J Biol Chem 1999; 274: 28828–35.

22 Itoh Y, Joh T, Tanida S, Sasaki M, Kataok H, Itoh K, *et al*. IL-8 promotes cell proliferation and migration through metalloproteinase-cleavage proHB-EGF in human colon carcinoma cells. Cytokine 2005; 29: 275–82.

23 Miyamoto S, Hirata M, Yamazaki A, Kageyama T, Hasuwa H, Mizushima H, *et al*. Heparin-binding EGF-like growth factor is a promising target for ovarian cancer therapy. Cancer Res 2004; 64: 5720–7.

24 Cheng K, Xie G, Raufman JP. Matrix metalloproteinase-7-catalyzed release of HB-EGF mediates deoxycholyltaurine-induced proliferation of a human colon cancer cell line. Biochem Pharmacol 2007; 73: 1001–12.

Acta Pharmacologica Sinica (2010) 31: 219–226
© 2010 CPS and SIMM All rights reserved 1671-4083/10 $32.00
www.nature.com/aps

Original Article

Bicyclol protects HepG2 cells against *D*-galactosamine-induced apoptosis through inducing heat shock protein 27 and mitochondria associated pathway

Xiu-qi BAO, Geng-tao LIU*

Department of Pharmacology, Institute of Materia Medica, Chinese Academy of Medical Sciences and Peking Union Medical College, Beijing 100050, China

---

Aim: To study the inducing effect of bicyclol on heat shock protein 27 (HSP27) and its role on anti-apoptosis in HepG2 cells intoxicated with *D*-galactosamine (*D*-GalN).
Methods: HepG2 cells were treated with various concentrations of bicyclol and then subjected to *D*-GalN intoxication. Apoptosis was assayed by hoechst 33258 staining and flow cytometry analysis. HSP27, cytochrome *c*, apoptosis inducing factor (AIF) and c-Jun N-terminal kinase (JNK) were assayed by Western blot. Heat shock factor 1 (HSF1) was determined by electrophoretic mobility shift assay and the interactions of HSP27 with cytochrome *c* and AIF were detected by co-immunoprecipitation.
Results: The results showed that bicyclol induced HSP27 protein and mRNA expression in HepG2 cells in both time- and dose-dependent manners (the maximal response: 1.23 fold increase at 100 μmol/L). Bicyclol treatment stimulated HSF1 activation and increased the HSF1-HSE binding activity (the maximal response: 2.1 fold increase at 100 μmol/L). This inducing effect of bicyclol on HSP27 and HSF1 was markedly blocked by quercetin. Pretreatment of the cells with bicyclol markedly attenuated *D*-GalN-induced apoptosis and the release of cytochrome *c* and AIF from mitochondria. The induced HSP27 by bicyclol suppressed the activity of caspase-3 and the phosphorylation of JNK caused by *D*-GalN in HepG2 cells. All the above effect of bicyclol against *D*-GalN-induced hepatocytes apoptosis were significantly reversed by quercetin.
Conclusion: HSP27 is involved in the anti-hepatocytes apoptosis of bicyclol, and this effect of bicyclol-induced HSP27 is mainly through inhibition of mitochondria and JNK apoptotic pathways.

Keywords: bicyclol; heat shock protein; mitochondria; c-Jun N-terminal kinase; apoptosis; HepG2 cells; cytochrome *c*; D-galactosamine

---

Acta Pharmacologica Sinica (2010) 31: 219–226; doi: 10.1038/aps.2009.194

Introduction

Bicyclol is a novel anti-hepatitis drug which has been wildly used to treat chronic viral hepatitis in China since 2004. Its chemical name is 4,4′-dimethoxy-5,6,5′,6′-*bis*(methylenedioxy)-2-hydroxy-methyl-2′-methoxycarbonyl biphenyl. Pharmacologically, bicyclol protects against chemical-induced liver injury in mice and rats[1–3], inhibits hepatitis virus replication in duck viral hepatitis and in a HepG2.2.15 cell line[4, 5] and anti-liver fibrosis in rat carbon tetrachloride model[6]. Bicyclol exerts most of its effects by multiple pathways such as eliminating free radical, maintenance of mitochondrial glutathione redox status, anti-inflammation and inhibiting fibrogenesis[7].

Heat shock proteins (HSPs) are a family of constitutive and inducible expressed gene products that collectively function to maintain cellular protein conformation during stressful conditions. The synthesis of HSPs, which allows cells to adapt to gradual changes in their environment and to survive in otherwise lethal conditions, can be induced by a variety of mild stressors including exposure to oxidants, heat, hypoxia, and low pH, all of which can affect protein conformation[8]. It was reported that overexpression of HSPs suppressed apoptosis of hepatocytes *in vitro* and *in vivo*[9, 10]. In addition, induction of small HSPs such as HSP27 has been shown to exert cytoprotective effects against various stresses in many tissues including the liver[11].

Hepatocytes apoptosis plays an important role in pathogenesis of liver disease including viral hepatitis[12]. *D*-galactosamine (*D*-GaIN) induces hepatocyte cell death *in vivo*[13] and

---

* To whom correspondence should be addressed.
E-mail liugt@imm.ac.cn
Received 2009-09-21 Accepted 2009-12-09

in vitro[14], which is a suitable experimental model based on its capacity to reduce the intracellular pool of uridine monophosphate in hepatocytes, thus inhibiting the synthesis of RNA and proteins. Our recent study demonstrated that bicyclol significantly induced the hepatic heat shock protein 27 and 70 in normal mice, and the protective action of bicyclol against acetaminophen hepatotoxicity[15] and concanavalin A (Con A)[16] induced liver injury also attributed to its induction of hepatic HSPs. However, the molecular mechanism against hepatocyte injury is still not thoroughly elucidated. In this study, HepG2 cells were used to explore the mechanisms of bicyclol-induced HSP27 in the protection against D-GaIN-induced apoptosis of hepatocyte.

Materials and methods

Cell culture and treatment

Human hepatoma HepG2 cells were cultured in minimal essential medium with Earle's salts supplemented with 10% (*v/v*) heat-inactivated fetal bovine serum and incubated in a humidified incubator with 5% CO_2/95% air at 37 °C.

In the time-course study of the inducing effect of bicyclol on HSP27, a dose of bicyclol 50 μmol/L was used. Three different dosages of bicyclol 25 μmol/L, 50 μmol/L, and 100 μmol/L were added to the cells for dose-effect relationship study, each with 20 μmol/L of quercetin (Sigma,USA) simultaneously. To investigate the protective effects of bicyclol and its active mechanism on HepG2 cells challenged by *D*-GaIN (Sigma, USA), the cells were pre-treated with bicyclol 100 μmol/L and quercetin 20 μmol/L for 2 h, and the cells were then stimulated with *D*-GaIN 50 mmol/L, and harvested 8 h later.

Hoechst 33258 staining and flow cytometry analysis

HepG2 cells were grown in 24 microwell plates and treated as described above. To observe cells undergoing apoptosis, Hoechst 33258 staining was performed according to the kit instruction (Beyotime Institute Biotechnology, China). The cells were counted and examined by fluorescence microscopy at 480 nm (Eclipse TE300, Nikon, Japan). At minimum, 500 cells were counted from more than 5 random microscopic fields by two observers (Darzynkiewicz *et al*, 1992). For the flow cytometry study, HepG2 cells were cultured in 25 cm^2 culture flask and treated as described in materials and methods. Cells were washed in a balanced salt solution, resuspended in 70% ethanol and stored at -20 °C for analysis. One hour before flow cytometry analysis, the fixed cells were washed twice and incubated for 30 min at room temperature in Hank's balanced salt solution in order to allow the release of apoptotic cells characterized with DNA of low molecular weight. Cells were resuspended in PBS, and then incubated in the presence of propidium iodide (PI) and DNase-free RNase A for 20 min at room temperature. The samples were analyzed using an EPICS Profile II flow cytometer (Coulter) equipped with an argon laser working at 15 mW. EPICS Profile Software (Coulter) was run for data acquisition and MultiCycle AV (Phoenix Flow System, San Diego, CA) for DNA ploidy. A minimum of 10^5 cells within the gated region was analyzed [17].

Caspase-3 activity determination

Caspase-3 activity was determined according to the manufacturer's protocol (Sigma). In brief, HepG2 cell lysates were prepared by lysis buffer (25 mmol/L HEPES, pH 7.4, 2.5 mmol/L CHAPS, 2.5 mmol/L dithiothreitol). Caspase-3 activity was determined by monitoring proteolysis of the colorimetric substrates. Ac-DEVD-p-nitroaniline was used as colorimetric p-nitroaniline linked substrate. The whole-cell lysate was added to a buffer containing 200 μmol/L substrates. After 1.5 h of incubation, the cleavage of the peptide by the caspase was quantified spectrophotometrically at 405 nm in a 96 well plate. The unit of the optical density was converted to nmols of p-nitroaniline using a standard curve generated with free p-nitroaniline.

Reverse transcription-polymerase chain reaction (RT-PCR) assay

Total RNA was isolated from HepG2 cells using Trizol reagent (Invitrogen CA, USA) following the manufacturer's protocol. RT-PCR was performed using One-Step RT-PCR Kit (Promega, WI, USA). The reaction mixture contains AMV/Tfl reaction buffer 10 μL, dNTP 0.2 mmol/L, 1 μmol/L of each primer, 1 mmol/L $MgSO_4$, 0.1 u/μL AMV reverse transcriptase and Tfl DNA polymerase, 2 μg RNA template. The reaction was heated at 45 °C for 45 min for reverse transcription, and 94 °C for 2 min for AMV RT inactivation and RNA/cDNA/primer denaturation for 40 cycles. Denaturation, annealing and extension steps for detecting HSP27 transcripts were 94 °C for 30 s, 55 °C for 1 min, and 68 °C for 2 min, respectively. The final extension was at 68 °C for 7 min. The following primers used in the PCR reactions were synthesized by Shanghai Sangon Biological Engineering Technology & Services Company (Shanghai, China): HSP27-forward 5′-CCCACCCTCTATCACGGCTAC-3′ and reverse 5′-GGGCTCAACTCTGGCTATCTC-3′, which leads to a 426-bp product. Amplified products were separated on a 1% agarose gel in TBE buffer (45 mmol/L Tris borate, 1 mmol/L EDTA). RT-PCR bands were photographed with a Kodak Gel Logic 100 Imaging System (Life Technologies, Inc, Eastman Kodak Co, New Haven, CT) and the density of the bands was determined using Gel-Pro Analyzer 4.0 software.

Western blot analysis

HepG2 cells were lysed in nondenaturing lysis buffer (Applygen Technologies Inc Beijing, China). 30 μg of sample proteins were separated by SDS-polyacrylamide gel electrophoresis (SDS-PAGE) in a 10% polyacrylamide gel, and transferred to a polyvinylidene difluoride (PVDF) membrane. Membranes were blocked in 5% skim milk-TBS-T (20 mmol/L Tris-HCl, pH 7.5, 500 mmol/L NaCl. 0.1% Tween 20) at 4 °C overnight. Blots were probed with antibodies against HSP27, cytochrome *c*, apoptosis inducing factor (AIF) (Santa Cruz, CA, USA), apoptosis protease activating factor-1 (Apaf-1), (p)JNK (Cell Signaling, MA, USA) in 5% skim milk-TBS-T for 2 h at room temperature, and then incubated with the horseradish peroxidase-conjugated secondary antibody in skim milk-TBST for 2 h at room temperature. The blot was developed with LAS3000 chemiluminescence system (Fujifilm, Tokyo, Japan) and the density of the bands was determined using Gel-Pro Analyzer 4.0 software.

Electrophoretic mobility shift assay (EMSA)

HepG2 cells nuclear extracts for EMSA were prepared using nuclear-cytosol extraction kit (Applygen Technologies Inc). Annealed double-stranded heat shock element (HSE) oligonucleotides (5′-AGA CGC GAA ACT GCT GGA AGA TTC CGT GCC-3′) labeled with biotin were synthesized by IDT (NJ, USA). EMSA Kit (Pierce, IL, USA) was used to perform the reaction. The binding reaction (20 μL in total) consists of 10 μg of protein extracts, 20 fmol of biotin labeled DNA, 2.5% glycerol, 5 mmol/L $MgCl_2$, 50 ng/μL Poly (dI·dC), and incubated for 20 min at room temperature. DNA-protein complexes were resolved by electrophoresis on a 6% polyacrylamide gel at 4 °C in 0.5×TBE buffer (45 mmol/L Tris borate, 1 mmol/L EDTA), and transferred to a nylon membrane. Then the membrane was detected with the enhanced LAS3000 chemiluminescence system.

Co-immunoprecipitation (Co-IP)

HepG2 cells were lysed in nondenaturing lysis buffer (Applygen Technologies Inc) The Co-IP assay was performed following the protocol of Co-IP kit (Pierce, IL, USA). Briefly, 50 μg of the purified HSP27 antibody was immobilized in 100 μL, 50% antibody coupling gel. Protein extracts 300 μg were incubated with gentle end-over-end mixing for 2 h at room temperature. Immunoprecipitated complexes were eluted thrice with 50 μL elution buffer, boiled and separated by SDS-PAGE, transferred to a PVDF membrane, incubated with cytochrome *c*, AIF or Apapf-1 antibodies, and detected with the enhanced LAS3000 chemiluminescence system.

Statistical analysis

Data were expressed as means±SD. Changes in different assays were analyzed by ANOVA followed by Tukey–Kramer test as the *post hoc* test. $P<0.05$ was considered to be significant statistically.

Results

Bicyclol induced expression of HSP27 in HepG2 cells

Since the induction of HSP is a universal stress response against various insults and it has been widely shown to have an anti-apoptosis effect, the expression of HSP27, one of the major members in HSPs family, was first detected by western blot in this experiment. Bicyclol 50 μmol/L induced HSP27 expression in HepG2 cells in a time-dependent manner. The maximum of the induction was at 6 h (0.93-fold increase, $P<0.05$), after which the induction gradually declined to the control level at 24 h (Figure 1A).

The dose-effect relationship of the inductive effect of HSP27 by bicyclol is shown in Figure 1B. Bicyclol induced both protein and mRNA levels of HSP27 expression in a dose-dependent manner. The inducing effect of HSP27 by bicyclol 100 μmol/L was more potent than those by bicyclol 50 μmol/L and 25 μmol/L (25 μmol/L: 0.37-fold increase; 50 μmol/L: 0.58-fold increase; 100 μmol/L: 1.23-fold increase, $P<0.01$).

Quercetin is a flavanoid and a known inhibitor of HSP synthesis which functions by inhibiting heat shock factor 1 (HSF1). Co-treatment of quercetin 20 μmol/L significantly inhibited bicyclol-induced HSP27 expression in protein (0.82-fold decrease, $P<0.05$) and mRNA level (0.65-fold decrease, $P<0.05$), suggesting that the inductive effect of bicyclol on HSP27 expression occurred at mRNA level.

Heat shock gene expression is mainly regulated at the transcriptional level by HSF1. The results of the effect of bicyclol on the activation of HSF1 indicated that bicyclol treatment resulted in decreased level of HSF1 in cytosol (bicyclol treatment: 50 μmol/L: 86.9% decrease, $P<0.01$; 100 μmol/L: 87.9% decrease, $P<0.01$) and concomitantly, increased level of HSF1 in nucleus (p-HSF1) (bicyclol treatment: 50 μmol/L: 2.3-fold increase, $P<0.05$; 100 μmol/L: 4.1-fold increase, $P<0.01$). EMSA assay showed that bicyclol was able to enhance HSF1-HSE binding activity in a concentration-dependent manner (bicyclol treatment: 25 μmol/L: 1.7-fold increase, $P<0.05$; 50 μmol/L: 1.9-fold increase, $P<0.05$; 100 μmol/L: 2.1-fold increase, $P<0.01$), and co-treatment of quercetin attenuated these effects of bicyclol (Figure 1C, 1D). The results indicated that bicyclol activated HSF1, which in turn induced HSP27 gene expression.

HSP27 induced by bicyclol attenuated apoptosis of HepG2 cells intoxicated with *D*-GaIN

As shown in Figure2A, the majority of HepG2 cells in control group had uniformly stained nuclei after staining with the membrane-permeable DNA-binding dye Hoechst 33258. Exposure of HepG2 cells to 50 mmol/L of *D*-GaIN for 8 h resulted in nuclei fragmentation as indicated in condensed chromatin and bright staining in morphology of HepG2 cells under fluorescent microscope, indicating apoptosis. The treatment of 100 μmol/L bicyclol attenuated apoptosis by 57.6% ($P<0.01$) as expressed in decrease of nuclei fragmentation of HepG2 cells induced by *D*-GaIN. When HSP27 synthesis was inhibited by 20 μmol/L quercetin, the protective effect of bicyclol against nuclei fragmentation was abrogated. The apoptosis percentage increased by 1.2-fold ($P<0.05$), suggesting that HSP27 was involved in the attenuating effect of bicyclol on nuclei fragmentation.

The flow cytometry analysis showed that 50 mmol/L of *D*-GaIN induced significant hypodiploid DNA peak before the narrow peak of diploid DNA, which indicated DNA degradation and the undergoing apoptosis of HepG2 cells. The treatment of bicyclol 100 μmol/L inhibited *D*-GaIN-induced hypodiploid DNA peak development by 61.5% ($P<0.01$). This effect of bicyclol was also attenuated by co-addition of 20 μmol/L quercetin, indicating that HSP27 participated in the protective effect of bicyclol on hepatocytes apoptosis (Figure 2B).

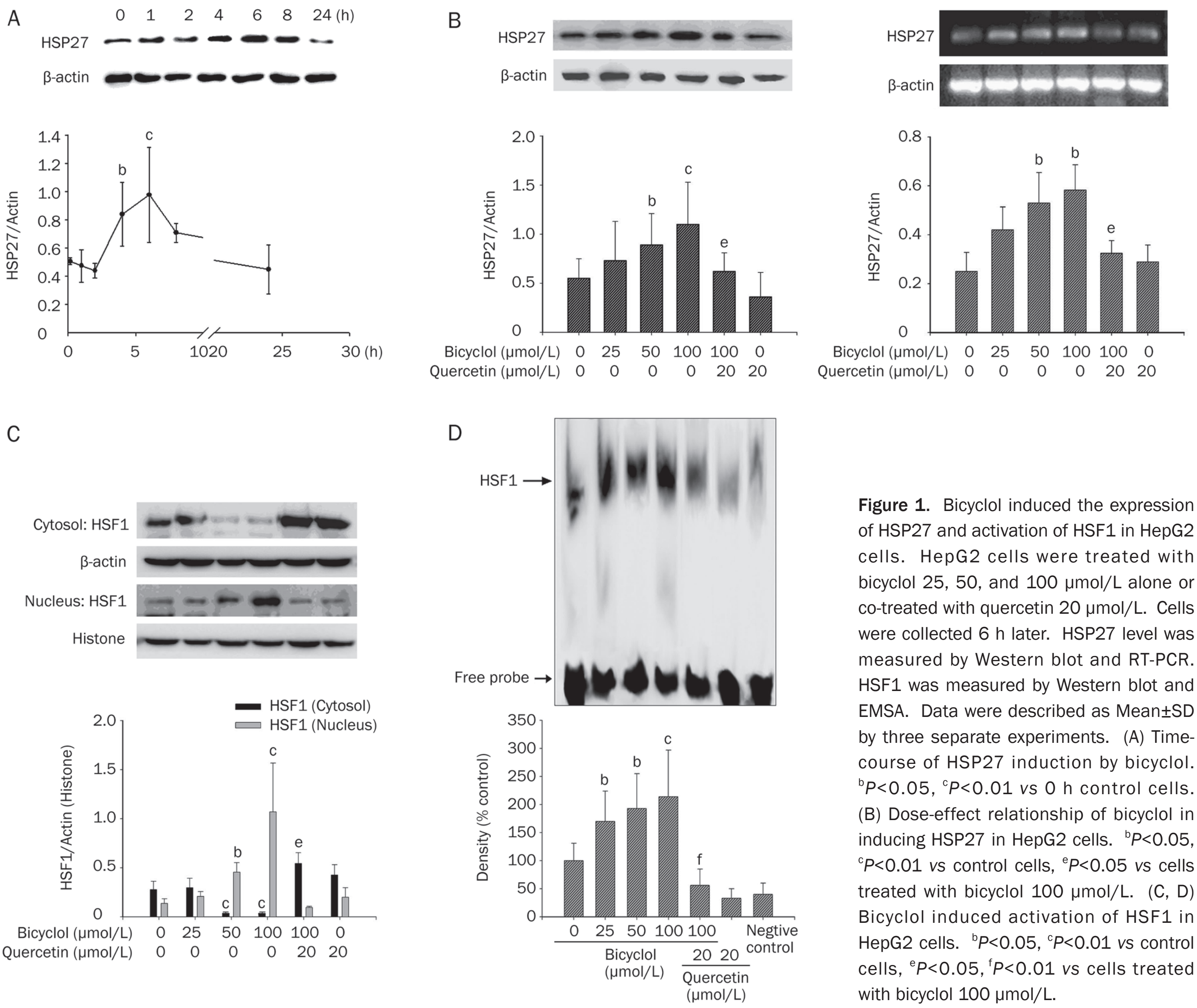

Figure 1. Bicyclol induced the expression of HSP27 and activation of HSF1 in HepG2 cells. HepG2 cells were treated with bicyclol 25, 50, and 100 μmol/L alone or co-treated with quercetin 20 μmol/L. Cells were collected 6 h later. HSP27 level was measured by Western blot and RT-PCR. HSF1 was measured by Western blot and EMSA. Data were described as Mean±SD by three separate experiments. (A) Time-course of HSP27 induction by bicyclol. $^{b}P<0.05$, $^{c}P<0.01$ *vs* 0 h control cells. (B) Dose-effect relationship of bicyclol in inducing HSP27 in HepG2 cells. $^{b}P<0.05$, $^{c}P<0.01$ *vs* control cells, $^{e}P<0.05$ *vs* cells treated with bicyclol 100 μmol/L. (C, D) Bicyclol induced activation of HSF1 in HepG2 cells. $^{b}P<0.05$, $^{c}P<0.01$ *vs* control cells, $^{e}P<0.05$, $^{f}P<0.01$ *vs* cells treated with bicyclol 100 μmol/L.

Bicyclol-induced HSP27 inhibited caspase-3 activation in HepG2 cells intoxicated with *D*-GalN

Caspase-3 has been identified as a key mediator of apoptosis of mammalian cells. The results of caspase-3 colorimetric assay indicated that cultivation of HepG2 cells with 50 mmol/L *D*-GalN for 8 h caused a significant increase in caspase-3 activity in the cells. Pre-incubation of HepG2 cells with 100 μmol/L bicyclol significantly inhibited *D*-GalN-induced activation of caspase-3 by 35.3% ($P<0.01$). Similarly, 20 μmol/L quercetin attenuated this effect of bicyclol as shown in 30.5% increase of caspase-3 activity ($P<0.05$) (Figure 3). The results suggested that HSP27 might be involved in the inhibitory effect of bicyclol on caspase-3 activity.

Bicyclol induced HSP27 inhibited the release of cytochrome *c* and AIF from mitochondria in HepG2 cells intoxicated with *D*-GalN

The releases of cytochrome c and AIF from mitochondria play a crucial role in apoptosis. The present results showed that the amount of cytochrome *c* and AIF released from mitochondria to cytosol significantly increased, accordingly, the levels of cytochrome *c* and AIF in mitochondria decreased significantly in HepG2 cells intoxicated with *D*-GaIN. The ratio of cytochrome *c* and AIF in cytosol/mitochondria increased 8.5-foldand 4.2-fold, respectively. Pre-treatment of bicyclol 100 μmol/L inhibited the release of cytochrome *c* and AIF from mitochondria to cytosol. The decrease of cytochrome *c* was 6.3-fold ($P<0.01$) and AIF decreased 3.8-fold ($P<0.01$). These effects of bicyclol were attenuated by simultaneously addition of quercetin as shown in 3.85-fold increase of release of cytochrome *c* ($P<0.01$) and 3.5-fold of AIF $P<0.01$) (Figure 4), indicating the role of HSP27 in the protection against *D*-GaIN induced hepatocytes apoptosis.

Bicyclol induced HSP27 interacts with cytochrome *c*, AIF, and Apaf-1 in HepG2 cells intoxicated with *D*-GalN

To further study the effect of HSP27 on cytochrome *c*, AIF and Apaf-1, a set of co-immunoprecipitation experiments were

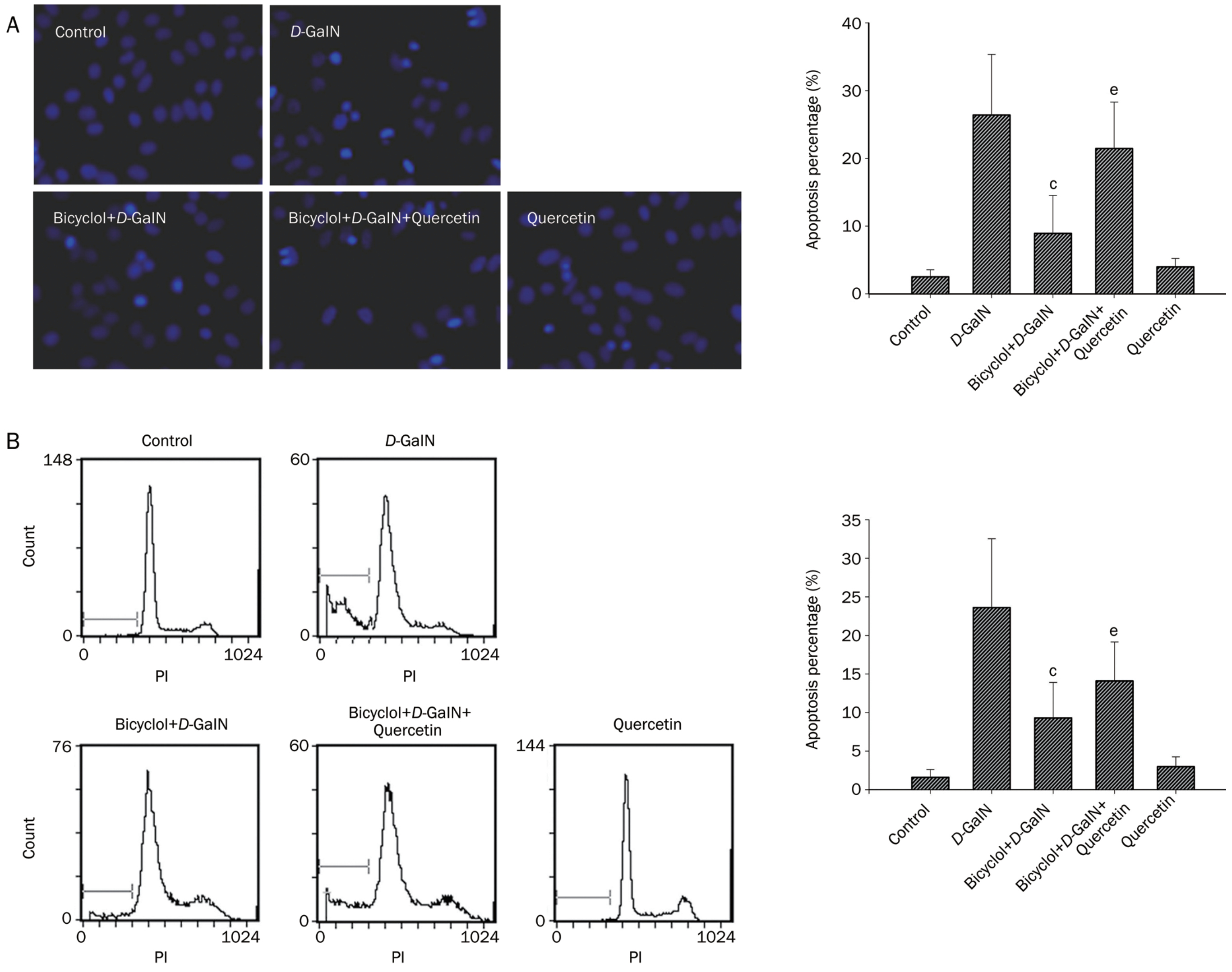

Figure 2. Bicyclol-induced HSP27 inhibited apoptosis of HepG2 cells intoxicated with *D*-GalN. The cells were pre-treated with bicyclol 100 μmol/L alone or co-treated with quercetin 20 μmol/L for 2 h simultaneously. The cells were then stimulated with *D*-GalN 50 mmol/L, and harvested 8 h later. (A) Hoechst 33258 staining of DNA in HepG2 cells. (B) Flow cytometry analysis of DNA in HepG2 cells. ^{c}*P*<0.01 *vs* *D*-GalN treated cells; ^{e}*P*<0.05 *vs* bicyclol+*D*-GalN treated cells. Each bar is the mean±SD of five separate experiments.

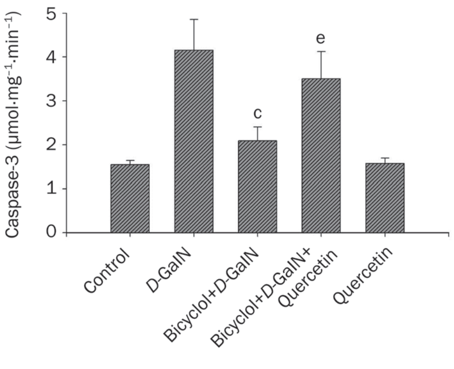

Figure 3. Inhibitory effect of bicyclol-induced HSP27 on caspase-3 activation in HepG2 cells intoxicated with *D*-GalN. The procedure of cell treatment was same as Figure 2. Data were described with Mean±SD by five separate experiments. ^{c}*P*<0.01 *vs* *D*-GalN treated cells; ^{e}*P*<0.05 *vs* bicyclol+*D*-GalN treated cells.

performed with cytochrome *c*, AIF, and Apaf-1 antibodies in HepG2 cell intoxicated with *D*-GalN. As shown in Figure 5, the interaction of HSP27 with cytochrome *c* was quite distinct, however, the interactions of HSP27 with AIF and Apaf-1were very weak. Blocking of HSP27 with quercetin reduced the association of HSP27 with cytochrome *c* (Figure 5), suggesting that bicyclol-induced HSP27 directly binds to the pro-apoptosis protein and inhibited the activity of the protein, thereby suppressed hepatocytes apoptosis.

HSP27 induced by bicyclol inhibited JNK activation in HepG2 cells intoxicated with *D*-GalN

JNK pathway is also involved in hepatocyte apoptosis. The protective action of HSP27 induced by bicyclol on the activation of JNK pathway was further studied. As shown in Figure 6, 50 mmol/L *D*-GalN caused JNK phosphorylation. The

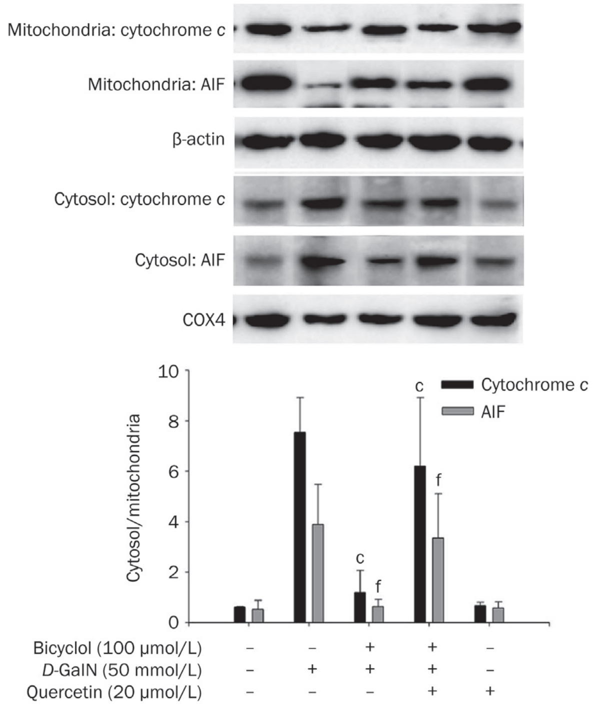

Figure 4. Bicyclol-induced HSP27 inhibited the releases of cytochrome *c* and AIF from mitochondria in HepG2 cells intoxicated with *D*-GalN. The treatment of cells was described above. Cytochrome *c* and AIF was measured by Western blot. A representative from three results is shown. $^cP<0.01$ *vs* *D*-GalN treated cells; $^fP<0.01$ *vs* bicyclol+*D*-GalN treated cells.

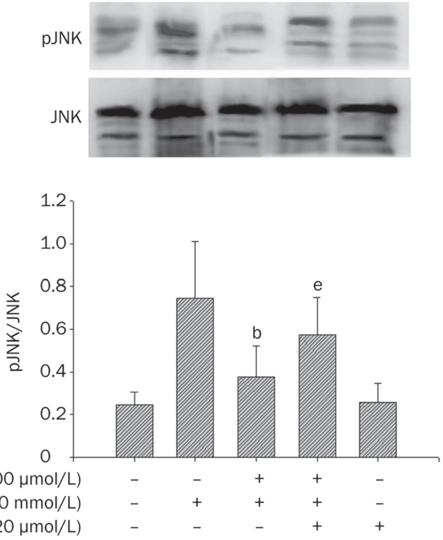

Figure 6. Inhibition of JNK activation by bicyclol-induced HSP27 in HepG2 cell intoxicated with *D*-GalN. The treatment of cells was described above. JNK was measured by Western blot. $^bP<0.05$ *vs* *D*-GalN treated cells; $^eP<0.05$ *vs* bicyclol+*D*-GalN treated cells. Similar results were obtained in three separate experiments.

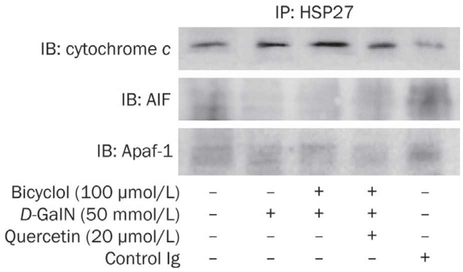
IP: HSP27
IB: cytochrome *c*
IB: AIF
IB: Apaf-1
Bicyclol (100 μmol/L) – – + + –
D-GalN (50 mmol/L) – + + + –
Quercetin (20 μmol/L) – – – + –
Control Ig – – – – +

Figure 5. Interactions of bicyclol-induced HSP27 with cytochrome *c*, AIF, and Apaf-1 in HepG2 cell intoxicated with *D*-GalN. Cells were pre-treated with bicyclol 100 μmol/L, and then they were subjected to *D*-GalN. Co-immunoprecipitation assays were performed with cytochrome *c*, AIF, and Apaf-1 antibodies. A representative of three experiments is shown.

pretreatment of 100 μmol/L of bicyclol suppressed JNK phosphorylation by 42% ($P<0.05$). Co-treatment of quercetin at 20 μmol/L significantly reversed the inhibitory effect of bicyclol on JNK phosphorylation ($P<0.05$), suggesting that bicyclol induced-HSP27 was involved in the inhibition of JNK.

Discussion

In the present study, bicyclol was further confirmed to induce the expression of HSP27 in protein and mRNA levels in HepG2 cells. HSP synthesis is tightly regulated at the transcriptional level by HSF1. The activation of HSF1 is associated with its oligomerization, nuclear localization, and acquisition of binding activity to HSE in the heat shock gene promoter to exert the transcriptional activation[18, 19]. The results of western blot and gel mobility shift assay indicated that bicyclol treatment led to HSF1 translocation to nucleus, phosphorylation and therefore produced an HSE sequence-specific complex in HepG2 cells, which resulted in a marked up-regulation of HSE-binding activity, indicating that bicyclol activates HSF1, which in turn induces HSP27 gene expression.

It was reported that apoptosis is a key pathologic change in liver disease, including viral hepatitis[20], liver ischemia[21], chemical[1] and drug-induced[2] liver injury as well as fatty liver disease[22]. The results of our study indicated that in associated with the induction of heat shock response by bicyclol, HepG2 cells acquired high resistance to apoptosis caused by *D*-GalN insult, which expressed in a decrease of percentage of hepatocytes apoptosis and caspase-3 activity. Recent paper pointed out that mitochondrial dysfunction is the commitment step in hepatocyte apoptosis[23]. Cell death signals induce the release of cytochrome *c* from the mitochondria, which then binds to Apaf-1, facilitating the formation of the apoptosome. Apoptosome formation results in the processing and activation of caspase-9, which triggers the caspase pathway by activating the downstream caspase-3[24]. AIF is another mitochondrial intermembrane protein released upon apoptotic stimulus, which translocates to the nucleus and triggers caspase-independent nuclear changes upon activation of the intrinsic pathway[25]. The highly conserved HSPs provide protection to injured cells. Overexpression of HSP27 increases the resistance of cells to various apoptotic stimuli[26]. One mechanism by which HSP27 could interfere with apoptosis is by directly binding to cytosolic cytochrome *c* and sequestering it from Apaf-1[27]. The present paper demonstrated that pretreatment of bicyclol inhibited the release of cytochrome c and AIF from mitochondria caused by *D*-GaIN, and enhanced the association of HSP27 with cytochrome *c*. It might be possible that overexpressed bicyclol-induced HSP27 may inhibit the apoptotic pathways. So, quercetin, an inhibitor of HSPs biosynthesis, was therefore chosen as a tool in the present study. Quercetin has been shown to block binding of activated HSF1 to its cognate DNA sequence, reduce the activation of the HSR, and decrease HSP expression[28, 29]. The present results also demonstrated that quercetin at 20 mol/L has no protective effect on hepatocyte apoptosis challenged by *D*-GaIN. Moreover, quercetin alone also does not affect cytochrome *c*, AIF and JNK expression. Therefore, the only effect of quercetin at 20 is to inhibit the synthesis HSPs. The present results showed that blocking HSP27 biosynthesis with quercetin markedly attenuated the effects of bicyclol on cytochrome *c* and AIF release from mitochondria as well as apoptosis of hepatocytes. A question arises as to why the interaction of HSP27 induced by bicyclol with cytochrome *c* was significant, whereas the interactions with AIF and Apaf-1 were very weak. The cause of different effects of bicyclol on the interaction with AIF and Apaf-1 may be interpreted by other reports that Apaf-1 and AIF mainly interact with HSP70 to antagonize AIF-dependent apoptosis[30] and prevent the recruitment of caspases to the apoptosome complex and thereby to block the apoptotic signaling relay. In the present paper, HSP27 was shown to have no interactions with AIF and Apaf-1. However, western blot data indicated that bicyclol can also inhibit the release of AIF from mitochondria to cytosol. Therefore, there might be other proteins such as HSP70 that were involved in the inhibition of bicyclol on AIF and Apaf-1 in HepG2 cells intoxicated by *D*-GaIN.

Caspase-3 can be activated by caspase-9, which is cleaved and activated by the release of cytochrome *c* from mitochondria to cytosol. Experimental depletion of HSP27 suggests that HSP27 mainly functions as an inhibitor of caspase activation. Knock-down of HSP27 by small interfering RNAs induces apoptosis through caspase-3 activation[31]. This phenomenon can be explained by the ability of HSP27 to prevent the formation of the apoptosome and the subsequent activation of caspases[32]. In agreement with these reports, the present paper provides evidence that HSP27 induced by bicyclol inhibited the activity of caspase-3 in HepG2 cells intoxicated with *D*-GaIN. It still needs further investigation for the inhibition of caspase-3 by HSP27 due to its effect on apoptosome formation and/or directly on caspase-3.

Mitochondrial outer membrane permeabilization can activate intracellular stress kinases, such as JNK, which is the most important kinase that determines the cell fate to death or survival[33]. Mice lacking either JNK1 or JNK2 are highly resistant to Con A-induced liver failure and show considerably lower amounts of apoptotic and necrotic hepatocyte death[34]. Recent studies further proposed that down-regulation of JNK activity is a mechanism of HSP27 mediated protection. Overexpression of HSP27 in stress can definitely play an inhibitory role in JNK signal transduction pathway, and thus blocks cell apoptosis induced by JNK signal transduction pathway[35]. In our study, the phosphorylation of JNK was also inhibited by pretreatment of bicyclol in HepG2 cells intoxicated by *D*-GaIN, which was attenuated by simultaneous administration of quercetin, inhibitor of HSPs synthesis. The suppression of JNK signaling by HSP27 induced bicyclol is also involved in anti-apoptosis process of hepatocytes.

Taken together, the present study revealed that bicyclol at non-toxic concentration elicits a significant induction of HSP27 response that is capable of protection against hepatocytes apoptosis mainly through inhibition of mitochondrial and JNK apoptotic pathways in HepG2 cells-intoxicated with D-GaIN.

Acknowledgements

This work was supported by grants from the Chinese Ministry of Science and Technology (96-901-01-45) and from the Chinese Medical Board in New York (93-582).

Author contribution

Geng-tao LIU designed research; Xiu-qi BAO performed research, analyzed data, and wrote the paper.

References

1 Zhao DM, Liu GT. Protective effect of bicyclol on concanavalin A induced liver nuclei DNA injury in mice. Natl Med J China 2001; 81: 844–8.

2 Li Y, Dai GW, Li Y, Liu GT. Effect of bicyclol on acetaminophen-induced hepatotoxicity: energetic metabolism and mitochondrial injury in acetaminophen-intoxicated mice. Yao Xue Xue Bao 2001; 36: 723–6.

3 Liu GT, Li Y, Wei HL, Zhang H, Xu JY, Yu LH. Mechanism of protective action of bicyclol against CCl4-induced liver injury in mice. Liver Int 2005; 25: 872–9.

4 Liu GT. The anti-virus and hepatoprotective effect of bicyclol and its mechanism of action. Chin J New Drugs 2001; 10: 325–7.

5 Yao GB, Ji YY, Wang QH, Zhou XQ, Xu DZ, Chen XY, *et al*. A randomized double-blind controlled trial of bicyclol in treatment of chronic hepatitis B. Chin J New Drugs Clin Rem 2002; 21: 457–62.

6 Li Y, Li Y, Liu GT. Protective effects of bicyclol on liver fibrosis induced by carbon tetrachloride. Natl Med J China 2004; 84: 2096–101.

7 Liu GT. Bicyclol: a novel drug for treating chronic viral hepatitis B and C. Med Chem 2009; 5: 29–43.

8 Morimoto RI. Cells in stress: transcriptional activation of heat shock genes. Science 1993; 259: 1409–10.

9 Park KJ, Gaynor RB, Kwak YT. Heat shock protein 27 association with the I-kappa B kinase complex regulates tumor necrosis factor alpha-induced NF-kappa B activation. J Biol Chem 2003; 278: 35272–8.

10 Sumioka I, Matsura T, Kai M, Yamada K. Potential roles of hepatic heat shock protein 25 and 70i in protection of mice against acetaminophen-induced liver injury. Life Sci 2004; 74: 2551–61.

11 Zborek A, Małusecka E, Krzyowska-Gruca S, Wysocka A, Krawczyk Z. Immunohistochemical studies on the expression pattern of molecular chaperones HSC70 and HSP25 and cell cycle-related proteins cyclin D1 and PCNA in rat liver after thioacetamide intoxication. Histochem Cell Biol 2002; 118: 311–9.

12 Fischer R, Baumert T, Blum HE. Hepatitis C virus infection and apoptosis. World J Gastroenterol 2007; 13: 4865–72.

13 Muntane J, Montero JL, Lozano JM, Miranda-Vizuete A, de la Mata M, Mino G. TNF-alpha but not Il-1alpha are correlated with PGE1-dependent protection against acute *D*-galactosamine-induced liver injury. Can J Gastroenterol 2000; 14: 175–80.

14 Fouad D, Siendones E, Costán G, Muntané J. Role of NF-kappaB activation and nitric oxide expression during PGE protection against d-galactosamine-induced cell death in cultured rat hepatocytes. Liver Int 2004; 24: 227–36.

15 Bao XQ, Liu GT. Bicyclol: a novel antihepatitis drug with hepatic heat shock protein 27/70-inducing activity and cytoprotective effects in mice. Cell Stress Chaperones 2008; 13: 347–55.

16 Bao XQ, Liu GT. Induction of heat shock protein 27 and 70 overexpression by bicyclol attenuates concanavalin A-induced liver injury through suppression of NF-{kappa}B in mice. Mol Pharmacol 2009; 75: 1180–8.

17 Darzynkiewicz Z, Bruno S, Del Bino G, Gorczyca W, Hotz MA, Lassota P, *et al*. Features of apoptotic cells measured by flow cytometry. Cytometry 1992; 13: 795–808.

18 Santoro MG. Heat shock factors and the control of the stress response. Biochem Pharmacol 2000; 59: 55–63.

19 Han SI, Oh SY, Woo SH, Kim KH, Kim JH, Kim HD, *et al*. Implication of a small GTPase Rac1 in the activation of c-Jun N-terminal kinase and heat shock factor in response to heat shock. J Biol Chem 2001; 276: 1889–95.

20 Wang WH, Hullinger RL, Andrisani OM. Hepatitis B virus X protein via the p38MAPK pathway induces E2F1 release and ATR kinase activation mediating p53 apoptosis. J Biol Chem 2008; 283: 25455–67.

21 Cursio R, Colosetti P, Auberger P, Gugenheim J. Liver apoptosis following normothermic ischemia-reperfusion: *in vivo* evaluation of caspase activity by FLIVO assay in rats. Transplant Proc 2008; 40: 2038–41.

22 Tessari P, Coracina A, Cosma A, Tiengo A. Hepatic lipid metabolism and non-alcoholic fatty liver disease. Nutr Metab Cardiovasc Dis 2009; 19: 291–302.

23 Malhi H, Gores GJ, Lemasters JJ. Apoptosis and necrosis in the liver: a tale of two deaths? Hepatology 2006; 43: S31–S44.

24 Wright KM, Vaughn AE, Deshmukh M. Apoptosome dependent caspase-3 activation pathway is non-redundant and necessary for apoptosis in sympathetic neurons. Cell Death Differ 2007; 14: 625–33.

25 Joza N, Susin SA, Daugas E, Stanford W, Cho SK, Li CY, *et al*. Essential role of the mitochondrial apoptosis inducing factor in programmed cell death. Nature 2001; 410: 549–54.

26 Rogalla T, Ehrnsperger M, Preville X, Kotlyarov A, Lutsch G, Ducasse C, *et al*. Regulation of Hsp27 oligomerization, chaperone function, and protective activity against oxidative stress/tumor necrosis factor alpha by phosphorylation. J Biol Chem 1999; 274: 18947–56.

27 Bruey JM, Ducasse C, Bonniaud P, Ravagnan L, Susin SA, Diaz-Latoud C, *et al*. Hsp27 negatively regulates cell death by interacting with cytochrome *c*. Nat Cell Biol 2000; 2: 645–52.

28 Jakubowicz-Gil J, Rzymowska J, Paduch R, Gawron A. The effect of quercetin on the expression of heat shock proteins and apoptosis induction in monkey kidney cell line GMK. Folia Histochem Cytobio 2002; 40: 137–8.

29 Masuda Y, Sumita S, Fujimura N, Namiki A. Geranylgeranylacetone attenuates septic diaphragm dysfunction by induction of heat shock protein 70. Crit Care Med 2003; 31: 2585–91.

30 Ravagnan L, Gurbuxani S, Susin SA, Maisse C, Daugas E, Zamzami N, *et al*. Heat-shock protein 70 antagonizes apoptosis-inducing factor. Nat Cell Biol 2001; 3: 839–43.

31 Rocchi P, Jugpal P, So A, Sinneman S, Ettinger S, Fazli L, *et al*. Small interference RNA targeting heat-shock protein 27 inhibits the growth of prostatic cell lines and induces apoptosis via caspase-3 activation *in vitro*. BJU Int 2006; 98: 1082–9.

32 Garrido C, Bruey JM, Fromentin A, Hammann A, Arrigo AP, Solary E. HSP27 inhibits cytochrome c-dependent activation of procaspase-9. FASEB J 1999;13: 2061–70.

33 Singh R, Czaja MJ. Regulation of hepatocyte apoptosis by oxidative stress. J Gastroenterol Hepatol 2007; 22 Suppl 1: S45–48.

34 Kamata H, Honda S, Maeda S, Chang L, Hirata H, Karin M. Reactive oxygen species promote TNF-α-induced death and sustained JNK activation by inhibiting MAP kinase phosphatases. Cell 2005; 120: 649–61.

35 Nakagomi S, Suzuki Y, Namikawa K, Kiryu-Seo S, Kiyama H. Expression of the activating transcription factor 3 prevents c-Jun N-terminal kinase-induced neuronal death by promoting heat shock protein 27 expression and Akt activation. J Neurosci 2003; 23: 5187–96.

Acta Pharmacologica Sinica (2010) 31: 227–236
© 2010 CPS and SIMM All rights reserved 1671-4083/10 $32.00
www.nature.com/aps

Original Article

Microarray analysis reveals the inhibition of nuclear factor-kappa B signaling by aristolochic acid in normal human kidney (HK-2) cells

Ya-yin CHEN[1, 2], Su-yin CHIANG[1], Hsiu-ching WU[3], Shung-te KAO[1, 2], Chien-yun HSIANG[4, #], Tin-yun HO[1, #], Jaung-geng LIN[1, #, *]

[1]School of Chinese Medicine, China Medical University, Taichung, Taiwan, China; [2]Department of Chinese Medicine, China Medical University Hospital, Taichung, Taiwan, China; [3]School of Post-Baccalaureate Chinese Medicine, China Medical University, Taichung, Taiwan, China; [4]Department of Microbiology, China Medical University, Taichung, Taiwan, China

---

Aim: To study the molecular mechanism underlying the effect of aristolochic acid (AA), a major active component of plants from the Aristolochiaceae family using microarray analysis.
Methods: Human kidney (HK-2) cells were treated with AA (0, 10, 30, and 90 μmol/L) for 24 h, and the cell viability was measured by a 3-(4,5-dimethylthiazol-2yl)-2,5-diphenyltetrazolium bromide assay. Complementary DNA microarrays were used to investigate the gene expression pattern of HK-2 cells exposed to AA in triplicate. A quantitative reverse transcriptase-polymerase chain reaction (qRT-PCR) assay was used to verify the microarray data for selected nuclear factor kappa B (NF-κB)-regulated genes. Furthermore, the subcellular localization of NF-κB p65 was visualized by immunofluorescence confocal microscopy in HK-2 cells. The NF-κB activity was examined by a luciferase reporter assay in HK-2/NF-κB transgenic cells.
Results: AA exhibited a dose-dependent cytotoxic effect in HK-2 cells and induced alterations in the gene expression profiles related to the DNA damage response, DNA repair, macromolecule metabolic process, carbohydrate metabolic process, DNA metabolic process, apoptosis, cell cycle, and transcription. In addition, 9 biological pathways associated with immunomodulatory functions were down-regulated in AA-treated HK-2 cells. A network analysis revealed that NF-κB played a central role in the network topology. Among NF-κB-regulated genes, 8 differentially expressed genes were verified by qRT-PCR. The inhibition of NF-κB activity by AA was further confirmed by immunofluorescence confocal microscopy and by NF-κB luciferase reporter assay.
Conclusion: Our data revealed that AA could suppress NF-κB activity in normal human cells, perhaps partially accounting for the reported anti-inflammatory effects of some plants from the genus Aristolochia.

Keywords: aristolochic acid; microarray analysis; nuclear factor-kappa B; human kidney HK-2 cells; confocal microscopy; luciferase reporter assay

---

Acta Pharmacologica Sinica (2010) 31: 227–236; doi: 10.1038/aps.2009.197

Introduction

Aristolochic acid (AA), a major active component of plants from the Aristolochiaceae family, was first detected in *Aristolochia clematitis* in 1943[1]. Many plant species of the genus Aristolochia have been used worldwide for centuries in folk medicine. For example, there are many formulas containing various species of the genus *Aristolochia* that are commonly used in traditional medicine in China, Japan, and Singapore[2]. Beside those used in East Asia, several species of the genus Aristolochia have been used to regulate menstruation, induce labor, expel parasites, relieve pain, and treat arthritis, cancer, diarrhea, and snake bites in India, West Africa, the Mediterranean, and South America[3–5].

Pharmacological studies have demonstrated that aristolochic acid I (AAI) and aristolochic acid II (AAII) are the major active components of plants in the Aristolochiaceae family[1, 6]. It has been shown that AA protects against infections and inflammation in several biological systems, including humans. AAI inhibits the growth of bacteria, including *Escherichia coli*, *Pseudomonas aeruginosa, Streptococcus faecalis, Staphylococcus aureus,* and *Staphylococcus epidermidis*[5]. AA can block H_2O_2-induced platelet aggregation and suppress hydroxyl radical-induced platelet activation through the arachidonic acid path-

---

[#] These authors contributed equally to this work.
[*] To whom correspondence should be addressed.
E-mail jglin@mail.cmu.edu.tw
Received 2009-07-29 Accepted 2009-12-21

way[7, 8]. AA was found to possess anti-inflammation effects as demonstrated by its ability to inhibit phospholipase A_2 (PLA_2) when administered by intramuscular or intraperitoneal injection[9, 10]. Furthermore, AA was also reported to inhibit Group I PLA_2 in humans with sepsis[11]. From *in vitro* studies, AA has been shown to suppress phospholipohydration of PLA_2 derived from human synovial fluid, cobra venom, porcine pancreas, and human platelets[12]. The anti-inflammatory activities of AA in different models of inflammation have promoted its use in many countries in herbal formulations for arthritis, rheumatism, gout and chronic inflammatory skin diseases[13, 14]. Moreover, double-blind studies in healthy volunteers show that AA increased the phagocytic activity of peripheral granulocytes after treatment with AA 0.9 mg/d for three to ten consecutive days[15].

Plants of the genus Aristolochia were used as therapeutic drugs until cases of rapidly progressive renal failure were reported in Belgium[16] in 1993, which were found in 1994 to be caused by the inadvertent replacement of *Stephania tetrandra* by *Aristolochia fangchi*[17]. High cumulative doses of AA have been reported to be associated with nephropathy in humans[18]. Aristolochic acid nephropathy complicated with urothelial malignancy has been described, and the cumulative dose (>200 g) of ingested Aristolochia was found to be a significant risk factor for urothelial carcinoma[19, 20]. Moreover, there is evidence that AA is nephrotoxic and carcinogenic in animals including humans[2, 6]. However, herbs of the genus Aristolochia administrated at low cumulative doses (<30 g of raw drugs) did not increase the risks for chronic kidney disease in a large Chinese cohort study of 200 000 subjects[21].

In this paper, the effects of AA and its underlying molecular mechanism were examined in normal human kidney cells (HK-2) through microarray analysis. Results from these analyses showed that NF-κB is an important modulator of gene expression in AA-treated normal human cells. Furthermore, AA-induced NF-κB inhibition was confirmed by immunofluorescence confocal microscopy in HK-2 cells and by a luciferase reporter assay in HK-2/NF-κB transgenic cells.

Materials and methods

Cell culture and reagents

HK-2 cells, derived from an immortalized proximal tubule epithelial cell line from the normal adult human kidney, were purchased from the Bioresource Collection and Research Center (Hsinchu, Taiwan). HK-2 cells were grown in keratinocyte serum-free basal medium (Gibco) supplemented with 5 ng/mL of recombinant epidermal growth factor and 50 μg/mL of bovine pituitary extract without antibiotics in 5% CO_2 at 37 °C. Aristolochic acid sodium salt, a mixture of AAI (41%) and AAII (56%) (Sigma, St Louis, MO) was dissolved in double-distilled water. HK-2 cells were seeded in 96-well plates and incubated for 24 h before the AA treatment. Various concentrations of AA (10, 30, or 90 μmol/L) were added to HK-2 cells for 24 h. The control cells received equal amounts of water only.

3-[4,5-dimethylthiazol-2yl]-2,5-diphenyltetrazolium bromide (MTT) assay

After the AA treatment for 24 h, 5 mg/mL MTT was added to the cells for 4 h. The purple formazan crystals were solubilized in 150 μL acidic isopropanol (0.1 mol/L HCl), and the absorbance was measured at a test wavelength of 570 nm and a reference wavelength of 650 nm using a microplate reader. The relative survival rate was calculated using the following equation: survival rate (%)=(absorbance of AA-treated cells/absorbance of untreated control cells)×100%. The data are expressed as the mean±SD of three independent experiments.

Total RNA extraction

Total RNA was extracted from HK-2 cells grown in 75 cm^2 flasks following treatment with AA (0, 10, 30, or 90 μmol/L) (n=3) using an RNeasy Mini kit (Qiagen, Valencia, CA). The total RNA was quantified using a Beckman DU800 spectrophotometer (Beckman Coulter, Fullerton, CA). Samples with A_{260}/A_{280} ratios greater than 1.8 were further evaluated using an Agilent 2100 Bioanalyzer (Agilent Technologies, Santa Clara, CA). RNA samples with an RNA integrity number greater than 8.0 were used for the subsequent microarray analysis.

Microarray analysis

The microarray analysis was performed as previously described[22]. Briefly, fluorescence-labeled RNA targets were prepared from 5 μg of total RNA samples using a MessageAmp™ RNA kit (Ambion, Austin, TX) and Cy5 dye (Amersham Pharmacia, Piscataway, NJ). Triplicate fluorescent targets were hybridized to the Human Whole Genome OneArray™ (Phalanx Biotech Group, Hsinchu, Taiwan) and scanned using an Axon 4000 scanner (Molecular Devices, Sunnyvale, CA). The Cy5 fluorescent intensity of each spot was analyzed using the Genepix 4.1 software (Molecular Devices). The signal intensity of each spot was corrected by subtracting the background signals in the surrounding area. Control probes were filtered out to measure the background-corrected signal intensity of each spot. We have submitted the original microarray data to Gene Expression Omnibus (GEO), series number GSE18243. Two samples and one series are included (samples=mock, treatment; series=mock+treatment). The sample numbers are GSM455880 (treatment) and GSM455881 (mock). The spots were normalized using the Limma package of the R program[23]. The normalized data were tested for differential expression using the Gene Expression Pattern Analysis Suite v3.1[24]. The 'GeneSetTest' function in the Limma package was used to test which biological pathways were affected by AA in HK-2 cells. This function computes a P-value to test the hypothesis that the selected genes in a pathway tend to be differentially expressed. The score for each pathway following the AA treatment was defined as follows: score=-log ($2P$), if P-value$\leqslant$0.5; or score=log [$2(1-P)$], if P-value>0.5. There were 352 pathways used in this analysis, and they were extracted from ArrayTrack (http://www.fda.

gov/nctr/science/centers/toxicoinformatics/ArrayTrack/), which included the KEGG pathways (http://www.genome.jp/kegg/pathway.html) and PathArt pathways (Jubilant Biosys). Furthermore, the interaction network for genes with fold changes >2.0 and false discovery rates <0.05 was constructed using BiblioSphere Pathway Edition software (Genomatix Applications, http://www.genomatix.de/index.html) based on knowledgebase analyses[25]. Finally, the Cytoscape software was used to visualize the interaction network of AA-regulated genes, including genes related to NF-κB[26].

Quantitative reverse transcriptase-polymerase chain reaction (qRT-PCR)

The expression levels of NF-κB-related genes were further validated by qRT-PCR. RNA samples were reverse-transcribed for 120 min at 37 °C with High Capacity cDNA Reverse Transcription Kit according to the standard protocol of the supplier (Applied Biosystems). Quantitative RT-PCR was performed using 1 μL of cDNA and 2×SYBR Green PCR Master Mix (Applied Biosystems, Foster City, CA). The reaction conditions were as follows: 10 min at 95 °C followed by 40 cycles of 15 s at 95 °C and 1 min at 60 °C. Each assay was run on an Applied Biosystems 7300 Real-time PCR system in triplicate. Fold changes were calculated using the comparative C_T method. The primer sets for selected genes are shown in Table 1.

Table 1. Primer sequences of selected genes for qRT-PCR.

Gene	Primer sequence
CCL20	Sense: 5′-GCTCCTGGCTGCTTTGATGT-3′ Antisense: 5′-GAATACGGTCTGTGTATCCAAGACA-3′
CD68	Sense: 5′-TCTGCCCACCCAGAACCA-3′ Antisense: 5′-CACAGGGCTGGGAACCATT-3′
CYP1A1	Sense: 5′-ATGGGCAAGCGGAAGTGTAT-3′ Antisense: 5′-CCAGTGGCACGCTGAATTC-3′
IGFBP3	Sense: 5′-CAGCGCTACAAAGTTGACTACGA-3′ Antisense: 5′-ATTTCTCTACGGCAGGGACCAT-3′
IL-8	Sense: 5′-FCTTTCCACCCCAAATTTATCAAAG-3′ Antisense: 5′-RAGAGCTCTCTTCCATCAGAAAGCT-3′
LTB	Sense: 5′-ACTTCTCTGGTGACCTTGTTGCT-3′ Antisense: 5′-AGCTTCTGAAACCCCAGTCCTT-3′
SAA2	Sense: 5′-CCGATCAGGCTGCCAATAAA-3′ Antisense: 5′-GCAGAGTGAAGAGGAAGCTCAGT-3′
TNFRSF9	Sense: 5′-TGCGAGAGAGCCAGGACACT-3′ Antisense: 5′-GAAACGGAGCGTGAGGAAGA-3′

Immunofluorescence and confocal microscopy

HK-2 cells were fixed with acetone for 30 min at 4 °C and incubated with the p65 subunit of the NF-κB rabbit polyclonal antibody (Abcam-ab7970) overnight at 4 °C. Alexa Fluor® 488-conjugated secondary goat anti-rabbit antibody was added, and the reaction was incubated at room temperature for 1 h. After the last step for the NF-κB single staining, cell nuclei were labeled by propidium iodide for 15 min at room temperature. The fluorescence imaging was conducted using a laser scanning confocal microscope (TCS SP2 system, Leica) equipped with an argon laser adjusted to 488 nm excitation with a HeNe1 laser.

Transfection and luciferase assay

HK-2 cells were transiently transfected with 5 μg of NF-κB expression plasmid or empty vector (pcDNA 3.1) using the SuperFect® transfection reagent (Qiagen, Valencia, CA, USA). Cells were cultured in 24-well plates overnight and then treated with 10 μmol/L AA for 24 h. The cells were then washed with ice-cold PBS, lysed with 350 μL Triton lysis buffer (50 mmol/L Tris-HCl, 1% Triton X-100, 1 mmol/L dithiothreitol, pH 7.8) and collected with a cell scraper. The luciferase activity was measured as described previously[22]. The relative luciferase activity was calculated by dividing the relative luciferase units (RLU) of the experimental groups by the RLU of untreated NF-κB-transfected cells.

Statistical analysis

Data are presented as the mean±SD. Student's *t*-test was used for comparisons between the control and AA-treated groups. A value of $P<0.05$ was determined to be statistically significant.

Results

Cell viability in AA-treated HK-2 cells

The cell viability (using the MTT assay) was measured after exposing HK-2 cells to various concentrations of AA (10, 30, or 90 μmol/L). AA exhibited cytotoxicity in a dose-dependent manner. The relative survival rates of cells after treatment with 10, 30, and 90 μmol/L AA were 81.9%±4.6%, 55.2%±3.7%, and 45.2%±1.9%, respectively. These results represent the average of three independent experiments (Figure 1).

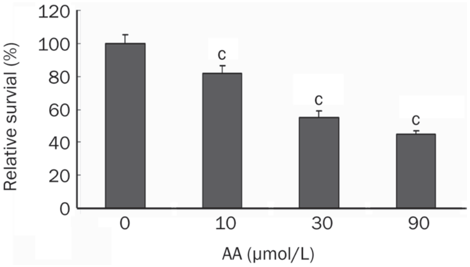

Figure 1. The cytotoxicity of various doses of AA in HK-2 cells. HK-2 cells were treated with 0, 10, 30, and 90 μmol/L of AA. The cell viability was measured by MTT assay. Values are mean±SD of three independent experiments. $^cP<0.01$ *vs* control group.

Cluster analysis of the gene expression profiles in AA-treated HK-2 cells

An unsupervised analysis was used to predict significant differences among the gene expression levels in HK-2 cells in response to 10, 30, and 90 μmol/L of AA treatment. As shown in Table 2, DNA repair, the response to the DNA damage stimulus, the macromolecule metabolic process, and the carbohydrate metabolic process were shown to be significantly regulated in cells in all AA treatment groups.

Pathway analysis of gene expression profiles in AA-treated HK-2 cells

The GeneSetTest function was used to investigate which biological pathways could be downregulated in HK-2 cells in response to treatment with 10, 30, or 90 μmol/L of AA. In this study, pathways with *P* values <0.001 (scores >2.7 or <-2.7) in all AA treatment groups were considered differentially regulated. The pathway analysis revealed that nine pathways were dysregulated following all AA treatments (Table 3). A negative score was indicative of an AA-induced downregulation at all doses. Most of the AA-regulated pathways were associated with immunomodulatory functions, indicating that AA might participate in the regulation of immune genes.

The gene interaction network regulated by AA treatment

To explore the pharmacological and molecular mechanisms of AA, we had first chosen the subtoxic dose of AA (10 μmol/L) to interpret the gene interaction network. Genes with fold changes >2.0 and false discovery rates <0.05 after the 10 μmol/L AA treatment were further selected to construct the interaction network using the Pathway Edition software. The connections between NF-κB and the 10μmol/L AA-regulated genes were noted following the analysis using the Cytoscape software. Nodes for regulated genes and NFKB1 were color-coded according to their $\log_2$ expression values (Figure 2). As shown in Figure 2, most genes were connected with NF-κB, suggesting that NF-κB played a central role in the network. The NF-κB-connected genes with fold changes >2.0 and false discovery rates <0.05 after the treatments of 10, 30, and 90 μmol/L AA are listed in Table 4. The upregulated genes were AOC3, CYP1A1, CYP2E1, DHX9, LTB4R, RASSF1, SPIB, TCF3, TRPV1, and VHL. The downregulated genes were CCL20, CCND2, CD68, CD74, CDH1, CXCL2, EBI3, IGFBP3, IKIP, IL8, LTB, MMP7, PPAP2A, SAA2, STAT1, TNFRSF9, and UCP2.

Validation of NF-κB-related gene expression changes by qRT-PCR

Eight NF-κB-regulated genes (downregulated: CCL20, CD68, IGFBP3, IL8, TNFRSF9, LTB, and SAA2; upregulated: CYP1A1) were chosen for qRT-PCR verification. The expression levels of NF-κB-related genes that were validated by qRT-PCR showed correlations in the general trends for the microar

Table 2. Biological processes significantly regulated by AA in HK-2 cells.

Biological processes	Genes	10 μmol/L _*P*	30 μmol/L_*P*	90 μmol/L_*P*
DNA repair	166	3.15×10^{-7}	7.70×10^{-5}	1.75×10^{-7}
Response to DNA damage stimulus	122	5.40×10^{-7}	2.00×10^{-4}	2.20×10^{-6}
Macromolecule metabolic process	202	4.07×10^{-6}	3.00×10^{-4}	3.18×10^{-6}
Carbohydrate metabolic process	205	4.90×10^{-5}	4.00×10^{-4}	6.17×10^{-5}
DNA metabolic process	236	1.00×10^{-4}	3.70×10^{-3}	7.43×10^{-7}
Apoptosis	295	4.00×10^{-4}	1.60×10^{-3}	1.19×10^{-5}
Cell cycle	169	2.40×10^{-3}	3.04×10^{-2}	8.30×10^{-6}
Transcription	148	5.40×10^{-3}	3.80×10^{-3}	2.20×10^{-5}

The biological pathways affected by AA in HK-2 cells were examined by 'GeneSetTest' function in the Limma package. This function computes a *P*-value to test the hypothesis that the selected genes in a pathway tend to be differentially expressed. "*P*" indicated *P* values.

Table 3. Estimates of various pathways regulated by different doses of AA.

Pathway	10 μmol/L_*P*	30 μmol/L_*P*	90 μmol/L_*P*	10 μmol/L_s	30 μmol/L_s	90 μmol/L_s
Cytokine-cytokine receptor interaction	$<2.20\times10^{-16}$	$<2.20\times10^{-16}$	$<2.20\times10^{-16}$	<-15.66	<-15.66	<-15.66
TNF signaling pathway	2.00×10^{-7}	5.70×10^{-5}	$<2.20\times10^{-16}$	-6.40	-3.94	<-15.66
Interleukin signaling pathway	4.05×10^{-5}	1.37×10^{-4}	$<2.20\times10^{-16}$	-4.09	-3.56	<-15.66
Hematopoietic cell lineage	3.45×10^{-5}	3.10×10^{-6}	4.30×10^{-5}	-4.16	-5.21	-4.07
Cell adhesion molecules (CAMs)	3.75×10^{-4}	7.20×10^{-6}	4.40×10^{-6}	-3.13	-4.84	-5.06
Insulin signaling pathway	3.13×10^{-4}	2.00×10^{-6}	6.84×10^{-5}	-3.20	-5.40	-3.86
IFN signaling pathway	5.44×10^{-5}	4.03×10^{-4}	2.80×10^{-6}	-3.96	-3.09	-5.25
Long-term depression	5.73×10^{-4}	3.24×10^{-5}	1.95×10^{-5}	-2.94	-4.19	-4.41
IL-2 signaling pathway	3.04×10^{-4}	3.19×10^{-5}	3.64×10^{-4}	-3.22	-4.20	-3.14

Pathways with *P* values <0.001 (scores >2.7 or <-2.7) calculated by "GeneSetTest" function in all AA treatments were considered differentially regulated. Pathway analysis revealed that 9 pathways were regulated in all AA treatments. The minus sign of scores in each pathway meant that all AA treatments downregulated every pathway. The results of this study were in triplicate. "*P*" indicated *P* values and "s" indicated score.

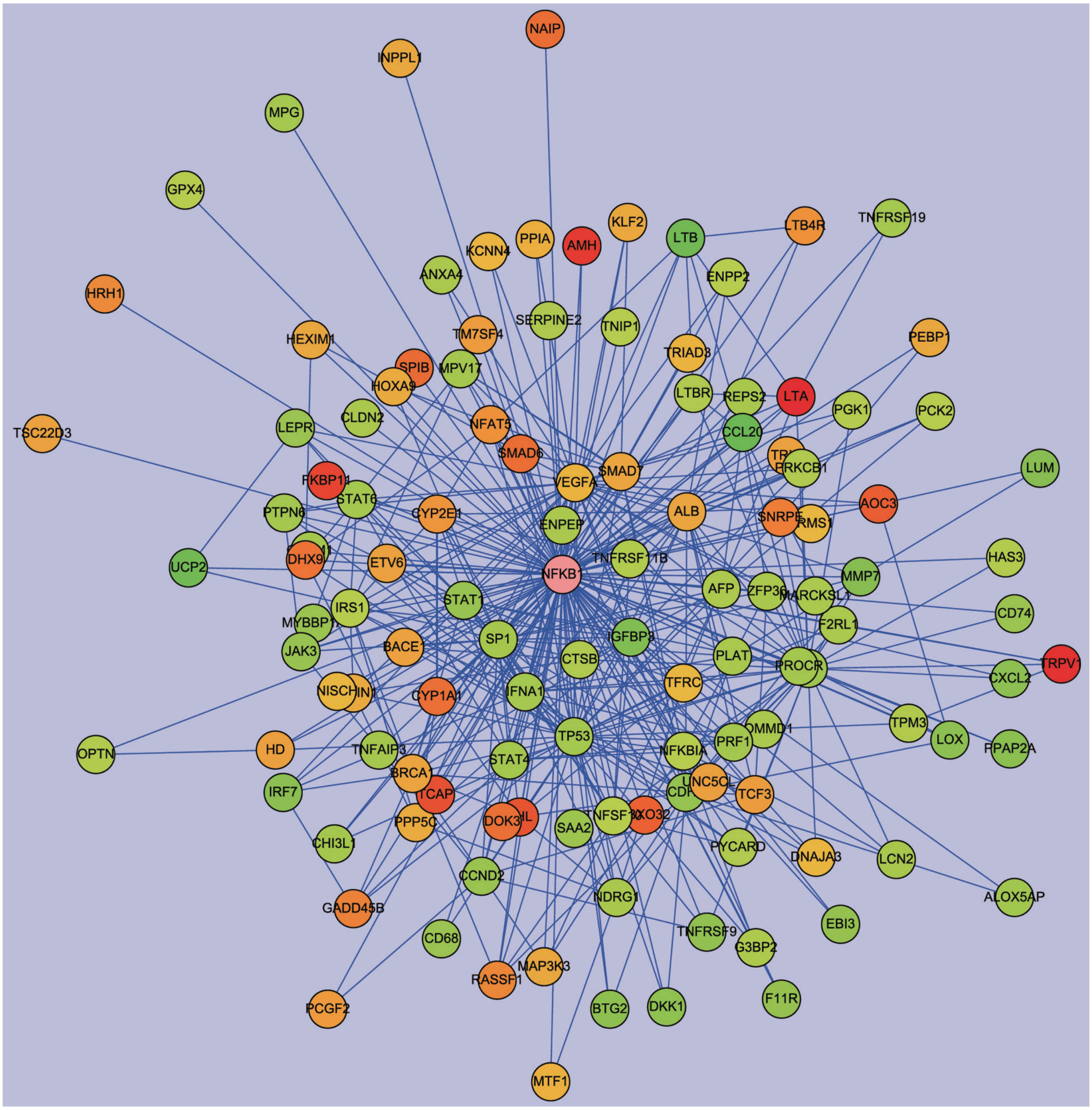
NAIP
INPPL1
MPG
GPX4
KLF2
LTB4R
TNFRSF19
PPIA
AMH
LTB
KCNN4
ANXA4
ENPP2
HRH1
SERPINE2
TNIP1
HEXIM1
TM7SF4
PEBP1
SPIB
MPV17
TRIAD3
HOXA9
LTBR
REPS2
LTA
PGK1
PCK2
CLDN2
TSC22D3
LEPR
NFAT5
CCL20
SMAD6
PRKCB1
LUM
FKBP11
VEGFA
SMAD7
STAT6
CYP2E1
ALB
SNRPE
RMS1
AOC3
PTPN6
ENPEP
HAS3
UCP2
DHX9
ETV6
NFKB1
TNFRSF11B
MMP7
AFP
ZFP36
MARCKSL1
CD74
IRS1
STAT1
F2RL1
MYBBP1
SP1
IGFBP3
JAK3
BACE1
CTSB
PLAT
PROCR
TRPV1
CXCL2
NISCHIN1
CYP1A1
IFNA1
TFRC
OMMD1
TPM3
LOX
OPTN
HD
TNFAIP3
TP53
NFKBIA
PRF1
PPAP2A
STAT4
BRCA1
UNC5CL
IRF7
TCAP
CDH
TCF3
PPP5C
DOK3
SAA2
TNFSF10
FOXO3
CHI3L1
PYCARD
DNAJA3
LCN2
CCND2
NDRG1
ALOX5AP
GADD45B
EBI3
TNFRSF9
G3BP2
CD68
MAP3K3
RASSF1
F11R
PCGF2
BTG2
DKK1
MTF1

Figure 2. Network analysis of expression profiles of 10 μmol/L AA in HK-2 cells. We constructed the interaction network by BiblioSphere Pathway Edition software which was selected the genes with fold changes >2.0 and false discovery rates <0.05 after 10 μmol/L AA treatment. Intensity of nodes for regulated genes and NFKB1 are color-coded according to their $\log_2$ expression values in gradient with red and green indicating the degree of gene upregulation or downregulation, respectively. As shown, NF-κB played a central role in the network.

ray analysis (Table 5).

Effect of AA on NF-κB localization and activity in HK-2 cells

The cellular localization of NF-κB was visualized by confocal microscopy after staining with an antibody against NF-κB p65 (green) (Figure 3D–3F) and propidium iodide (nuclear DNA, red) (Figure 3G–3I). The nuclear distribution of NF-κB in AA (10 μmol/L and 30 μmol/L)-treated cells was less apparent than in normal HK-2 cells. By contrast, the cytoplasmic distribution of NF-κB in AA (10 μmol/L and 30 μmol/L)-treated cells was increased compared with the distribution in normal HK-2 cells (Figure 3A–3F).

To further confirm that AA was able to affect the activity of NF-κB, transgenic cells carrying the NF-κB luciferase gene were used to estimate the NF-κB activity after AA treatment. Because the cell viability of HK-2 cells after treatment with 10 μmol/L of AA was 81.9%±4.6%, whereas that after 30 μmol/L of AA was 55.2%±3.7%, we chose the subtoxic dose of AA (10 μmol/L) to examine the effect of AA on the NF-κB activity by a luciferase assay. The HK-2 cells transfected with empty vec-

Table 4. Gene list of NF-κB connected significantly regulated genes in AA- treated HK-2 cells.

Symbol	Description	10 μmol/L AA FC±SD	 *P* value	30 μmol/L AA FC±SD	 *P* value	90 μmol/L AA FC±SD	 *P* value
AOC3	Amine oxidase, copper containing (vascular adhesion protein 1)	3 3.8±0.53	1.54×10^{-2}	10.16±1.55	5.94×10^{-3}	10.25±1.66	4.46×10^{-3}
CCL20	Chemokine (C-C motif) ligand 20	-11.46±2.20	2.15×10^{-3}	-11.4±1.04	4.31×10^{-4}	-17.4±4.26	5.29×10^{-4}
CCND2	Cyclin D2	-2.24±0.13	8.18×10^{-3}	-2.89±0.16	2.70×10^{-3}	-5.71±0.84	1.35×10^{-3}
CD68	CD68 antigen	-2.16±0.34	2.24×10^{-2}	1.21±0.24	2.98×10^{-1}	1.46±0.22	4.76×10^{-2}
CD74	CD74 molecule, major histocompatibility complex, class II invariant chain	-2.18±0.50	4.56×10^{-2}	-2.33±0.69	2.54×10^{-2}	-2.37±0.57	1.54×10^{-2}
CDH1	Cadherin 1, type 1, E-cadherin (epithelial)	-2.42±0.67	3.31×10^{-2}	-3.97±0.72	6.01×10^{-3}	-4.78±0.94	3.42×10^{-3}
CXCL2	Chemokine (C-X-C motif) ligand 2	-2.71±0.47	1.30×10^{-2}	-3.07±0.50	4.42×10^{-3}	-2.74±0.20	1.99×10^{-3}
CYP1A1	Cytochrome P450, family 1, subfamily A, polypeptide 1	3.21±0.82	2.17×10^{-2}	4.9±1.43	1.43×10^{-2}	4.85±1.24	4.53×10^{-3}
CYP2E1	Cytochrome P450, family 2, subfamily E, polypeptide 1	2.15±0.33	1.77×10^{-2}	4.21±0.78	7.35×10^{-3}	4.3±0.68	2.02×10^{-3}
DHX9	DEAH (Asp-Glu-Ala-His) box polypeptide 9	3.05±0.65	1.78×10^{-2}	2.45±0.66	3.27×10^{-2}	4.59±0.92	1.49×10^{-3}
EBI3	Epstein-Barr virus induced gene 3	-2.37±0.22	1.66×10^{-2}	-2.8±0.40	6.80×10^{-3}	-1.77±0.31	1.73×10^{-2}
IGFBP3	Insulin-like growth factor binding protein 3	-3.19±0.41	1.09×10^{-2}	-3.36±0.92	7.05×10^{-3}	-3.77±1.06	3.95×10^{-3}
IKIP	IKK interacting protein	-1.39±0.04	4.49×10^{-3}	-1.8±0.17	2.51×10^{-2}	-5.2±0.06	1.94×10^{-5}
IL8	Interleukin 8	-2.04±0.29	1.94×10^{-2}	-1.35±0.23	7.96×10^{-2}	-6.66±0.66	1.40×10^{-3}
LTB	Lymphotoxin beta (TNF superfamily, member 3)	-5.15±1.69	1.88×10^{-2}	-9.95±2.42	5.90×10^{-3}	-5.07±1.12	4.87×10^{-3}
LTB4R	Leukotriene B4 receptor	2.21±0.55	3.37×10^{-2}	2.74±0.64	5.75×10^{-3}	4.8±1.16	2.00×10^{-3}
MMP7	Matrix metallopeptidase 7 (matrilysin, uterine)	-2.97±0.23	4.19×10^{-3}	-2.93±0.35	2.70×10^{-3}	-4.23±0.22	8.69×10^{-4}
PPAP2A	Phosphatidic acid phosphatase type 2A	-2.81±0.89	4.39×10^{-2}	-2.51±0.44	1.83×10^{-2}	-3.21±0.61	1.05×10^{-2}
RASSF1	Ras association (RalGDS/AF-6) domain family 1	2.49±0.34	1.35×10^{-2}	4.24±0.84	1.19×10^{-2}	4.81±1.38	2.51×10^{-2}
SAA2	Serum amyloid A2	-2.08±0.34	2.25×10^{-2}	-4.48±0.77	3.66×10^{-3}	-7.18±0.86	1.86×10^{-3}
SPIB	Spi-B transcription factor (Spi-1/PU.1 related)	3.34±0.80	2.12×10^{-2}	6.82±1.67	6.33×10^{-3}	6.95±1.86	6.94×10^{-3}
STAT1	Signal transducer and activator of transcription 1, 91kDa	-2.28±0.24	1.88×10^{-2}	-3.34±0.63	6.61×10^{-3}	-4.21±0.42	2.86×10^{-3}
TCF3	transcription factor 3 (E2A immunoglobulin enhancer binding factors E12/E47)	2.01±0.14	8.79×10^{-3}	2.24±0.33	1.65×10^{-2}	1.61±0.11	3.94×10^{-3}
TNFRSF9	Tumor necrosis factor receptor superfamily, member 9	-2.45±0.37	9.97×10^{-3}	-3.76±0.16	8.99×10^{-4}	-6.05±0.58	6.01×10^{-4}
TRPV1	Transient receptor potential cation channel, subfamily V, member 1	7.62±1.46	8.18×10^{-3}	10.86±1.96	1.53×10^{-3}	13.12±2.94	4.50×10^{-3}
UCP2	Uncoupling protein 2 (mitochondrial, proton carrier)	-4.75±0.63	1.35×10^{-2}	-5.04±1.08	6.01×10^{-3}	-2.91±0.51	6.07×10^{-3}
VHL	Von Hippel-Lindau tumor suppressor	4.19±0.54	7.12×10^{-3}	2.49±0.62	3.96×10^{-2}	4.12±0.71	5.83×10^{-3}

[a] The statistical analysis was performed by *t*-statistics. Genes with $P<0.05$ are listed.

Table 5. Expression levels of selective NF-κB regulated genes by qRT-PCR in AA-treated HK-2 cells.

Gene	Fold changes 10 μmol/L AA	 30 μmol/L AA
CCL20	-9.09	-9.09
CD68	-1.45	1.01
CYP1A1	1.79	3.83
IGFBP3	-4.55	-3.57
IL8	-1.69	-2.17
LTB	-4.17	-4.17
SAA2	-2.38	-3.23
TNFRSF9	-2.22	-2.08

The data represent the mean fold changes in triplicates.

tor behaved like non-transfected cells. Both non-transfected and empty vector-transfected control groups showed a significantly much lower luciferase activity compared to cells transfected with the NF-κB luciferase reporter gene (Figure 4). NF-κB transgenic HK-2 cells were treated with 10 μmol/L AA, and the luciferase activity was analyzed. The results from these analyses indicated that AA significantly inhibited the luciferase activity in these cells compared with the untreated cells (Figure 4). These data revealed that 10 μmol/L AA can significantly suppress the NF-κB activity in HK-2 cells.

Discussion

Microarray analysis has become a popular and useful tool to study the effects of agents on gene expression in cells, tissues, and organs; however, only a few studies have applied DNA

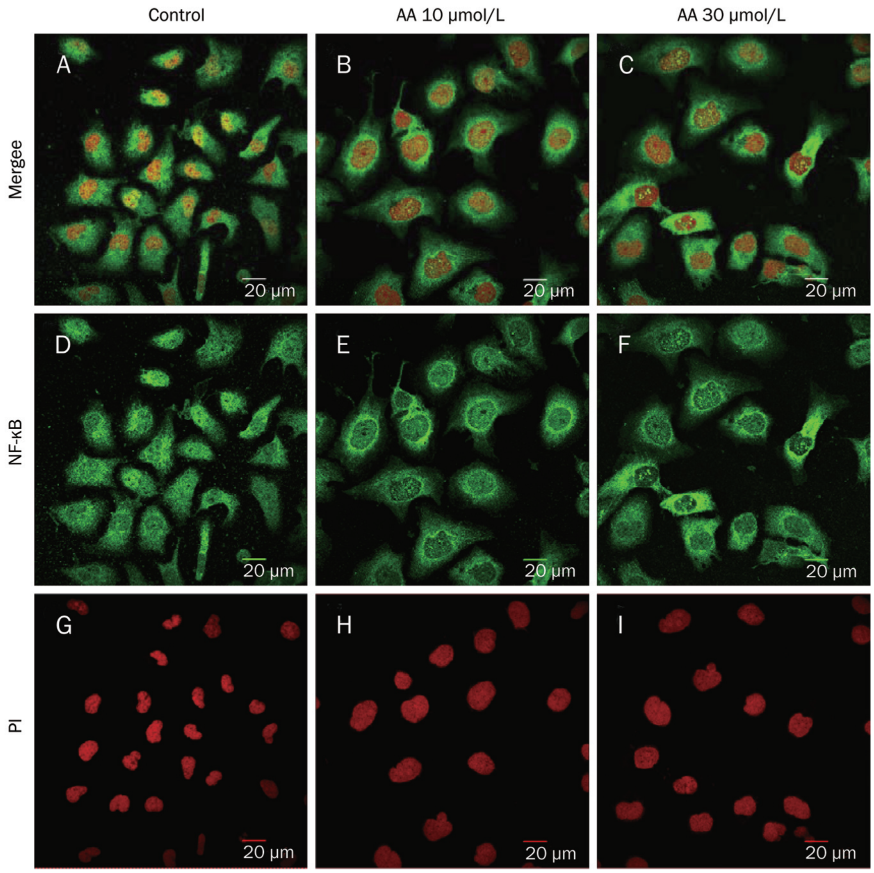

Figure 3. Cellular localization of the p65 subunit of NF-κB before and after AA treatment in HK-2 cells. NF-κB localization was visualized in panel D–F (green) and PI was used for nuclear staining (red) (panel G–I) by immunofluorescence and confocal microscopy. The nuclear distribution of NF-κB in AA-treated cells was less apparent than that in normal HK-2 cells (A–F).

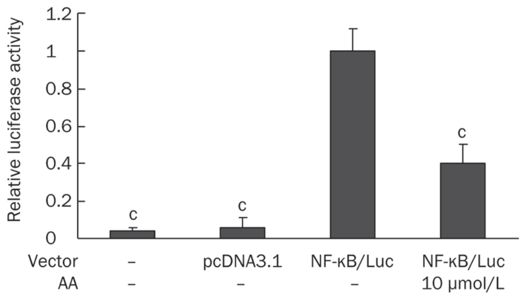

Figure 4. The inhibitory effect of 10 μmol/L AA on NF-κB activity in HK-2 cells. HK-2 cells were transfected with NF-κB luciferase gene and were subsequently incubated with 10 μmol/L AA for 24 h. Experiments were done in triplicate and all results of luciferase assay expressed as relative luciferase units (RLU). Relative luciferase activity was calculated by dividing RLU of non-transfected cells, empty vector (pcDNA 3.1)-transfected cells, and AA-treated NF-κB-transfected cells by the RLU of untreated NF-κB-transfected cells. Error bars represent mean±SD of relative luciferase activity. $^{c}P<0.01$ *vs* untreated NF-κB-transfected cells.

microarray analysis to investigate the effects of AA. In this *in vitro* study on the gene expression profiles of AA-treated (HK-2) cells, the normal human proximal tubular cell line was used, in contrast with the human colorectal cancer cell line (HCT 116) used by Simoes[27]. Our results showed that HK-2 cells were more sensitive to AA-induced cytotoxicity than HCT 116 cells. The IC_{50} values of AA after 24 h treatment in HK-2 cells and HCT 116 cells were 30 μmol/L and 100 μmol/L, respectively. Moreover, the effect of AA on gene expression was more profound in HK-2 cells than in HCT 116 cells[27]. A previous report indicated no significant difference in TP53 expression in P53-WT HCT 116 cells after a 24 h exposure to AA (100 μmol/L), whereas our study showed a marked downregulation of TP53 gene expression (fold change -1.92 after qRT-PCR confirmation) in 10 μmol/L AA-treated HK-2 cells (data not shown). In an *in vivo* study exploring the gene expression profiles of AA, rats were exposed to AA to distinguish the carcinogenic effects on target (kidney) and non-target (liver) tissues[28]. The microarray analysis after the AA treatment showed that there were more significantly altered genes and biological processes in the kidney compared to the liver. These data suggest that the analysis of gene expression profiles can be used to define the different responses of the kidney and liver to AA. Another experiment using gene expression profiling was conducted to study AA-induced renal tumorigenesis in the short-term AA-treated Eker rats (heterozygous for a mutation in the tuberous sclerosis 2 [Tsc2] tumor suppresser gene) and wild-type rats[29]. The results indicated that the gene expression profiles of AA-treated Eker and wild-type rats were Tsc2-independent.

Our finding revealed that AA exhibited cytotoxicity in a dose-dependent manner. These results were similar to an earlier study by Guo *et al*[30] demonstrating that AAI, AAIa, and

AAII inhibited the growth of HK-2 cells in a concentration-dependent and time-dependent manner. They also found that AAI, AAIa and AAII could affect the cell cycle and even induce cell apoptosis. Moreover, by microarray analysis, we noticed that genes involved in DNA repair, response to DNA damage stimulus, apoptosis, and cell cycle were significantly regulated by different concentrations of AA (Table 2). The pathway analysis showed that most of the AA-regulated pathways were associated with immunomodulatory functions, indicating that AA might participate in the regulation of immune genes. Furthermore, it has been noted that NF-κB is downregulated following AA exposure, and that it plays a central role in the gene networks regulated by AA (Figure 2). NF-κB is a nuclear transcription factor consisting of heterodimers including Rel A (p65), Rel B, c-Rel, p50, and p52. NF-κB activity can be induced by infection, pathogenic microorganisms, carcinogens, necrotic cell products, and inflammatory cytokines. When stimulated, activated NF-κB is translocated from the cytoplasm to the nucleus, where it binds to specific DNA sequences in the promoter regions of genes and initiates the expression of genes that encode proteins to control stress responses, cell adhesion, proliferation, and apoptosis[31]. After NF-κB is activated, it may serve as a transcription factor, and a small change in the gene expression of NF-κB may lead to significant changes in the expression levels of NF-κB-regulated downstream genes. In our study, the mRNA expression level of NF-κB in 10, 30, and 90 μmol/L AA-treated cells was 1.24±0.14, 1.04±0.24, and 1.20±0.23, respectively.

Constitutive NF-κB activity can induce the overexpression of proinflammatory genes, which can lead to acute or chronic inflammatory disease, such as rheumatoid arthritis, inflammatory bowel disease, and atherosclerosis[32]. Similarly, the upregulated expression of NF-κB has been found in pancreatic cancer, hepatocellular carcinoma, and colorectal cancer[33]. Recent research strongly suggests a relationship between chronic inflammation, NF-κB activation, and cancer[33, 34]. Because NF-κB target genes promote tumor cell proliferation, survival, migration and angiogenesis, the inhibition of NF-κB was thought to be useful as an anticancer therapy in clinical studies. However, the inhibition of NF-κB has been found to promote squamous cell carcinomas in epidermal skin[35, 36]. Although plants of the genus Aristolochia have been used as an anti-inflammatory (*eg*, for arthritis), analgesic, diuretic, and anticancer agents in the past, it was interesting to note that more recently, AA has been reported to be nephrotoxic and carcinogenic. These different properties of AA are similar to the dual effects of NF-κB. In our study, the results from immunofluorescence confocal microscopy and a luciferase reporter assay revealed that NF-κB activity in HK-2 cells was inhibited by AA. The nuclear localization of NF-κB in AA (10 μmol/L and 30 μmol/L)-treated cells was less apparent than in normal HK-2 cells. It was suggested that AA decreased the nuclear staining of NF-κB by the inhibition of NF-κB translocation from the cytoplasm to the nucleus. Concurrently, our study showed that AA significantly inhibited NF-κB activity in HK-2/NF-κB transgenic cells compared with the control cells.

Among the list of genes significantly regulated by the 10, 30, and 90 μmol/L AA treatments, chemokine ligand 20 (CCL20) was the most markedly downregulated. CCL20 is a macrophage inflammatory protein that plays a role in B-cell adhesion to the inflamed endothelium[37]. Interleukin 8 (IL-8) was another downregulated gene identified in our study. The gene expression of IL-8 can be induced by IL-1 and TNF and simultaneously regulated by NF-κB[38]. Insulin-like growth factor binding protein 3 (IGFBP3) was also shown to be downregulated following AA treatment in this study. IGFBP-3 can inhibit the proliferative function and anti-apoptotic functions of insulin-like growth factor (IGF)[39]. Recently, it has been shown that the regulation of IGFBP-3 involves the phosphatidylinositol-3 kinase (PI3K) and NF-κB pathways[39, 40]. Another downregulated gene identified in this study was CD68, which is a transmembrane glycoprotein highly expressed in human monocytes and tissue macrophages. CD68 is also a member of the scavenger receptor family and typically functions to clear cellular debris, promote phagocytosis, and mediate the recruitment and activation of macrophages. Based on immunohistochemistry, CD68 is histiocytic (similar to the T-lymphocytic marker CD3) and is associated with multicentric reticulohistiocytosis[41], rheumatoid arthritis[42], Crohn's disease[43], and vasculitic neuropathies[44]. Besides the genes mentioned above, the gene expression of other NF-κB downregulated genes, including SAA2, LTB, TNFRSF9, was confirmed by real-time qRT-PCR. Most of these NF-κB downregulated genes are involved the inflammatory response. In summary, the downregulation of NF-κB regulated genes by AA may partly explain the use of Chinese herbs of *Aristolochiaceae* to treat inflammatory diseases such as arthritis in the past.

In conclusion, AA exhibited a dose-dependent cytotoxic effect in HK-2 cells and induced alterations in gene expression profiles related to DNA damage response, stress response, and other pathways. In addition, we demonstrated that AA treatment downregulated nine biological pathways, most of which were associated with immunomodulatory functions in HK-2 cells, and NF-κB plays a central role in the network topology. The relationship between AA and NF-κB was further confirmed by real-time qRT-PCR, confocal microscopy in AA-treated HK-2 cells and the luciferase reporter assay in HK-2/ NF-κB transgenic cells. Our study reveal that AA can suppress NF-κB activity in human cells, and these results may partly explain the toxicological and pharmacological effects of the genus Aristolochia.

Acknowledgements

We thank Mr Wei-shuen SHEN, Miss Zih-syuan WANG, Miss Wan-yu TIEN, Miss Wei-pin HUANG, and Miss Zhao-ying DING for their technical assistance. This work was supported by grants from the National Research Program for Genomic Medicine, the National Science and Technology Program for Agricultural Biotechnology, the National Science Council, the Committee on Chinese Medicine and Pharmacy of the Department of Health (CCMP 96-RD-201 and CCMP 97-RD-201), and China Medical University (CMU95-051).

Author contribution

Jaung-geng LIN conceived and coordinated the study; Su-yin CHIANG, Tin-yun HO, and Chien-yun HSIANG designed the study and supervised the data collection; Ya-yin CHEN, Hsiu-ching WU, and Shung-te KAO performed the experiments; Tin-yun HO and Chien-yun HSIANG contributed analytical tools; and Ya-yin CHEN analyzed the data and wrote the manuscript.

References

1 Rosenmund H, Reichstein T. Zur Kenntnis der Aristolochiasäure. Pharm Acta Helv 1943; 18: 243–61.

2 Debelle FD, Vanherweghem JL, Nortier JL. Aristolochic acid nephropathy: a worldwide problem. Kidney Int 2008; 74: 158–69.

3 Zhang G, Shimokawa S, Mochizuki M, Kumamoto T, Nakanishi W, Watanabe T, *et al*. Chemical constituents of Aristolochia constricta: antispasmodic effects of its constituents in guinea-pig ileum and isolation of a diterpeno-lignan hybrid. J Nat Prod 2008; 71: 1167–72.

4 Messiano GB, Vieira L, Machado MB, Lopes LM, de Bortoli SA, Zukerman-Schpector J. Evaluation of insecticidal activity of diterpenes and lignans from Aristolochia malmeana against Anticarsia gemmatalis. J Agric Food Chem 2008; 56: 2655–9.

5 Hinou J, Demetzos C, Harvala C, Roussakis C. Cytotoxic and antimicrobial principles from the roots of Aristolochia longa. Int J Crude Drug Res 1990; 28: 149–51.

6 Arlt VM, Stiborova M, Schmeiser HH. Aristolochic acid as a probable human cancer hazard in herbal remedies: a review. Mutagenesis 2002; 17: 265–77.

7 Loiko EN, Samal AB, Shulyakovskaya SM. H_2O_2-induced platelet aggregation and increase in intracellular Ca^{2+} concentration are blocked by inhibitors of intracellular signaling. Biochemistry (Mosc) 2003; 68: 1210–6.

8 Iuliano L, Pedersen JZ, Pratico D, Rotilio G, Violi F. Role of hydroxyl radicals in the activation of human platelets. Eur J Biochem 1994; 221: 695–704.

9 Marshall LA, Chang JY, Calhoun W, Yu J, Carlson RP. Preliminary studies on phospholipase A_2-induced mouse paw edema as a model to evaluate antiinflammatory agents. J Cell Biochem 1989; 40: 147–55.

10 Vishwanath BS, Fawzy AA, Franson RC. Edema-inducing activity of phospholipase A_2 purified from human synovial fluid and inhibition by aristolochic acid. Inflammation 1988; 12: 549–61.

11 Lindahl M, Tagesson C. Selective inhibition of group II phospholipase A_2 by quercetin. Inflammation 1993; 17: 573–82.

12 Rosenthal MD, Vishwanath BS, Franson RC. Effects of aristolochic acid on phospholipase A_2 activity and arachidonate metabolism of human neutrophils. Biochim Biophys Acta 1989; 1001: 1–8.

13 Moreno JJ. Effect of aristolochic acid on arachidonic acid cascade and *in vivo* models of inflammation. Immunopharmacology 1993; 26: 1–9.

14 Shirwaikar A, Somashekar AP, Udupa AL, Udupa SL, Somashekar S. Wound healing studies of Aristolochia bracteolata Lam. with supportive action of antioxidant enzymes. Phytomedicine 2003; 10: 558–62.

15 Kluthe R, Vogt A, Batsford S. Double blind study of the influence of aristolochic acid on granulocyte phagocytic activity. Arzneimittelforschung 1982; 32: 443–5. German.

16 Vanherweghem JL, Depierreux M, Tielemans C, Abramowicz D, Dratwa M, Jadoul M, *et al*. Rapidly progressive interstitial renal fibrosis in young women: association with slimming regimen including Chinese herbs. Lancet 1993; 341: 387–91.

17 Vanhaelen M, Vanhaelen-Fastre R, But P, Vanherweghem JL. Identification of aristolochic acid in Chinese herbs. Lancet 1994; 343: 174.

18 Martinez MC, Nortier J, Vereerstraeten P, Vanherweghem JL. Progression rate of Chinese herb nephropathy: impact of Aristolochia fangchi ingested dose. Nephrol Dial Transplant 2002; 17: 408–12.

19 Cosyns JP, Jadoul M, Squifflet JP, Van Cangh PJ, Van Ypersele de Strihou C. Urothelial malignancy in nephropathy due to Chinese herbs. Lancet 1994; 344: 188.

20 Nortier JL, Martinez MC, Schmeiser HH, Arlt VM, Bieler CA, Petein M, *et al*. Urothelial carcinoma associated with the use of a Chinese herb (Aristolochia fangchi). N Engl J Med 2000; 342: 1686–92.

21 Lai MN, Lai JN, Chen PC, Tseng WL, Chen YY, Hwang JS, *et al*. Increased risks of chronic kidney disease associated with prescribed Chinese herbal products suspected to contain aristolochic acid. Nephrology 2009; 14: 227–34.

22 Cheng WY, Hsiang CY, Bau DT, Chen JC, Shen WS, Li CC, *et al*. Microarray analysis of vanillin-regulated gene expression profile in human hepatocarcinoma cells. Pharmacol Res 2007; 56: 474–82.

23 Smyth GK, editor. Limma: linear models for microarray data. New York: 2005. p 397–420.

24 Montaner D, Tarraga J, Huerta-Cepas J, Burguet J, Vaquerizas JM, Conde L, *et al*. Next station in microarray data analysis: GEPAS. Nucleic Acids Res 2006; 34: W486–91.

25 Seifert M, Scherf M, Epple A, Werner T. Multievidence microarray mining. Trends Genet 2005; 21: 553–8.

26 Shannon P, Markiel A, Ozier O, Baliga NS, Wang JT, Ramage D, *et al*. Cytoscape: a software environment for integrated models of biomolecular interaction networks. Genome Res 2003; 13: 2498–504.

27 Simoes ML, Hockley SL, Schwerdtle T, da Costa GG, Schmeiser HH, Phillips DH, *et al*. Gene expression profiles modulated by the human carcinogen aristolochic acid I in human cancer cells and their dependence on TP53. Toxicol Appl Pharmacol 2008; 232: 86–98.

28 Chen T, Guo L, Zhang L, Shi L, Fang H, Sun Y, *et al*. Gene expression profiles distinguish the carcinogenic effects of aristolochic acid in target (Kidney) and non-target (Liver) tissues in rats. BMC Bioinformatics 2006; 7: S20.

29 Stemmer K, Ellinger-Ziegelbauer H, Ahr HJ, Dietrich DR. Carcinogen-specific gene expression profiles in short-term treated Eker and wild-type rats indicative of pathways involved in renal tumorigenesis. Cancer Res 2007; 67: 4052–68.

30 Guo YC, Lin ZX, Li H, Luo WH. The toxic effects of three Aristolochia compounds on HK-2 cell. Carcinog Teratog & Mutagen 2006; 18: 88–92. Chinese.

31 Beinke S, Ley SC. Functions of NF-kappaB1 and NF-kappaB2 in immune cell biology. Biochem J 2004; 382: 393–409.

32 Valledor AF, Ricote M. Nuclear receptor signaling in macrophages. Biochem Pharmacol 2004; 67: 201–12.

33 Zhang Z, Rigas B. NF-kappaB, inflammation and pancreatic carcinogenesis: NF-kappaB as a chemoprevention target (review). Int J Oncol 2006; 29: 185–92.

34 Dobrovolskaia MA, Kozlov SV. Inflammation and cancer: when NF-kappaB amalgamates the perilous partnership. Curr Cancer Drug Targets 2005; 5: 325–44.

35 Dajee M, Lazarov M, Zhang JY, Cai T, Green CL, Russell AJ, *et al*. NF-kappaB blockade and oncogenic Ras trigger invasive human epidermal neoplasia. Nature 2003; 421: 639–43.

36 van Hogerlinden M, Rozell BL, Ahrlund-Richter L, Toftgard R. Squamous cell carcinomas and increased apoptosis in skin with inhibited Rel/nuclear factor-kappaB signaling. Cancer Res 1999; 59:

3299–303.

37 Meissner A, Zilles O, Varona R, Jozefowski K, Ritter U, Marquez G, *et al*. CC chemokine ligand 20 partially controls adhesion of naive B cells to activated endothelial cells under shear stress. Blood 2003; 102: 2724–7.

38 Mukaida N, Mahe Y, Matsushima K. Cooperative interaction of nuclear factor-kappa B- and cis-regulatory enhancer binding protein-like factor binding elements in activating the interleukin-8 gene by pro-inflammatory cytokines. J Biol Chem 1990; 265: 21128–33.

39 Gewirtz DA. Growth arrest and cell death in the breast tumor cell in response to ionizing radiation and chemotherapeutic agents which induce DNA damage. Breast Cancer Res Treat 2000; 62: 223–35.

40 Deng DX, Spin JM, Tsalenko A, Vailaya A, Ben-Dor A, Yakhini Z, *et al*. Molecular signatures determining coronary artery and saphenous vein smooth muscle cell phenotypes: distinct responses to stimuli. Arterioscler Thromb Vasc Biol 2006; 26: 1058–65.

41 Luz FB, Gaspar TAP, Kalil-Gaspar N, Ramos-e-Silva M. Multicentric reticulohistiocytosis. J Eur Acad Dermatol Venereol 2001; 15: 524–31.

42 Catalina-Fernandez I, Alvarez AC, Martin FC, Fernandez-Mera JJ, Saenz-Santamaria J. Cutaneous intralymphatic histiocytosis associated with rheumatoid arthritis: report of a case and review of the literature. Am J Dermatopathol 2007; 29: 165–8.

43 Franchimont N, Reenaers C, Lambert C, Belaiche J, Bours V, Malaise M, *et al*. Increased expression of receptor activator of NF-kappaB ligand (RANKL), its receptor RANK and its decoy receptor osteoprotegerin in the colon of Crohn's disease patients. Clin Exp Immunol 2004; 138: 491–8.

44 Haslbeck KM, Bierhaus A, Erwin S, Kirchner A, Nawroth P, Schlotzer U, *et al*. Receptor for advanced glycation endproduct (RAGE)-mediated nuclear factor-kappaB activation in vasculitic neuropathy. Muscle Nerve 2004; 29: 853–60.

Acta Pharmacologica Sinica (2010) 31: 237–243
© 2010 CPS and SIMM All rights reserved 1671-4083/10 $32.00
www.nature.com/aps

Original Article

Effect of lactoferrin- and transferrin-conjugated polymersomes in brain targeting: *in vitro* and *in vivo* evaluations

Hui-le GAO, Zhi-qing PANG, Li FAN, Kai-li HU, Bing-xian WU, Xin-guo JIANG*

Department of Pharmaceutics, School of Pharmacy, Fudan University, Shanghai 201203, China

Aim: To evaluate the effect of lactoferrin (Lf) and transferrin (Tf) in brain targeting.
Methods: Polymersomes (PSs), employed as vectors, were conjugated with Lf or Tf and were characterized by morphology, particle size, zeta potential, and surface densities of the Lf or Tf molecules. *In vitro* uptake of Lf-PS and Tf-PS by bEnd.3 cells was investigated using coumarin-6 as a fluorescent probe. *In vivo* tissue distribution and pharmacokinetics of ^{125}I-Lf-PS and ^{125}I-Tf-PS were also examined.
Results: The mean particle size of PS, Lf-PS, and Tf-PS was around 150 nm and the zeta potential of the PSs was about -20 mV. Less than 0.12% of the coumarin was released from coumarin-6-loaded PS in 84 h indicating that coumarin-6 was an accurate probe for the PSs' behavior *in vitro*. It was shown that the uptake of Lf-PS and Tf-PS by bEnd.3 cells was time-, temperature-, and concentration-dependent. Both Lf and Tf could increase the cell uptake of PSs at 37 °C, but the uptake of Tf-PS was significantly greater than that of Lf-PS. *In vivo* tissue distribution and pharmacokinetics in mice revealed higher brain uptake and distribution of Tf-PS than Lf-PS, which was in accordance with *in vitro* uptake results. The drug targeting index (DTI) of Tf-PS with regard to Lf-PS was 1.51.
Conclusion: Using a PS as the delivery vector and bEnd.3 cells as the model of the blood-brain barrier (BBB), Tf was more effective than Lf in brain targeting.

Keywords: blood-brain barrier; lactoferrin; transferrin; brain drug targeting

Acta Pharmacologica Sinica (2010) 31: 237–243; doi: 10.1038/aps.2009.199

Introduction

The blood-brain barrier (BBB), the most formidable obstacle in the treatment of brain diseases, protects the central nervous system (CNS) from exogenous toxicants, but at the same time, also excludes potential therapeutics[1]. In fact, almost all of the large-molecule drugs and more than 98% of small-molecule drugs cannot cross the BBB[2]. Realizing that so few drugs cross the BBB, researchers have continuously committed to developing various drug delivery and targeting strategies to overcome this obstacle[3–5]. However, the efforts are still far from sufficient.

As local invasive (direct injection/infusion) delivery has been associated with many disadvantages[6], global noninvasive strategies taking advantage of endogenous nutrient transport systems present at the BBB can facilitate widespread transport across the whole brain without disruption of the barrier properties[7]. Among the various noninvasive approaches, receptor-mediated systems seem to be one of the most promising. Coupling vectors with specific receptors on the BBB to loading vehicles combines the advantages of brain targeting, high incorporation capacity, reduction of side effects, and circumvention of the multidrug efflux system[8].

Lactoferrin (Lf) and transferrin (Tf) belong to the transferrin family. Tf is a single-chain glycoprotein containing about 700 amino acids whereas Lf contains about 690 amino acids[9, 10]. Though Tf and Lf are quite similar overall in sequence and structure, and coordinate iron in the same manner, they differ in the structure of their inter-lobe linker, the salt bridge between the helical linker, their pattern of disulfide bonding, and their receptor binding properties[11]. Lf receptor (LfR) and Tf receptor (TfR) have been demonstrated to exist on the BBB in different species and to be involved in Lf and Tf transport across the BBB *in vitro* and *in vivo*[12–15]. There are interesting reports that the expression of LfR in the brain is increased under some disease conditions such as Parkinson's disease and Alzheimer's disease[16–18] and that TfR is more highly expressed on tumor cells than on ordinary cells[19]. These data suggest Lf and Tf have prospective benefits in brain targeting.

Recently, Ji *et al* compared the brain uptake of Lf with that of Tf; the uptake of Lf was much higher than Tf, indicating that

---

* To whom correspondence should be addressed.
E-mail xgjiang@shmu.edu.cn
Received 2009-08-06 Accepted 2009-12-21

Lf might be more useful as a ligand for facilitating drug delivery into the brain[20]. However, there are several factors that can affect the brain targeting of drug delivery systems, such as the binding affinity and capacity of targeting ligands, the surface density of the ligands conjugated with each vector, the characteristics of vectors, and blood elimination. The characteristics of targeting ligands might change after they conjugate with vectors, and the targeting effect of drug delivery systems is not always coincident with that of targeting ligands. Therefore, it has not been confirmed which ligand – Lf or Tf – has better brain targeting ability after conjugation with vectors, which is important for researchers to develop new effective brain drug delivery systems.

To evaluate the effect of two targeting ligands, Tf and Lf, in enhancing drug delivery into the brain, a vector could be employed. Polymersomes (PSs), as a new class of synthetic thin-shelled capsules based on block copolymer chemistry, are self-assembled vesicles of amphiphilic block copolymers with thicker and tougher membranes than lipids[21, 22]. Compared with liposomes, PSs contain many advantages such as adjustable amphiphile molecular weight (MW) and ratio, tunable physical and chemical properties, and tunable *in vivo* behavior[23]. Pang *et al* confirmed that PSs could be employed as vectors to develop a brain targeting drug delivery system[23].

The objective of this paper is to develop two brain delivery systems, Lf-conjugated PS (Lf-PS) and Tf-conjugated PS (Tf-PS), and to compare the relative superiority of Lf and Tf in brain drug targeting.

Materials and Methods

Materials and animals

Poly (butadiene-b-ethylene oxide) (PBD-PEO, 5000-2300) was purchased from Polymer Source Inc, America. Poly (ethylene glycol-b-lactic acid) (PEG-PLA, 3400:4000) and maleimide-PEG-PLA (Mal-PEG-PLA, 3400:4000) was custom-synthesized by Chengdu Organic Chemicals Co, Ltd, China. Holo-transferrin (human), lactoferrin (from bovine colostrum), 2-iminothiolane (Traut's reagent) and coumarin-6 were purchased from Sigma, America. Na^{125}I was purchased from Chengdu Gaotong Isotope Corporation, China. Sepharose CL-4B was purchased from Pharmacia, Sweden. Other agents (analytical pure) were all from Sinopharm Chemical Reagent Co, Ltd, China.

KM mice (18–20 g, ♀) were obtained from Shanghai Slac Laboratory Animal Co, Ltd and maintained at 22±2 °C on a 12-h light-dark cycle with access to food and water *ad libitum*. The animals used for the experiment were treated according to the protocols evaluated and approved by the ethical committee of Fudan University.

Preparation and characterization of PS, Lf-PS, and Tf-PS

Preparation of PSs

PSs were prepared using film rehydration as described by Photos *et al*[24]. Briefly, 2 mL of copolymer solution in dichloromethane (5 g/L, PBD-PEO:PEG-PLA:MAL-PEG-PLA=7:2:1) was first thoroughly dried onto the walls of a 100-mL glass vial for at least 1 h on the rotary evaporator (R-200, Buchi, Germany). A volume of 2 mL of 0.01 mol/L sodium phosphate buffer (PBS), pH 7.4, was added to rehydrate the film for 30 min at 37 °C. The liquid was subjected to sonication (200 W) for 200 s, followed by passing through a 0.22 μm microporous membrane. Coumarin-6-loaded PSs were prepared with the same procedure except that 0.1% (*w/v*) of coumarin-6 was added to the dichloromethane solution before film formation and the obtained PSs were subjected to a 1.5×20 cm sepharose CL-4B column and eluted with 0.01 mol/L PBS, pH 7.4, to remove the unentrapped coumarin-6.

Preparation of Lf-PS and Tf-PS

Lf and Tf were thiolated by a reaction for 60 min with a 30:1 molar excess of 2-iminothiolane in 0.15 mol/L sodium borate buffer, pH 8.0, supplemented with 0.1 mmol/L EDTA, as described previously[25]. The product was then applied to a Hitrap™ Desalting column (Pharmacia, Sweden) and eluted with 0.01 mol/L PBS, pH 7.4. The protein fractions were collected and introduced thiol groups were determined spectrophotometrically (λ/nm=412) with Ellman's reagent[26].

Lf-PS and Tf-PS were prepared by incubating the purified thiolated Lf or Tf with the PS at room temperature for 5 h. The products were then subjected to a 1.5×20 cm sepharose CL-4B column and eluted with 0.01 mol/L PBS, pH 7.4, to remove the unconjugated proteins. The particles concentration was determined by turbidimetry using a UV-2401 spectrophotometer at 350 nm (Shimadzu, Japan).

^{125}I-Lf-PS and ^{125}I-Tf-PS were prepared by incubating the Lf or Tf with Na^{125}I (1 mg 74 MBq and 1 mg 92 MBq, respectively) at 35 °C for 5 min. The products were applied to a Hitrap Desalting column and eluted with 0.01 mol/L PBS, pH 7.4. The protein fractions were subjected to the above procedure to prepare ^{125}I-Lf-PS and ^{125}I-Tf-PS.

Morphology, particle size, and zeta potential

The mean diameter and zeta potential of the PS, Lf-PS, and Tf-PS were determined by dynamic light scattering (DLS) using a Zeta Potential/Particle Sizer NICOMP™380 ZLS (Santa Barbara, CA). The morphological examination of PS was carried out by transmission electron microscope (H-600, Hitachi, Japan).

The number of Lf or Tf molecules conjugated with each Lf-PS or Tf-PS

The calculation for the surface number of Lf or Tf molecules per Lf-PS or Tf-PS was based on the relation between concentration of Lf-PS or Tf-PS and intensity of radioactivity of Lf or Tf[25, 27]. The procedure is as follows:

If A_1 is the intensity of radioactivity of ^{125}I-Lf or ^{125}I-Tf, m_1 is the weight of Lf or Tf; then the specific radioactivity (k1) can be calculated by: $k_1=A_1/m_1$;

If m_2 is the weight of ^{125}I-Lf-PS or ^{125}I-Tf-PS; D is the particle diameter of ^{125}I-Lf-PS or ^{125}I-Tf-PS; then the number (N_1) of ^{125}I-Lf-PS or ^{125}I-Tf-PS can be calculated by $N_1=6\times m_2\times 10^{-3}/[\pi\times(D^3-d^3)\times 10^{-21}\times\rho]$, where ρ=1.06 g/cm^3, d=8 nm[28];

If A_2 is the intensity of radioactivity of ^{125}I-Lf-PS or ^{125}I-Tf-PS; M is molecular weight of Lf or Tf; then the number of ^{125}I-Lf or ^{125}I-Tf conjugated with PS can be calculated by: $N_2=A_2×k_1/M×6.02×10^{23}$;

Then, the number of Lf or Tf per ^{125}I-Lf-PS or ^{125}I-Tf-PS can be calculated by: $n=N_2/N_1$.

In vitro release of coumarin-6 from PS

In vitro release experiments of coumarin-6 from the PS were performed at 37 °C in 0.01 mol/L PBS (pH 4 and pH 7.4) to evaluate if the fluorescent probe remained associated with the particles during an 84-h incubation period. pH 4 and pH 7.4 represented the pH in the endo-lysosomal compartment and physiologic pH, respectively. Coumarin-6-loaded PSs were incubated at a particle concentration of 7 mg/L with shaking at 100 r/min under a predetermined sink condition. Periodic samples were lyophilized, then reconstituted by 1 mL methanol, and used for HPLC analysis of coumarin-6 after centrifugalization at 10 000×*g* for 10 min.

In vitro uptake of coumarin-6-labeled PS, Lf-PS, and Tf-PS by bEnd.3 cells

Cell culture

bEnd.3 cells, the immortalized mouse brain endothelial cell line, were maintained in 10-cm tissue culture dishes in Dulbecco's Modified Eagle's Medium supplemented with 10% fetal bovine serum (FBS), penicillin (100 kU/L) and streptomycin (100 mg/L).

Fluorescent microscopy of PS, Lf-PS, and Tf-PS uptake by bEnd.3 cells

bEnd.3 cells were seeded at a density of 10^4 cells/cm^2 on a polylysine-coated glass cover slip. On the second day, after preincubation with HBSS for 15 min, the cells were incubated with coumarin-6-loaded PS, Lf-PS, and Tf-PS suspensions (300 mg/L in HBSS, pH 7.4) for 0.5, 1, and 2 h at 37 °C, respectively[29, 30]. At the end of the experiment, the cells were washed three times with PBS and fixed by 4% paraformaldehyde for 20 min. Then, they were washed three times with PBS, mounted in Dako fluorescent mounting medium and observed under a fluorescent microscope (Olympus, Japan).

Quantitative analysis of coumarin-6-labeled PS, Lf-PS, and Tf-PS uptake

bEnd.3 cells were seeded at a density of 10^4 cells/cm^2 onto 24-well plates. On the second day, after preincubation with HBSS for 15 min, the medium was replaced with the suspension of PS, Lf-PS, or Tf-PS (10–600 mg/L) and incubated for 1 h at 4 °C and 1 h at 37 °C. In a separate experiment, to study the effects of incubation time on particle uptake, the medium was replaced with 1 ml 100 mg/L suspension of PS, Lf-PS, or Tf-PS in HBSS per well and the plate was incubated for 15 min, 30 min, 1 h, and 2 h at 37 °C. At the end of the incubation period, the cells were washed with ice-cold PBS five times. Subsequently, the cells were solubilized in 400 µL 1% Triton X-100 and 20 µL cell lysate from each well was used to determine the total cell protein content using the BCA protein assay (Shanghai Shenergy Biocolor Bioscience and Technology Co, Ltd, China). A volume of 200 µL of the cell lysates were lyophilized and used for HPLC analysis of coumarin-6 after extraction by 700 µL methanol. The uptake of PS, Lf-PS, and Tf-PS by bEnd.3 cells was calculated from the standard curve and expressed as the amount of PS, Lf-PS and Tf-PS (mg) taken up per gram of cell protein.

Pharmacokinetics and tissue distribution of ^{125}I-Lf-PS and ^{125}I-Tf-PS

A total of 145 mice were randomly divided into two groups, receiving ^{125}I-Lf-PS or ^{125}I-Tf-PS. The animals were injected in the tail vein at a dose of 20 mg/kg ^{125}I-Lf-PS or ^{125}I-Tf-PS. At 0.083, 0.25, 0.5, 1, 2, 4, 6, 8, 12, 16, 24, and 48 h following *iv* injection, the blood samples were collected and the mice were sacrificed. The brain, heart, liver, spleen, lung, and kidney tissues were harvested, followed by a quick washing with cold saline and then subjected to weighing and detection by radioimmune γ detector (SN-695, Hesuo Rihuan, China).

Concentration data were dose-normalized and plotted as drug concentration-time curves in the blood and brain. The $C_{\max}$ and $t_{\max}$ values were read directly from the concentration-time profile and the area under the concentration-time curve (AUC) was calculated by the trapezoidal rule. The statistical differences between Lf-PS and Tf-PS were assessed using a paired Student's *t*-test and a *P* value of less than 0.05 was accepted as significant.

Results

Preparation and characterization of PS, Lf-PS, and Tf-PS

The mean particle size of PSs was around 150 nm and the average zeta potential was around -20 mV, which is regarded as favorable for brain transport. After Lf or Tf conjugation, the particle size and zeta potential changed slightly. The mean particle size of Lf-PS and Tf-PS changed from 166.4 nm and 141.0 nm to 167.6 nm and 146.1 nm, respectively, while the average zeta potential of Lf-PS and Tf-PS changed from -24.25 mV to -22.08 mV and -20.45 mV, respectively. TEM photographs showed PSs were generally spherical and of regular size (Figure 1).

The average number of Lf or Tf molecules conjugated with

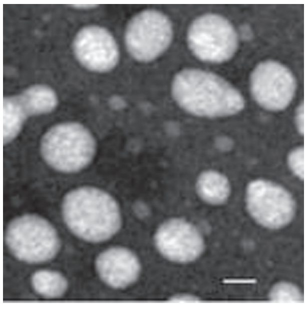

Figure 1. Transmission electron micrograph of PS negatively stained with uranyl acetate solution. The bar is 50 nm.

PSs was 45.5 and 50.4 per particle, respectively. Therefore, the material ratio was slightly changed in the experiment thereafter to make sure the average molecular number of Lf and Tf were as close to each other as possible.

The particle size and zeta potential of particles did not change much after conjugation with Lf or Tf, and the amount of protein conjugated with particles was extremely little compared with the amount of particles and it would not affect the permeability of the membrane of particles. Thus, the *in vitro* release experiments of coumarin-6 from the PSs can represent that from Lf-PS and Tf-PS. Coumarin-6 has high fluorescence efficiency, liposolubility and detection sensibility, and coumarin-6 has a detection limit as low as 4 ng/L by HPLC. Many researchers have used it as a fluorescence probe of nano drug delivery systems in quality and quantity analysis[5, 27]. Although the release speed at pH 4.0 was quicker than that at pH 7.4, the cumulative released percentage of both was smaller than 0.12% (Figure 2), which is similar to other studies[5, 23, 27]. This suggested that most of the incorporated coumarin-6 remained in the particles and indicated that the fluorescence signal detected in the cell or tissue samples was attributed mainly to the coumarin-6 encapsulated into the particles.

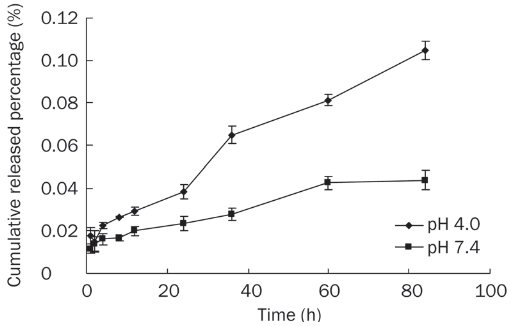

Figure 2. *In vitro* release of 6-coumarin from PS in 0.01 mol/L PBS (pH 7.4 and 4.0).

Uptake of coumarin-6-loaded PS, Lf-PS, and Tf-PS by bEnd.3 cells

The uptake of PS, Lf-PS, and Tf-PS by bEnd.3 cells was dependent on the incubation time within 2 h (Figure 3B). At each timepoint, the uptake amount of Lf-PS and Tf-PS was higher than that of PS, about 1.56 and 1.86 times higher than that of PS at 2 h, respectively; and the uptake amount of Tf-PS was 1.19 times as much as that of Lf-PS. The uptake amount of all PS, Lf-PS and Tf-PS under 37 °C was much higher than that under 4 °C, suggesting that the uptake of all particles was temperature-dependent (Figure 3A). The uptake of PS, Lf-PS, and Tf-PS was also concentration-dependent. At 37 °C, the uptake increased with an increase in the concentration, showing almost first-order kinetics (Figure 3A). The uptake of Lf-PS and Tf-PS was 2.19- and 3.33-fold greater than that of PS at 600 mg/L, respectively; and the uptake of Tf-PS was 1.52 times greater than that of Lf-PS at 600 mg/L. Under 4 °C, the uptake of PS, Lf-PS, and Tf-PS quickly reached saturation at a concentration of 100 mg/L, showing no significant difference between the three kinds of PSs.

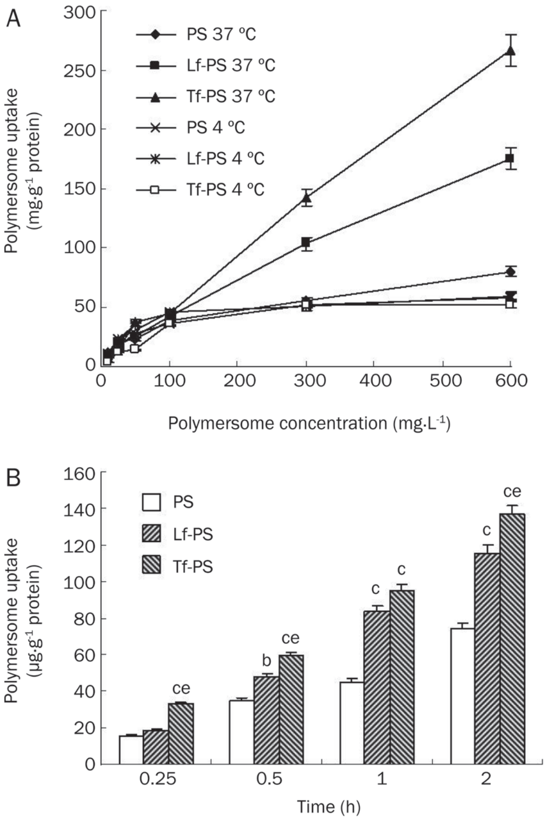

Figure 3. BCECs uptake (A) 10–600 mg/L PS, Lf-PS, and Tf-PS at 37 °C and 4 °C incubation for 1 h, respectively; (B) 100 mg/L PS, Lf-PS, and Tf-PS at 37 °C incubation for different time. *n*=3. Mean±SD. ${}^bP<0.05$, ${}^cP<0.01$ *vs* PS. ${}^eP<0.05$ *vs* Lf-PS.

Fluorescent microscopy photographs of bEnd.3 cells exposed to PS, Lf-PS, and Tf-PS at the same concentration (300 mg/L) demonstrated that the increase of fluorescent intensity in the cells correlated with an increase in the time of incubation (Figure 4). There was an obvious accumulation of dye of Lf-PS and Tf-PS in the cells compared with that of PS for 30, 60, and 120 min at 37 °C. Our *in vitro* release results confirmed the relative inertia of the coumarin-6 in the particles. Thus, we concluded coumarin-6 detected in the cells reflected the particles.

Tissue distribution of ^{125}I-Lf-PS and ^{125}I-Tf-PS

To evaluate the brain uptake and tissue distribution of the Lf-PS and Tf-PS, ^{125}I was labeled on Lf and Tf, and the blood and other tissues' concentrations of the particles were detected with a radioactive method. Both Lf-PS and Tf-PS exhibited similar concentration-time profiles (Figure 5A). However, the blood AUC_{0-t} of Tf-PS was much higher than that of Lf-PS, about 1.84-fold greater (Table 1). The elimination rate constant (β) of Lf-PS was 3.12-fold greater than that of Tf-PS, and the distribution rate constant (α) of Lf-PS was 2.11-fold greater

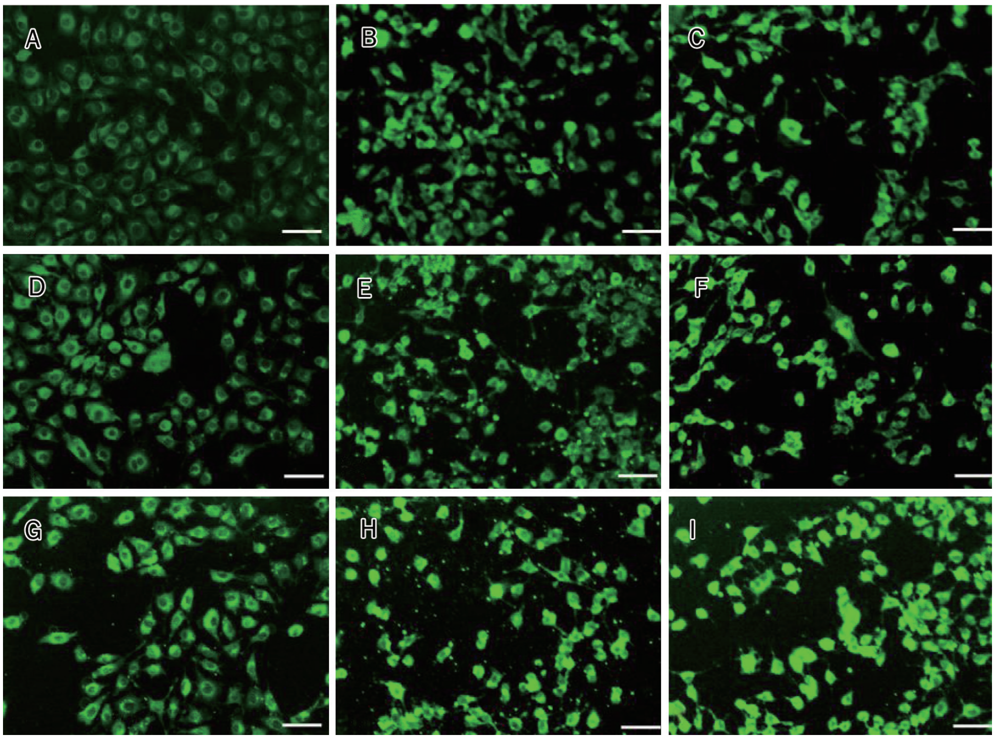

Figure 4. Cell uptake of polymersomes by bEND.3 cells. 300 mg/L PS at 37 °C for 30 min (A), 60 min (D), 120 min (G) ; 300 mg/L Lf-PS for 30 min (B), 60 min (E), 120 min (H) and 300 mg/L of Tf-PS for 30 min (C), 60 min (F), 120 min (I), respectively, bar 50 μm.

Table 1. Pharmacokinetic parameters of Lf-PS and Tf-PS in whole blood and brain following iv injection of ^{125}I-Lf-PS or ^{125}I-Tf-PS in mice.

PK parameters	Blood Lf-PS	 Tf-PS	Brain Lf-PS	 Tf-PS
α^a (h^{-1})	0.107	0.0508	–	–
$t_{1/2\alpha}{}^a$ (h)	6.49	13.6	–	–
β^b (h^{-1})	2.43	0.780	0.0216	0.0223
$t_{1/2\beta}{}^b$ (h)	0.285	0.888	32.1	31.1
t_{max} (h)	0	0	0.25	0.5
C_{max} (mg/L or ng/g)	55.68±5.32	49.86±5.80	43.44±6.88	80.04±7.02^c
AUC$_{0-t}$ (mg/L·h or ng/g·h)	219.5±25.6	403.8±49.17^c	458.6±89.5	1277±143^c

a: α and $t_{1/2\alpha}$ denotes distribution rate constant and distribution half life respectively; b: β and $t_{1/2\beta}$ denotes elimination rate constant and elimination half life respectively; C_{max} and AUC$_{0-t}$ are Mean±SD; ^{c}*P*<0.01 *vs* Lf-PS.

than that of Tf-PS (Table 1).

The brain uptake of Tf-PS was higher than that of Lf-PS at every timepoint (Figure 5B). The AUC$_{0-t}$ of brain concentration of Tf-PS was about 2.79-fold greater than that of Lf-PS (Table 1). However, in other tissues, this was not the case. The AUC$_{0-t}$ in heart, kidney, and lung of Tf-PS were significantly higher than that of Lf-PS (Figure 5C); the AUC$_{0-t}$ in spleen tissue had no significant difference with that in brain tissue; but the liver AUC$_{0-t}$ of Lf-PS was 1.34 times greater than that of Tf-PS, indicating that the Lf-PS was more easily phagocytized by macrophages than Tf-PS, which could make the blood AUC$_{0-t}$ lower.

To determine the difference between Lf-PS and Tf-PS in brain targeting, the drug targeting index (DTI) was calculated:

$$\text{DTI}=(\text{AUC}_{\text{brain}}/\text{AUC}_{\text{blood}})_{\text{Tf-PS}}/(\text{AUC}_{\text{brain}}/\text{AUC}_{\text{blood}})_{\text{Lf-PS}}$$

The closer a compound's DTI is to 1, the less targeting effect it has[31]. The brain DTI of Tf-PS with regard to Lf-PS was 1.51, which indicated that Tf-PS was more effective than Lf-PS in brain targeting.

Discussion and conclusion

bEnd.3 cells are an immortalized mouse brain endothelial cell line exhibiting endothelial properties. The cells express von Willebrand factor, vascular endothelial growth factor receptors and can internalize acetylated low-density lipoprotein[32]. They are an attractive candidate as a model of the BBB due to their rapid growth, maintenance of blood-brain barrier characteristics over repeated passages, formation of functional barriers and amenability to numerous molecular interventions[5, 33]. Thus, bEnd.3 cells were chosen as an easy BBB model to study the brain delivery properties of Lf-PS and Tf-PS *in vitro*.

The time-, temperature-, and concentration-dependent uptake of the particles suggested a process of active endocytosis. The enhanced uptake of Lf-PS and Tf-PS compared to PS by bEnd.3 cells might be caused by an additional endocytosis mechanism involving Lf and Tf, and this has been demonstrated by several researchers[5, 15]. The results also showed that Tf was more effective than Lf in facilitating cell uptake of PSs, which might have several reasons including the following: (1) The dissociation constant of Tf and TfR was approximately 1 nmol/L but the dissociation constant of Lf with LfR was 7 nmol/L and 5 μmol/L (LfR has two Lf bind-

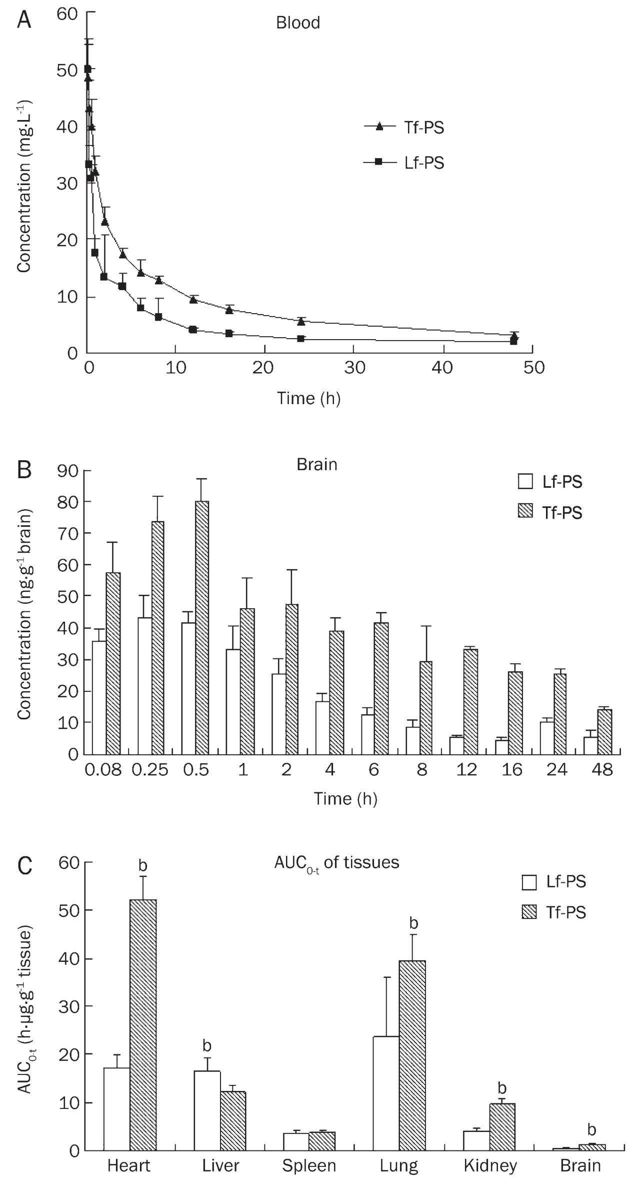

Figure 5. (A) The average PS's concentration-time curve in whole blood followed by iv injection of Lf-PS or Tf-PS in mice. *n*=6. Mean±SD. (B) The Lf-PS and Tf-PS concentration in brain at different time; (C) The Lf-PS and Tf-PS AUC_{0-t} in different tissues. $^bP<0.05$, $^cP<0.01$ *vs* Lf-PS.

ing sites)[15, 34], which means the affinity of Tf with TfR is much higher than that of Lf with LfR bEnd.3; (2) bEnd.3 cells may exhibit a greater amount of TfR than LfR; and (3) the conjugated PSs down-regulated the affinity of Lf with LfR more than that of Tf with TfR. The last two hypotheses should be identified by further experiments.

TfR and LfR have been demonstrated to exist on the BBB in different species and to be involved in Tf and Lf transport across the BBB *in vitro* and *in vivo*[11, 12, 14, 15]. In the standard protocol, perfusion is performed before tissues are harvested, and in most of our past experiments, perfusion was performed. In this study, considering the aim was to compare the relative effect of Tf and Lf, and the blood effect may be neutralized, the perfusion was omitted. Several studies published recently have also omitted perfusion[35]. Our results showed that the difference of particles' AUC_{0-t} of brain was partly affected by the blood elimination, which meant that Lf-PS was more easily identified and eliminated by cells of the mononuclear phagocytic system (MPS). The concentration of circulating Tf is about 25 μmol/L[34], whereas the plasma concentration of endogenous Lf is approximately 16 nmol/L[20]: 1000-fold lower than Tf. The added Lf and Tf (conjugated with PSs) in the blood were about 14 nmol/L at the peak. Therefore, the added Lf greatly changed the circulating amount of Lf, whereas that of Tf only changed a little, which may have caused the MPS to more easily eliminate the Lf-PS, but the definite mechanism was unclear. Tf-PS was still better than Lf-PS in brain targeting, which was coincident with the results of bEnd.3 cells uptake *in vitro*. However, the ligands' conjugation with PSs increased not only the brain uptake but also the liver and spleen uptake of drug delivery systems, which might cause increased toxicities to these organs, a general obstacle that the nanoparticle systems have faced. Considering the BBB prevents almost 100% of large molecule drugs and about 98% of small molecule drugs from entering the brain, researchers mainly focused on increasing the brain drug concentration while ignoring other tissues' drug concentrations. Nowadays, researchers have gradually realized that increasing the site-specific distribution to the brain and decreasing the distribution to other tissues have become the key point in the treatment of brain diseases. Unfortunately, researchers have only been able to increase the distribution of nanoparticle systems to the brain while hardly decreasing the distribution to other tissues, which is the main obstacle researchers are unceasingly devoted to overcoming in brain drug delivery systems.

The brain targeting property of drug delivery systems is largely affected by the targeting ligands, so it is very important to choose the right targeting ligand in research design. Recently, most of the brain targeting moieties are either the related ligands of known receptors, or carriers on the BBB or the cationic proteins, which can bind with the anionic BBB, such as transferrin receptor monoclonal antibody OX26, insulin, and cationic albumin[23, 27, 36]. However, these targeting ligands generally present problems such as low specificity and not ideal brain targeting properties. Several researchers have tried to select peptides or nucleic acids as targeting moieties, which may contain much better characteristics, through several methods including phage display[37] and systematic evolution of ligands by exponential enrichment[38]. These have shown their efficacy in a development perspective, which may largely increase the brain targeting effect of drug delivery systems.

Acknowledgments

We are very grateful to Prof Yao-cheng RUI, Department of Pharmacology, School of Pharmacy, The Second Military Medical University, China, for providing the bEnd.3 cell line. We also acknowledge Dr Jian-hua ZHU, School of Pharmacy, Fudan University, China, for his help on radioactive element

labeling and detecting.

This work was supported by National Basic Research Program of China (973 Program) 2007CB935800, National Natural Science Foundation of China (30762544), National Key Program of Pharmaceutical Creation and Development (2009ZX09310-006), and the ChunTsung Foundation for undergraduate of China.

Author contribution

Xin-guo JIANG designed the research; Hui-le GAO, Li FAN, and Bing-xian WU performed the research; Zhi-qing PANG and Kai-li HU contributed new reagents and analytic tools; Hui-le GAO analyzed the data; and Hui-le GAO, Zhi-qing PANG, and Kai-li HU wrote the paper.

References

1 Pardridge WM. Blood-brain barrier delivery. Drug Discov Today 2007; 12: 54–61.
2 Pardridge WM. Drug targeting to the brain. Pharm Res 2007; 24: 1733−44.
3 Begley DJ. Delivery of therapeutic agents to the central nervous system: the problems and the possibilities. Pharmacol Ther 2004; 104: 29–45.
4 Liu X, Chen C. Strategies to optimize brain penetration in drug discovery. Curr Opin Drug Disc 2005; 8: 505–12.
5 Hu KL, Li JW, Shen YH, Lu W, Gao XL, Zhang QZ, *et al*. Lactoferrin-conjugated PEG-PLA nanoparticles with improved brain delivery: *In vitro* and *in vivo* evaluations. J Control Release 2009; 134: 55–61.
6 Garcia-Garcia E, Andrieux K, Gilb S, Couvreur P. Colloidal carriers and blood brain barrier (BBB) translocation: away to deliver drugs to the brain? Int J Pharm 2005; 298: 274–92.
7 Boer AG, Gaillard PJ. Strategies to improve drug delivery across the blood brain barrier. Clin Pharmacokinet 2007; 46: 553–76.
8 Calvo P, Gouritin B, Chacun H, Desmaële D, D'Angelo J, Noel JP. Long circulating PEGylated polycyanoacrylate nanoparticles as new drug carrier for brain delivery. Pharm Res 2001; 18: 1157–66.
9 Nuijens JH, Berkel PHC, Schanbacher FL. Structure and biological actions of lactoferrin. J Mammary Gland Biol 1996; 3: 285–95.
10 Qian ZM, Li HY, Sun HZ, Ho K. Targeted drug delivery via the transferrin receptor-mediated endocytosis pathway. Pharmacol Rev 2002; 54: 561–87.
11 Buchanan J. A structural comparison of human serum transferrin and human lactoferrin. Biometals 2007; 20: 249−62.
12 Fillebeen C, Descamps L, Dehouck MP, Fenart L. Receptor-mediated transcytosis of lactoferrin through the blood-brain barrier. J Biol Chem 1999; 274: 7011−7.
13 Moos T, Morgan EH. Transferrin and transferrin receptor function in brain barrier systems. Cell Mol Neurobiol 2000; 20: 77−95.
14 Suzuki YA, Lopez V, Lönnerdal B. Mammalian lactoferrin receptors: structure and function. Cell Mol Life Sci 2005; 62: 2560−75.
15 Huang RQ, Ke WL, Qu YH, Zhu JH, Pei YY, Jiang C. Characterization of lactoferrin receptor in brain endothelial capillary cells and mouse brain. J Biomed Sci 2007; 14: 121–8.
16 Kawamata T, Tooyama I, Yamada T, Walker DG, McGeer PL. Lactotransferrin immunocytochemistry in Alzheimer and normal human brain. Am J Pathol 1993; 142: 1574–85.
17 Faucheux BA, Nillesse N, Damier P, Spik G, Mouatt-Prigent A, Pierce A, *et al*. Expression of lactoferrin receptors is increased in the mesencephalon of patients with Parkinson disease. Proc Natl Acad Sci USA 1995; 92: 9603−7.
18 Grau AJ, Willig V, Fogel W, Werle E. Assessment of plasma lactoferrin in Parkinson's disease. Mov Disord 2001; 16: 131−4.
19 Inoue T, Cavanaugh PG, Steck PA, Brunner N, Nicolson GL. Differences in transferrin response and numbers of transferrin receptors in rat and human mammary carcinoma lines of different metastatic potentials. J Cell Physiol 1993; 156: 212–7.
20 Ji B, Maeda J, Higuchi M. Pharmacokinetics and brain uptake of lactoferrin in rats. Life Sci 2006; 78: 851–5.
21 Discher BM, Won YY, Ege DS, Lee J, Bates FS, Discher DE, *et al*. Polymersomes: tough vesicles made from diblock copolymers. Science 1999; 284: 1143–6.
22 Discher DE, Eisenberg A. Polymer vesicles. Science 2002; 297: 967–73.
23 Pang ZQ, Lu W, Gao HL, Hu KL, Chen J, Zhang CL, *et al*. Preparation and brain delivery property of biodegradable polymersomes conjugated with OX26. J Control Release 2008; 128: 120–7.
24 Photos PJ, Bacakova L, Discher B, Bates FS, Discher DE. Polymer vesicles *in vivo*: correlations with PEG molecular weight. J Control Release 2003; 90: 323–34.
25 Huwyler J, Wu DF, Pardridge WM. Brain drug delivery of small molecules using immunoliposomes. Proc Natl Acad Sci USA 1996; 93: 14164–9.
26 Ellman GL. Tissue sulfhydryl groups. Arch Biochem Biophys 1959; 82: 70–7.
27 Lu W, Zhang Y, Tan YZ, Hu KL, Jiang XG, Fu SK. Cationic albumin-conjugated pegylated nanoparticles as novel drug carrier for brain delivery. J Control Release 2005; 107: 428–48.
28 Bermudez H, Brannan AK, Hammer DA, Bates FS, Discher DE. Molecular weight dependence of polymersome membrane structure, elasticity, and stability. Macromol 2002; 35: 8203–8.
29 Davda J, Labhasetwar V. Characterization of nanoparticle uptake by endothelial cells. Int J Pharm 2002; 233: 51–9.
30 Panyam J, Sahoo SK, Prabha S, Bargar T, Labhasetwar V. Fluorescence and electron microscopy probes for cellular and tissue uptake of poly(*D*,*L*-lactide-coglycolide) nanoparticles. Int J Pharm 2003; 262: 1–11.
31 Hunt CA, MacGregor RD, Siegel RA. Engineering targeted *in vivo* drug delivery: I. The physiological and physicochemical principles governing opportunities and limitations. Pharmaceut Res 1986; 3: 333–44.
32 Pepper MS, Tacchini-Cottier F, Sabapathy TK, Montesano R, Wagner EF. A model for haemangiomas and other vascular tumours. In: R Bicknell CE Lewis, N Ferrara (Eds), Tumour Angiogenesis, Endothelial Cells Transformed by Polyomavirus Middle T Oncogene. Oxford, UK, Oxford University Press, 1997; p 309–31.
33 Brown RC, Morris AP, O'Neil RG. Tight junction protein expression and barrier properties of immortalized mouse brain microvessel endothelial cells. Brain Res 2007; 30: 17–30.
34 Sawyer ST, Krantz SB. Transferrin receptor number, synthesis, and endocytosis during erythropoietin-induced maturation of Friend virus-infected erythroid cells. J Biol Chem 1986; 261: 9187–95.
35 Milane A, Tortolano L, Fernandez L, Bensimon G, Meininger V, Farinotti R. Brain and plasma riluzole pharmacokinetics: effect of minocycline combination. J Pharm Pharmaceut Sci 2009; 12: 209–17.
36 Jones AR, Shusta EV. Blood-brain barrier transport of therapeutics via receptor-mediation. Pharmaceut Res 2007; 24: 1759–71.
37 Schluesener HJ, Xianglin T. Selection of recombinant phages binding to pathological endothelial and tumor cells of rat glioblastoma by *in vivo* display. J Neurol Sci 2004; 224: 77–82.
38 Yang Y, Yang D, Schluesener HJ, Zhang Z. Advances in SELEX and application of aptamers in the central nervous system. Biomol Eng 2007; 24: 583–92.

Acta Pharmacologica Sinica (2010) 31: 244–258
© 2010 CPS and SIMM All rights reserved 1671-4083/10 $32.00
www.nature.com/aps

Original Article

Structural studies of B-type Aurora kinase inhibitors using computational methods

MM NEAZ[2,3], M MUDDASSAR[2,3], FA PASHA[2,#], Seung Joo CHO[1,*]

[1]Department of Cellular Molecular Medicine and Research Center for Resistant Cells, College of Medicine, Chosun University, Gwangju 501-759, South Korea; [2]Computational Science Center, Future Fusion Technology Division, Korea Institute of Science and Technology, PO Box 131, Seoul 130-650, South Korea; [3]Korea University of Science and Technology, 52, Eoeun-dong, Yuseong-gu, Daejon 305–333, South Korea

Aim: To characterize the structural features of quinazoline-based Aurora B inhibitors that influence its inhibitor activity.
Methods: Two geometrical methods, Method 1 and Method 2, were used to develop the 3D-QSAR models. The most active ligand was used as the template for the alignment of all the ligands in Method 1, and a conformer of the cocrystal ligand was used as the template for the alignment of all the ligands in Method 2.
Results: The models suggest that highly active ligands can be designed by varying the R1 substituent at position 7 of the quinazoline ring with positively charged, bulky, hydrophobic groups, while bulky and hydrophobic groups around the thiazole ring are desirable for higher activity.
Conclusion: This study emphasizes that the bioactive conformer is rather different from the minima. The steric, electrostatic, and hydrophobic field effects contribute to its inhibitory activity.

Keywords: 3D-QSAR; drug design; CoMFA; CoMSIA; Aurora B; kinase

Acta Pharmacologica Sinica (2010) 31: 244–258; doi: 10.1038/aps.2009.188

Introduction

The Aurora proteins are a small family of serine/threonine kinases that are expressed during mitosis and are involved in chromosome segregation and cytokinesis. Humans express three Aurora kinase paralogs, Aurora A, B, and C, the biologies of which have been reviewed extensively[1–3]. All Aurora kinases contain a variable N-terminal domain, followed by a conserved catalytic domain and a short C-terminal extension. Despite significant sequence homology, the localization and functions of these kinases are largely distinct from one another. Aurora A localizes on centrosomes from the early S phase and is involved in centrosome maturation and separation, bi-polar spindle assembly, and mitotic entry and exit. Aurora B kinase belongs to the chromosome passenger protein family. The expression and activity of Aurora B are cell cycle regulated, and Aurora B is only expressed during mitosis. Aurora B first associates with centromeres, then relocalizes to the midzone of the central spindle, and finally concentrates at the midbody between the dividing cells[4–6]. At least three more proteins, INCEP (inner centrosome protein), survivin and borealin, participate in a multiprotein complex with Aurora B[4–6]. The inhibition of Aurora B by RNA interference demonstrated that it is required for cytokinesis[7], where its important function is the regulation of the kinesin-like protein pavarotti, which is essential for the establishment of the central spindle during anaphase. Aurora A and B are overexpressed in a variety of solid tumors, including those from the colon[8], breast[9–11], prostate[12], pancreas[13], thyroid[14], head, and neck[15]. In addition, it has been found recently that Aurora A and B are aberrantly expressed in hematological malignancies including acute myelogenous leukemia (AML), chronic myelogenous leukemia (CML), and acute lymphoblastic leukemia (ALL)[16]. The contribution of Aurora B to carcinogenesis has been studied less than that of Aurora A. Aurora B is located in a chromosomal region that is not typically amplified in human malignancies. However, the overexpression of Aurora kinase B has been shown in a variety of human cancers, including glioblastoma multiforme[17], malignant mesothelioma[18], and hematological malignancies[16]. High levels of Aurora B are associated with adverse clinical

---

[#] Now in the Applied Chemistry and Physical Chemistry Division, Institut Français du Pétrole (IFP), 1 et 4 rue Bois Préau -92582 ruiel Malmaison, France.

[*] To whom correspondence should be addressed.

E-mail chosj@chosun.ac.kr

Received 2009-10-19 Accepted 2009-12-04

outcomes in patients with endometrial carcinoma[19]. The forced expression of Aurora B in Chinese hamster embryo cells results in chromosomal instability and increased tumor invasiveness in association with the constitutive expression of phosphorylated (p)-histone H3 on Ser10[20], suggesting that Aurora B can act as an oncogene. The development of Aurora kinase inhibitors evidence linking Aurora kinases to malignancies has raised the possibility of targeting these kinases for cancer therapy.

Many Aurora inhibitors in various stages of development have been reported[21]. Among them, MK-0457/VX-680, MLN8054, ZM447439, PHA-739358, AZD1152, and AT9283 are in clinical development. These compounds are of different scaffolds with various specificities to the subtypes of Aurora kinases. VX-680 is a potent inhibitor of all three Aurora kinases with K_i values of 0.6, 1.8, and 4.6 nmol/L for the A, B, and C isoforms, respectively[22], and is undergoing clinical trials for solid tumors and hematological malignancies. PHA-739358, a pyrazole derivative, is a non-selective agent with IC_{50} values of 13, 79 and 61 nmol/L for Aurora A, B, and C, respectively[23]. AZD1152 and ZM447439 are both quinazoline derivatives in clinical stages. AZD1152 selectively inhibits Aurora B rather than A or C and resulted from the optimization of a series of 5-acetanilide-3-aminopyrazole (3-pyrazole)-substituted quinazolines[24]. Recently, a new class of 1-acetanilide-4-aminopyrazole-substituted quinazoline has been reported as selective Aurora B inhibitors[25]. These findings suggest the possibility of designing more potent quinazoline-based Aurora B inhibitors. The three-dimensional (3D) quantitative structure-activity relationship (3D-QSAR) techniques, such as the comparative molecular field analysis (CoMFA) and comparative molecular similarity analysis (CoMSIA)[26–28], are routinely used in modern drug design to understand the drug–receptor interaction. It has been shown in the literature that these computational techniques can strongly support and aid in the design of novel, more potent inhibitors by revealing the mechanics of the drug–receptor interactions[29–31]. To explore the further possibilities of novel drugs, we have developed predictive 3D-QSAR models using quinazoline-based Aurora B inhibitors[24, 32].

Materials and methods

The basic structure of the quinazolines is shown in Figure 1. A series of 48 quinazoline derivatives with their inhibitory activities was retrieved from the literature[24, 32]. We have considered only the IC_{50} value for the cell-based assay (not an enzyme-based assay), which is the inhibition of histone H3 in SW620 cells. Histone H3 is a cellular substrate of Aurora B and a marker of Aurora B kinase inhibition *in vivo*. The IC_{50} values in the micro-molar (μmol/L) range were converted into the molar (M) range and then into pIC_{50} values using the relationship $pIC_{50}=-\log IC_{50}$ values. The pIC_{50} values were used as the dependent variables in the statistical modeling. The dataset of Aurora B kinase inhibitors was divided into training (37 compounds) and test (11 compounds) sets considering the fact that the test set molecules must present a range of biological activity and the typical chemical structures similar to those of the training set as reported in Table 1. The test set compounds are marked by asterisks in Table 1. Molecular modeling and all calculations were performed using SYBYL 7.3[33] running on Linux cluster. The molecules were aligned using two different geometric methods.

Molecular Alignment

In the 3D-QSAR model development, molecular alignment is a key step, and usually the molecules are aligned with a suitable conformational template that is supposed to be bioactive so that the inhibitors have comparable conformations and similar orientations in space[26]. In this study, two different geometrical methods, Method 1 and Method 2, were used.

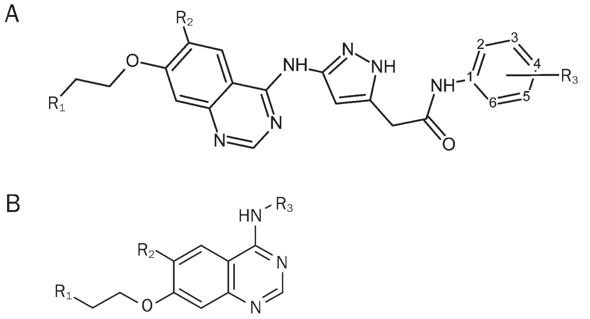

Figure 1. Basic structures of quinazolines.

Method 1

The most active molecule (compound 40) was drawn and optimized using Tripos Force Field (TFF)[34] with a convergence criterion of 0.005 kcal/mol/Å and 10 000 iterations. The random search-based minimum energy conformer of the most active compound (compound 40) was obtained and used as the template. This template was modified for further ligands, and all of the molecules were optimized using the TFF level with a convergence criterion of 0.005 kcal/mol and 10 000 iterations. These minimized structures were aligned over the template using the common substructure method (Figure 2) and subsequently used for the CoMFA/CoMSIA.

Method 2

A recently reported crystal structure for a similar ligand (PDB=2c6e) was obtained from the public domain. The ligand position within the active site is displayed in Figure 3. The docked ligand was extracted and used as template to align all of the ligands. The ligands were all minimized within the receptor site using TFF, but the whole protein active site was fixed during the minimization. All of the minimized structures were aligned over the template using a common substructure method and directly used for CoMFA and CoMSIA. The aligned structures of Method 2 are displayed in Figure 4.

3D-QSAR

The 3D-QSAR models were developed using the Comparative

Table 1. The quinazolines derivatives (structures A and B) and their observed (cell line IC$_{50}$) activities from Ref[24, 32].

No	Structure	R1	R2	R3	IC$_{50}$ (μmol/L)	pIC$_{50}$ (mol/L)	Reference
1*(6)	A	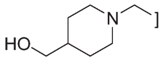	OMe	H	1.2	5.92	[24]
2(7)	A	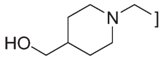	OMe	2-F	0.47	6.33	[24]
3(8)	A	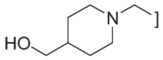	OMe	3-F	0.68	6.17	[24]
4*(9)	A	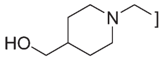	OMe	4-F	2.6	5.59	[24]
5(10)	A	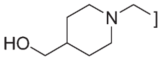	OMe	2,3-di-F	0.54	6.27	[24]
6*(11)	A	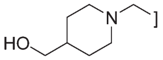	OMe	3,5-di-F	0.37	6.43	[24]
7*(12)	A	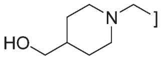	OMe	3-Cl	1.2	5.92	[24]
8(16)	A	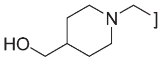	OMe	3-OMe	5.5	5.26	[24]
9*(17)	A	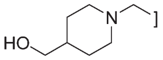	OMe	3-CF3	1.8	5.74	[24]
10(18)	A	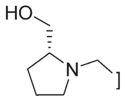	OMe	2,3-di-F	0.042	7.38	[24]
11(19)	A	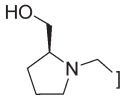	OMe	2,3-di-F	0.045	7.35	[24]
12(20)	A	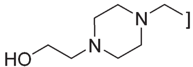	OMe	2,3-di-F	0.071	7.15	[24]
13*(21)	A	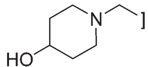	OMe	2,3-di-F	0.078	7.11	[24]
14(22)	A	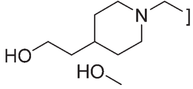	OMe	2,3-di-F	0.13	6.89	[24]
15(23)	A	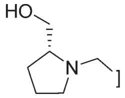	OMe	3-F	0.33	6.48	[24]
16(24)	A	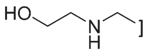	OMe	3-F	0.63	6.20	[24]
17(25)	A	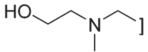	OMe	3-F	0.12	6.92	[24]
18(26)	A	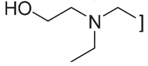	OMe	3-F	0.27	6.57	[24]
19(27)	A	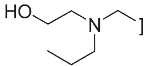	H	3-F	0.29	6.54	[24]
20(28)	A	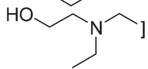	H	2,3-di-F	0.045	7.35	[24]
21*(29)	A	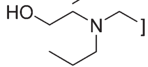	H	2,3-di-F	0.018	7.74	[24]
22(31))	A	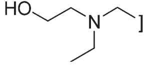	H	2,3-di-F	0.007	8.15	[24]
23(32)	A	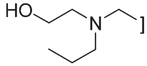	H	2,3-di-F	0.002	8.7	[24]
24(33)	A	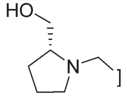	H	2,3-di-F	0.005	8.30	[24]
25(34)	A	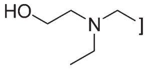	H	3-F	0.017	7.77	[24]

(Continued)

No	Structure	R1	R2	R3	IC_{50} (μmol/L)	pIC_{50} (mol/L)	Reference
26(35)	A	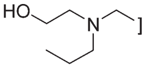	H	3-F	0.007	8.15	[24]
27*(36)	A	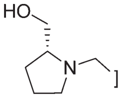	H	3-F	0.024	7.62	[24]
28(15)	B	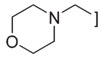	OMe	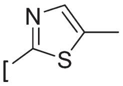	1.1	5.96	[32]
29(16)	B	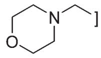	OMe	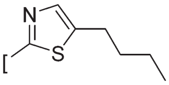	1.9	5.72	[32]
30(26)	B	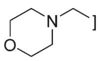	OMe	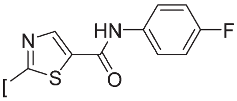	0.6	6.22	[32]
31(28)	B	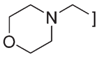	OMe	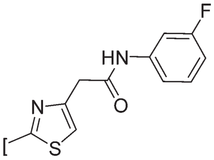	0.2	6.70	[32]
32(24)	B	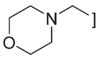	OMe	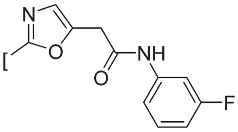	1	6.00	[32]
33(31)	B	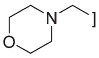	OMe	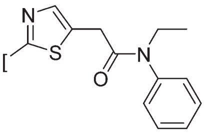	2.3	5.64	[32]
34*(32)	B	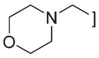	OMe	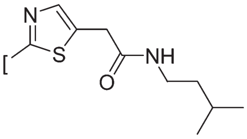	0.4	6.40	[32]
35(61)	B	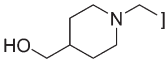	OMe	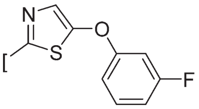	0.2	6.70	[32]
36(62)	B	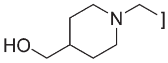	OMe	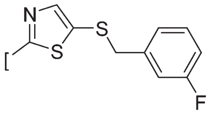	0.4	6.40	[32]
37*(66)	B	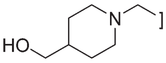	OMe	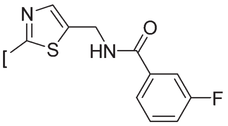	2.8	5.55	[32]
38(67)	B	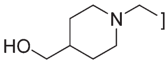	OMe	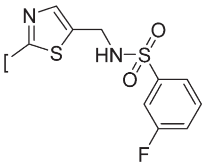	0.8	6.10	[32]
39(44)	B	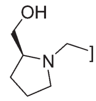	OMe	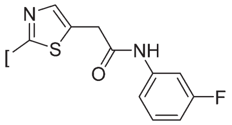	0.004	8.40	[32]

(Continued)

No	Structure	R1	R2	R3	IC_{50} (μmol/L)	pIC_{50} (mol/L)	Reference
40(45)	B	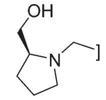	OMe	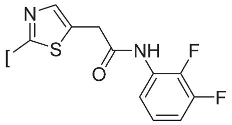	0.001	9.00	[32]
41(51)	B	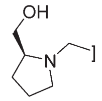	OMe	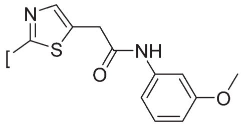	1	6.00	[32]
42(52)	B	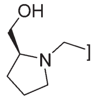	OMe	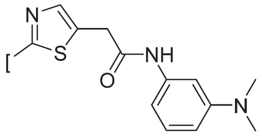	0.6	6.22	[32]
43(40)	B	OMe	OMe	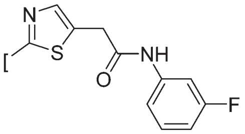	0.01	8.00	[32]
44(42)	B	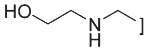	OMe	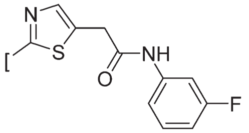	0.08	7.10	[32]
45(43)	B	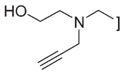	OMe	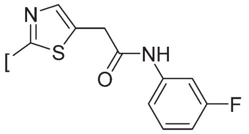	0.02	7.70	[32]
46(47)	B	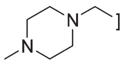	OMe	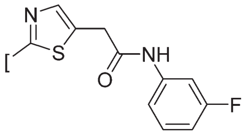	0.002	8.70	[32]
47*(46)	B	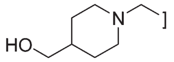	OMe	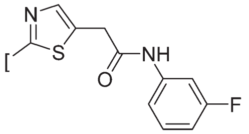	0.005	8.30	[32]
48(48)	B	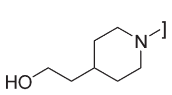	OMe	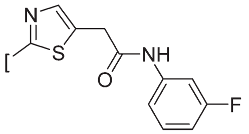	0.019	7.72	[32]

The structures A and B correspond to Figure 1 and the test set compounds were indicated by asterisk (*) the cell line IC_{50} values collected from literature. () serial number of compounds in literature.

Molecular Field Analysis (CoMFA) and Comparative Molecular Similarity Indices Analyses (CoMSIA) techniques.

CoMFA

The steric and electrostatic potential fields for the CoMFA were calculated at each lattice intersection of a regularly spaced grid of 2.0 Å. The lattice was defined automatically and extended up to four units past the Van der Waals volume of all molecules in the X, Y, and Z directions. The Van der Waals potential and columbic terms, which represent the steric and electrostatic fields, respectively, were calculated using TFF and a distance-dependent dielectric constant. An sp^3 carbon atom with a Van der Waals radius of 1.52 Å and a charge of +1.0 served as the probe atom to calculate the steric and electrostatic fields. The steric and electrostatic contributions were truncated at ±30 kcal/mol; the electrostatic contributions were ignored at the lattice intersections with the maximum steric interactions. The CoMFA steric and electrostatic fields generated and scaled by the CoMFA standard option are given in SYBYL[33].

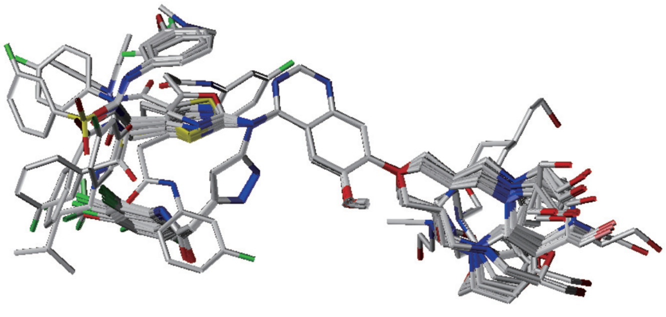

Figure 2. The molecular alignment by geometrical Method 1.

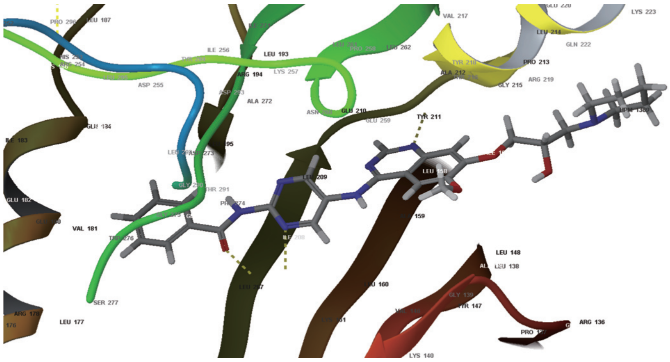
PRO 296
LEU 187
ILE 271
ILE 256
LEU 193
TYR 294
HIS 253
ARG 254
LEU 295
ASP 255
ARG 194
LYS 257
ASP 293
ALA 272
LEU 261
PRO 258
LEU 262
VAL 217
GLU 220
LYS 223
LEU 214
GLN 222
TYR 218
PRO 213
ALA 212
ARG 219
GLY 215
ASN 260
GLU 210
GLU 259
TYR 211
HPM 1389
GLU 184
ILE 183
LEU 292
ASP 273
LEU 209
LEU 158
GLY 290
THR 291
PHE 274
GLU 182
159
VAL 181
TRP 276
ILE 208
LEU 148
LEU 138
LEU 160
SER 277
GLY 139
TYR 147
ARG 178
176
LEU 177
ARG 136
PRO 137
LYS 140

Figure 3. The co-crystallized ligand which is used as template.

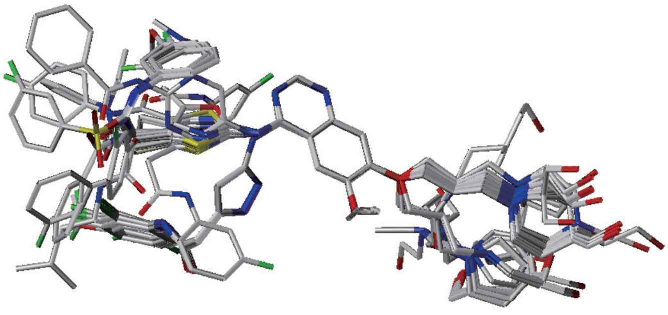

Figure 4. The molecular alignment by geometrical Method 2.

CoMSIA

The reported CoMSIA method is based on molecular similarity indices[27] with the same lattice box used for the CoMFA. Molecular similarity expressed in terms of five different properties (steric, electrostatic, hydrophobic, H-bond donors and H-bond acceptors) was calculated using a C^+ probe atom with a radius of 1.0 Å placed at a regular grid spacing of 2.0 Å. The CoMSIA similarity indices (A_F) for molecule j with atoms i at grid point q are calculated by

$$A^{q}_{F,K}(j)=-\sum\omega_{prob,k}\,\omega_{ik}\,e^{-ar^2}iq \qquad (1)$$

where k represents the following physicochemical properties: steric, electrostatic, hydrophobic, H-bond donor, and H-bond acceptor. A Gaussian type distance dependence was used between grid point q and each atom i of the molecule. The default value (0.3) was used as the attenuation factor (α). The steric indices are related to the third power of the atomic radii, the electrostatic descriptors are derived from the atomic partial charges, the hydrophobic fields are derived from atom-based parameters[35], and the H-bond donor and acceptor indices are obtained by a rule based method based on experimental results[36].

Partial Least Square (PLS) analysis and validation of the QSAR models

To derive the 3D-QSAR models, the CoMFA and CoMSIA descriptors were used as independent variables and the pIC_{50} values as the dependent variable. The PLS method[37, 38] was used to linearly correlate the CoMFA and CoMSIA descriptors to the activity. The CoMFA cutoff value was set to 30 kcal/mol for both the steric and the electrostatic fields, and all of the fields were scaled by the default options in SYBYL. The cross-validation analysis was performed using the leave one out (LOO) method[39, 40] in which one compound was removed from the dataset and its activity was predicted using the model derived from the rest of the dataset. The cross-validated correlation coefficient (q^2) that resulted in an optimum number of components and the lowest standard error of prediction was considered for further analysis and calculated using

$$q^2=1-\frac{\sum_{y}(y_{pred}-y_{observed})^2}{\sum_{y}(y_{observed}-y_{mean})^2} \qquad (2)$$

$$PRESS=\sum_{y}(y_{predicted}-y_{observed})^2 \qquad (3)$$

where, y_{pred}, y_{actual}, and y_{mean} are the predicted, actual and mean values of the target property (pIC_{50}), respectively, and *PRESS* is the sum of the predictive sum of squares. The non-cross-validated PLS analyses were performed with a column filter value of 2.0 to reduce the analysis time with a small effect on the q^2 values. To have robustness and statistical confidence of the derived models, a bootstrapping analysis was used for 100 runs. To assess the predictive power of the derived 3D-QSAR models, the activity of the test set of eleven molecules was predicted. The predictive ability of the models is expressed by the predictive r^2 value, which is analogous to the cross-validated r^2 (q^2) and is calculated using

$$r^2_{pred}=\frac{SD\text{-}PRESS}{SD} \qquad (4)$$

where *SD* is the sum of the squared deviations between the biological activities of the test set and the mean activities of the training molecules and *PRESS* is the sum of the squared deviation between the predicted and observed activity of the test set molecules and is calculated using equation 4.

Results

The 3D-QSAR analyses were performed by two different geometric methods using ligand-based and receptor-guided techniques.

A comparison of the two geometric methods

The structures of conformers A (green) and B (red) of the most active ligand (compound 40) are shown in Figure 5. Structure A was obtained from a minimum energy conformer of the most active compound, while structure B was drawn from a modification of the crystallized ligand (gray) and further minimized within the active site. It is clear (Figure 5) that the receptor guided conformer (red) is closer to residues 211–223, and the key interaction with residue 161 is more significant for compound 40. For this interaction, the distance between the carbonyl carbon and the hydrogen of Lys was reported as 1.78 Å for the co-crystallized ligand, while this distance for the most active ligand (compound 40) was 1.2 Å. The minimum energy conformer (green) has a distance of 3.5 Å. The molecular field analyses and this comparison of different conformers emphasize that the bioactive conformer is not the minimum energy conformer.

Comparative molecular fields analyses (CoMFA)

A Gasteiger Huckel charge was used for the aforementioned different geometrical methods. Six models (CoMFA$_1$ to CoMFA$_6$) were developed. CoMFA$_1$ to CoMFA$_3$ were based on minimum energy geometries with steric, electrostatic, and both fields combined, respectively. The statistical summary of these three models is presented in Table 2. Model 3 (CoMFA$_3$) was better than the other two models because it was based on both fields having high LOO values of q^2=0.54 and r^2=0.86. The electrostatic contribution was dominant in the interaction. The model was successfully validated for internal predictivity with r^2_{bs}=0.90 and the test-set predictivity of 11 compounds with $r^2_{\text{predictive}}$=0.74.

CoMFA$_4$ to CoMFA$_6$ were based on the co-crystal geometry with steric, electrostatic, and both fields combined, respectively. The result of both geometries was good; the co-crystal geometry-based model was statistically significant (Table 2). The best-fit model (CoMFA$_6$) was based on the X-ray geometry and both fields jointly have LOO values of q^2=0.56 and r^2=0.96. Even though this model involved both steric and electrostatic interactions, the electrostatic contribution was dominant in the interaction. The model was successfully validated for the internal predictivity with r^2_{bs}=0.97 and for the test set predictivity of 11 compounds with $r^2_{\text{predictive}}$=0.76. The q^2 value of model CoMFA$_3$ was better than that of model CoMFA$_6$, but the other values indicated the significance of model CoMFA$_6$. This model is more realistic because it is based on the co-crystallized binding mode in which all molecules have nearly the same conformation as in the co-crystal structure, and all have a key contact hydrogen bonding between residue 161 and the carbonyl carbon. All molecules acquired the same binding site and an almost equal interaction with the hinge region. The predicted activities by the CoMFA are summarized in Table 3. The trend of the observed and predicted activities using model CoMFA$_6$ is displayed in Figure 6.

CoMFA maps

The 3D-CoMFA contour maps using the best-fit model CoMFA$_6$ are displayed in Figures 7 and 8 with both kinds of field effects on compound 40. The green contours indicate the area in which steric bulk substations might beneficially affect the activity and the yellow region is favorable for small groups (Figure 7). The blue contour indicates the region where a positive group is required for high activity, while the red zone indicates the region favorable for negative groups (Figure 8). The green contour was evident around the pyrrolidine ring, which is directed toward residues 211 to 223, and around the thiazole ring, which is directed toward 207–209 and 161–162, indicating that a bulkier group around these regions will be favorable for higher activity. Particularly, the contact with residue 161 was described as a key interaction for activity. A small yellow contour was evident just near the methoxy group, indicating that a small group would be favorable for higher activity. Blue contours appear around the methoxy and pyrrolidine rings, as well as around the thiazole ring (Figure 8), which indicated that except for the methoxy region, a positive group with steric bulk would be desirable at this position, which is in support of previous findings[41]. A small positive group would be helpful around the methoxy substituent. There is a red contour in the far region of the thiazole ring indicating that a negative group would have a good effect on the activity, which is also clear from the data of the most active compound (compound 40), which has halogens at the same place that are probably key to its higher activity.

Table 2. The regression summary of different CoMFA models.

No	Model	Field	q^2	N	SEE	r^2	*F*	r^2_{bs}	r^2_{prd}	*SD*
Ligand based										
1	CoMFA$_1$	S	0.455	6	0.210	0.961	123.989	–	–	–
2	CoMFA$_2$	E	0.206	1	0.637	0.585	49.413	–	–	–
3	CoMFA$_3$	0.49S/0.51E	0.54	3	0.387	0.856	65.203	0.898	0.74	0.033
Receptor guided										
4	CoMFA$_4$	S	0.44	7	0.21	0.96	104	–	–	–
5	CoMFA$_5$	E	0.55	2	0.56	0.68	35.83	–	–	–
6	CoMFA$_6$	0.45S/0.55E	0.56	5	0.22	0.96	135.791	0.969	0.76	0.01

S=steric field, E=electrostatic field, N=No of components, q^2=cross-validated r^2, r^2=non cross-validated, *F*=Fischer's *F* value for test of significance, SEE=standard error of estimate, r^2_{bs}=coefficient of determination after 100 bootstrapping runs, SD=standard deviation.

Table 3. Observed [24, 32] and predicted activities by CoMFA6 and CoMSIA25 models.

No	pIC_{50}	PA_{COMFA6}	Resid	$PA_{CoMSIA25}$	Resid
2	6.33	6.36	-0.03	6.16	0.17
3	6.17	5.73	0.44	5.88	0.29
5	6.27	6.5	-0.23	6.43	-0.16
8	5.26	5.28	-0.02	5.27	-0.01
10	7.38	7.43	-0.05	7.28	0.1
11	7.35	7.49	-0.14	7.49	-0.14
12	7.15	7.22	-0.07	7.14	0.01
14	6.89	6.96	-0.07	6.99	-0.1
15	6.48	6.57	-0.09	6.72	-0.24
16	6.2	6.32	-0.12	6.27	-0.07
17	6.92	6.67	0.25	6.68	0.24
18	6.57	6.51	0.06	6.62	-0.05
19	6.54	6.62	-0.08	6.78	-0.24
20	7.35	7.32	0.03	7.26	0.09
22	8.15	8.45	-0.3	8.29	-0.14
23	8.7	8.55	0.15	8.54	0.16
24	8.3	8.27	0.03	8.31	-0.01
25	7.77	7.8	-0.03	7.84	-0.07
26	8.15	7.79	0.36	7.91	0.24
28	5.96	5.78	0.18	5.8	0.16
29	5.72	5.46	0.26	5.67	0.05
30	6.22	6.3	-0.08	6.42	-0.2
31	6.7	6.61	0.09	6.63	0.07
32	6	6	0	6.13	-0.13
33	5.64	5.61	0.03	5.63	0.01
35	6.7	7.01	-0.31	6.67	0.03
36	6.4	6.67	-0.27	6.37	0.03
38	6.1	6.08	0.02	6.03	0.07
39	8.4	8.2	0.2	8.3	0.1
40	9	8.72	0.28	9.04	-0.04
41	6	6.52	-0.52	6.21	-0.21
42	6.22	6.32	-0.1	6.19	0.03
43	8	7.7	0.3	7.85	0.15
44	7.1	7.07	0.03	7.11	-0.01
45	7.7	7.47	0.23	7.58	0.12
46	8.7	8.92	-0.22	8.8	-0.1
48	7.72	7.75	-0.03	7.77	-0.05
Test set					
1	5.92	5.61	0.31	5.62	0.3
4	5.59	5.47	0.12	5.8	-0.21
6	6.43	5.92	0.51	6.06	0.37
7	5.92	5.6	0.32	5.91	0.01
9	5.74	5.91	-0.17	6.21	-0.47
13	7.11	6.97	0.14	6.91	0.2
21	7.74	7.25	0.49	7.22	0.52
27	7.62	7.45	0.17	7.74	-0.12
34	6.4	5.95	0.45	6.06	0.34
37	5.55	6.05	-0.5	6.01	-0.46
47	8.3	8.9	-0.6	8.64	-0.34

PA_{CoMFA}=predicted activity by CoMFA model, PA_{CoMSIA}=predicted activity by CoMSIA model. Resid=difference of observed and predicted activities.

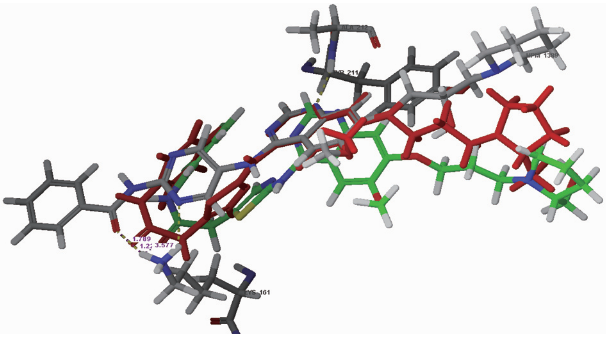

Figure 5. The structures of docked mode A and B in green and red color respectively.

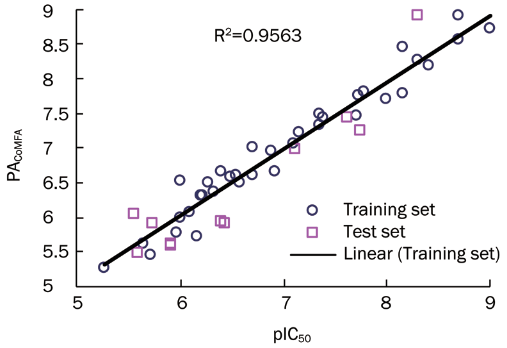

Figure 6. The trend of observed and predicted activities for the training and test set using CoMFA based model.

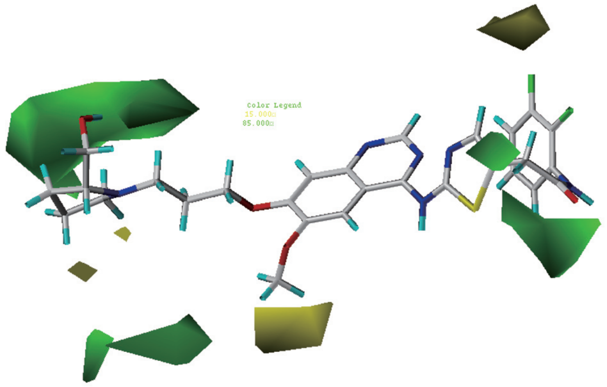

Figure 7. CoMFA steric map based on SE model.

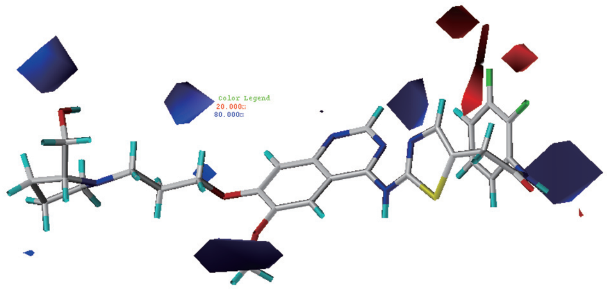

Figure 8. CoMFA electrostatic map based on SE model.

Comparative molecular similarity indices analyses (CoMSIA)

The CoMSIA was conducted in a similar manner to the CoMFA. $CoMSIA_1$ to $CoMSIA_{16}$ were based on the steric, electrostatic, hydrophobic, hydrogen bond donor, and hydrogen bond acceptor field effects in different combinations. The field combinations and the statistical summary are reported in Table 4. The model ($CoMSIA_9$) based on the steric, electrostatic, and hydrophobic effects provided good results, with LOO values of q^2=0.75 and r^2=0.98. For this model, the correlation coefficient for the internal predictivity was r^2_{bs}=0.98 and the correlation coefficient for the test set predictivity of 11 compounds was $r^2_{predictive}$=0.73.

Similarly, the models $CoMSIA_{17}$ to $CoMSIA_{32}$ are based on the X-ray geometries and combinations of different field effects. The best-fit model ($CoMSIA_{25}$) was based on the X-ray geometry and the steric, electrostatic and hydrophobic fields effects, which provided LOO square of cross-validated correlation coefficients of q^2=0.77 and r^2=0.98. The model was tested for the internal predictivity (r^2_{bs}=0.98) and test set predictivity of 11 compounds ($r^2_{predictive}$=0.77). The statistical value of model $CoMSIA_{25}$ was better than that of model $CoMSIA_9$, which indicated the significance of model $CoMFA_{25}$. The predicted activities by model $CoMSIA_{25}$ are summarized in Table 3. The trend of the observed and predicted activities using model $CoMSIA_{25}$ is displayed in Figure 9.

CoMSIA maps

Like the CoMFA, the CoMSIA contour maps were also developed using the best-fit model $CoMSIA_{25}$, which was based on steric, electrostatic, and hydrophobic interactions. Each

Table 4. The regression summary of different CoMSIA models.

No	Models	Field	q^2	n	SEE	r^2	F	r^2_{bs}	r^2_{pred}	SD
Ligand based										
1	$CoMSIA_1$	S	0.46	6	0.21	0.96	123.99	–	–	–
2	$CoMSIA_2$	E	0.62	6	0.22	0.96	110.78	–	–	–
3	$CoMSIA_3$	H	0.69	7	0.199	0.967	119.713	–	–	–
4	$CoMSIA_4$	D	0.44	3	0.55	0.71	26.71	–	–	–
5	$CoMSIA_5$	A	0.47	7	0.40	0.86	26.66	–	–	–
6	$CoMSIA_6$	0.38S/0.62E	0.67	6	0.19	0.97	146.85	–	–	–
7	$CoMSIA_7$	0.33S/0.67H	0.66	7	0.18	0.97	139.64	–	–	–
8	$CoMSIA_8$	0.47S/0.53D	0.46	5	0.38	0.87	40.084	–	–	–
9	$CoMSIA_9$	0.21S/0.39E/0.40H	0.755	6	0.151	0.98	244.652	0.983	0.725	0.009
10	$CoMSIA_{10}$	0.29S/0.45E/0.26D	0.68	7	0.174	0.974	158.272	–	–	–
11	$CoMSIA_{11}$	0.23S/0.40E/0.34A	0.685	7	0.21	0.963	107.267	–	–	–
12	$CoMSIA_{12}$	0.24S/0.48H/0.28D	0.64	7	0.17	0.97	151.21	–	–	–
13	$CoMSIA_{13}$	0.16S/0.32E/0.33H/0.19D	0.738	6	0.162	0.977	211.882	–	–	–
14	$CoMSIA_{14}$	0.16S/0.29E/0.30H/0.25A	0.74	7	0.167	0.976	170.532	–	–	–
15	$CoMSIA_{15}$	0.20S/0.33E/0.18D/0.29A	0.71	8	0.18	0.97	126.36	–	–	–
16	$CoMSIA_{16}$	0.14S/0.25E/0.26H0.14D/0.21A	0.74	7	0.16	0.98	189.50	–	–	–
Receptor guided										
17	$CoMSIA_{17}$	S	0.37	5	0.403	0.853	35.892	–	–	–
18	$CoMSIA_{18}$	E	0.65	5	0.25	0.94	98.27	–	–	–
19	$CoMSIA_{19}$	H	0.705	7	0.176	0.974	154.393	–	–	–
20	$CoMSIA_{20}$	D	0.43	3	0.56	0.7	25.14	–	–	–
21	$CoMSIA_{21}$	A	0.49	7	0.39	0.87	27.81	–	–	–
22	$CoMSIA_{22}$	0.37S/0.63E	0.68	6	0.18	0.97	165.27	–	–	–
23	$CoMSIA_{23}$	0.33S/0.67H	0.662	7	0.172	0.975	161.687	–	–	–
24	$CoMSIA_{24}$	0.47S/0.53D	0.44	5	0.39	0.86	34.44	–	–	–
25	$CoMSIA_{25}$	0.20S/0.42E/0.38H	0.77	6	0.15	0.98	248.454	0.98	0.77	0.007
26	$CoMSIA_{26}$	0.28S/0.48E/0.24D	0.68	8	0.14	0.98	190.35	–	–	–
27	$CoMSIA_{27}$	0.25S/0.41E/0.34A	0.71	8	0.17	0.98	141.16	–	–	–
28	$CoMSIA_{28}$	0.24S/0.5H/0.26D	0.642	7	0.172	0.975	161.121	–	–	–
29	$CoMSIA_{29}$	0.17S/0.34E/0.32H/0.17D	0.749	6	0.161	0.977	215.729	–	–	–
30	$CoMSIA_{30}$	0.15S/0.3E/0.28H/0.27A	0.752	6	0.175	0.973	181.309	–	–	–
31	$CoMSIA_{31}$	0.2S/0.34E/0.17D/0.29A	0.71	8	0.17	0.97	137.15	–	–	–
32	$CoMSIA_{32}$	0.14S/0.26E/0.25H/0.12D/0.23A	0.757	7	0.165	0.977	176.332	–	–	–

S=steric field, E=electrostatic field, H=hydrophobic field, D=hydrogen bond donor field, A=hydrogen bond acceptor field, n=No of components, q^2=cross-validated r^2, r^2=non cross-validated, F=Fischer's F value for test of significance, SEE=standard error of estimate, r^2_{bs}=coefficient of determination after 100 bootstrapping runs, SD=standard deviation.

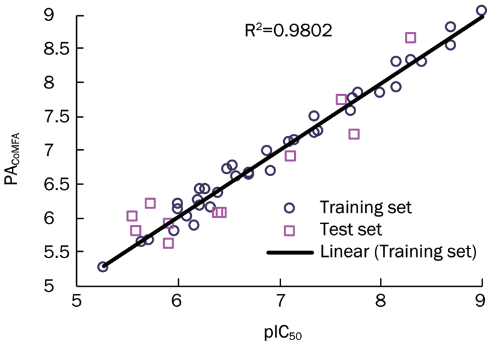

Figure 9. The trend of observed and predicted activities for the training and test using CoMSIA based model.

interaction is individually displayed (Figures 10–12) with compound 40. The green contours indicate the area in which steric bulky substations might beneficially affect the activity and the yellow region is favorable for small groups (Figure 10). The map is quite similar to the CoMFA steric map because the green contour appears around the pyrrolidine ring and other green contours appear around the thiazole ring, which indicates that a bulkier group will be favorable for higher activity. The blue contour indicates the region where a positive group is required for high activity, while the red zone indicates the region favorable for negative groups (Figure 11). Blue and red contours appeared around the thiazole ring, which is similar to the CoMFA electrostatic map. These contours indicate a suitable site for positive and negative substituents. The CoMSIA map with the hydrophobic field effect is displayed in Figure 12. The white contour favorable for hydrophobic groups was evident around the pyrrolidine and near the thiazole ring. The small yellow contour favorable for the hydrophilic group appeared at a certain distance from the thiazole ring. A comparison indicated that there is a dominance of the hydrophobic and bulky groups around the same region (Figures 10 and 12).

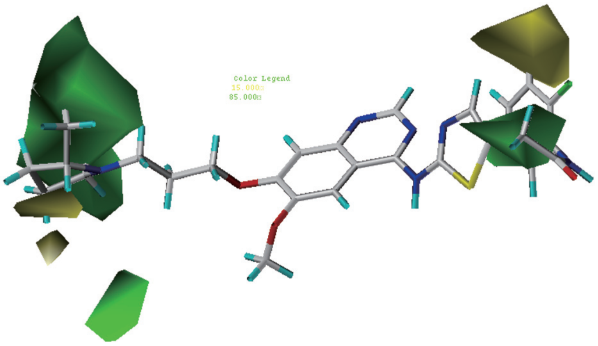

Figure 10. CoMSIA steric map based on SEH model.

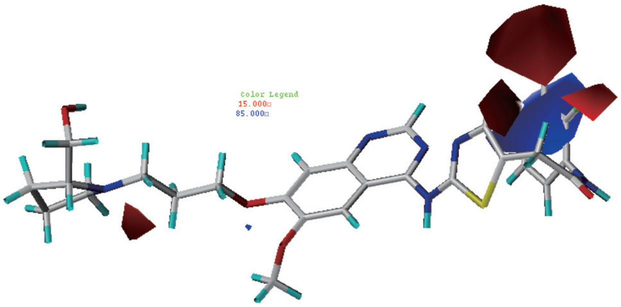

Figure 11. CoMSIA electrostatic map based on SEH model.

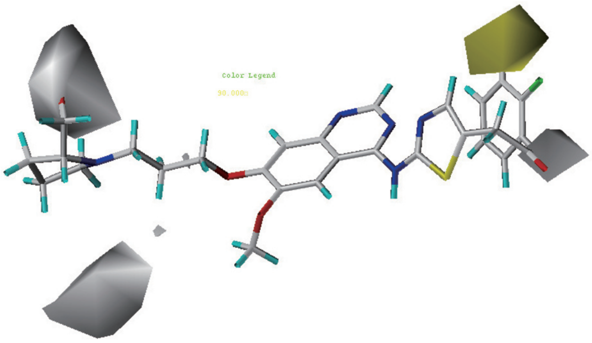

Figure 12. CoMSIA hydrophobic map based on SEH model.

Discussion

In earlier publications, a number of quinazoline-based series have been described as Aurora kinase inhibitors[2, 22, 42-44]. Particularly, the *p*-benzamidoanilinoquinazoline series was shown to inhibit Aurora A and Aurora B equipotently. The investigation of the SAR around the anilino ring linking the key hinge (quinazoline) and the lipophilic pocket (benzamide) binding groups showed that this ring could be replaced with a number of heterocyclic systems to give improvements in both the potency and the physicochemical properties[42]. The linker group also has an important role for the cellular activity. For example, the ether and thiomethyl groups in compound 35 and 36 gave poor cellular potency compared to the acetanilide series. Other linkers like the reverse amide and sulfonamide in compounds 37 and 38 also are responsible for their lower cellular activity. Comparing all the linkers, it is clear that acetanilide shows the potent cellular activity that is present in the most active compound 40. Furthermore, it was found that Aurora A is able to accommodate highly polar functional groups within the side chain at the quinazoline C-7 position. Compounds with elaborated C-7 side chains show good cellular activity and benefit from much better solubility and free drug levels. The quinazoline C-7 side chain might result in a further enhancement of the cellular potency[42]. In the thiazole series, the length of the aliphatic spacer, between the oxygen atom on the C-7 position of the quinazoline ring and the basic nitrogen atom within the side chain of the R1 substituent, governs the ability of the polar group to solvate[42]. Both cyclic and noncyclic amide chains are tolerated by the Aurora kinases.

Among the five and six membered ring compounds, the prolinol side chains have greater cellular activity. The preference for five membered rings can be helpful to support the findings of the 3D-CoMFA model, which suggest a bulkier substituent in this position. The structure-activity relationships of the pyridino- and pyrimidinoquinazoline compounds have been described recently and include one of the first crystal structures with a small inhibitor bound to the Aurora kinase[45]. It was helpful in rationalizing the observed high potency and high specificity for the Aurora kinases. Both the CoMFA and the CoMSIA models suggested that small and lipophilic groups were particularly favorable in the terminal lipophilic binding pocket. Fluoro groups at the ortho and meta positions were found to be particularly favorable for better activity. The 2,3-difluoro and 3-fluoro acetanilide groups generally give rise to better cellular potency compared to larger and more polar functional groups. These findings can be observed from the comparison of compounds 5 and 3 with compound 8 in the pyrazole series. The comparison of compound 47 with the mentioned compounds provides evidence for the binding conformation for both (pyrazole and thiazole) series. These studies suggest that a further hydrogen bond donor in the pyrazole ring (compared to the thiazole ring) may allow additional binding to the protein backbone. The improved physical properties, together with reasonable enzymatic and cellular activities, made the pyrazole series an attractive proposition for further medicinal chemistry aimed at optimizing the cellular potency, while at the same time maintaining the drug-like properties.

A number of crystal structures of Aurora A in different conformations with ATP analogues have been published[45–48]. A crystal structure of Aurora A complexed with a small molecule inhibitor from the pyrimidinoquinazoline series adopts an inactive conformation with the displacement of the DFG motif (DFG-out)[45]. In the crystal structure (Figure 5), the distance between the carbonyl oxygen (black skeleton) and the hydrogen of the amino group was 1.8 Å. While using molecular docking, the best active compound acquired the same site as the X-ray structure and apparently the noted distance was 1.2 Å, which facilitates the interaction and results in a more potent inhibitor. Similar binding interactions may exist with the acetanilide chain; however, the interposed methylene and the inversion of the amide may lead to a different binding mode within the hydrophobic pocket that could translate into higher cellular potency.

Compound 40 binds in the ATP-binding site. The quinazoline ring of compound 40 fit into the hinge region (Figure 13A), and the N-atom formed a hydrogen bond with the main chain of Ala212. In addition, the quinazoline ring also formed hydrophobic interactions with the surrounding residues, including Leu138, Val146, Ala159, and Leu262. In particular, Leu262 made extensive interactions with the quinazoline ring. The prolinol moiety extended into the solvent-exposed region of the binding site. The amide carbonyl near the thiazole shows a hydrogen bond to the conserved Lys161. The terminal aromatic ring fits into a hydrophobic pocket of the kinase and is mainly surrounded by hydrophobic residues, Trp276, Leu163, Leu177, and Leu207. The pyrazole ring and amino nitrogen near the quinazoline of compound 8 form hydrogen bonds (Figure 13B) with the hinge residues (Glu210 and Ala212, respectively). The O-atom of 3-methoxy acetamide shows a hydrogen-bonding interaction. This may cause inhibitor 8 not to occupy the terminal lipophilic binding pocket fully, which is important for cellular potency.

The Thr217/Glu161 difference has been proposed recently to explain the selectivity of indirubin-based inhibitors for Aurora B[49]. A docking study was performed to observe the ligand-receptor interaction regarding the selectivity for Aurora B. The docking data showed that compound 40 could fit into the catalytic cleft of Aurora B (PDB ID 2VGP) and bind strongly to the residues surrounding the cleft (Figure 14A). The elaborate docking indicates that compound 40 occupies the ATP binding pocket of the active center of Aurora B with multiple interactions with the residues around the pocket: the quinazolino nitrogen and amino hydrogen are hydrogen bonded to Ala173 and the amide hydrogen to Pro174. At the same time, the hydroxyl of prolinol binds to Glu177 with a hydrogen bond, occupying the entry site to the catalytic cleft in Aurora B (Figure 14B). This binding mode is similar to the recently reported[50] Aurora B inhibitor. This interaction can be explained by considering the property of the glutamate residue. Glutamate is an acidic residue with a longer and more flexible side chain and is located near the catalytic edge of the catalytic pocket, in a subsite referred to as the ribose binding region. It is a hydrophilic part of the binding site, where interactions between the receptor and the sugar moiety of the natural substrate are formed, as demonstrated in crystal structures such as adenosine complexed with cAMP-dependent kinase (1FMO) or ATP complexed with CDK2 (1HCK). Moreover, crystallographic studies revealed that the direct or water mediated interaction of the inhibitor with residues located in the ribose-binding site enhances the ligand affinity. The superimposition of Aurora A (PDB ID 2C6E) and B (PDB ID 2VGP) shows a clear difference between the active site residues (Figure 15). One of the Aurora B residue equivalents (Lys 122) to Aurora A (Lys 161) lacks a hydrogen bond interaction because of its different orientation. Also, the position of the nonconserved residue Glu177 explains the distinct interaction responsible for the selectivity. The Glu177 residue is closer to the hydroxyl of prolinol to make the hydrogen bond interaction. This type of important interaction revealed from the docking study can be a useful guideline for future selective inhibitor design.

Modification of the R1 substituent at the C7 position of the quinazoline inhibitors is known to profoundly influence their activity and selectivity[51–54]. The R1 substituent accesses the solvent channel, explaining why a wide range of strongly polar groups is tolerated, provided that a suitable linear spacer is included between the solubilizing group and the quinazoline. Variation of the R1 substituent at the quinazoline C7 side chain allowed the fine-tuning of the overall properties of the compounds. From the above discussion, it can be said that

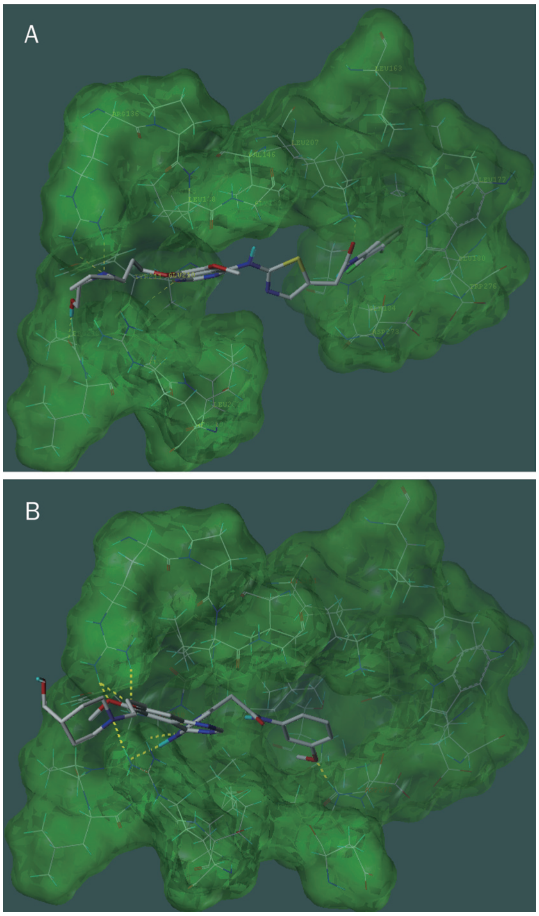

Figure 13. (A) The docking mode of compound 40 (atom type, stick model) to the active site of Aurora A (PDB ID 2C6E). (B) The docking mode of compound 8 (atom type, stick model) to the active site.

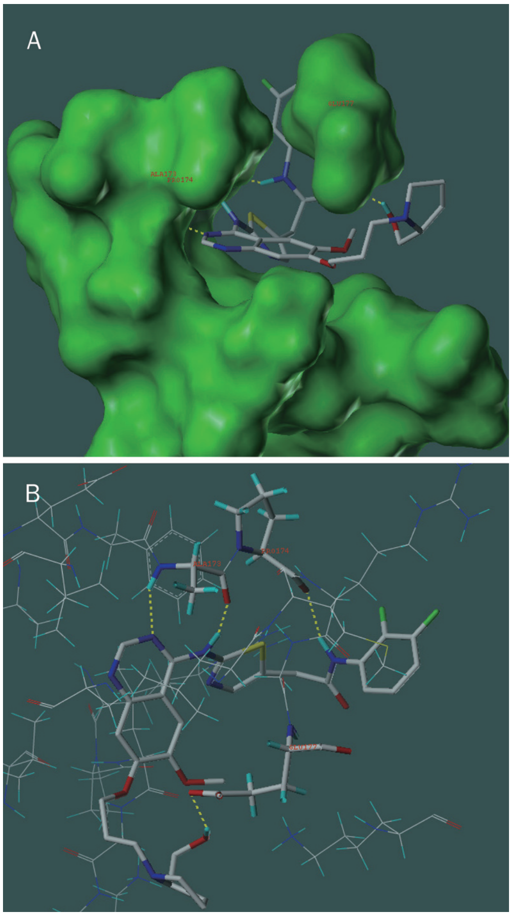

Figure 14. (A) The docking mode of compound 40 (atom type, stick model) to the active site of Aurora B (PDB ID 2VGP). (B) Hydrogen bonds (yellow dotted line) between compound 40 and residues (atom type) around the active site shown in stick model.

variation of the R1 substituent at the quinazoline C7 position along with an optimized linker and terminal aromatic substituent may help to design more potent and selective Aurora B inhibitors. Beside these findings, a progressive scrambling technique was employed to determine the possibility of a chance correlation in the QSAR model. The cSDEP values are almost at a minimum and the Q^2 values are at a maximum (Tables 5 and 6). The values for the slope in the 2, 3, and 4 component models are acceptable, while a value greater than 1.2 is indicative of a bad model. Thus, we used the CoMFA and CoMSIA models having the least number of components for a stable QSAR model.

Conclusion

The overall study implies that steric and hydrophobic effects, along with a positive electrostatic interaction, play crucial roles in the inhibitory activity of quinazoline derivatives. The activity is quite sensitive to the conformation, and the contact between the carbonyl oxygen and the Lys hydrogen is important to the activity. The importance of steric bulk with electronic interaction is evidenced by the statistics. The ligand-

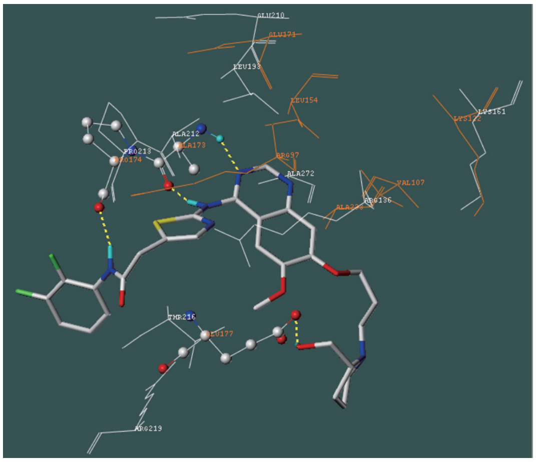

Figure 15. Docked pose of compound 40 (stick model in atom type) in Aurora A (PDB ID 2C6E) and B (PDB ID 2VGP) is superimposed. Compound 40 in active site of Aurora A is not shown for comparison of residues in active site of B (orange) with that of A (white). Hydrogen bond (yellow dotted line) forming residues (atom type) in Aurora B are shown in ball model.

Table 5. CoMFA model scrambling stability test.

Component	Q^2	cSDEP	$\frac{dq^2}{dr^2yy}$
1	0.099	0.938	0.416
2	0.363	0.800	0.465
3	0.417	0.776	0.643
4	0.441	0.77	0.806
5	0.448	0.779	1.013
6	0.433	0.803	1.296
7	0.432	0.817	1.482
8	0.422	0.841	1.341

Table 6. CoMSIA model scrambling stability test.

Component	Q^2	cSDEP	$\frac{dq^2}{dr^2yy}$
1	0.106	0.934	0.454
2	0.329	0.821	0.663
3	0.459	0.748	0.68
4	0.504	0.726	0.713
5	0.526	0.721	0.996
6	0.562	0.705	1.08
7	0.739	0.739	1.273
8	0.55	0.743	1.304

based 3D QSAR model has proven significant, but a more definitive conclusion requires consideration of the receptor site. The receptor-guided CoMFA model has a high value of LOO, q^2=0.56, r^2=0.96 and $r^2_{\text{predictive}}$=0.76; similarly, the CoMSIA model has a high value of LOO, q^2=0.77, r^2=0.98 and $r^2_{\text{predictive}}$=0.77, suggesting that a highly active ligand can be designed by variations of the R1 substituent at position 7 of the quinazoline ring with positively charged, bulky and hydrophobic groups, while around the thiazole ring, bulky and hydrophobic groups are desirable for higher activity. Also, the formation of a hydrogen bond with Glu177 can be useful for selectivity.

Author contribution

MM NEAZ performed the research; FA PASHA designed the research; M MUDDASSAR contributed modeling ideas; Seung Joo CHO provided computational resources and guidelines.

References

1 Andrews PD. Aurora kinases: shining lights on the therapeutic horizon? Oncogene 2005; 24: 5005–15.

2 Matthews N, Visintin C, Hartzoulakis B, Jarvis A, Selwood DL. Aurora A and B kinases as targets for cancer: will they be selective for tumors? Expert Rev Anticancer Ther 2006; 6: 109–20.

3 Girdler F, Gascoigne KE, Eyers PA, Hartmuth S, Crafter C, Foote KM, *et al*. Validating Aurora B as an anti-cancer drug target. J Cell Sci 2006; 119: 3664–75.

4 Andrews PD, Knatko E, Moore WJ, Swedlow JR. Mitotic mechanics: the auroras come into view. Curr Opin Cell Biol 2003; 15: 672–83.

5 Carmena M, Earnshaw WC. The cellular geography of aurora kinases. Nat Rev Mol Cell Biol 2003; 4: 842–54.

6 Meraldi P, Honda R, Nigg EA. Aurora kinases link chromosome segregation and cell division to cancer susceptibility. Curr Opin Genet Dev 2004; 14: 29–36.

7 Giet R, Glover DM. Drosophila Aurora B kinase is required for histone H3 phosphorylation and condensin recruitment during chromosome condensation and to organize the central spindle during cytokinesis. J Cell Biol 2001; 152: 669–81.

8 Bischoff JR, Anderson L, Zhu YF, Mossie K, Ng L, Souza B, *et al*. A homologue of Drosophila aurora kinase is oncogenic and amplified in human colorectal cancers. Embo J 1998; 17: 3052–65.

9 Royce ME, Xia WY, Sahin AA, Katayama H, Johnston DA, Hortobagyi G, *et al*. STK15/aurora-A expression in primary breast tumors is correlated with nuclear grade but not with prognosis. Cancer 2004; 100: 12–9.

10 Sen S, Zhou HY, White RA. A putative serine/threonine kinase encoding gene BTAK on chromosome 20q13 is amplified and overexpressed in human breast cancer cell lines. Oncogene 1997; 14: 2195–200.

11 Tanaka T, Kimura M, Matsunaga K, Fukada D, Mori H, Okano Y. Centrosomal kinase AIK1 is overexpressed in invasive ductal carcinoma of the breast. Cancer Res 1999; 59: 2041–44.

12 Chieffi P, Cozzolino L, Kisslinger A, Libertini S, Staibano S, Mansueto G, *et al*. Aurora B expression directly correlates with prostate cancer malignancy and influence prostate cell proliferation. Prostate 2006; 66: 326–33.

13 Li DH, Zhu JJ, Firozi PF, Abbruzzese JL, Evans DB, Cleary K, *et al*. Overexpression of oncogenic STK15/BTAK/aurora A kinase in human pancreatic cancer. Clin Cancer Res 2003; 9: 991–7.

14 Ulisse S, Delcros JG, Baldini E, Toller M, Curcio F, Giacomelli L, *et al*. Expression of Aurora kinases in human thyroid carcinoma cell lines and tissues. Int J Cancer 2006; 119: 275–82.

15 Reiter R, Gais P, Jutting U, Steuer-Vogt MK, Pickhard A, Bink K, *et al*. Aurora kinase A messenger RNA overexpression is correlated with tumor progression and shortened survival in head and neck squamous cell carcinoma. Clin Cancer Res 2006; 12: 5136–41.

16 Ikezoe T, Yang J, Nishioka C, Tasaka T, Taniguchi A, Kuwayama Y, *et al*. A novel treatment strategy targeting Aurora kinases in acute myelogenous leukemia. Mol Cancer Ther 2007; 6: 1851–7.

17 Zeng WF, Navaratne K, Prayson RA, Weil RJ. Aurora B expression correlates with aggressive behaviour in glioblastoma multiforme. J Clin Pathol 2007; 60: 218–21.

18 Lopez-Rios F, Chuai S, Flores R, Shimizu S, Ohno T, Wakahara K, *et al*. Global gene expression profiling of pleural mesotheliomas: Overexpression of aurora kinases and P16/CDKN2A deletion as prognostic factors and critical evaluation of microarray-based prognostic prediction. Cancer Res 2006; 66: 2970–9.

19 Kurai M, Shiozawa T, Shih HC, Miyamoto T, Feng YZ, Kashima H, *et al*. Expression of Aurora kinases A and B in normal, hyperplastic, and malignant human endometrium: Aurora B as a predictor for poor prognosis in endometrial carcinoma. Human Pathol 2005; 36: 1281–8.

20 Ota T, Suto S, Katayama H, Han ZB, Suzuki F, Maeda M, *et al*. Increased mitotic phosphorylation of histone H3 attributable to AIM-1/Aurora-B overexpression contributes to chromosome number instability. Cancer Res 2002; 62: 5168−77.

21 Mountzios G, Terpos E, Dimopoulos MA. Aurora kinases as targets for cancer therapy. Cancer Treat Rev 2008; 34: 175−82.

22 Harrington EA, Bebbington D, Moore J, Rasmussen RK, Ajose-Adeogun AO, Nakayama T, *et al*. VX-680, a potent and selective small-molecule inhibitor of the Aurora kinases, suppresses tumor growth *in vivo*. Nat Med 2004; 10: 262−7.

23 Fancelli D, Moll J, Varasi M, Bravo R, Artico R, Berta D, *et al*. 1,4,5,6-tetrahydropyrrolo[3,4-c] pyrazoles: Identification of a potent aurora kinase inhibitor with a favorable antitumor kinase inhibition profile. J Med Chem 2006; 49: 7247−51.

24 Mortlock AA, Foote KM, Heron NM, Jung FH, Pasquet G, Lohmann JJM, *et al*. Discovery, synthesis, and *in vivo* activity of a new class of pyrazoloquinazolines as selective inhibitors of aurora B kinase. J Med Chem 2007; 50: 2213−24.

25 Foote KM, Mortlock AA, Heron NM, Jung FH, Hill GB, Pasquet G, *et al*. Synthesis and SAR of 1-acetanilide-4-aminopyrazole-substituted quinazolines: Selective inhibitors of Aurora B kinase with potent anti-tumor activity. Bioorg Med Chem Lett 2008; 18: 1904−9.

26 Cramer RD, Patterson DE, Bunce JD. Comparative Molecular-Field Analysis (Comfa). 1. Effect of shape on binding of steroids to carrier proteins. J Am Chem Soc 1988; 110: 5959−67.

27 Morshed MN, Muddassar M, Pasha FA, Cho SJ. Pharmacophore identification and validation study of CK2 inhibitors using CoMFA/CoMSIA. Chem Biol Drug Des 2009; 74: 148–58.

28 Klebe G, Abraham U, Mietzner T. Molecular similarity indices in a comparative analysis (CoMSIA) of drug molecules to correlate and predict their biological activity. J Med Chem 1994; 37: 4130−46.

29 Pasha FA, Muddassar M, Cho SJ, Ahmad K, Beg Y. 3D and quantum QSAR of non-benzodiazepine compounds. Eur J Med Chem 2008; 43: 2361−72.

30 Muddassar M, Pasha FA, Yoo KH, Lee SH, Cho SJ. Docking and quantum mechanics-guided CoMFA analysis of b-RAF inhibitors. Bull Korean Chem Soc 2008; 29: 1499−504.

31 Pasha FA, Muddassar M, Chung HW, Cho SJ, Cho H. Hologram and 3D-quantitative structure toxicity relationship studies of azo dyes. J Mol Model 2008; 14: 293−302.

32 Jung FH, Pasquet G, Lambert-van der Brempt C, Lohmann JJM, Warin N, Renaud F, *et al*. Discovery of novel and potent thiazoloquinazolines as selective Aurora A and B kinase inhibitors. J Med Chem 2006; 49: 955−70.

33 SYBYL 7.3. Tripos Inc, St Louis, MO 63114, USA 2007.

34 Clark M, Cramer RD, Vanopdenbosch N. Validation of the general-purpose tripos 5.2 Force-field. J Comput Chem 1989; 10: 982−1012.

35 Viswanadhan VN, Ghose AK, Revankar GR, Robins RK. Atomic physicochemical parameters for 3 dimensional structure directed quantitative structure-activity relationships. 4. additional parameters for hydrophobic and dispersive interactions and their application for an automated superposition of certain naturally-occurring nucleoside antibiotics. J Chem Information Computer Sci 1989; 29: 163−72.

36 Klebe G. The use of composite crystal-field environments in molecular recognition and the de novo design of protein ligands. J Mol Biol 1994; 237: 212−35.

37 Wold S, Ruhe A, Wold H, Dunn WJ. The collinearity problem in linear-regression — the partial least-squares (pls) approach to generalized inverses. Siam J Sci Statistical Comput 1984; 5: 735−43.

38 Geladi P, Xie YL, Polissar A, Hopke P. Notes on the history and nature of partial least squares (PLS) modeling. J Chemometrics 1988; 2: 231−46.

39 Cramer RD, Bunce JD, Patterson DE, Frank IE. Cross-validation, bootstrapping, and partial least-squares compared with multiple-regression in conventional QSAR studies. Quant Struct-Act Relat 1988; 7: 18−25.

40 Wold S. Cross-validatory estimation of number of components in factor and principal components models. Technometrics 1978; 20: 397−405.

41 Pinto-Bazurco M, Tsakovska I, Pajeva I. QSAR and 3D QSAR of inhibitors of the epidermal growth factor receptor. Int J Quantum Chem 2006; 106: 1432−44.

42 Mortlock A, Keen NJ, Jung FH, Heron NM, Foote KM, Wilkinson RW, *et al*. Progress in the development of selective inhibitors of aurora kinases. Curr Top Med Chem 2005; 5: 807−21.

43 Fancelli D, Moll J. Inhibitors of Aurora kinases for the treatment of cancer. Expert Opin Ther Patents 2005; 15: 1169−82.

44 Fancelli D, Berta D, Bindi S, Cameron A, Cappella P, Carpinelli P, *et al*. Potent and selective aurora inhibitors identified by the expansion of a novel scaffold for protein kinase inhibition. J Med Chem 2005; 48: 3080−84.

45 Heron NM, Anderson M, Blowers DP, Breed J, Eden JM, Green S, *et al*. SAR and inhibitor complex structure determination of a novel class of potent and specific Aurora kinase inhibitors. Bioorg Med Chem Lett 2006; 16: 1320−23.

46 Bayliss R, Sardon T, Vernos I, Conti E. Structural basis of Aurora-A activation by TPX2 at the mitotic spindle. Mol Cell 2003; 12: 851−62.

47 Nowakowski J, Cronin CN, McRee DE, Knuth MW, Nelson CG, Pavletich NP, *et al*. Structures of the cancer-related aurora-A, FAK, and EphA2 protein kinases from nanovolume crystallography. Structure 2002; 10: 1659−67.

48 Cheetham GMT, Knegtel RMA, Coll JT, Renwick SB, Swenson L, Weber P, *et al*. Crystal structure of aurora-2, an oncogenic serine/threonine kinase. J Biol Chem 2002; 277: 42419−22.

49 Myrianthopoulos V, Magiatis P, Ferandin Y, Skaltsounis AL, Meijer L, Mikros E. An integrated computational approach to the phenomenon of potent and selective inhibition of aurora kinases B and C by a series of 7-substituted indirubins. J Med Chem 2007; 50: 4027−37.

50 Fu DH, Jiang W, Zheng JT, Zhao GY, Li Y, Yi H, *et al*. Jadomycin B, an Aurora-B kinase inhibitor discovered through virtual screening. Mol Cancer Ther 2008; 7: 2386−93.

51 Hennequin LF, Thomas AP, Johnstone C, Stokes ESE, Ple PA, Lohmann JJM, *et al*. Design and structure-activity relationship of a new class of potent VEGF receptor tyrosine kinase inhibitors. J Med Chem 1999; 42: 5369−89.

52 Hennequin LF, Stokes ESE, Thomas AP, Johnstone C, Ple PA, Ogilvie DJ, *et al*. Novel 4-anilinoquinazolines with C-7 basic side chains: Design and structure activity relationship of a series of potent, orally active, VEGF receptor tyrosine kinase inhibitors. J Med Chem 2002; 45: 1300−12.

53 Pandey A, Volkots DL, Seroogy JM, Rose JW, Yu JC, Lambing JL, *et*

al. Identification of orally active, potent, and selective 4-piperazinylquinazolines as antagonists of the platelet-derived growth factor receptor tyrosine kinase family. J Med Chem 2002; 45: 3772−93.

54 Smaill JB, Rewcastle GW, Loo JA, Greis KD, Chan OH, Reyner EL, *et al*. Tyrosine kinase inhibitors. 17. Irreversible inhibitors of the epidermal growth factor receptor: 4-(phenylamino)quinazoline- and 4-(phenylamino)pyrido[3,2-d]-pyrimidine-6-acrylamides bearing additional solubilizing functions. J Med Chem 2000; 43: 1380−97.

16th World Congress of Basic and Clinical Pharmacology, WorldPharma2010

Copenhagen, Denmark
17–23 July 2010

www.iuphar2010.dk/
Deadline for Abstract Submission:
15 January 2010
Deadline for the low registration fee:
15 March 2010

Acta Pharmacologica Sinica (2010) 31: 259–264
© 2010 CPS and SIMM All rights reserved 1671-4083/10 $32.00
www.nature.com/aps

Original Article

Cytotoxicity and reversal of multidrug resistance by tryptanthrin-derived indoloquinazolines

Sung-tsai YU[1], Ji-wang CHERN[1], Tzer-ming CHEN[3], Yi-fan CHIU[1], Hui-ting CHEN[1], Yen-hui CHEN[1,2,*]

[1]Graduate Institute of Pharmaceutical Sciences and [2]Graduate Institute of Clinical Pharmacy, Nation Taiwan University, No 1 Sec 1, Jen-Ai Road, Taipei 10051, Taiwan, China; [3]Department of Obstetrics and Gynecology, Nation Taiwan University Hospital, No 7 Chung San South Road, Taipei 10051, Taiwan, China

Aim: To evaluate the effects and elucidate the mechanisms of a series of indoloquinazolines as novel anticancer agents.
Methods: Condensation of the substituted isatoic anhydride with the substituted isatin was performed to prepare compounds **1–4**, followed by adding malononitrile to prepare compounds **5–7**. Cytotoxicity was measured by MTT assays. Apoptosis induction was evaluated using DNA fragmentation, cell cycle assay, caspase 3/7 activity and Western blot.
Results: Compounds **3**, **4**, and **5** display cytotoxicity against MCF-7, HeLa, SKOV3, and A498 cancer cells. DNA ladders appear in cells treated with compounds **3**, **4**, and **5**. Within those, compound **4** exhibits the greatest activity in regards to sub-G_1 accumulations in the cell cycle and the activation of caspase-3/7. Furthermore, Fas and Fas ligand levels are elevated by compound **4**, implying that the apoptosis is in part mediated through the signals. On the other hand, compounds **1** and **7** display chemosensitizing activity since cytotoxicity of doxorubicine and etoposide is enhanced in combination with compound **1** and **7**, respectively, in MCF-7/adr (doxorubicin-resistant) and MCF-7/vp (etoposide-resistant).
Conclusion: The cytotoxicity of indoloquinazolines is structure-dependent rather than cell type-dependent due to the similar degree of cytotoxicity induced by the individual compounds in all four cell lines. Further modification of the tryptanthrin skeleton is important to develop novel anticancer agents bearing either cytotoxicity against MCF-7 cells or drug resistance reversal in MCF-7/adr and MCF-7/vp.

Keywords: apoptosis, cytotoxicity, drug resistance, MCF-7, tryptanthrin

Acta Pharmacologica Sinica (2010) 31: 259–264; doi: 10.1038/aps.2009.198

Introduction

In the last decade, basic cancer research has produced remarkable advances in our understanding of cancer biology and cancer genetics. Among the most important advances is that apoptosis and the genes that regulate it have a profound effect on the malignant phenotype. For example, it is now clear that some oncogenic mutations interrupt apoptosis, leading to tumor initiation, progression or metastasis. Finally, it is now well documented that most cytotoxic anticancer agents induce apoptosis, raising the possibility in apoptotic programs.

Apoptosis is a form of programmed cell death that plays a fundamental role in many normal biological processes as well as several disease states. Apoptosis can be induced by various stimuli that all produce the same end result: systematic and deliberate cell death[1]. Recent developments strongly implicate a number of central mediators of apoptosis[2]. The cell surface molecule Fas (APO-1/CD95) transduces the intracellular apoptotic death signaling upon stimulation by Fas ligand[3]. Fas plays a dominant role in various physiological cell death and disease states, leading to the caspase 8-dependent activation of effector caspases, such as caspase 3[4, 5]. Among caspases, an essential role of caspase 3 in Fas-mediated apoptosis has been reported[6]. Caspase 3 exists in the cytoplasm of intact cells as a proenzyme form and is activated by proteolysis induced by the stimulation of Fas[7]. Caspase 3 is the essential factor in Fas-initiated death signaling, since it directly induces the activation of DNA fragmentation factor[8].

Multidrug resistance (MDR) is recognized as the most common cause of failure of cancer chemotherapy. MDR is an overall phenomenon resulting from cross-resistance to a variety of structurally and functionally unrelated natural products such as anthracyclines, *Vinca* alkaloids, epipodophyllotoxins and taxanes. Chemotherapeutic agents such as doxorubicin can select for mutations leading to increased expression of

---

[*] To whom correspondence should be addressed.
E-mail tcyhchen@ntu.edu.tw
Received 2009-06-04 Accepted 2009-12-22

P-glycoprotein and the phenotype of MDR in tissue culture models[9]. Development of adjuvant agents to overcome multidrug resistance (MDR) becomes a new trend in cancer chemotherapy.

Indigo plants have been a familiar and important source of dye for Asians since ancient times. Honda *et al* first isolated an indoloquinazoline, tryptanthrin, from Indigo plant *Strobilanthes cusia*[10]. Tryptanthrin with chemical name indolo[2,1-b] quinazolin-6,12-dione was reported to carry anti-microbial activity against a variety of microorganisms including bacteria, yeasts, dermatophytes and phytopathogens[10, 11]. Recently, tryptanthrin has been paid much attention as an aryl hydrocarbon receptor agonist[12], anti-inflammatory agent[13], inducer of caspase-3/Fas mediated apoptosis[14], cytostatic agent[15] and drug resistance reversal agent[16]. In this study, a series of tryptanthrin derivatives were synthesized and designated as compounds **1–7**. Anticancer and chemosensitizing activities were examined in MCF-7 cells. Results showed that compounds **3**, **4**, and **5** exhibited cytotoxicity at micromolar or lower concentrations. DNA fragmentation and cell cycle progression were determined by treating with compounds **3**, **4**, and **5**. Changes in Fas/Fas ligand and casepase-3/7 activities reveal the anticancer mechanisms involving Fas-mediated apoptosis pathway. On the other hand, compounds **1** and **7** which are not (or mild) cytotoxic are capable of sensitizing drug-resistant MCF-7 cells.

Materials and methods

Chemicals

Synthesis of 6,12-dihydro-6,12-dioxoindolo-[2,1-b]qinazoline (tryptanthrin) and its analogues were as described with modifications[15, 17]. As outlined in Scheme 1, compounds **1–4** were prepared by condensation of the substituted isatoic anhydride with the substituted isatin in *N*-methylmorpholine, *N*,*N*′-diisopropyl carbodiimide and pyridine. The solution of *N*,*N*′-diisopropyl carbodiimide in anhydrous pyridine was added with *N*-methylmorpholine to increase solubility. The resulting solution was added with the substituted isatoic anhydride and substituted isatin, then subjected to reflux at 120–130 °C for 6 h. Compounds **5–7** containing dicyanomethylene substituent were made as showed in Scheme 2 by treating substituted tryptanthrin with malononitrile in DMSO or NaH/THF, and then stirring for 5 h. The structures of tryptanthrin and its analogues were determined by ^{1}H and ^{13}C NMR spectra (Bruker AX-400, AX-300 spectrometer, Billerica, MA). The substituents of the tryptanthrin skeleton were systematically modified as in Schemes 1 and 2 (Figure 1), and tabulated in Table 1.

Cell lines and cell culture

MCF-7/wt, MCF-7/adr and MCF-7/vp cell lines were provided by Dr Chih-hsin YANG (National Taiwan University Hospital, Taiwan, China). HeLa, A498, and SKOV3 cell lines were purchased from ATCC (http://www.atcc.org). Cells were maintained in DMEM medium with 10% fetal calf serum and 100 ng/mL penicillin and streptomycin (Invitrogen, Carlsbad, CA) at 37 °C in 5% CO_2. MCF-7/adr and MCF-7/vp cells were grown in the presence of 0.1 μmol/L of doxorubicin or etoposide that was removed from the medium 1 week before each assay.

Scheme 1: Preparation of tryptanthrins. (Compounds **1–4**)

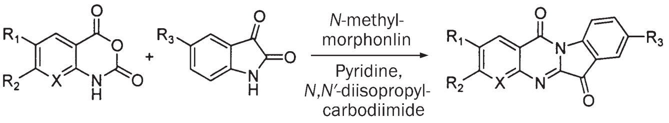

Scheme 2: Preparation of 6,12-dihydro-6-(dicyanomethylene)-12-oxoindolo [2,1-b] quinazoline derivatives. (Compounds **5–7**)

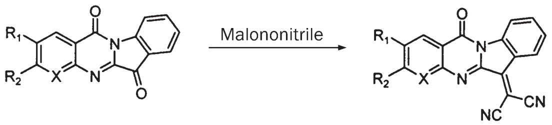

Figure 1. The synthetic strategy depicted in Schemes 1 and 2 to synthesize the tryptanthrin derivatives.

Cell survivability assay

To detect growth inhibition by the series of compounds, cells were seeded onto 96-well plates at a density of 5×10^3/well before compound treatment. Cytotoxicity of the series of compounds in a variety of cell lines was determined using the MTT assay after incubation of cells with these compounds at various concentrations for 3 d. IC$_{50}$ (the concentration of 50% inhibition of cell growth) was determined by interpolation of the dose-response curves.

DNA fragmentation

MCF-7/wt cells were plated at 4×10^5 cells/well onto each of 6-well plates. After overnight growth, cells were treated with tryptanthrins for various time periods. DNA was extracted by a Wizard® Genomic DNA Purification Kit (Promega, Madison, WI) and then dissolved in TE buffer. The purified DNA was quantified and equally loaded onto a 2% agarose gel for electrophoresis. The resulting bands were stained with ethidium bromide and visualized under UV light.

Cell cycle analysis

Cells were treated with various concentrations of tryptanthrin derivatives for 1 d, and then harvested by 0.25% trypsin and washed with PBS. Cells (2×10^5) were fixed in 70% ice-cold EtOH/PBS for 20 min on ice, and then washed with PBS and incubated in PI solution (69 mmol/L PI, 388 mmol/L sodium citrate, 100 μg/mL RNase A). Then the cells were analyzed immediately using a FACS Caliber (Beckton Dickinson, USA).

Caspase 3/7 assay

Caspase 3/7 activity was measured using the Caspase-glo 3/7 assay kit (Promega, Madison, WI). After treatment with tryptanthrins at different time points, the cells were incubated with Caspase-glo reagent for 1 h in the dark, and the luminescence was measured using a luminometer (Berthold Technologies, Bad Wildbad, Germany). Equal amount of cells were analyzed by counting a parallel set of cells and determining the total cell number for each sample.

Western blot analysis

The MCF-7 cells were treated with 10^{-6} mol/L tryptanthrins for various time periods. At the end of each treatment, the cells were trypsinized from the subconfluent monolayers, and their proteins were extracted using CelLytic™ M Cell Lysis Reagent (Sigma-Aldrich, St Louis, MO). The protein concentration of each sample was determined using a Bio-rad protein assay kit (Bio-Rad Laboratories, Hercules, CA). Total cellular proteins (80 μg/lane) were electrophoresized on 10% SDS-polyacrylamide gels and transferred to a PVDF membrane (GE Healthcare, Little Chalfont, Buckinghamshire, UK). Proteins were labeled with primary antibody: anti-Fas B-10 and anti-Fas Ligand (Santa Cruz, Santa Cruz, CA). Immunoreactive bands were detected by anti-mouse HRP or anti-rabbit peroxidase-conjugated secondary antibody (Chemicon, Temecula, CA). Proteins were visualized via enhanced chemiluminescence (ECL detection kit, GE Healthcare, Buckinghamshire, UK).

Statistical analysis

Data are presented as mean±SD for the indicated number of separate experiments. Comparisons between groups were analyzed via Student's *t*-tests. Probability values of $P<0.05$ are considered statistically significant.

Results

Effect of tryptanthrin derivatives on inhibition of proliferation in several cancer cell lines

Tryptanthrin-derived indoloquinazolines were synthesized by condensation. Compounds **1–4** were prepared via Scheme 1 and compounds **5–7** containing dicyanomethylene substituent were made via Scheme 2. Growth inhibition of the series of compounds at 1 μmol/L was measured in MCF-7, HeLa, A498, and SKOV3 cells (Table 1). Compounds **3–5** demonstrate higher than 40% inhibition of proliferation in four cell lines. The IC_{50} of compounds **3–5** is lower than 1×10^{-6} mol/L in four cell lines among which A498 and MCF-7 are more sensitive to the compounds. Compound **4** is the most potent tryptanthrin derivative presenting cytotoxic activity. The IC_{50} is 3.10×10^{-7} mol/L in A498 and 3.9×10^{-7} mol/L in MCF-7, respectively (Table 2).

Table 1. Structures and anticancer activities of tryptanthrin derivatives.

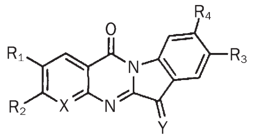

Compound	R_1	R_2	X	R_3	R_4	Y	Growth inhibition (%)[a]			
							MCF-7	HeLa	A498	SKOV3
1	H	H	C	H	H	O	26	24	17	8
2	OMe	OMe	C	H	H	O	0	12	-8	6
3	H	H	C	I	H	O	40	48	68	47
4	H	H	N	H	H	O	77	46	78	50
5	H	H	C	H	H	A[b]	41	49	45	46
6	OMe	OMe	C	H	H	A[b]	17	3	-5	8
7	Cl	H	C	H	H	A[b]	5	10	10	17
Doxorubicin							95	95	84	86

[a] Growth inhibition was calculated as the ratio of cell viability of the treated cells over the untreated cells. Data are representative of three independent experiments. The compounds tested were at the concentration of 1 μmol/L.

[b] A=

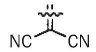

Table 2. The IC_{50} of compounds **3–5** (μmol/L).

Cell line	Doxorubicin	**3**	**4**	**5**
MCF-7	0.14±0.03	1.50±0.28	0.39±0.31	1.40±0.12
HeLa	0.59±0.02	1.86±0.21	2.34±0.36	1.26±0.17
SKOV3	0.33±0.03	1.20±0.29	2.00±0.39	8.51±0.23
A498	0.58±0.04	0.65±0.04	0.31±0.02	1.48±0.13

Cell viability was determined using the MTT assay. Data are presented as mean±SD of triplicate determinations.

Apoptotic biomarkers in MCF-7 cells treated with compounds 3–5

DNA fragmentation is a characteristic feature of apoptosis. Fragmented DNA, subjected to electrophoresis on an agarose gel, is in a manner of ladders, suggesting the formation of nucleosomes in apoptosis progress. When MCF-7 cells were treated with compound **4** at 10^{-6} mol/L for 6 h, DNA ladders appeared. The intensity of the ladders significantly increased after the cells were longer exposed to compound **4** up to 9 h (Figure 2A). A delayed appearance (up to 40–44 h) of the DNA ladders was shown in cells treated compounds **3** or **5**.

Cell cycle analysis of MCF-7 cells was performed after 24 h of incubation with compounds **3**, **4**, or **5** at 10^{-6} mol/L. As compared to the untreated cells, compounds **3** and **5** did not induce considerable cell cycle arrest, while an important sub-G_1 peak appeared in cells treated with compound **4** at 10^{-6} mol/L for 24 h (Figure 2B).

Activity of caspase-3/7 which is essential for apoptosis was determined in MCF-7 cells treated with compounds **3**, **4**, and **5**. After exposure to compound **4** at 10^{-6} mol/L for 36 h, caspase-3/7 activity was elevated about five folds, compared to the control (Figure 2C). Only a slight increase in caspase-3/7 activity was observed in cells with compound **3** or **5**.

Changes in Fas and Fas ligand levels in MCF-7 cells treated with compound 4

To verify if compound **4**-induced apoptosis was mediated

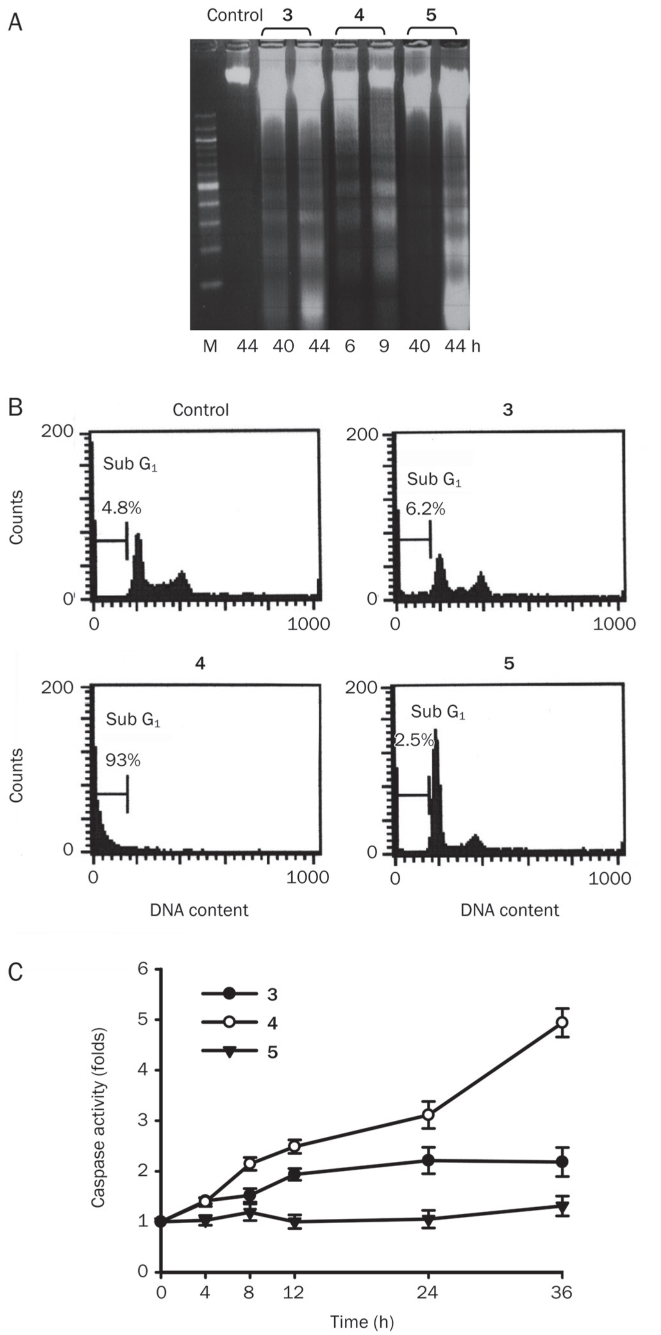

Figure 2. Apoptotic biomarkers induced by compounds **3**, **4**, and **5** in MCF-7 cells. (A) DNA fragmentation in MCF-7 cells treated with compounds **3**, **4**, and **5**. DNA extracts from the cells treated with the compounds for various time periods as indicated were electrophoresed on a 2% agarose gel and stained with ethidium bromide. (B) The cell cycle analysis of MCF-7 cells with compounds **3**, **4**, and **5**. DNA contents of MCF-7 cells were analyzed by flow cytometry. (C) Caspase 3/7 activity assays. MCF-7 cells were exposed to 10^{-6} mol/L compound **3** (●), **4** (○), or **5** (▼) for 0–36 h and subjected to casepase 3/7 assay. Assays were performed in triplicates for each treatment.

through Fas/Fas ligand pathway, Fas and Fas ligand proteins were determined in MCF-7 cells treated with compound **4**. Immunoblots against anti-Fas B-10 and anti-Fas Ligand showed that Fas level was raised within 2 h after cells treated with compound **4** and followed by an increase in Fas ligand level in cells after 4 h exposure to compound **4**. The promptly elevated Fas did not sustain since a drop of Fas levels was detected in cells with 4–8 h exposure to compound **4** (Figure 3).

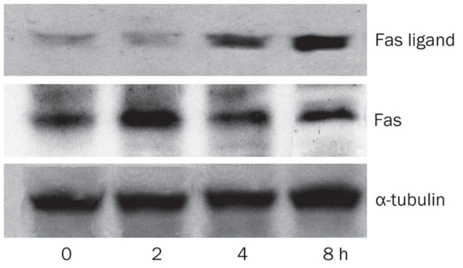

Figure 3. Fas and Fas ligand levels increased by compound **4**. MCF-7 cells were treated with 10^{-6} mol/L **4** for different periods of time. Proteins from whole-cell extracts were electrophoresed and Western blots were performed as described in Methods. α-tubulin was used as the loading controls. Data are representative of three independent experiments.

Effect of tryptanthrin and its derivatives in drug-resistant MCF-7 cells

Instead of compounds **3–5** bearing cytotoxicity through activation of apoptosis process, the rest tryptanthrin derivatives, compounds **1**, **2**, **6**, and **7**, were not as potent as to inhibit cell proliferation. The IC_{50} of compound **1** was 8.23 μmol/L and compounds **2**, **6**, and **7** existed greater than 10 μmol/L of IC_{50} in MCF-7 cells, compared to doxorubicin of which the IC_{50} was 0.14 μmol/L in MCF-7 cells. In terms of non-cytotoxic agents, compounds **1**, **2**, **6**, and **7** did not or slightly show growth inhibition in neither MCF-7 nor MCF-7/adr cells (Table 3). However, in combination with doxorubicin, compounds **1** and **7** at 10^{-6} mol/L enhanced growth inhibition activity of doxorubicin in MCF-7/adr cells from 19% to 63% and 53%, respectively.

Table 3. MTT assays of tryptanthrin derivatives in MCF-7 and MCF-7/adr cells.

	IC_{50} (μmol/L)		Growth inhibition			
			Compounds		Compounds+Dox	
Compound	MCF-7	MCF-7/adr	MCF-7	MCF-7/adr	MCF-7	MCF-7/adr
1	8.23±0.37	5.63±0.53	26%	18%	95%	63%
2	>100	>100	0%	0%	99%	25%
6	>10	>10	17%	1%	97%	12%
7	>100	>100	5%	0%	92%	53%
Dox	0.14±0.03	9.13±0.51	95%	19%		

10^{-6} mol/L tryptanthrin derivatives and 10^{-6} mol/L doxorubicin were used for growth inhibition assays. Data are from three independent experiments.

Etoposide which is also a cytotoxic agent is capable of inducing drug resistance in MCF-7 cells, named MCF-7/vp. MCF-7/vp cells were still viable when the cells were treated with compound **1**, **7**, or etoposide, while the cells turned out to be sensitive to the combination of either compound **1** plus etoposide or compound **7** plus etoposide at concentrations of 1 μmol/L of each (Figure 4). Compound **7** raised a higher chemosensitizing activity than compound **1** in MCF-7/vp cells. On the contrary, MCF-7/adr cells are more susceptible to compound **1** for enhancing cytotoxicity of doxorubicin.

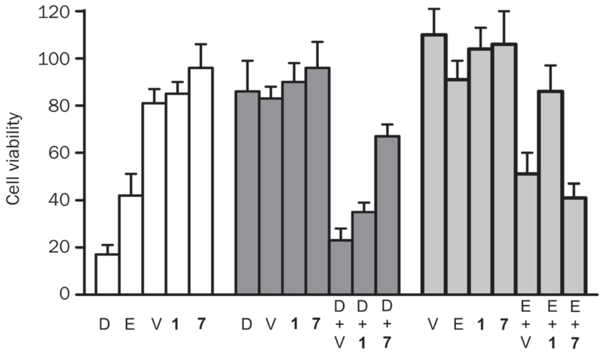

Figure 4. Effect of compounds **1** and **7** on sensitizing drug-resistant cells to doxorubicin or etoposide. Cells were treated with 10^{-6} mol/L doxorubicin (D), 10^{-6} mol/L etoposide (E), 10^{-5} mol/L verapamil (V), 10^{-6} mol/L compound **1** (1) or **7** (7), either alone or in combination as indicated for 5 d. The percentage of cell viability of MCF-7 (□), MCF-7/adr (■), and MCF-7/vp (▨) was determined by the MTT assay. Data are presented as mean±SD of triplicate determinations.

Similar to compounds **1** and **7**, a known MDR reversing agent verapamil at 10^{-5} mol/L did not exist cytotoxicity though, it enhanced cytotoxicity of doxorubincin and etoposide in MCF-7/adr and MCF-7/vp, respectively, with various degrees.

Disscussion

Tryptanthrin and its derivatives have been reported to exhibit anticancer effects[15, 17]. In this study, we synthesized a series of tryptanthrin-derived indoloquinazolines, designated as compounds **1–7** and screened for anticancer activity. Compouds **1–4** were prepared by condensation as shown in Scheme 1 and compounds **5–7** containing dicyanomethylene substituents were made via Scheme 2. Among those, either compound **3** bearing an iodine substituent at R_3 or compound **4** with nitrogen containing A ring demonstrated effective growth inhibition activity. The oxygen or dicyanomethylene substitution at Y was indifferent to the cytotoxicity in four cell lines. In fact, the malononitrile derivatives, including compounds **5–7** with dicyanomethylene substitution at Y, exhibited various degree of cytotoxicity. Methoxy group at R_1 and R_2 or chlorine at R_1 did not influence the growth inhibition activity. According to structure-activity relationship analysis, modification of tryptanthrin skeleton with substituents in A ring or D ring enhances the cytotoxicity, except the dimethoxy substitution in A ring. Nitrogen-containing A ring seems to be important to increase cytotoxicity. The cytotoxicity is structure-dependent rather than cell line-dependent because a compound presents similar degree of cytotoxicity in all four cell lines. Tryptanthrin derivatives exhibited double-stranded DNA binding activity[17], which may in part account for structure-dependent cytotoxicity.

Although the tryptanthrin derivatives are not as potent as doxorubicin to kill the cancer cells, compounds **3–5** exhibit growth inhibition (40%–77%) activity in MCF-7, HeLa, A498, and SKOV3 cells. The apoptotic biomarkers, including DNA fragmentation, elevated sub-G_1 accumulation and an increase in caspase 3/7 activity, appear in the cells treated with compounds **3–5** with various intensities. Among them, compound **4** is of most importance. Mechanisms other than apoptosis may be involved in cell growth inhibition by compounds **3** and **5**. The MCF-7 cell line which has been described to be Fas-sensitive[18] undergoes apoptosis through Fas/Fas ligand activation. The Fas/Fas ligand system is a key signaling transduction pathway of apoptosis in cells and tissues. Engagement of Fas by a Fas-ligand lead to the formation of a protein complex known as death-inducing signaling complex and permit acute execution of apoptosis by caspase-8 activation[19]. Reimer *et al*[20] reported that the selection process leading to highly aggressive breast tumor variants might be enhanced by Fas ligand-mediated tumor fratricide, eventually a possible target for novel therapeutic strategies. Our results show the consistent elevation of Fas ligand levels by treating compound **4** in different time periods (4 and 8 h), in spite of the various levels of Fas with time. Elevation of Fas ligand levels may be important to engage Fas and activate the Fas/Fas ligand-mediated apoptosis afterwards. Results may suggest that compound **4** resents cytotoxicity in part through Fas/Fas ligand pathway. It is possible of crosstalk between extrinsic pathway and intrinsic pathway through mitochondria. It would be worth examining if tryptanthrin derivatives induce mitochondria-related signals such as cytochrome c, caspase 9, *etc*. To differentiate activity of caspase 8 from caspase 9 enables us to confirm which pathway induced by compound **4**. It would be interesting to check this issue in the future experiments.

Resistance to chemotherapy has been remaining a major cause of treatment failure in cancer patients. Development of adjuvant agents to circumvent MDR becomes a new trend in cancer chemotherapy. Many attempts, such as inhibition of MDR-related genes, to overcome MDR have been proposed[21]. Inhibition of *MDR1* gene function, either by blocking P-gp function or inhibiting *MDR1* gene expression, has been one of the most extensive studies[22, 23]. In this report, compounds **1** and **7** in combination with cytotoxic agents such as doxorubicin and etoposide enhance cytotoxicity of the cytotoxic agents against drug-resistant MCF-7 cells. It suggests that compounds **1** and **7** can sensitize drug-resistant cells to the cytotoxic agents, which may contribute to reverse multidrug resistance. It is still unclear the mechanisms involved in MDR reversal. As compound **1** largely sensitizes MCF-7/adr rather than MCF-7/vp, it is speculated that compound **1** may act on *MDR1* gene or its function. Nevertheless, compound **7** sensitizes both MCF-7/adr and MCF-7/vp, implying either MDR1-related or MRP-related pathway is affected by compound **7**.

In summary, tryptanthrin-derived indoloquinazolines synthesized in this study undergo multiple ways to display their anticancer activity via inducing cytotoxicity against MCF-7 cells by compounds **3–5** or evoking resistance reversal activity by compounds **1** and **7** in MCF-7/adr and MCF-7/vp cells. Further modification of the tryptanthrin skeleton, based on the structure-activity relationships sketched in this study, becomes important to develop novel anticancer agents bearing either cytotoxicity or resistance reversal activity.

Acknowledgements

This work was supported by National Science Council grant NSC 89-2320-B-002-232. We thank Dr Chih-hsin YANG for kindly providing drug-sensitive and drug-resistant cell lines.

Author contribution

Yen-hui CHEN designed and corresponded to the study. Ji-wang CHERN and Hui-ting CHEN synthesized a series of indoloquinazoline compounds. Sung-tsai YU and Yi-fan CHIU performed the experiments. Sung-tsai YU, Tzer-ming CHEN, and Yen-hui CHEN analyzed data and prepared the manuscript.

References

1 Zakeri Z, Lockshin RA. Cell death: history and future. Adv Exp Med Biol 2008; 615: 1−11.
2 Debatin KM. Apoptosis pathways in cancer and cancer therapy. Cancer Immunol Immunother 2004; 53: 153−9.
3 Thorburn A. Death receptor-induced cell killing. Cell Signal 2004; 16: 139−44.
4 Nagata S, Golstein P. The Fas death factor. Science 1995; 267: 1449−56.
5 Hengartner MO. The biochemistry of apoptosis. Nature 2000; 407: 770−6.
6 Janicke RU, Sprengart ML, Wati MR, Porter AG. Caspase-3 is required for DNA fragmentation and morphological changes associated with apoptosis. J Biol Chem 1998; 273: 9357−60.
7 Ashkenazi A, Dixit VM. Death receptors: signaling and modulation. Science 1998; 281: 1305−8.
8 Liu X, Zou H, Slaughter C, Wang X. DFF, a heterodimeric protein that functions downstream of caspase-3 to trigger dna fragmentation during apoptosis. Cell 1997; 89: 175−84.
9 Luqmani YA. Mechanisms of drug resistance in cancer chemotherapy. Med Princ Pract 2005; 14: 35−48.
10 Honda G, Tabata M. Isolation of antifungal principle tryptanthrin, from Strobilanthes cusia O. Kuntze. Planta Med 1979; 36: 85−90.
11 Honda G, Tabata M, Tsuda M. The antimicrobial specificity of tryptanthrin. Planta Med 1979; 37: 172−4.
12 Schrenk D, Riebniger D, Till M, Vetter S, Fiedler H-P. Tryptanthrins: A novel class of agonists of the aryl hydrocarbon receptor. Biochem Pharmacol 1997; 54: 165−71.
13 Ishihara T, Kohno K, Ushio S, Iwaki K, Ikeda M, Kurimoto M. Tryptanthrin inhibits nitric oxide and prostaglandin E2 synthesis by murine macrophages. Eur J Pharmacol 2000; 407: 197−204.
14 Kimoto T, Hino K, Koya-Miyata S, Yamamoto Y, Takeuchi M, Nishizaki Y, *et al*. Cell differentiation and apoptosis of monocytic and promyelocytic leukemia cells (U-937 and HL-60) by tryptanthrin, an active ingredient of Polygonum tinctorium Lour. Pathol Int 2001; 51: 315−25.
15 Sharma VM, Prasanna P, Seshu KV, Renuka B, Rao CV, Kumar GS, *et al*. Novel indolo[2,1-b]quinazoline analogues as cytostatic agents: synthesis, biological evaluation and structure-activity relationship. Bioorg Med Chem Lett 2002; 12: 2303−7.
16 Yu ST, Chen TM, Tseng SY, Chen YH. Tryptanthrin inhibits MDR1 and reverses doxorubicin resistance in breast cancer cells. Biochem Biophys Res Commun 2007; 358: 79−84.
17 Chen GS, Bhagwat BV, Liao PY, Chen HT, Lin SB, Chern JW. Specific stabilization of DNA triple helices by indolo[2,1-b]quinazolin-6,12-dione derivatives. Bioorg Med Chem Lett 2007; 17: 1769−72.
18 Gibson S, Tu S, Oyer R, Anderson SM, Johnson GL. Epidermal growth factor protects epithelial cells against Fas-induced apoptosis. requirement for Akt activation. J Biol Chem 1999; 274: 17612−8.
19 Nagata S. Fas ligand-induced apoptosis. Annu Rev Genet 1999; 33: 29−55.
20 Reimer T, Herrnring C, Koczan D, Richter D, Gerber B, Kabelitz D, *et al*. FasL: Fas ratio -- a prognostic factor in breast carcinomas. Cancer Res 2000; 60: 822−8.
21 Gottesman MM, Ling V. The molecular basis of multidrug resistance in cancer: The early years of P-glycoprotein research. FEBS Lett 2006; 580: 998−1009.
22 Kimura Yasuhisa MS-yMMUK. Mechanism of multidrug recognition by MDR1/ABCB1. Cancer Sci 2007; 98: 1303−10.
23 Xu D, Hyunmin K, Michael F, Juliano RL. Strategies for inhibition of MDR1 gene expression. Mol Pharmacol 2004; 66: 268−75.